Measurements Of Jet Properties In Small Collision Systems At LHC With ALICE

Thesis submitted for the degree of

Doctor of Philosophy (Science)

In Physics (Experimental)

By

Prottoy Das

Department of Physics

University of Calcutta

2024

Dedicated to my parents

Mrs. Sankari Das & Mr. Arun Das

and my younger brother

Mr. Prem Das

for their endless support and motivation in every aspect of my life

Declaration

I do hereby declare that the thesis entitled **"Measurements Of Jet Properties In Small Collision Systems At LHC With ALICE"** is based on my research works under the supervision of Dr. Sidharth Kumar Prasad. These works are original and have not been submitted earlier as a whole or in part for a degree/diploma at this or any other Institution/University.

Prottoy Das

Acknowledgement

This thesis is the outcome of the last few years of my work at the Department of Physical Sciences, Bose Institute, Kolkata. Embarking on this Ph.D. journey has been an incredible odyssey, and I am deeply grateful to everyone who has played a part in making it a reality.

First and foremost, I would like to thank God. You have given me the power to believe in my passion and pursue my dreams. I could never have reached the end of this journey without the faith I have in you, the Almighty. Thank you for the strength and courage you provided me.

I am indebted to my family members for their unwavering love, unconditional support, encouragement, and understanding throughout this endeavor. Their belief in me has been my source of strength and motivation. I want to express my deepest gratitude to my father, Mr. Arun Das, and my mother, Mrs. Sankari Das, who have been my source of inspiration for pursuing higher studies all along. Their consistent sacrifice and never-ending kindness enabled me to overcome the barriers of life and society and pursue the quest for scientific discoveries. I will never forget the unfathomable role of my younger brother, Mr. Prem Das, in making my journey congenial during the period of my doctoral research. Despite being younger than me, he has always been there for me and never got tired of picking me up when I felt down. Prem has always taken heed of family responsibilities and was watchful to protect the rest of us from any adversary. I feel fortunate to have him as my brother, who has been the source of happiness in my life since he was born.

I owe an immense debt of gratitude to my supervisor, Dr. Sidharth Kumar Prasad. His unwavering support, expert guidance, and genuine interest in my research have been the cornerstones of my academic growth. From navigating through conceptual and theoretical perspectives to refining experimental methodologies, his mentorship has been invaluable every step of the way. While giving me considerable freedom in my research direction,

Dr. Prasad always ensured that the outputs of the research works maintained a certain standard. In the early years of my Ph.D., Dr. Prasad introduced me to research works prevalent in my research domain and helped me better understand my project. In the later years, he encouraged me to become a more self-reliant researcher. Dr. Prasad's positive, encouraging, and active leadership helped me grow into an autonomous researcher. I am truly fortunate to have had the privilege of learning from such a dedicated and inspiring mentor.

I am indebted to many people who have taught me physics, especially my teachers, for their kind assistance with giving wise advice, helping with various problems and applications, and whatnot. Their words have deeply motivated me and given me inspiration for my dream of research in physics. Special thanks to Dr. Saikat Biswas, Prof. Supriya Das, Prof. Sanjay Kumar Ghosh, Prof. Somshubhro Bandhyopadhyay, Prof. Rajarshi Ray, Prof. Sibaji Raha, Prof. Dhurba Gupta, Prof. Achintya Singha, Prof. Soumen Roy, Prof. Sushanta Duttagupta, Prof. Swapan Saha, Prof. Debapriyo Syam, Prof. Mahendra Sinha Roy, Prof. Shibshankar Bhattacharyya, Prof. Soumya Mitra, Prof. Gopinath Laha, Prof. Sankhasubhra Nag and Prof. Sankar De for their invaluable classes on various fields of physics. I am very much thankful to Dr. Saikat Biswas and Prof. Supriya Das for their clear guidance, valuable suggestions and continuous support and encouragement throughout the journey. I am grateful to Prof. Sanjay Kumar Ghosh for his inspiring way of teaching physics and motivating me to pursue research.

I would like to express my gratitude to Prof. Subhasis Chattopadhyay, VECC, and Prof. Bedangadas Mohanty, NISER, for being inspirational figures to me, always giving support and invaluable suggestions and motivating me to move forward. I would like to thank Dr. Sabyasachi Ghosh, IIT Bhilai, for always being willing to provide assistance and valuable suggestions regarding the journey of my research career. I am grateful to Prof. Claude Pruneau, Wayne State University (USA), for his invaluable advice and

suggestions regarding the multiplicity-dependent study of jet properties in pp collisions using PYTHIA simulation.

I extend my appreciation to the faculty and staff of the Department of Physical Sciences for fostering an enriching academic environment conducive to research and learning. I especially would like to thank Prof. Uday Bandyopadhyay, Director of Bose Institute, for providing me with the infrastructure and necessary facilities to conduct my research uninterruptedly. I would like to acknowledge my institutional fellowship for carrying out my research.

It has been an enriching journey as a member of the esteemed ALICE Collaboration at CERN. I am deeply grateful to all my colleagues in the collaboration for their unwavering support throughout this endeavor. I extend my heartfelt gratitude to Prof. Marco Van Leeuwen, the Spokesperson of the ALICE Collaboration, for his invaluable guidance, encouragement, and insightful suggestions, which have been instrumental in shaping my research journey. I am indebted to the convenors and members of the Physics Working Group of Jets (PWG-JE) and the Physics Analysis Group of Jet Substructures (PAG-JSUB) within ALICE. The vibrant discussions, intellectual exchanges, and constructive feedback received from this group have been instrumental in refining my research work and enhancing its scientific rigor. I am particularly grateful to the Analysis Review Committee for their meticulous review of my analysis with ALICE data. Their valuable insights, suggestions, and critiques have significantly contributed to the improvement and validation of my research findings. Special thanks are due to the members of the Conference Committee and the Editorial Board in ALICE for their continuous assistance and support during the review processes of my presentation materials and proceedings. Their constructive feedback and meticulous attention to detail have ensured the quality and integrity of my contributions at various conferences and publications. I sincerely appreciate the collaborative spirit and camaraderie within the ALICE Collaboration, which has fostered

a stimulating and conducive environment for scientific exploration and discovery.

I would like to express my deep gratitude to my colleagues for providing a stimulating and fun environment in which to learn and grow. I am incredibly grateful to my colleagues and some of my dearest friends, Mr. Abhi Modak, Ms. Debjani Banerjee, Dr. Sayak Chatterjee, Mr. Tanmay Saha, Dr. Arindam Sen, Mr. Arnab Karmakar, Ms. Nishita Mandal and Mr. Sayan Chakraborty for helping me get through the difficult times, and for all the emotional support, camaraderie, entertainment, and caring they provided. Special thanks to my dearest lab-members-cum-friends, Mr. Abhi Modak and Ms. Debjani Banerjee, for their endless help, intellectual exchanges and debates, and moral and emotional support, and for always being there as my indispensable sources of motivation during the long journey of Ph.D. Their friendship has made the journey more enjoyable and meaningful.

I would like to express my warmest thanks to my childhood friends, school friends, and my friends at the graduate level. I am fortunate to have friends like Mr. Kuntal Sen and Dr. Ayan Nandi, who have always been there for me, and I can not thank them enough.

I would like to express my sincere thanks to my senior scholars at Bose Institute. I am especially grateful to Dr. Rathijit Biswas, Dr. Debojit Sarkar, Dr. Sanchari Thakur, Dr. Sumit Saha, Dr. Shreya Roy, Mr. Prateek Ghoshal, and Dr. Deeptak Biswas for providing assistance in my studies and mental support in pursuing research in physics. I would also like to thank my juniors, visiting students, project students and summer students, Mr. Mintu Halder, Mr. Subir Mandal, Ms. Rudrapriya Das, Mr. Debanjan Roy, Mr. Shubham Jaiswal, Ms. Krishna Nivedita G, Mr. Vipul Pant, Mr. Shivam Maharaj, Mr. Umesh Kumar, Mr. Sunil Batesar, Mr. Soumyadip Mandal, Ms. Subhalaxmi Mishra and many others, who have helped me in every possible way.

I would always be in debt to the singers like Hemanta Mukhopadhyay, Manna Dey, Kishor Kumar, Ed Sheeran and many more, whose songs kept me sane at difficult times.

Last but not the least, I would also like to thank myself for never giving up. My

future self should always remember the version of me during the Ph.D., who kept working through diseases, headaches, imposter syndrome, depression, heartbreak, festivals, birthdays, bright and gloomy mornings, sunny and rainy evenings, sleepless nights, happy salary weeks and gloomy end-of-month weeks, global pandemic, and endless researcher's blocks. Over these past few years, I have learned research and developed specific skills. I am incredibly grateful for this opportunity. I am also very proud of myself for keeping at it and making it to the finishing line.

Prottoy Das

Abstract

Heavy-ion collisions at ultra-relativistic energies produce a deconfined state of partonic matter, known as quark-gluon plasma (QGP). Small collision systems, previously thought not to form QGP, show collectivity at the LHC energies, challenging the conventional notion, albeit no observation of jet production suppression, a prominent signature of QGP formation. Study of internal jet properties and their multiplicity dependence in small collision systems, i.e., proton-proton (pp) and proton-lead (p–Pb) collisions, presents a promising approach, given their sensitivity to both the perturbative and non-perturbative aspects of quantum chromodynamics.

This thesis reports the measurements of jet properties, including mean number of charged-particle multiplicity within jets and jet fragmentation function in minimum bias pp and minimum bias and central p–Pb collisions at the nucleon-nucleon center-of-mass energy of 5.02 TeV using the ALICE experiment at CERN, for charged-particle leading jets in the transverse momentum (p_{T}) interval of 20–100 GeV/c. Jets are reconstructed from charged particles at mid-rapidity using the sequential recombination anti-k_{T} algorithm with jet resolution parameter $R = 0.4$. The corrected distributions (corrected for instrumental effects and underlying events) are presented in comparison to various theoretical MC model predictions. Jet p_{T}-dependent modifications of jet fragmentation are observed between minimum bias p–Pb and pp collisions and between central and minimum bias p–Pb collisions, marking the first experimental observation of jet modification in p–Pb collisions at LHC energies. Surprisingly, MC models without implementation of QGP-medium effects, are also found to qualitatively reproduce the features of jet modification observed in data.

This thesis also presents the study of internal jet properties, including jet shape and fragmentation function in minimum bias and high-multiplicity pp collisions at the center-

of-mass energy of 13 TeV using PYTHIA 8 Monte Carlo event generator. The study is performed in presence and absence of multiparton interactions and color reconnection mechanisms of PYTHIA. Significant jet modification is observed in high-multiplicity events compared to minimum bias ones for low-p_{T} jets. The main sources contributing to the observed jet modification are found to be multiparton interactions, color reconnection and increase in the fraction of gluon-initiated jets in high-multiplicity events.

List of Publications

Thesis is based on the following publications

Peer-reviewed Journals:

- "*Jet modification in absence of QGP-medium: the role of multiparton interactions and color reconnection*"

  Prottoy Das, Abhi Modak, Debjani Banerjee, Rathijit Biswas, Supriya Das, Sanjay K. Ghosh, Sibaji Raha, Sidharth Kumar Prasad

  Chinese Phys. C 48 (2024) 1, 013105, DOI: 10.1088/1674-1137/ad0b6c

  arXiv:2209.00972 [hep-ph]

- "*Measurement of charged-particle leading jet properties in pp and p-Pb collisions at* $\sqrt{s_{\mathrm{NN}}} = 5.02$ *TeV* "

  ALICE Collaboration

  Paper Committee Members: **Prottoy Das (Chair)**, Debjani Banerjee, Sidharth Kumar Prasad

  Target Journal: *Journal of High Energy Physics*

  To be submitted (under review within ALICE Collaboration)

Conference Proceedings:

- "*Measurement of leading charged-particle jet properties in p–Pb collisions at* $\sqrt{s_{\mathrm{NN}}}$ *= 5.02 TeV with ALICE*"

  Prottoy Das for the ALICE Collaboration

  arXiv:2307.15369 [nucl-ex]

  Submitted to Springer Nature as a Proceeding of XXV DAE-BRNS High Energy Physics Symposium 2022

- "*Investigating jet modification in high multiplicity proton-proton collisions at 13 TeV using PYTHIA8 event generator*"

  Prottoy Das, Abhi Modak, Debjani Banerjee, Rathijit Biswas, Supriya Das, Sanjay K. Ghosh, Sibaji Raha, Sidharth Kumar Prasad

  Submitted to Springer Nature as a Proceeding of XXV DAE-BRNS High Energy Physics Symposium 2022

- "*Multiplicity dependence of intra-jet properties in small collision systems with ALICE* "

  Prottoy Das for the ALICE Collaboration

  PoS LHCP2022 (2023) 303

- "*Measurement of charged-particle jet properties in p–Pb collisions at* $\sqrt{s_{\rm NN}}$ = *5.02 TeV with ALICE* from *Dynamics of Hot QCD Matter – Current status and developments* "

  Prottoy Das for the ALICE Collaboration

  Int. J. Mod. Phys. E 31 (2022) 12 (pages: 37–40)

- "*Multiplicity and* $\sqrt{s}$ *dependent study of jet properties in pp collisions at LHC energies*"

  Prottoy Das, Abhi Modak, Rathijit Biswas, Sidharth Kumar Prasad, Supriya Das, Sanjay K. Ghosh, Sibaji Raha

  DAE Symp.Nucl.Phys. 64 (2019) (pages: 824–825)

ALICE Analysis Note:

- "*Centrality dependence of charged-particle jet properties in p-Pb collisions at* $\sqrt{s_{\rm NN}}$ = *5.02 TeV with ALICE*"

  Prottoy Das, Debjani Banerjee and Sidharth Kumar Prasad

  https://alice-notes.web.cern.ch/node/1310

Other Publications

Peer-reviewed Journals:

- "*Effect of magnetic field on jet transport coefficient $\hat{q}$* "

  Debjani Banerjee, **Prottoy Das**, Souvik Paul, Abhi Modak, Ankita Budhraja, Sabyasachi Ghosh, Sidharth Kumar Prasad

  Pramana - J Phys 97, 206 (2023), DOI: 10.1007/s12043-023-02683-1 arXiv:2103.14440 [hep-ph]

- "*Multiplicity dependence of charged-particle intra-jet properties in pp collisions at $\sqrt{s} = 13$ TeV* "

  ALICE Collaboration

  Paper Committee Members: Debjani Banerjee (chair), **Prottoy Das**, Sidharth Kumar Prasad

  Submitted to *European Physical Journal C - Particles and Fields*, arXiv:2311.13322 [hep-ex]

Conference Proceeding:

- "*Effect of magnetic field on jet transport coefficient $\hat{q}$ for quark and gluon jets* "

  Debjani Banerjee, Souvik Paul, **Prottoy Das**, Abhi Modak, Ankita Bhudraja, Sabyasachi Ghosh, Sidharth Kumar Prasad

  DAE Symp. Nucl. Phys. 65 (2022) (pages: 696–697)

ALICE Analysis Note:

- "*Charged-particle jet properties and their multiplicity dependence in pp collisions at $\sqrt{s} = 13$ TeV with ALICE*"

  Debjani Banerjee, **Prottoy Das** and Sidharth Kumar Prasad

  https://alice-notes.web.cern.ch/node/1303

Contents

List of Figures

List of Tables

“Begin at the beginning," the King said, very gravely, “and go on till you come to the end: then stop."

— Lewis Carroll, Alice in Wonderland

Chapter 1

Introduction

Throughout history, people have always wanted to understand things they can not see or know. Their curiosity keeps them exploring new things, even though they are often scared of what they might find. As time goes on, they learn more, but they also realize how much they still do not know about how everything started, how the universe was created, and why things are the way they are now. From a long time ago to now, discoveries in science have changed the way people live and think. Things that used to seem impossible are now real achievements, showing how much people keep wanting to learn. But even with all this progress, there are still big mysteries we do not understand, like where life came from and why we are here. Ideas come and go, and each new one brings more questions. With each change in how we see the world, we find new things to wonder about, like how everything in the universe is connected in ways we can not see or feel. We are not sure where science will take us next, but through the lens of physics, we hope to learn more about how everything works, unlocking endless possibilities. With this knowledge, we can look forward to a better future and appreciate the mysteries around us even more.

This thesis outlines some of the recent developments in high-energy particle and nuclear physics. The first part of this introductory chapter provides a theoretical background

about our understanding of the universe at its smallest scales. Particular emphasis is placed on the strong nuclear interaction and the methods employed to investigate it at high energies. The second part presents an overview of jets, the main actors in this thesis. The chapter concludes with brief outlines of the work presented in subsequent chapters of the thesis.

1.1 Theoretical background

1.1.1 The fundamental forces

To date, we are aware of four fundamental forces of nature: gravitational, electromagnetic, weak, and strong[1], classified based on the type of the interaction. Each of these forces follows certain laws of nature described by particular physical theory and governs the dynamics of particles. Each fundamental force or interaction is mediated by the exchange of a particle known as the mediator, which transmits the force between the interacting particles. The mediators and the interacting particles can be categorized into two different classes based on their intrinsic spin: bosons and fermions, respectively (see Sec. 1.1.2 for more details). The mediators for the gravitational and electromagnetic interactions are gravitons and photons, respectively. The intermediate vector bosons, $W\pm$ and Z, mediate the weak interaction, whereas the strong interaction is mediated by gluons.

The gravitational force is in action between all physical objects of different sizes, ranging from elementary particles to astronomical bodies. The classical theory of gravitational interaction is Newton's law of gravitation, which Einstein generalized including the relativistic case with his famous general theory of relativity. The gravitational force is always attractive. The interaction strength of gravitational interaction is proportional

[1]The four forces can be reduced to three as the Glashow-Weinberg-Salam (GWS) theory considers the electromagnetic and weak forces as different manifestations of a single electroweak force.

to the product of the masses of the interacting objects and is, therefore, very small in comparison to other forces for sub-atomic particles.

Electromagnetic force comes into play whenever there are objects with electric charge. Electric charge comes in two polarities, positive and negative, in contrast to gravitational force where mass can only be positive, and therefore the electromagnetic force can be either attractive or repulsive[2]. The physical theory that explains electromagnetic interactions is known as electrodynamics. Maxwell established the classical formulation of electrodynamics more than a century ago and the theory aligned with Einstein's special theory of relativity, which it served as the primary source of inspiration for. Feynman, Tomonaga, and Schwinger refined the quantum theory of electrodynamics during the 1940s. The magnitude of the electromagnetic force is proportional to the product of the electric charges of the interacting objects and gets reduced with increasing distance between the objects. Being the second strongest among all the fundamental forces, only after the strong force, it is one of the important forces to consider on a sub-atomic scale.

The weak and strong forces are mostly in action in the sub-atomic nuclear scales ($<$ 1 fermi = 10^{-15} m) and are, therefore, known as nuclear forces. The weak nuclear force mostly accounts for the radioactive decays, e.g., nuclear beta decay, decays of pions, muons, and a lot of strange particles. The theory of weak interactions, often referred to as flavordynamics, was proposed by Fermi in 1933. Lee and Yang, Feynman and Gell-Mann, among many others, improved the theoretical description in the 1950s, and Glashow, Weinberg, and Salam brought it to its current state (GWS theory) in the 1960s.

The strong nuclear force is the strongest fundamental force within the nuclear scale and is experienced by particles having color charges. Color charge comes in three categories, termed red (R), green (G), and blue (B)[3]. Although color charge was not yet a notion, Yukawa's groundbreaking work in 1934 laid the groundwork for the physical theory of

[2]Charges of opposite polarities attract and those of same polarities repulse each other.
[3]Although they have nothing to do with the mentioned colors in the visible spectrum.

strong interaction, now known as chromodynamics, which later found its solid ground in the 1960s and 1970s. Due to the particular nature of its potential, the strong force acts as an attractive force between particles moving away from each other and as a repulsive force when the particles are close or coming toward each other.

The strong and weak nuclear forces, along with the electromagnetic force, are described theoretically by what is commonly known as the Standard Model of particle physics [1–3]. A brief description of the Standard Model is presented in the next section.

1.1.2 The Standard Model of particle physics

Regarded as one of the most successful theories in physics, the Standard Model of particle physics describes the fundamental constituents of matter and their interactions. It has correctly predicted the behavior of the particles and their interactions in numerous experiments carried out over several decades. Below is an overview of the key components and principles of the Standard Model.

The foundation of the Standard Model is the notion that fundamental particles, which fall into two main classes, bosons, and fermions, make up all the matter in the universe. Figure 1.1 shows the various families of fundamental particles in the Standard Model.

1. **Fermions**: Fermions are particles that make up matter. They have half-integral spins and adhere to the Pauli exclusion principle, according to which no two fermions can occupy the same quantum state simultaneously. Fermions in the Standard Model can be further classified into two categories:

- **Quarks**: Quarks are elementary particles that experience the strong nuclear force due to their color charges. They are bound together to form hadrons, which can be further categorized into baryons (combinations of three quarks or anti-quarks) and mesons (made up of a quark and an anti-quark). The quark family consists of six varieties or “flavors" of quarks: up, down, charm, strange, top, and bottom, and

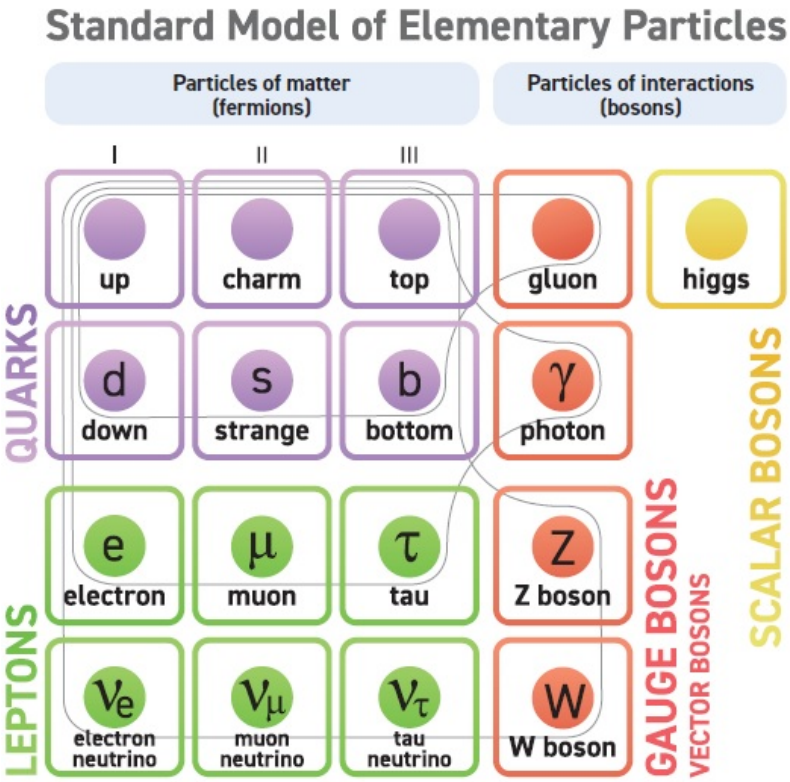

Figure 1.1: Fundamental constituents of the Standard Model of Particle Physics [4].

their corresponding anti-particles.

- **Leptons**: Leptons are also elementary particles that are not affected by the strong nuclear force; instead, they can be affected by the electromagnetic and weak nuclear forces. The electron, muon, tau, corresponding neutrinos, and their respective anti-particles form the lepton family. Because of their small masses and incredibly weak interactions with other particles, neutrinos are particularly fascinating particles whose experimental detection itself is very challenging.

2. **Bosons**: Particles called bosons act as mediators between the fundamental forces of nature. They have integral spins and do not obey the Pauli exclusion principle, which means that multiple bosons can occupy the same quantum state simultaneously, unlike fermions. Bosons in the Standard Model come in four varieties:

- **Photon**: Photons are the mediators or force carriers of the electromagnetic interactions between charged particles.
- **Gluon**: Gluons are responsible for mediating the strong nuclear force that binds quarks together within protons, neutrons, and other hadrons.
- $W\pm$ **and** Z **Bosons**: $W\pm$ and Z bosons are the mediators of the weak nuclear force.
- **Higgs Boson**: By means of the so-called Higgs mechanism, the Higgs boson, a unique kind of particle, introduces mass to other particles. Its discovery in 2012 validated a key component of the Standard Model.

As delineated in the preceding section (Sec. 1.1.1), the following three fundamental forces of nature elucidate the interactions among these particles:

- **Electromagnetic force**: Described by quantum electrodynamics (QED) [5–7], which incorporates the principles of quantum mechanics and special relativity
- **Weak nuclear force**: Described by the electroweak theory [2, 8, 9], which unifies the electromagnetic and weak forces into a single theory
- **Strong nuclear force**: Described by quantum chromodynamics (QCD) [10], which explains the interactions between quarks mediated by gluons

The strong interaction is essentially responsible for the very existence of atomic nuclei. In general, approximately 95% of the universe's observable mass can be attributed to the strong interaction. Its current theoretical description, i.e., quantum chromodynamics, which is also relevant in the context of the studies presented in this thesis, is discussed in the next section.

1.1.3 Quantum Chromodynamics: theory of strong interaction

One of the main pillars of the Standard Model of particle physics is quantum chromodynamics (QCD), which offers a thorough framework for understanding the behavior of quarks and gluons, the building blocks of matter, within the influence of the strong nuclear force. The theory of QCD is governed by the laws of quantum mechanics and the symmetries of the underlying theory.

QCD is a quantum field theory that follows the non-Abelian gauge symmetry and, therefore, allows gluons to interact with each other, unlike photons which mediate the electromagnetic force. Gluons possess a combination of color and anti-color charges. On the other hand, quarks can interact not only through the exchange of gluons but also through the exchange of virtual quark-antiquark pairs, leading to a complicated network of interactions that describes the dynamics of the strong interaction.

Another important consequence of QCD being a quantum field theory that follows the non-Abelian gauge symmetry is that the coupling constant of strong interaction α_s (also known as the strong coupling constant) is a universal one in the sense that the quarks must couple to gluons with the same strength. However, the strength of the strong coupling constant varies depending upon the scales of energy and/or distance at which the interaction occurs. Due to this running nature of the strong coupling constant, the strong force has a number of unique and noteworthy characteristics. Asymptotic freedom [11] is one such characteristic that manifests at high energies or small distances. At these scales, the QCD coupling constant becomes small, i.e., the strong force that holds quarks and gluons together decreases, enabling them to behave nearly like free particles. This characteristic of QCD arises from the anti-shielding of color charges, which is completely different from that in the case of QED, where electric charges (positive and negative) effectively shield themselves from each other. Due to the small values of the coupling constant, perturbation theory can be applied, which helps to make accurate predictions for

high-energy processes in particle collisions possible.

On the other hand, confinement [12], a phenomenon where quarks and gluons are bound together within color-neutral composite particles (hadrons) like protons, neutrons, mesons, and so on, is another important characteristic exhibited only by the strong force at large distances or low energies. This comes from a strong, non-linear coupling constant that ensures the entrapment of quarks and gluons inside the hadrons by increasing the binding energy with increasing distances. The mechanism underpinning confinement dictates the non-perturbative aspects of QCD, and despite significant theoretical and computational efforts, it still remains as one of the most important unresolved issues in modern physics.

In the non-perturbative domain, the spontaneous breaking of chiral symmetry [13–15] is another important characteristic of strong interaction. This results in the production of hadrons, such as protons and neutrons, which make up the majority of the mass of hadrons. Effective Field Theories [16–18] and Lattice QCD [19–21] are two theoretical methods that can be used to describe the non-perturbative regime of strong interactions.

To have a thorough understanding of any type of interaction, it is necessary to understand the behavior of extended many-body systems subjected to that interaction. QCD also provides the opportunity to study a many-body system consisting of quarks and gluons, known as Quark-Gluon Plasma (QGP), at extremely high temperatures and/or densities. The formation and characteristics of QGP that constitute a fascinating realm of study within the field of high-energy physics, are discussed in detail in the next section.

1.1.4 The Quark-Gluon Plasma

It is believed that the Quark-Gluon Plasma existed in the early cosmos, just a few microseconds after the Big Bang, when energy densities and temperatures were incredibly high. Modern experiments replicate QGP-like conditions in the laboratory by colliding heavy ions (e.g., gold, lead nuclei, etc.) at relativistic speeds in particle accelerators such as the

Large Hadron Collider (LHC) at CERN and the Relativistic Heavy Ion Collider (RHIC) at BNL. It is a novel state of matter in which two key properties of low-temperature QCD, color confinement and breaking of chiral symmetry, disappear [22–24]. To understand the formation of QGP and its unique characteristics, one needs to explore the complex interplay of quantum chromodynamics, extreme temperatures, and extreme energy densities; and the best approach to do so is to understand the evolution of a heavy-ion collision at ultra-relativistic energies.

1.1.4.1 Formation of QGP in heavy-ion collisions

Colliding heavy ions at ultra-relativistic energies yields enough energy density to produce the QGP, a deconfined state of QCD matter made up of quarks and gluons in the laboratory. However, due to the color confinement property of QCD, the produced quarks and gluons can not be isolated and can only be detected in the form of their bound states, i.e., hadrons, in the detector. The creation and evolution of the QGP in a heavy-ion collision, ultimately leading to production of the hadrons, can be factorized in the following succession of stages, as schematically depicted in Fig. 1.2:

- **Initial state:** The initial state can be described by the wave functions of the incoming heavy ions. These wave functions are universal and independent of the scattering processes involved.

- **Interactions with large momentum transfer:** Partons coming from the colliding nuclei undergo scatterings with large momentum transfer (large Q^2[4]). These processes, termed as hard scatterings, lead to the production of high-momentum quarks and gluons. Due to their shorter wavelengths, these partons interact with other partons on a microscopic level and lose energy via both bremsstrahlung radiation [26–28] and elastic collisions [29] while traversing through the produced

[4] Q^2: squared momentum transfer between partons

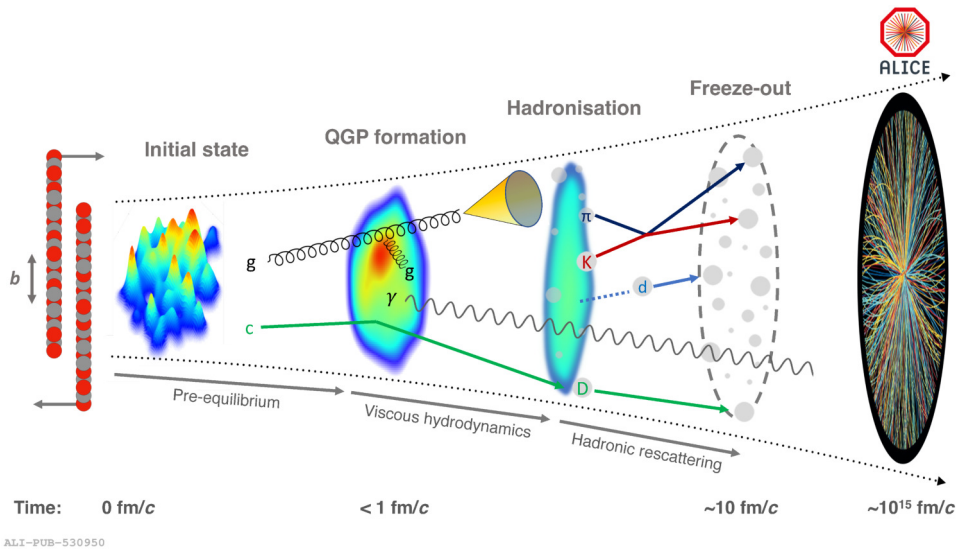

Figure 1.2: Evolution of a heavy-ion collision at LHC energies. Figure is taken from Ref. [25].

partonic medium. These partons eventually undergo fragmentation processes, leading to collimated partonic showers, known as jets, and their fragmentation patterns typically get modified due to the jet-medium interactions, in comparison to the vacuum-like collisions where no QGP-medium is formed.

- **Interactions with small momentum transfer:** Interactions between the partons mostly involve small amount of momentum transfer and generate a pre-equilibrated parton gas. These partons essentially determine the initial energy density and entropy deposition in the collision region and such interactions cause a lumpiness in the initial density profile as shown in Fig. 1.2, resulting from the fluctuations in the nuclear matter distribution. The pre-equilibrium phase where these small-Q^2 interactions usually take place, are weakly coupled. These interactions then produce even softer partons, leading to the formation of a strongly coupled QGP phase.

- **Equilibration and expansion of the QGP:** The formed partonic medium soon attains equilibrium state. This equilibrated partonic medium, known as the QGP

medium, cools down through expansion. The expansion is driven by multiple interactions among the constituents of QGP as their mean free path in most of the cases are substantially smaller than the size of the produced QGP medium. The initial non-uniformity in the energy distribution gives rise to pressure gradients inside the medium and influences its expansion. Usually the length scales of these gradients exceed the mean free path and therefore the evolution can be explained as a liquid as considered in case of hydrodynamics, giving rise to a radial flow and a common velocity field in the outward direction from the collision center.

- **Formation of hadrons:** During the evolution, once the QGP cools down to below the transition temperature, the partons will start to form hadrons. Typically the hadronization of the partonic shower produced from a hard-scattered parton, i.e., a jet, occurs in a similar fashion as in the case of vacuum-like collisions. Partons with lower momenta may combine with other partons with a similar space and momenta to form hadrons via coalescence.

- **Chemical freeze-out of hadrons:** In presence of enough energy density, the newly formed hadrons may undergo inelastic interactions, consequently leading to evolution of their chemical composition, i.e., new species of hadrons. This continues until the temperature goes below a certain value, known as the chemical freeze-out temperature [30–32], whereafter the particle composition gets fixed.

- **Kinetic freeze-out of hadronic interactions:** Even after the chemical freeze-out happens, the particles can still have enough momenta to undergo elastic interactions between themselves and this stops at the kinetic freeze-out temperature. Beyond this temperature, the momenta of the particles are somewhat fixed since there are no further interactions.

- **Free-streaming of the final-state hadrons to the detector:** Finally the particles

travel and reach the detectors placed in various directions and get detected by giving signals in the detector readouts.

1.1.4.2 Characteristics of QGP

The most striking feature of the quark-gluon plasma is its unique properties that are different from those of conventional matter and other phases of high-energy systems. These characteristics emerge from the fundamental properties of quarks, gluons, and their interactions under extreme conditions:

1. **Deconfinement:** The deconfinement of quarks and gluons from their typical bound states within hadrons is the most prominent feature of the QGP. Within the QGP, quarks and gluons are not restricted to specific protons, neutrons, or other hadronic structures; rather, they are free to roam around, despite being within a strongly interacting environment.

2. **Collective behavior:** The Quark-Gluon Plasma exhibits collective behavior like a fluid characterized by hydrodynamic flow. This fluid-like behavior emerges from the strong interactions among quarks and gluons, leading to the formation of a strongly coupled, nearly perfect liquid.

3. **Temperature and energy density:** The QGP exists at extreme temperatures on the order of several hundred thousand to several million kelvin, far exceeding the critical temperature for QCD phase transition. Similarly, the energy density of the QGP is several orders of magnitude higher than that of ordinary nuclear matter.

4. **Partonic medium:** Within the Quark-Gluon Plasma, quarks and gluons retain their individual identities, albeit in a highly interacting and thermalized state, and yet they show collectivity as a partonic medium.

1.1.5 Experimental signatures of QGP

The two most distinctive signatures of QGP formation in heavy-ion collisions, among several others, are collective flow [33] and jet quenching [34] (energy loss of high-momentum partons), which are discussed in detail in this section.

1.1.5.1 Collective flow

Experimental studies show that QGP mostly behaves like a fluid, and its properties can be understood in the light of relativistic hydrodynamics. One of the important experimental probes to do so is the collective or hydrodynamic flow. The initial geometry of a heavy-ion collision is characterized by the impact parameter (distance between the centers of the two colliding nuclei) of the collision, and in case of non-central collisions, the overlap region of the nuclei takes an almond-like shape. This initial state spatial anisotropy gives rise to an azimuthal anisotropy in the momentum space and leads to non-uniform pressure gradients in the azimuthal plane, which is transverse to the reaction plane (defined by the beam direction and the direction along which the impact parameter of the collision is measured), as illustrated in Fig. 1.3. The pressure gradient is large in the direction along the reaction plane (in-plane) and small in the direction transverse to the reaction plane (out-of-plane).

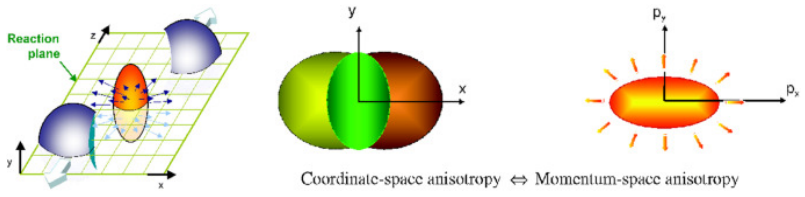

Figure 1.3: Anisotropic flow in heavy-ion collisions. Figure is taken from Ref. [35].

Since the non-uniform pressure gradients act on the medium in the azimuthal plane, utilizing the Fourier Transform of the azimuthal angular distribution of the final-state

particles, their invariant cross-section can be calculated by the expression:

$$E\frac{d^3N}{d^3p} = \frac{1}{2\pi}\frac{d^3N}{p_{\mathrm{T}}dp_{\mathrm{T}}dyd\varphi} = \frac{1}{2\pi}\frac{d^2N}{p_{\mathrm{T}}dp_{\mathrm{T}}dy}\left(1 + \sum_{1}^{\infty} 2v_n cos(n[\varphi - \Psi_{\mathrm{r}}])\right) \tag{1.1}$$

where φ is the azimuthal angle transverse to the reaction plane, $p_{\mathrm{T}} = \sqrt{p_{\mathrm{x}}^2 + p_{\mathrm{y}}^2}$ is the transverse momentum, $y = \frac{1}{2}ln(\frac{E+p_z}{E-p_z})$ is the rapidity[5], v_n's are the anisotropic flow coefficients and Ψ_{r}'s are the reaction plane angles. v_n quantifies the strength of the n-th harmonic component in the azimuthal angular distribution. v_1 is called the flow coefficient for the directed flow; similarly, v_2 for elliptic flow, v_3 for triangular flow and so on. The survival of the momentum anisotropy leads to non-zero elliptic flow as the produced medium experiences a larger force in the direction of the higher pressure gradient, as shown in Fig. 1.3 (right). On the other hand, semi-central collisions, where the non-uniformity of the pressure gradient is more than other types of collisions, are expected to have larger elliptic flow.

A measurement of the elliptic flow, v_2 for different species of identified charged particles in several centrality bins of Pb–Pb collisions by ALICE [37] is shown in Fig. 1.4. For $p_{\mathrm{T}} < 2-3$ GeV/c, mass-ordering of v_2 is observed for the particle species considered, the lighter particles having larger v_2 than others. This indicates the presence of a strong radial flow that gives an additional isotropic boost to all particles along with the prevailing effect of the anisotropic expansion of the medium [38–40]. The particles are found to be grouped according to their number of constituent quarks, supporting the quark coalescence hypothesis of particle production. Due to the larger radial flow in central collisions than that in peripheral ones, the crossing between mesons and baryons occurs at higher p_{T} in the central collisions compared to the other. As expected, the semi-central collisions (40–50%) are found to exhibit larger v_2 compared to the other types of collisions.

[5]For a detailed description of the observables used in relativistic kinematics, such as rapidity, please see Ref. [36].

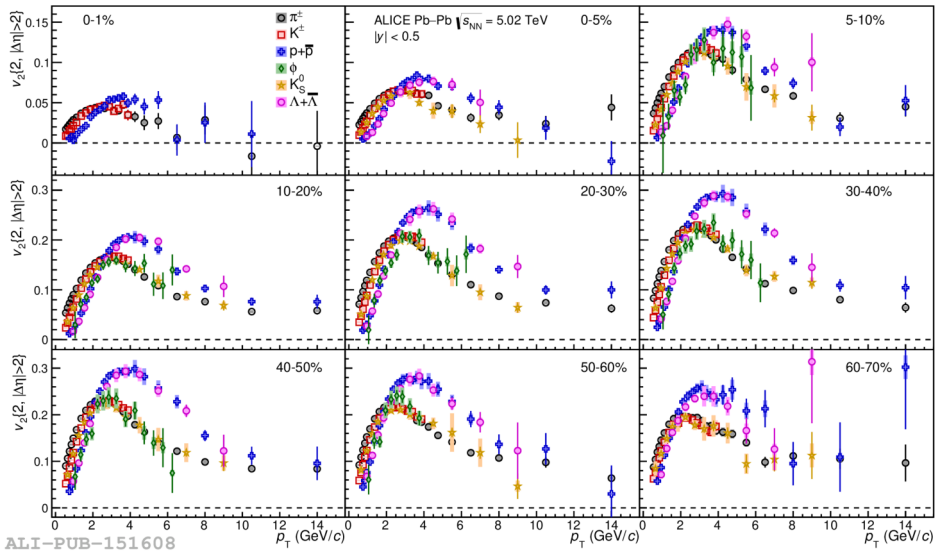

Figure 1.4: The p_{T}-differential v_2 of $\pi^{\pm}$, $\mathrm{K}^{\pm}$, p+$\overline{\mathrm{p}}$, $\Lambda+\overline{\Lambda}$, $\mathrm{K}^0_{\mathrm{S}}$, and the ϕ-meson for various centrality classes of Pb–Pb collisions at $\sqrt{s_{\mathrm{NN}}}$ = 5.02 TeV [37].

1.1.5.2 Jet quenching

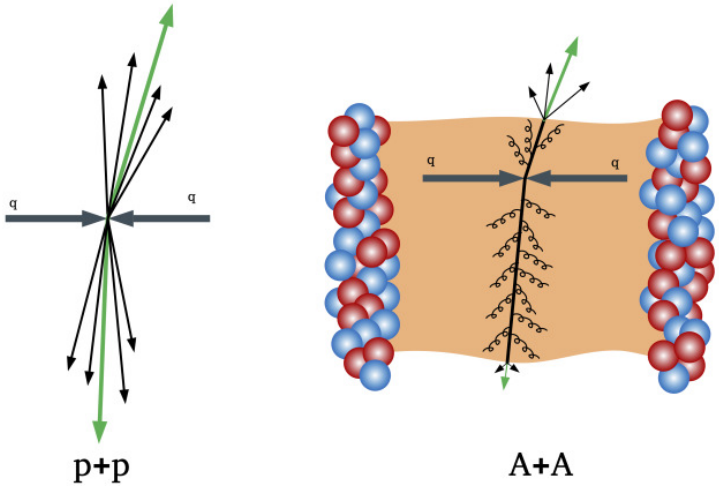

Figure 1.5: Jet quenching in presence of QGP-medium. Figure is taken from Ref. [41].

As mentioned earlier, jets are collimated showers of particles produced from the fragmentation and hadronization of hard-scattered partons. Due to their inherent sensitivity to QCD at different momentum scales Q^2 of interactions, jets and their properties provide a unique tool to probe the evolution of QGP through several stages. Typically, the pro-

duction rates and transverse momentum distributions of initial hard-scattered partons can be estimated from first principles of perturbative QCD due to the fact that jets are hard probes (produced from large momentum transfer between initiating partons). However, in presence of medium, not only the probability of radiation in the form of gluons get enhanced by medium-induced emissions of gluons compared to the case of vacuum (no medium is formed), but also the initial parton undergoes one or more elastic collisions during its journey through the partonic medium. Both phenomena lead to loss of energy and momentum of the resulting jet as well as modification of the substructure inside the jet. These effects are collectively known as jet quenching. Figure 1.5 illustrates the process of partonic energy loss [42–44] in heavy-ion (A+A or AA) collisions compared to pp collisions.

There are several jet observables that have different degrees of sensitivity to the jet quenching effects. The most straightforward and simplest way of measuring the jet quenching effects experimentally is through the jet nuclear modification factor. It is defined as,

$$R_{\mathrm{AA}}(p_{\mathrm{T}}) = \frac{d^2N_{\mathrm{AA}}/dp_{\mathrm{T}}d\eta}{\langle T_{\mathrm{AA}}\rangle d^2\sigma_{\mathrm{nn}}/dp_{\mathrm{T}}d\eta} \tag{1.2}$$

where N_{AA} is the yield of jets in AA collisions, σ_{nn} is the jet cross-section in nucleon-nucleon (e.g., pp) collisions, $\langle T_{\mathrm{AA}}\rangle$ is the average number of binary nucleon-nucleon collisions per AA collision scaled by the inelastic nucleon-nucleon cross-section. If the heavy-ion collision had been a simple superposition of the nucleon-nucleon collisions, the value of the nuclear modification factor R_{AA} would be at unity. Measurements of jet R_{AA} in heavy-ion collisions to date have always shown $R_{\mathrm{AA}} < 1$, indicating suppression of jet production in presence of the QGP-medium, as expected. A measurement of jet R_{AA} by ATLAS [45] in Pb–Pb collisions for different centrality classes are shown in Fig. 1.6. Significant jet quenching is observed, and a larger effect of jet quenching is present in more central collisions. This is expected as the more central collision will produce a medium of

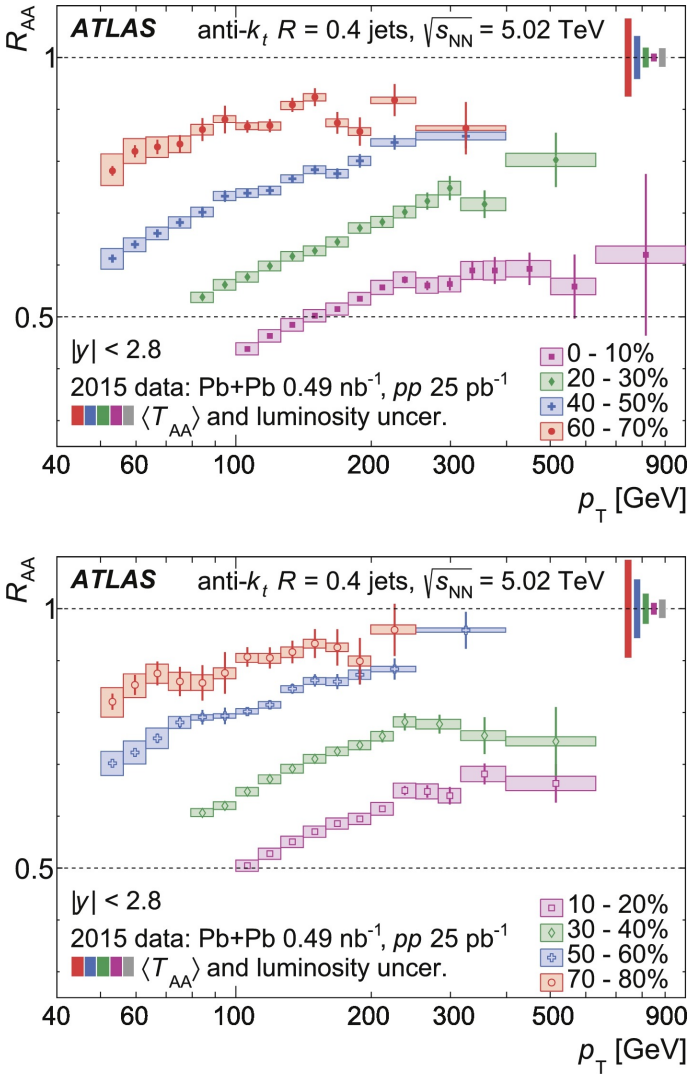

Figure 1.6: The R_{AA} values as a function of jet p_T for different centrality intervals of Pb–Pb collisions at $\sqrt{s_{NN}}$ = 5.02 TeV [45].

a larger volume, thereby introducing more energy loss. The jet quenching effect decreases with increasing jet momentum since a highly energetic jet will be more likely to escape the QGP-medium compared to a jet with lower energy.

Apart from R_{AA}, jet substructure and fragmentation properties are also essential observables to probe the jet quenching effects since they are more sensitive to the splitting process of the initiating parton into shower of partons and also to the hadronization process, and therefore carry more information about both the perturbative and non-perturbative as-

pects of jet-medium interactions. So, the modification of these jet properties in presence of medium compared to the vacuum-like case is a crucial observation of jet quenching effects. The path-length dependence of jet quenching can also be studied through the measurements of imbalance in dijets (jets produced back-to-back in φ, from the initiating partons undergoing large momentum transfer), known as dijet asymmetry, in heavy-ion collisions.

1.1.6 Small collision systems

As discussed previously, heavy-ion collisions generate sufficient energy density to produce a Quark-Gluon Plasma (QGP) medium, whose presence is confirmed by various distinct signatures. To observe most of these signatures accurately, a clean, vacuum-like environment is necessary as a reference where QGP formation is not anticipated. Such a reference allows comparison to understand the effects of QGP-medium creation in heavy-ion collisions. Proton-proton (pp) collisions and proton-lead (p–Pb) collisions serve as essential references, as they typically are not expected to reach the energy density required for QGP formation. These collisions are also commonly known as small collision systems. Among these, pp collisions are the simplest and cleanest, lacking initial state nuclear matter effects. Besides serving as a crucial reference for QGP formation, pp collisions offer the advantage of being amenable to precise perturbative Quantum Chromodynamics (QCD) calculations. This enables accurate predictions of particle behavior, such as inclusive and heavy-flavor jet production cross sections. In essence, jet measurements in pp collisions serve as rigorous tests of perturbative QCD within the realm of high-energy physics.

On the other hand, collisions of p–Pb, where Quark-Gluon Plasma (QGP) effects are also not anticipated, play an additional complementary role. They act as a reference to account for and distinguish the initial state effects caused by the presence of a nucleus, known as cold nuclear matter (CNM) effects, from the effects caused by the presence of a

QGP-medium, called hot nuclear matter effects. One of the most apparent and unique CNM effects is the alteration of parton distribution functions in the initial state of the collision compared to those in proton-proton (pp) collisions. Furthermore, various CNM effects are expected in p–Pb collisions due to the presence of the lead (Pb) nucleus, including multiple scatterings of nucleons, absorption of produced particles by the nucleus, and partonic energy loss within cold nuclear matter. It is important to note that these effects are also expected to occur in heavy-ion collisions. Therefore, measurements of p–Pb collisions are crucial to disentangle the CNM effects from the QGP effects, both of which have distinct impacts in heavy-ion collisions.

It is worth noting that the theoretical explanation provided earlier is based on the assumption that there is no Quark-Gluon Plasma (QGP) formation in small collision systems. However, this notion was challenged during the LHC era, as numerous experimental measurements began exhibiting distinct features, typically associated with heavy-ion collisions, in small collision systems, particularly at high multiplicity [46–57].

Figure 1.7a shows the first experimental observation of the heavy-ion-like features in small systems where the double ridge extended in pseudorapidity in the two-particle correlation distributions was observed in high-multiplicity pp collisions [51], hinting toward collectivity in such systems. However, the nuclear modification factor, which is an essential observable to understand the formation of QGP-medium in heavy-ion collisions, has also been measured for p–Pb collisions in different centrality classes, with minimum bias pp collisions serving as the vacuum-like reference. Intriguingly, no suppression of the nuclear modification factor has been observed to date [58, 59]. Figure 1.7b shows one such measurement of the jet nuclear modification factor. These observations have prompted several intriguing questions: Could Quark-Gluon Plasma (QGP) be generated in small collision systems? What mechanisms are at play during the early stages of these collisions, potentially leading to a high enough energy density for a phase transition of

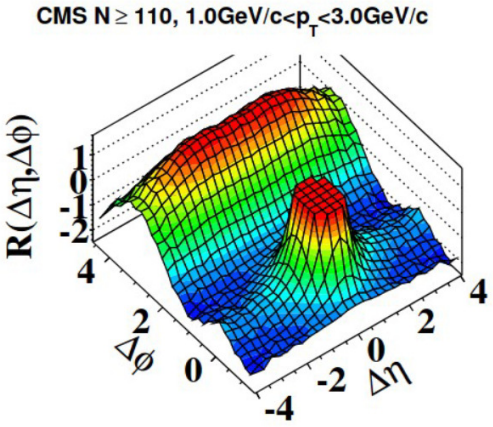

(a) 2-D two-particle correlation functions for 7 TeV pp collisions at high multiplicity [51]. The sharp near-side peak from jet correlations is cut off to better illustrate the structure outside that region.

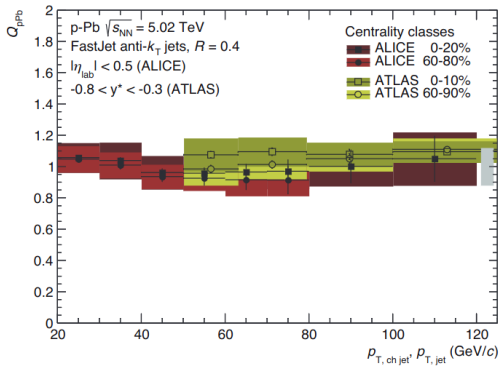

(b) Nuclear modification factor of charged jets measured by ALICE [58] in comparison to the same for full jets measured by ATLAS [59].

nuclear matter? If QGP is not produced in small collision systems, what could be causing the observed QGP-like signatures?

These fundamental questions have garnered considerable attention and represent a unique aspect of the LHC physics program. This situation has motivated the research presented in this thesis, which delves into investigating this scenario within small collision systems, primarily focusing on internal jet properties. These properties are highly sensitive to the intricacies of parton showering and hadronization processes, making them promising avenues for understanding the origin of heavy-ion-like signatures in small collision systems. The following section provides a concise introduction to the basics of jets and their properties, as well as their importance in the field of high-energy physics.

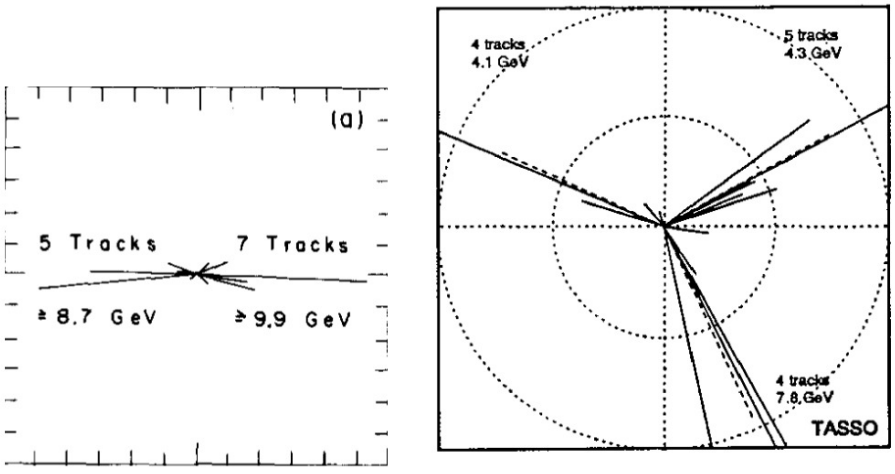

Figure 1.8: Observation of 2-jet final states [60] (left) and 3-jet final states [61] (right) in the TASSO experiment.

1.2 Jets

1.2.1 Jets as experimental evidence for quarks and gluons

As mentioned earlier, jets arise from the fragmentation of high-momentum quarks or gluons, which subsequently hadronize. Therefore, jets serve as proxies for the initial hard-scattered partons (quarks and gluons). The first experimental evidence of quarks dates back to high-energy electron-positron collisions conducted in the TASSO experiment at DESY [60]. The collimated sprays of particles produced back-to-back in the transverse plane, as shown in the left panel of Fig. 1.8, provided confirmation of the existence of quark jets.

On the other hand, the observation of three-jet events, also known as Mercedes-style events (as depicted in the right panel of Fig 1.8), was another significant discovery at the TASSO experiment [61] which demonstrated consistency with the theoretical expectation of gluon bremsstrahlung radiation at a large angle from one of the partons, thereby confirming the existence of gluons, which contribute to the formation of the third jet.

1.2.2 Jet production: theoretical understanding

After experiencing significant momentum transfer, hard-scattered partons emit collimated showers of additional partons, as each newly produced parton from the initial ones may radiate, leading to a cascading effect. Since jets serve as hard probes originating from high-Q^2 processes, perturbative Quantum Chromodynamics (pQCD) theory can be applied. This allows for the estimation of the total scattering cross section by assuming QCD factorization [62], which enables the separate treatment of perturbative and non-perturbative contributions.

For the scattering between two protons resulting in the production of hadrons, the total cross section can be mathematically expressed as [63]:

$$\sigma^{pp\to hadrons} = f_i(x_1, Q^2) \otimes f_j(x_2, Q^2) \otimes \sigma^{ij\to kl}(x_1, x_2, Q^2) \otimes D_k(z, Q^2) \otimes D_l(z, Q^2) \quad (1.3)$$

Here, $f_i(x, Q^2)$ represents the parton distribution functions (PDF) for the colliding protons, indicating the probability of a parton i carrying the momentum fraction x at a scattering energy scale Q^2. The term $\sigma^{ij\to kl}(x_1, x_2, Q^2)$ denotes the cross section for the scattering between a partonic system with partons i and j, resulting in a partonic system with partons k and l. This scattering cross section can be calculated using perturbation theory provided the corresponding strong interaction coupling constant, $\alpha_s(Q^2)$, is sufficiently small. $D_k(z, Q^2)$ is the fragmentation function containing information about the fragmentation and hadronization processes undergone by parton k to result in final-state hadrons with momentum fraction z. The fragmentation of a parton with a given energy scale Q^2 is typically assumed to be independent of the process from which the parton is produced.

The PDF and fragmentation function are non-perturbative features that are encapsulated into universal objects and are measured experimentally across a wide kinematic range of x and Q^2. The Dokshitzer-Gribov-Lipatov-Altarelli-Parisi (DGLAP) equations

can then be employed to evaluate the evolution of the PDFs with Q^2. The remaining components of the equation are perturbatively calculable. Hence, using QCD factorization, it is possible to estimate the jet production rate quite successfully, particularly in the high-transverse-momentum regime.

1.2.3 Jet definition: reconstruction of jets

In principle, employing a jet finding algorithm allows for the clustering of all daughter particles originating from a specific parton, thereby providing access to the parent parton's full energy and momentum. However, defining a jet can be ambiguous, even at the partonic level. For instance, if a quark emits a gluon at small angles relative to the quark, it is typically considered part of the same jet; however, if emitted at large angles, it may be regarded as a separate third jet. To address this ambiguity, the Snowmass Accord [64] was established, setting principles for jet reconstruction that ensure consistency between theoretical and experimental definitions of jets for comparability.

A jet-initiating parton can split into two partons with approximately equal energy moving in the same direction. However, calculating this process in QCD theory is challenging and often leads to divergences. Therefore, it is crucial for jet finding algorithms to be robust against collinear and infrared issues [65]. Collinear and infrared safety ensures that the algorithm can reconstruct the same jets with the same transverse momentum (p_{T}), regardless of the fragmentation process or the presence of numerous soft particles.

Jet finding algorithms [65] can be broadly classified into two categories: cone algorithms and sequential recombination algorithms. Cone algorithms, commonly used in early experimentation, require constituent tracks to fall within a predetermined cone radius, resulting in strictly circular-shaped jets. Some of the early cone algorithms, like the Iterative Cone algorithms with Progressive Removal (IC-PR) or with the Split Merge procedure (IC-SM), are susceptible to collinear and infrared issues. The Seedless Infrared

Safe Cone (SISCone) algorithm emerged as an infrared-safe jet reconstruction algorithm, offering better time complexity than other cone algorithms. Additionally, cone algorithms exhibited resilience to effects from the underlying event (UE), making them popular among experimentalists at that time.

On the other hand, sequential recombination algorithms cluster particles using two distance metrics. The first metric, calculated for each particle pair i and j, is based on momentum space information and is defined as:

$$d_{i,j} = \min(p_{\mathrm{T},i}^{2b}, p_{\mathrm{T},j}^{2b}) \frac{\Delta R_{i,j}^2}{R^2} \tag{1.4}$$

where p_{T} represents transverse momentum, R is a user-defined parameter known as the jet resolution parameter (also sometimes called the jet radius), and $\Delta R_{i,j}$ is the distance between particles i and j in the phase space determined by pseudorapidity (η) and azimuthal angle (φ). The parameter b is a generalized parameter and determines the particular type of sequential recombination algorithm. The second metric calculates the distance of each particle from the beam:

$$d_{i,\mathrm{B}} = p_{\mathrm{T},i}^{2b} \tag{1.5}$$

Once these distance metrics are calculated for all the particles, the algorithm finds the smallest value among all of them. If the smallest one is a $d_{i,j}$, the corresponding particle pair (i and j) is combined into a single jet candidate by summing their four momenta. The summation of the four momenta is carried out using one of the reasonable recombination schemes, such as E-scheme, p_{T}-scheme, etc. The individual particles i and j are also removed from the list of particles. If the smallest one is a $d_{i,\mathrm{B}}$, then the particle i is considered as the final jet candidate. This process is repeated until all the particles are included as part of the jet candidates and the distance between the jet axes $\Delta R_{i,j}$ becomes larger than R.

The parameter b influences the shape of reconstructed jets and the order in which particles are clustered. For $b = 1$, the algorithm starts by clustering soft particles first, resulting in jets with non-circular shapes, which are useful for determining background or underlying events. This is commonly known as the k_{T} algorithm.

For $b = 0$, the algorithm becomes p_{T}-independent and clusters particles based solely on spatial closeness in the η-φ phase space, yielding jets with angular ordering resembling the expected pattern from the DGLAP equation theory. This algorithm is known as the Cambridge/Aachen (CA) algorithm. The jets reconstructed using this algorithm are also irregular in shape.

For $b = -1$, the algorithm, known as the anti-k_{T} algorithm [66], starts by clustering harder particles first, resulting in circular cone-like jets with consistent areas. The reconstructed jets are resilient against soft and non-perturbative effects, making it preferable for collision systems with large backgrounds.

1.2.4 Jet observables and their importance

Various jet observables are defined and measured with specific physics objectives in mind. As previously discussed, jets in a vacuum-like environment serve as valuable tools for rigorously testing perturbative Quantum Chromodynamics (pQCD) calculations. This is because they are produced from scatterings with large momentum transfer, resulting in a small strong coupling constant. The ability to utilize pQCD calculations is advantageous, as it allows for highly accurate theoretical predictions of jet production cross sections. Furthermore, it aids in fine-tuning Monte Carlo event generators by comparing theoretical model calculations with experimental data which put constraints on these generators.

Additionally, internal jet properties, such as jet shape, jet fragmentation, and jet substructure observables, offer detailed insights into the evolution of the initiating parton through fragmentation and hadronization processes. These properties encompass both

perturbative and non-perturbative aspects of Quantum Chromodynamics (QCD), making their study crucial for improving our understanding of strong interactions. In addition to hadron-hadron collision systems (e.g., proton-proton (pp) collisions), studying jets in hadron-nucleus collision systems (e.g., proton-lead (p–Pb) collisions) allows to test the impact of cold nuclear matter effects on them. In summary, investigating these observables in vacuum-like systems aids in unraveling the intricate interplay between QCD interactions at various energy scales.

On the other hand, in the presence of a medium, jets lose energy and undergo modifications in their internal structure, including changes in the number and momentum distributions of jet constituents. Medium-induced radiative loss and redistribution of momenta of jet constituents during interactions with the medium lead to the broadening and softening of the jets. Consequently, a multitude of jet observables, ranging from jet momentum spectra to various internal jet properties, exhibit significant suppression and modification compared to those observed in vacuum-like systems. Thus, jets emerge as crucial probes for investigating the formation of Quark-Gluon Plasma (QGP) in heavy-ion collisions.

Given that internal jet properties are sensitive to both perturbative and non-perturbative aspects of QCD, including medium effects, they are considered promising candidates for elucidating the anomalous behavior observed in small collision systems at LHC energies, as discussed in Section 1.1.6.

1.3 About the thesis work

This thesis aims to delve into and analyze the peculiar behavior observed in small collision systems, namely proton-proton (pp) and proton-lead (p–Pb) collisions, especially at high multiplicity. This exploration is conducted through the measurements of jets and their

internal properties, utilizing both experimental data and a Monte Carlo event generator based on perturbative Quantum Chromodynamics (pQCD).

This thesis focuses on measuring internal jet properties for charged-particle jets in pp and p–Pb collisions at the nucleon-nucleon center-of-mass energy $\sqrt{s_{\mathrm{NN}}} = 5.02$ TeV, using data from the ALICE experiment at CERN. Specifically, two internal jet properties, namely the average number of charged-particle jet constituents ($\langle N_{\mathrm{ch}} \rangle$) and the jet fragmentation function (z^{ch}), are measured as a function of jet transverse momentum (p_{T}). The measurements are performed for leading jets with transverse momenta ranging from 20 to 100 GeV/c, for jet resolution parameter $R = 0.4$. The resulting distributions of these jet observables are corrected for instrumental effects and contributions from the underlying event before being compared with theoretical predictions from various Monte Carlo event generators. Additionally, the corrected distributions are compared between minimum bias pp and p–Pb collisions, and between minimum bias and central p–Pb collisions, shedding light on potential jet modifications in small collision systems.

This thesis also delves into the study of the multiplicity dependence of internal jet properties in pp collisions at a center-of-mass energy of 13 TeV, utilizing the PYTHIA 8 Monte Carlo event generator. This investigation examines the possible modifications of jet shape ($\rho(r)$) and jet fragmentation function (z^{ch}) in high-multiplicity pp collisions compared to minimum bias ones. It also explores the underlying physics mechanisms, such as multiparton interactions (MPI) and color reconnection (CR), implemented in PYTHIA 8, to elucidate the observed jet modifications in absence of QGP-medium effects as PYTHIA 8 does not incorporate QGP-medium formation. These mechanisms have shown promise in explaining certain heavy-ion-like features observed in experimental data.

1.4 Organization of the thesis

The thesis is structured as follows:

- This chapter introduces the field of high-energy physics and discusses the significance of jets, laying out the motivation behind the research presented in this thesis.
- Chapter 2 offers a brief overview of the collider facility, the Large Hadron Collider (LHC) located at CERN and the ALICE experimental setup used in this thesis work.
- Chapter 3 delves into the analysis strategy employed for measuring internal jet properties in both proton-proton (pp) and proton-lead (p–Pb) collisions at a center-of-mass energy of 5.02 TeV. Additionally, this chapter presents and discusses the fully corrected results obtained from the analysis.
- Chapter 4 focuses on the study of jet modification in high-multiplicity pp collisions in comparison to the minimum bias ones, at a center-of-mass energy of 13 TeV, using the PYTHIA 8 Monte Carlo event generator.
- The thesis concludes with Chapter 5, which summarizes the work presented in this thesis and offers insights into potential future research directions.

Bibliography

[1] S. L. Glashow, "Partial Symmetries of Weak Interactions," *Nucl. Phys.* **22** (1961) 579–588.

[2] S. Weinberg, "A Model of Leptons," *Phys. Rev. Lett.* **19** (1967) 1264–1266.

[3] P. W. Higgs, "Broken Symmetries and the Masses of Gauge Bosons," *Phys. Rev. Lett.* **13** (1964) 508–509.

[4] "The Standard Model of particle physics." https://shaastramag.iitm.ac.in/first-principles/standard-model-particle-physics.

[5] R. P. Feynman, "Space - time approach to quantum electrodynamics," *Phys. Rev.* **76** (1949) 769–789.

[6] R. P. Feynman, *QED: The Strange Theory of Light and Matter*. Princeton University Press, 10, 2014.

[7] R. P. Feynman, "Mathematical formulation of the quantum theory of electromagnetic interaction," *Phys. Rev.* **80** (1950) 440–457.

[8] S. L. Glashow, "The renormalizability of vector meson interactions," *Nucl. Phys.* **10** (1959) 107–117.

[9] A. Salam and J. C. Ward, "Weak and electromagnetic interactions," *Nuovo Cim.* **11** (1959) 568–577.

[10] E. V. Shuryak, "Quantum Chromodynamics and the Theory of Superdense Matter," *Phys. Rept.* **61** (1980) 71–158.

[11] D. J. Gross, "The discovery of asymptotic freedom and the emergence of QCD," *Proc. Nat. Acad. Sci.* **102** (2005) 9099–9108.

[12] J. Greensite, *An introduction to the confinement problem*, vol. 821. 2011.

[13] J. Goldstone, A. Salam, and S. Weinberg, "Broken Symmetries," *Phys. Rev.* **127** (1962) 965–970.

[14] V. Koch, "Aspects of chiral symmetry," *Int. J. Mod. Phys. E* **6** (1997) 203–250, arXiv:nucl-th/9706075.

[15] JLQCD, H. Fukaya, S. Aoki, S. Hashimoto, T. Kaneko, J. Noaki, T. Onogi, and N. Yamada, "Determination of the chiral condensate from 2+1-flavor lattice QCD," *Phys. Rev. Lett.* **104** (2010) 122002, arXiv:0911.5555 [hep-lat]. [Erratum: Phys.Rev.Lett. 105, 159901 (2010)].

[16] C. P. Burgess, "Introduction to Effective Field Theory," *Ann. Rev. Nucl. Part. Sci.* **57** (2007) 329–362, arXiv:hep-th/0701053.

[17] G. T. Bodwin, E. Braaten, and G. P. Lepage, "Rigorous QCD analysis of inclusive annihilation and production of heavy quarkonium," *Phys. Rev. D* **51** (1995) 1125–1171, arXiv:hep-ph/9407339. [Erratum: Phys.Rev.D 55, 5853 (1997)].

[18] N. Brambilla, A. Pineda, J. Soto, and A. Vairo, "Potential NRQCD: An Effective theory for heavy quarkonium," *Nucl. Phys. B* **566** (2000) 275, arXiv:hep-ph/9907240.

[19] R. Gupta, "Introduction to lattice QCD: Course," in *Les Houches Summer School in Theoretical Physics, Session 68: Probing the Standard Model of Particle Interactions*, pp. 83–219. 7, 1997. arXiv:hep-lat/9807028.

[20] S. Muroya, A. Nakamura, C. Nonaka, and T. Takaishi, "Lattice QCD at finite density: An Introductory review," *Prog. Theor. Phys.* **110** (2003) 615–668, arXiv:hep-lat/0306031.

[21] C. Ratti, "Lattice QCD and heavy ion collisions: a review of recent progress," *Rept. Prog. Phys.* **81** no. 8, (2018) 084301, arXiv:1804.07810 [hep-lat].

[22] N. Cabibbo and G. Parisi, "Exponential Hadronic Spectrum and Quark Liberation," *Phys. Lett. B* **59** (1975) 67–69.

[23] E. V. Shuryak, "Theory of Hadronic Plasma," *Sov. Phys. JETP* **47** (1978) 212–219.

[24] HotQCD, A. Bazavov *et al.*, "Equation of state in (2+1)-flavor QCD," *Phys. Rev. D* **90** (2014) 094503, arXiv:1407.6387 [hep-lat].

[25] ALICE, "The ALICE experiment – A journey through QCD," arXiv:2211.04384 [nucl-ex].

[26] M. Gyulassy and X.-n. Wang, "Multiple collisions and induced gluon Bremsstrahlung in QCD," *Nucl. Phys. B* **420** (1994) 583–614, arXiv:nucl-th/9306003.

[27] R. Baier, Y. L. Dokshitzer, S. Peigne, and D. Schiff, "Induced gluon radiation in a QCD medium," *Phys. Lett. B* **345** (1995) 277–286, arXiv:hep-ph/9411409.

[28] R. Baier, Y. L. Dokshitzer, A. H. Mueller, S. Peigne, and D. Schiff, "Radiative energy loss of high-energy quarks and gluons in a finite volume quark - gluon plasma," *Nucl. Phys. B* **483** (1997) 291–320, arXiv:hep-ph/9607355.

[29] J. D. Bjorken, "Energy Loss of Energetic Partons in Quark - Gluon Plasma: Possible Extinction of High p(t) Jets in Hadron - Hadron Collisions,".

[30] STAR, J. Adams *et al.*, "Experimental and theoretical challenges in the search for the quark gluon plasma: The STAR Collaboration's critical assessment of the evidence from RHIC collisions," *Nucl. Phys. A* **757** (2005) 102–183, arXiv:nucl-ex/0501009.

[31] Z. Fodor and S. D. Katz, "Critical point of QCD at finite T and mu, lattice results for physical quark masses," *JHEP* **04** (2004) 050, arXiv:hep-lat/0402006.

[32] ALICE, J. Adam *et al.*, "Production of light nuclei and anti-nuclei in pp and Pb-Pb collisions at energies available at the CERN Large Hadron Collider," *Phys. Rev. C* **93** no. 2, (2016) 024917, arXiv:1506.08951 [nucl-ex].

[33] U. Heinz and R. Snellings, "Collective flow and viscosity in relativistic heavy-ion collisions," *Ann. Rev. Nucl. Part. Sci.* **63** (2013) 123–151, arXiv:1301.2826 [nucl-th].

[34] M. Gyulassy and M. Plumer, "Jet Quenching in Dense Matter," *Phys. Lett. B* **243** (1990) 432–438.

[35] R. Chatterjee, "Anisotropic flow of photons in relativistic heavy ion collisions," *Pramana* **95** no. 1, (2021) 15.

[36] C. Y. Wong, *Introduction to high-energy heavy ion collisions*. 1995.

[37] ALICE, S. Acharya *et al.*, "Anisotropic flow of identified particles in Pb-Pb collisions at $\sqrt{s_{\rm NN}}$ = 5.02 TeV," *JHEP* **09** (2018) 006, arXiv:1805.04390 [nucl-ex].

[38] P. Huovinen, P. F. Kolb, U. W. Heinz, P. V. Ruuskanen, and S. A. Voloshin, "Radial and elliptic flow at RHIC: Further predictions," *Phys. Lett. B* **503** (2001) 58–64, arXiv:hep-ph/0101136.

[39] D. Teaney, J. Lauret, and E. V. Shuryak, "Flow at the SPS and RHIC as a quark gluon plasma signature," *Phys. Rev. Lett.* **86** (2001) 4783–4786, arXiv:nucl-th/0011058.

[40] S. A. Voloshin, "Transverse radial expansion and directed flow," *Phys. Rev. C* **55** (1997) R1630–R1632, arXiv:nucl-th/9611038.

[41] H. Xing, "Quenching of heavy flavors in heavy-ion collisions." https://indico.fnal.gov/event/10528/contributions/3304/.

[42] X.-N. Wang, "Effect of jet quenching on high p_T hadron spectra in high-energy nuclear collisions," *Phys. Rev. C* **58** (1998) 2321, arXiv:hep-ph/9804357.

[43] M. Gyulassy, P. Levai, and I. Vitev, "NonAbelian energy loss at finite opacity," *Phys. Rev. Lett.* **85** (2000) 5535–5538, arXiv:nucl-th/0005032.

[44] M. Djordjevic and M. Gyulassy, "Heavy quark radiative energy loss in QCD matter," *Nucl. Phys. A* **733** (2004) 265–298, arXiv:nucl-th/0310076.

[45] ATLAS, M. Aaboud *et al.*, "Measurement of the nuclear modification factor for inclusive jets in Pb+Pb collisions at $\sqrt{s_{\mathrm{NN}}}$ = 5.02 TeV with the ATLAS detector," *Phys. Lett. B* **790** (2019) 108–128, arXiv:1805.05635 [nucl-ex].

[46] ALICE, B. B. Abelev *et al.*, "Multiplicity Dependence of Pion, Kaon, Proton and Lambda Production in p-Pb Collisions at $\sqrt{s_{NN}}$ = 5.02 TeV," *Phys. Lett. B* **728** (2014) 25–38, arXiv:1307.6796 [nucl-ex].

[47] ALICE, J. Adam *et al.*, "Multiplicity dependence of charged pion, kaon, and (anti)proton production at large transverse momentum in p-Pb collisions at $\sqrt{s_{\mathrm{NN}}}$ = 5.02 TeV," *Phys. Lett. B* **760** (2016) 720–735, arXiv:1601.03658 [nucl-ex].

[48] CMS, V. Khachatryan *et al.*, "Multiplicity and rapidity dependence of strange hadron production in pp, pPb, and PbPb collisions at the LHC," *Phys. Lett. B* **768** (2017) 103–129, arXiv:1605.06699 [nucl-ex].

[49] CMS, S. Chatrchyan *et al.*, "Observation of Long-Range Near-Side Angular Correlations in Proton-Lead Collisions at the LHC," *Phys. Lett. B* **718** (2013) 795–814, arXiv:1210.5482 [nucl-ex].

[50] ALICE, B. Abelev *et al.*, "Long-range angular correlations on the near and away side in p-Pb collisions at $\sqrt{s_{NN}}$ = 5.02 TeV," *Phys. Lett. B* **719** (2013) 29–41, arXiv:1212.2001 [nucl-ex].

[51] CMS, V. Khachatryan *et al.*, "Observation of Long-Range Near-Side Angular Correlations in Proton-Proton Collisions at the LHC," *JHEP* **09** (2010) 091, arXiv:1009.4122 [hep-ex].

[52] CMS, "Observation of long-range near-side two-particle correlations in pp collisions at $\sqrt{s}$ = 13 TeV,".

[53] ALICE, B. B. Abelev *et al.*, "Long-range angular correlations of π, K and p in p-Pb collisions at $\sqrt{s_{\mathrm{NN}}}$ = 5.02 TeV," *Phys. Lett. B* **726** (2013) 164–177, arXiv:1307.3237 [nucl-ex].

[54] CMS, V. Khachatryan *et al.*, "Evidence for collectivity in pp collisions at the LHC," *Phys. Lett. B* **765** (2017) 193–220, arXiv:1606.06198 [nucl-ex].

[55] ALICE, J. Adam *et al.*, "Enhanced production of multi-strange hadrons in high-multiplicity proton-proton collisions," *Nature Phys.* **13** (2017) 535–539, arXiv:1606.07424 [nucl-ex].

[56] ALICE, J. Adam *et al.*, "Multi-strange baryon production in p-Pb collisions at $\sqrt{s_{\mathrm{NN}}}$ = 5.02 TeV," *Phys. Lett. B* **758** (2016) 389–401, arXiv:1512.07227 [nucl-ex].

[57] ALICE, B. B. Abelev *et al.*, "Multiplicity dependence of the average transverse momentum in pp, p-Pb, and Pb-Pb collisions at the LHC," *Phys. Lett. B* **727** (2013) 371–380, arXiv:1307.1094 [nucl-ex].

[58] ALICE, J. Adam *et al.*, "Centrality dependence of charged jet production in p-Pb collisions at $\sqrt{s_{\mathrm{NN}}}$ = 5.02 TeV," arXiv:1603.03402 [nucl-ex].

[59] ATLAS, G. Aad *et al.*, "Centrality and rapidity dependence of inclusive jet production in $\sqrt{s_{\mathrm{NN}}}$ = 5.02 TeV proton-lead collisions with the ATLAS detector," *Phys. Lett. B* **748** (2015) 392–413, arXiv:1412.4092 [hep-ex].

[60] TASSO, R. Brandelik *et al.*, "Evidence for Planar Events in e+ e- Annihilation at High-Energies," *Phys. Lett. B* **86** (1979) 243–249.

[61] B. H. Wiik, "First Results from PETRA," *Conf. Proc. C* **7906181** (1979) 113–154.

[62] J. C. Collins, D. E. Soper, and G. F. Sterman, "Factorization of Hard Processes in QCD," *Adv. Ser. Direct. High Energy Phys.* **5** (1989) 1–91, arXiv:hep-ph/0409313.

[63] G.-Y. Qin and X.-N. Wang, "Jet quenching in high-energy heavy-ion collisions," *Int. J. Mod. Phys. E* **24** no. 11, (2015) 1530014, arXiv:1511.00790 [hep-ph].

[64] J. E. Huth *et al.*, "Toward a standardization of jet definitions," in *1990 DPF Summer Study on High-energy Physics: Research Directions for the Decade (Snowmass 90)*, pp. 0134–136. 12, 1990.

[65] G. P. Salam, "Towards Jetography," *Eur. Phys. J. C* **67** (2010) 637–686, arXiv:0906.1833 [hep-ph].

[66] M. Cacciari, G. P. Salam, and G. Soyez, "The anti-k_t jet clustering algorithm," *JHEP* **04** (2008) 063, arXiv:0802.1189 [hep-ph].

"One accurate measurement is worth a thousand expert opinions"

— Grace Murray Hopper

Chapter 2

The Experimental facility

This chapter discusses the experimental facility utilized for the measurement presented in this thesis. A brief overview of the Large Hadron Collider (LHC), the accelerator facility where the experiment has been performed, is given in Sec. 2.1. A description of A Large Ion Collider Experiment (ALICE), focusing more on the sub-detectors used for the analysis together with the data processing framework, is presented in Sec. 2.2.

2.1 The Large Hadron Collider (LHC)

The world's largest and highest-energy hadron and ion collider, the Large Hadron Collider (LHC) [1–4], is situated beneath the Swiss-French border at a depth of 50 to 175 meters in a 27-kilometer circular subterranean tunnel. The world's most powerful accelerator, built on the synchrotron principle and running at an ultra-high vacuum of around 10^{-10} to 10^{-11} mbar, is part of the Large Hadron Collider at CERN. The schematic of the CERN accelerator complex is shown in Fig. 2.1. It consists of two beam pipe rings encapsulated in superconducting magnets and a number of additional accelerating facilities. Beams of hadrons and/or ions are accelerated to a speed close to the speed of light in vacuum inside the accelerator rings. The acceleration process is carried out step-by-step, starting

with obtaining the beam particles (proton beam from hydrogen or heavy-ion beams from heavy atoms). The beam particles are then accelerated to energies of 750 keV using radio frequency quadrupole (QRF). Subsequently, the beams gain energy to around 50 MeV before being introduced into the Proton Synchrotron Booster (PSB), which is the first circular accelerator stage. Before being injected into the LHC ring, the particles are first sent into the Proton Synchrotron, which accelerates them to 25 GeV, and then into the Super Proton Synchrotron (SPS), which boosts the energy to 450 GeV prior to injection into the LHC ring.

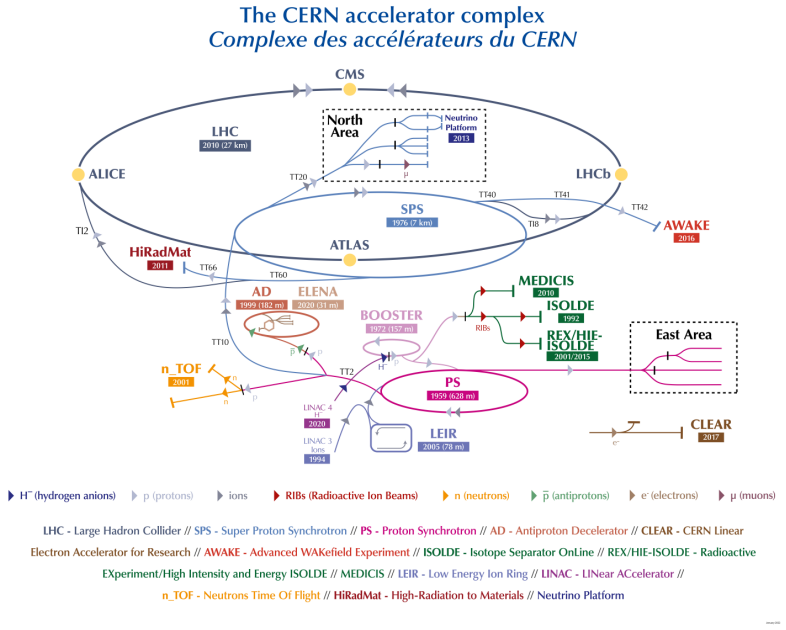

Figure 2.1: Schematic of the CERN accelerator complex [5]

Radio frequency (RF) alternating current is used to accelerate the beam particles, and the resulting oscillatory electric field helps to keep the particles in bunches that traverse the rings before collisions are made to happen. Particle acceleration inside the rings is regulated by superconducting electromagnets cooled to 1.9 K using liquid helium. The LHC ring itself consists of eight arcs separated by eight insertions. Each of these arcs is composed of 154 dipole magnets. Each of the dipole magnets, measuring 14.3 m in length

and 35 metric tonnes in weight, produces around 8.3 T magnetic field and helps to bend the beam particles inside the rings. The beam focusing is maintained using quadrupole magnets.

The accelerated beams of hadrons and/or heavy ions are made to collide with each other (coming from opposite directions through separate rings) at four crossing points, where the four major experiments of CERN: ALICE (A Large Ion Collider Experiment) [6], ATLAS (A Toroidal LHC Apparatus) [7], LHCb (Large Hadron Collider-beauty) [8] and CMS (Compact Muon Solenoid) [9] are built. These large-scale experiments are optimized to meet their unique physics objectives. ATLAS and CMS are multi-purpose detectors and are specifically engineered to investigate the pp collisions in order to search for extremely rare processes both within and beyond the Standard Model of particle physics. The primary goal of LHCb is to study the physics of beauty (bottom) quarks in order to determine the limits of the parameters of CP violation. ALICE, with its excellent tracking abilities, is the only large-scale detector in LHC that is dedicated to studying the physics of heavy-ion collisions in order to understand the properties of quark-gluon plasma, although ATLAS and CMS experiments are also active in heavy-ion programs and provide measurements complimentary to the ALICE results.

2.2 A Large Ion Collider Experiment (ALICE)

2.2.1 Overview

One of the four major experiments at the Large Hadron Collider, A Large Ion Collider Experiment (ALICE), is situated in the commune of Saint-Genis-Pouilly, France, at Point 2 (IP2) of the LHC accelerator tunnel. Installed 56 meters below the surface, this multi-component particle detector weighs about 10^4 tonnes. The ALICE detector measures 26 meters in length, 16 meters in width, and 16 meters in height overall. It is the only major

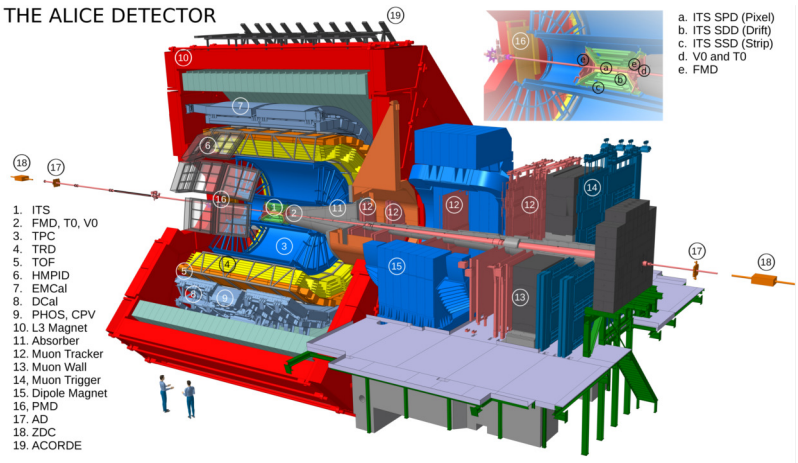

Figure 2.2: 3D schematic of ALICE detector setup during LHC Run 2 [10].

experimental facility at the LHC that is primarily and exclusively designed to explore the nuclear matter produced in ultra-relativistic heavy-ion collisions at extremely high temperatures and densities. In order to achieve its physics goals by studying the wide variety of observables of interest, the ALICE detector system needs to be able to precisely measure particle momentum over a wide range (0.15 GeV/c < p_{T} < 100 GeV/c), identify particles down to low momentum range, and perform well in the chaotic environment of high multiplicity (up to 8000 particles per unit rapidity). Fig. 2.2 schematically illustrates the 18 sub-detectors of ALICE, the majority of which are positioned encompassing the mid-rapidity region (a region of high energy density and low baryon density). This offers ALICE not only the opportunity to study the highest energy domain more thoroughly but also to perform QCD studies that are complementary to those carried out at lower energies.

With its point of origin at the nominal interaction point (IP, where (x, y, z) ≡ 0), the right-handed orthogonal Cartesian system is followed by the ALICE coordinate system, as shown in Fig. 2.3. The z-axis of the ALICE coordinate system is defined as parallel to the beam, whereas the x and y-axes point in the direction of the accelerator ring's center and straight upward, respectively. The standard conversion from cartesian coordinate (x,

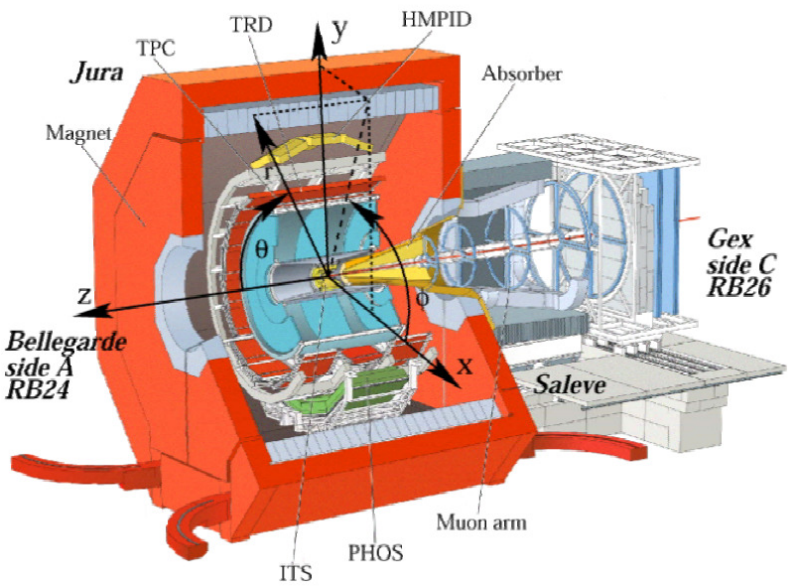

Figure 2.3: Schematic of the ALICE coordinate system: axes, angles and detector sides [11].

y) to cylindrical one (r, φ) is used.

The entire ALICE detector system can be broadly categorized into two main parts: central barrel detectors and forward (and backward) detectors. The central barrel detectors covering the pseudorapidity range $-0.9 < \eta < 0.9$ (with good momentum resolution and high tracking efficiency) are housed inside a large solenoidal magnet (inherited from the L3 experiment at LEP) that generates a magnetic field $B = 0.5$ T. A brief description of these detectors is given in Table 2.1.

Among the forward detectors, a forward muon spectrometer spanning the pseudorapidity coverage $-4.0 < \eta < -2.4$ operates under an additional magnetic field strength of 0.67 T that helps the bending of muons at forward rapidities. Additionally, a few detectors are placed at different forward rapidities, mainly used for triggering purposes. For a complete description of all the sub-detectors in ALICE, please see Ref. [6]. The detectors used for the measurement presented in this thesis are discussed in more detail in the following section.

Table 2.1: Brief description of central barrel detectors in ALICE.

Detector	Description	Acceptance	Radial distance (cm)	Main Purpose
Inner Tracking System (ITS)	silicon detector	$\|\eta\| < 0.9$, $\varphi = 360^{o}$	3.9-43	tracking, vertex determination, triggering
Time Projection Chamber (TPC)	gaseous detector	$\|\eta\| < 0.9$, $\varphi = 360^{o}$	85-250	tracking, momentum measurement, PID
Transition Radiation Detector (TRD)	transition radiation detector	$\|\eta\| < 0.84$, $\varphi = 360^{o}$	290-368	e^{-} identification
Time-Of-Flight (TOF)	Multigap Resistive Plate Chamber strip	$\|\eta\| < 0.9$, $\varphi = 360^{o}$	378	time of flight, PID
High-Momentum Particle Identification Detector (HMPID)	Ring Imaging Cherenkov detector	$\|\eta\| < 0.6$, $\varphi = 1.2^{o} - 58.8^{o}$	500	PID at high momentum
Electromagnetic Calorimeter (EMCal)	sampling calorimeter	$\|\eta\| < 0.7$, $\varphi = 80^{o} - 187^{o}$	460**	measurements of electrons, photons and neutral mesons, triggering
Di-Jet Calorimeter (DCal)	sampling calorimeter	$\|\eta\| < 0.7$, $\varphi = 253^{o} - 320^{o}$**	460**	dijet measurements
Photon Spectrometer (PHOS)	sampling calorimeter	$\|\eta\| < 0.12$, $\varphi = 220^{o} - 320^{o}$**	460**	measurements of electrons, photons and neutral mesons
ALICE Cosmic Ray Detector (ACORDE)	plastic scintillator	$\|\eta\| < 1.3$, $\varphi = -60^{o} - 60^{o}$**	850	trigger on high-energy cosmic rays

2.2.2 Inner Tracking System (ITS)

The Inner Tracking System [12] is one of the most important central barrel detectors in ALICE and is installed closest to the beam pipe. It is a multi-purpose detector which is used to

- determine the position of the primary vertex to a very high precision (the primary vertex is the position where the collision has occurred)
- reconstruct secondary vertices (a secondary vertex is the position of heavy-particle decay)
- improve the measurements of momentum and angular resolution of charged particles in coordination with other central barrel detectors

- reconstruct tracks that pass through the dead areas of the Time Projection Chamber (TPC)
- select events and estimate centrality

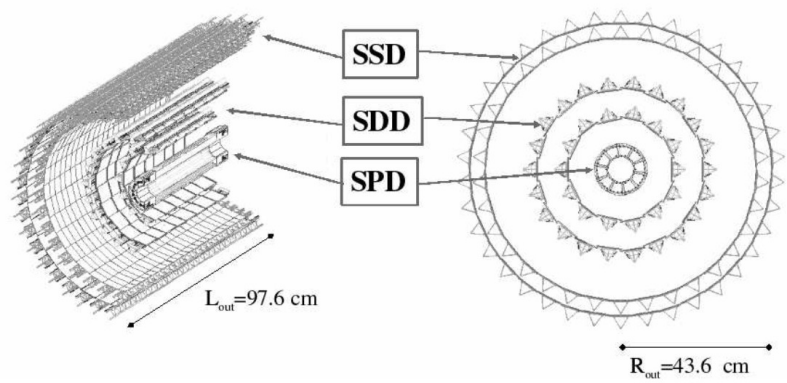

Figure 2.4: Cross-sectional view of the ITS detector in ALICE [6].

The schematic layout of the ITS layers is displayed in Fig. 2.4. It consists of 6 coaxial cylindrical layers of silicon detectors, ranging from 3.9 to 43 cm radii and spanning the pseudorapidity range of $|\eta| < 0.9$ with full azimuth coverage. The two innermost layers of the ITS, placed near the nominal interaction point (IP) at radii 3.9 cm and 7.6 cm from the z axis, comprise the Silicon Pixel Detectors (SPD) due to its very high resolution for resolving high particle density (up to 50 particles per square cm) with very high speed (chip clock frequency of 10 MHz). Consequently, these parts of the ITS play a quintessential role in determining the position of the primary vertex and measuring the impact parameter of secondary tracks produced from decays. The pixels in the SPDs are reverse-biased silicon detector diodes arranged in a sensor matrix on each of the 240 modules, and they work by measuring ionization charges or holes. The application of reverse bias voltage creates an electric field across the pixel, causing drift of the ionization charges and creating current pulses. The value of the current pulse crossing a particular threshold value is counted as a hit in the detector. The two layers of the SPD contain around 9.8 million pixel cells to

ensure large acceptance and high granularity (the spatial precision of the SPD reaches 12 μm in $r\varphi$ and 100 μm in z) [12].

The next two layers of the ITS, situated at radii 15.0 cm and 23.9 cm, utilize the Silicon Drift Detectors (SDD). Each unit sensor of the SDDs has a sensitive area that comprises drift regions. These drift regions are divided into two by a central cathode strip with a high voltage. The cathode strips are placed on both surfaces of each drift region. They are made to generate a drift field of around 8 μm ns^{-1}. The SDDs are used for particle identification by measuring the energy deposition dE/dx in the non-relativistic domain utilizing the Bethe-Bloch formula [13]. They have an average spatial precision of 35 μm in $r\varphi$ and 25 μm in z [6].

The two outermost layers of the ITS, located at radii 38.0 cm and 43.0 cm, do not require the level of resolution like other ITS layers and, therefore, are equipped with the Silicon Strip Detector (SSD). Nevertheless, these layers play an essential role in matching tracks between the ITS and the TPC. Double-sided silicon micro-strip detectors are used to make the modules of the SSDs. Like SDDs, the SSDs also contribute to particle identification by measuring dE/dx in the non-relativistic region. They exhibit a spatial precision reaching up to 20 μm in $r\varphi$ and 830 μm in z [6].

2.2.3 Time Projection Chamber (TPC)

The Time Projection Chamber is the main tracking detector of the ALICE central barrel. The schematic layout of the TPC is displayed in Fig. 2.5. Together with other central barrel detectors, it is capable of measuring charged-particle momentum over a broad range with good momentum resolution, identification of particles, and determination of the position of the primary vertex. It also has an excellent position resolution of about 1 mm both in $r\varphi$ and z [14]. The TPC can measure tracks within the accepted phase space of $|\eta| < 0.9$ and full azimuth. It is made of a large cylindrical field cage divided into two parts by a

vertical central electrode, while each end plate consists of 18 trapezoidal readout sectors of multi-wire proportional chambers. The TPC in ALICE is the largest TPC in the world. It has an active volume of around 90 m^3, spanning over 510 cm in length and covering a radial distance of 85-250 cm from the beam line, as shown in Fig. 2.5. It is filled with a gaseous mixture of argon (Ar) and carbon dioxide (CO_2). Upon incidence of charged particles/radiation, ionization of gas occurs and the produced ionization charges drift to the end plates due to high electric potential between the electrodes. Their drift time and the known electric potential provide the longitudinal positions (t projecting into z) of the tracks of the charges, while the transverse positions (x, y) can be determined from the position of charge collection at the end plates. Utilizing these two information, a 3D picture can be reconstructed. Moreover, correlating the amount of collected charge with the amount of energy deposition provides an effective measurement of dE/dx, which, in turn, helps in particle identification.

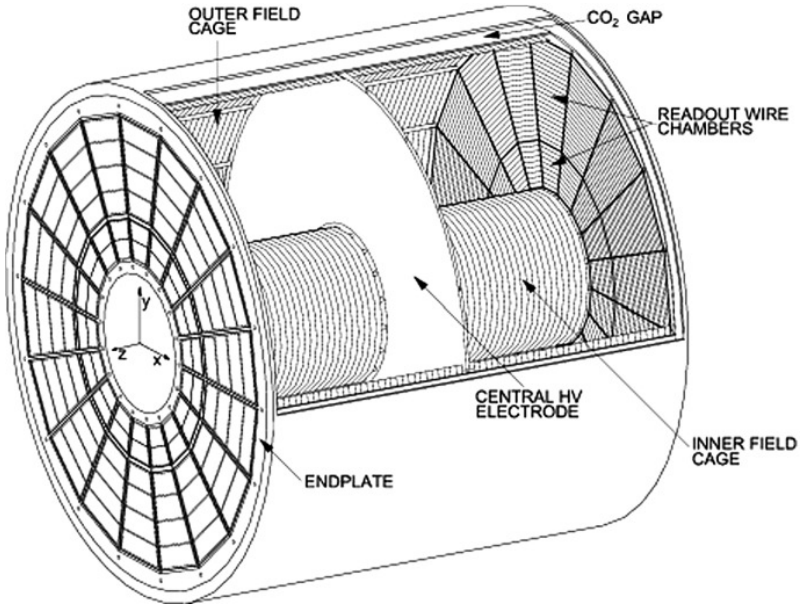

Figure 2.5: Schematic view of the ALICE TPC [15].

There are 159 rows in total between the inner and outer multi-wire proportional chambers (MWPCs) at the end plates, which are read out using cathode pads. It implies

that up to 159 hits can be obtained from a single track that passes through the detector. There are three different sizes of pads: 4 x 7.5 mm^2, 6 x 10 mm^2, and 6 x 15 mm^2. The pad size increases with increasing radial distance as the track density drops. In all, more than 500,000 readout pads are there in TPC.

Since the TPC works in the principle of drifts of particles, it is one of the slowest detectors and is responsible for the low luminosity[1] provided to ALICE. Additionally, space-charge fluctuations, which are brought on by other charges in the TPC that induce non-uniformity in the electric field, can have a significant impact on the diffusion coefficient, limiting the TPC's resolution. In order to avoid these problems, Gas Electron Multipliers (GEMs) have taken the place of MWPCs, together with an enhanced readout system [16] for LHC Run 3, in which data is continuously recorded at higher event rates than before, in contrast to the previous event triggering technique. More information is available in Ref. [17].

2.2.4 VZERO (V0) scintillator detectors

The ALICE V0 detectors, comprising two small-angle arrays of scintillator counters called V0A and V0C, are located asymmetrically on either side of the nominal interaction point (IP) along the beam line [18, 19]. The V0A and V0C detectors are placed at +340 cm and -90 cm away from the nominal IP, respectively, as displayed in Fig. 2.6, and span the pseudorapidity coverages of $2.8 < \eta < 5.1$ (V0A) and $-3.7 < \eta < -1.7$ (V0C). Each of the detector arrays consists of 32 plastic scintillators arranged in 4 concentric rings, each of the rings being sliced azimuthally into 8 sections.

The V0 detectors are multi-functional, as they

- provide minimum-bias (MB) triggers (and some centrality triggers for Pb–Pb collisions) for the central barrel detectors

[1] Luminosity measures how tightly packed the particles are in the beams

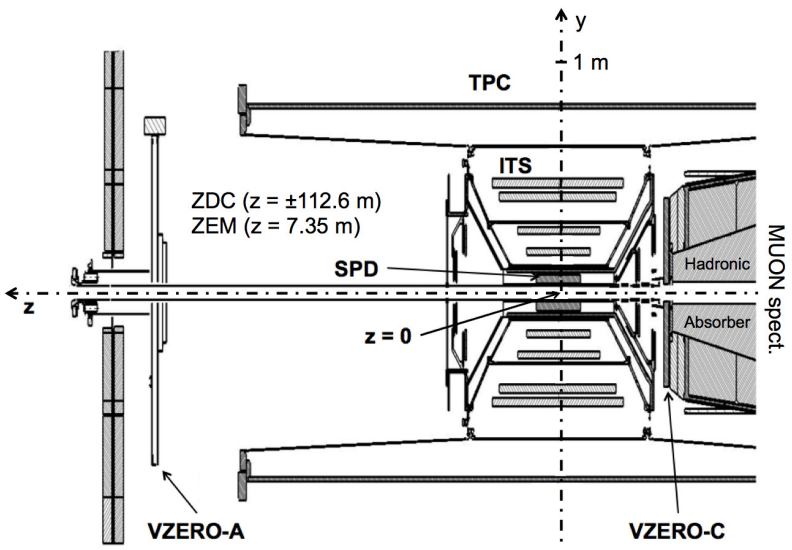

Figure 2.6: Position of the two V0 detectors within the general layout of the ALICE detector setup [18, 19].

- estimate collision centrality and event plane based on multiplicity of charged particles
- discriminate the beam-gas interactions by measuring the relative time-of-flight of the particles between the two detectors
- help to measure beam luminosity and azimuthal distributions of charged particles

2.2.5 Data processing in ALICE

The raw data collected from detectors must be processed and prepared for physics analysis. The processing of the massive volume of recorded data is coordinated by the Worldwide LHC Computing Grid (WLCG) [20–22], which is spread across numerous computing centers throughout the world. An offline framework named AliROOT [23, 24] was explicitly developed for the reconstruction of data and simulations performed in ALICE. It is based on the analysis framework ROOT [25], which is widely used in high-energy physics for the processing and analysis of enormous amounts of data. Additionally, ALICE provides

its users access to the CERN Analysis Facility (CAF), a system that makes it possible to conduct various analyses using parallel computing clusters.

The LHC records data at extremely high luminosities, and there will always be limitations on the amount of data that can be stored. Therefore, a triggering system is used to select data that must be of good quality and relevant physics interests. In ALICE, a Central Trigger Processor (CTP) is responsible for making the triggering selections online. In order to select good events while minimizing contamination from undesirable processes (e.g., beam-gas interactions), a Minimum Bias (MB) trigger that requires signal information from VZERO and/or ITS detectors is generally used. Furthermore, depending on the physics interests, many other triggers are also utilized to choose events with only rare processes. The triggered events are then made to pass through further selection criteria for them to be used in analysis.

In any high-energy physics experiments, it is essential and customary to perform simulations for various purposes, e.g., correcting raw data for instrumental effects, providing theoretical predictions to the corrected results for physics interpretation, etc. Two types of simulations are commonly carried out in order to correct the raw experimental data obtained from the detectors. Initially, events are generated wherein event generators employ Monte Carlo techniques to replicate collisions as closely as feasible to the actual events. The event generators use several sets of parameter tunings based on existing experimental data in addition to the current theoretical understanding of the relevant collision dynamics, however their implementations vary in each event generator. In the second type of simulation, the primary goal is to reproduce as closely as possible the raw distributions of particles measured from experimental data, by transporting the particles generated by the event generators through a precise realization of the detectors' geometry and behavior in simulation. The measured raw data is corrected for any instrumental effects with the help of these two types of simulations so that the final results can be compared to results from

other experiments as well as to theoretical predictions.

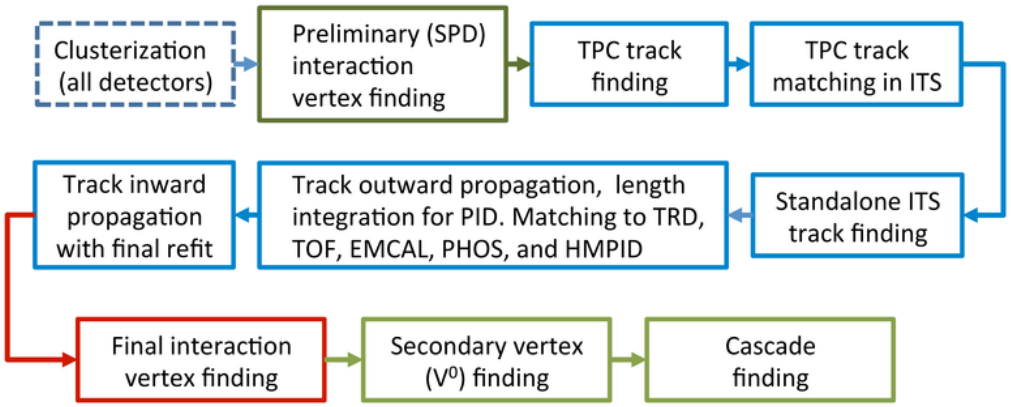

Figure 2.7: Event reconstruction flow [26].

Prior to analysis of raw data, it is crucial to ensure that the possible misalignments of whole or part of the used detectors are taken care of and the proper calibrations are performed as well. The necessary information is stored in the Offline Conditions Data Base (OCDB) as alignment and calibration objects separately that are utilized during the reconstruction of raw data.

The systematic procedure of track finding in the ALICE central barrel is schematically shown in Fig. 2.7 [26]. It begins with clusterization of data from each detector separately to form clusters. These clusters are typically groups of adjacent cells and are defined by their characteristic positions, signal amplitudes, signal times, and associated errors. The following stage involves exploiting clusters in the first two ITS layers (SPD) to identify the preliminary interaction vertex as the single space point where the maximum number of SPD tracklets[2] converge. Track finding and fitting are then carried out in TPC and ITS in three iterations using an inward-outward-inward scheme with the Kalman filter method [27]. The first iteration starts with locating tracks in the outer radius of TPC. Two TPC clusters and the preliminary vertex point are initially used to build track seeds; then, three clusters are used to build track seeds without using the vertex point. At each

[2]tracklets are lines defined by two clusters, one from each of the SPD layers

step, the track seeds are propagated inward and updated with the nearest TPC cluster if they meet a proximity cut. At this stage, a preliminary particle identification is carried out using the dE/dx information. Once these so-called "TPC-tracks" are reconstructed, they are transmitted to the outermost ITS layer and are used as new seeds for track finding within the ITS. The seeds are then prolonged to the initial preliminary vertex point with the distance of closest approach. Utilizing the clusters reconstructed in the preceding iteration, these tracks from the preliminary vertex are transmitted backward to the TPC's outer radius in the second iteration. The specific energy loss is taken into account when updating particle identification, and the tracks are then transmitted toward additional outer central barrel detectors for cluster matching. The last iteration involves refitting the tracks with the previously discovered clusters and propagating all tracks inwards once more, starting from the outer radius of the TPC. These are called "global tracks" and are used to find the final interaction vertex with a higher precision than the preliminary interaction vertex finding. A search for photon conversions and secondary vertices from particle decays is carried out after the tracks and interaction vertex have been identified during the event reconstruction process, and that concludes the central barrel tracking procedure.

After passing through the reconstruction process, the raw data is stored in the form of Event Summary Data (ESD) files. These files contain detailed information on reconstruction, including the primary and secondary vertices, PID information of the reconstructed tracks, and the trigger information obtained from different sub-detectors. Consequently, ESD files consume massive storage and are inconvenient for performing local analyses. Hence, a user-friendly format is adopted that is relatively smaller in size and contains only the necessary and relevant information to carry out particular analyses. These are known as Analysis Object Data (AOD). The analysis reported in this thesis is performed using AOD files.

Bibliography

[1] LHC Study Group, "The Large Hadron Collider: Conceptual design,". http://cds.cern.ch/record/291782.

[2] "LHC: the Large Hadron Collider accelerator project,". http://cds.cern.ch/record/257706.

[3] "LHC Design Report Vol.1: The LHC Main Ring,". http://cds.cern.ch/record/782076.

[4] "LHC Machine," *JINST* **3** (2008) S08001.

[5] E. Lopienska, "The CERN accelerator complex, layout in 2022. Complexe des accélérateurs du CERN en janvier 2022,". https://cds.cern.ch/record/2800984. General Photo.

[6] ALICE, K. Aamodt *et al.*, "The ALICE experiment at the CERN LHC," *JINST* **3** (2008) S08002.

[7] ATLAS, G. Aad *et al.*, "The ATLAS Experiment at the CERN Large Hadron Collider," *JINST* **3** (2008) S08003.

[8] LHCb, A. A. Alves, Jr. *et al.*, "The LHCb Detector at the LHC," *JINST* **3** (2008) S08005.

[9] CMS, S. Chatrchyan *et al.*, "The CMS Experiment at the CERN LHC," *JINST* **3** (2008) S08004.

[10] ALICE, "The ALICE experiment – A journey through QCD," arXiv:2211.04384 [nucl-ex].

[11] ALICE, L. Betev *et al.*, "Definition of the ALICE coordinate system and basic rules for sub-detector components numbering,". http://edms.cern.ch/document/406391. ALICE-INT-2003-038.

[12] ALICE, K. Aamodt *et al.*, "Alignment of the ALICE Inner Tracking System with cosmic-ray tracks," *JINST* **5** (2010) P03003, arXiv:1001.0502 [physics.ins-det].

[13] M. Thomson, *Modern Particle Physics*. Cambridge University Press, 2013.

[14] ALICE, P. Cortese *et al.*, "ALICE: Physics performance report, volume I," *J. Phys. G* **30** (2004) 1517–1763.

[15] J. Alme *et al.*, "The ALICE TPC, a large 3-dimensional tracking device with fast readout for ultra-high multiplicity events," *Nucl. Instrum. Meth. A* **622** (2010) 316–367, arXiv:1001.1950 [physics.ins-det].

[16] ALICE, P. Hauer, "The upgraded ALICE TPC," *Nucl. Instrum. Meth. A* **1039** (2022) 167023.

[17] ALICE, F. Reidt, "Upgrade of the ALICE ITS detector," *Nucl. Instrum. Meth. A* **1032** (2022) 166632, arXiv:2111.08301 [physics.ins-det].

[18] ALICE, P. Cortese *et al.*, "ALICE technical design report on forward detectors: FMD, T0 and V0,". http://cds.cern.ch/record/781854.

[19] ALICE, E. Abbas *et al.*, "Performance of the ALICE VZERO system," *JINST* **8** (2013) P10016, arXiv:1306.3130 [nucl-ex].

[20] "Worlwide LHC Computing Grid." https://wlcg-public.web.cern.ch/.

[21] "LHC computing Grid. Technical design report,". http://cds.cern.ch/record/840543.

[22] I. Bird *et al.*, "Update of the Computing Models of the WLCG and the LHC Experiments,". http://cds.cern.ch/record/1695401.

[23] R. Brun, P. Buncic, F. Carminati, A. Morsch, F. Rademakers, and K. Safarik, "Computing in ALICE," *Nucl. Instrum. Meth. A* **502** (2003) 339–346.

[24] ALICE, "ALICE technical design report of the computing,". http://cds.cern.ch/record/832753.

[25] R. Brun and F. Rademakers, "ROOT: An object oriented data analysis framework," *Nucl. Instrum. Meth. A* **389** (1997) 81–86.

[26] ALICE, B. B. Abelev *et al.*, "Performance of the ALICE Experiment at the CERN LHC," *Int. J. Mod. Phys. A* **29** (2014) 1430044, arXiv:1402.4476 [nucl-ex].

[27] R. Fruhwirth, "Application of Kalman filtering to track and vertex fitting," *Nucl. Instrum. Meth. A* **262** (1987) 444–450.

"An experiment is a question which science poses to Nature, and a measurement is the recording of Nature's answer."

— Max Planck

Chapter 3

Measurements of charged-particle jet properties in pp and p–Pb collisions with ALICE

This chapter presents the measurements of charged-particle jet properties in proton-proton (pp) and proton-lead (p–Pb) collisions at $\sqrt{s_{\rm NN}}$ = 5.02 TeV using ALICE. Jet is a complex object, and its experimental measurements are very challenging. The ALICE detector setup has a unique potential to reconstruct charged-particle precisely down to as low transverse momentum as 150 MeV/c within $|\eta| < 0.9$ over full azimuth. Using the information from TPC [1] and ITS [2], charged-particle tracks are reconstructed and used for the reconstruction of charged-particle jets with $20 < p_{\rm T} < 100$ GeV/c and within $|\eta| < 0.5$. The properties of reconstructed leading jets are studied for pp and p–Pb collisions. The correction for instrumental effects is performed using a well-known unfolding technique. The measured jet observables are also corrected for the underlying event (UE) contribution, and the systematic uncertainties from various sources are estimated. The final results are compared to theoretical Monte Carlo (MC) models. The details of the analysis, including

event selection, track selection, jet reconstruction, definition of jet observables, correction for instrumental effects and UE, estimation of systematic uncertainties, and discussion of final results compared to theoretical models, are presented in detail in the following sections.

3.1 Analysis strategy

3.1.1 Selection of data sets

This analysis uses the data recorded by the ALICE detector (see Sec. 2.2 of chapter 2) during LHC Run 2. The p–Pb data was collected at the nucleon-nucleon center-of-mass energy $\sqrt{s_{\mathrm{NN}}}$ = 5.02 TeV in 2016, while the pp data was collected in 2017 at the same center-of-mass energy ($\sqrt{s}$ = 5.02 TeV). The data-taking configurations are periodically reset by software throughout the raw data collection from the collisions. A new "run" is initiated at that point, denoted by a "run number", which increases at the beginning of each "run". The massive volume of data collected over time is categorized into what are known as "production cycles" or "data taking periods" (or "data periods", in short). The data sets, including the data periods and run numbers utilized in this analysis, are detailed below:

pp data sets

The data sets of pp collisions consist of the AOD (see Sec. 2.2.5 of chapter 2) files obtained for two kinds of trigger clusters, FAST and CENT_woSDD, during the first reconstruction pass (pass 1) of two data periods, LHC17p and LHC17q. The reconstruction of these trigger clusters was carried out using the central barrel tracking ("CENT" clusters) but excluding the SDD information from the tracking. The resulting data sets from the two trigger clusters are combined to boost the statistics for this analysis, as is typically done

for jet analyses that require large statistics. This analysis makes use of the following list of runs from the two data periods, which the ALICE Data Preparation Group (DPG) has recognized as good runs with globally good tracking performance.

- **LHC17p** (41 runs): 282343, 282342, 282341, 282340, 282314, 282313, 282312, 282309, 282307, 282306, 282305, 282304, 282303, 282302, 282247, 282230, 282229, 282227, 282224, 282206, 282189, 282147, 282146, 282127, 282126, 282125, 282123, 282122, 282120, 282119, 282118, 282099, 282098, 282078, 282051, 282050, 282031, 282025, 282021, 282016, 282008
- **LHC17q** (3 runs): 282367, 282366, 282365

p–Pb data sets

The p–Pb data sets used in this analysis are taken from two data periods, LHC16q and LHC16t. These data sets, like the pp data sets, also comprise AOD files reconstructed for the FAST and CENT_woSDD trigger clusters during reconstruction pass 1 of the considered data periods. The good runs defined by the ALICE DPG and used for this analysis are enlisted below:

- **LHC16q** (32 runs): 265525, 265521, 265501, 265500, 265499, 265435, 265427, 265426, 265425, 265424, 265422, 265421, 265420, 265419, 265388, 265387, 265385, 265384, 265383, 265381, 265378, 265377, 265344, 265343, 265342, 265339, 265338, 265336, 265335, 265334, 265332, 265309
- **LHC16t** (4 runs): 267166, 267165, 267164, 267163

3.1.2 Monte Carlo event samples

As alluded in Sec. 2.2.5 of chapter 2, simulations play pivotal roles in several stages of the data analysis procedure. This analysis also uses various simulations, in the form of Monte

Carlo event generators and detector simulation. For the analysis of pp data, a centrally available MC production of PYTHIA 8 [3] with Monash 2013 [4] tune is utilized while for its p–Pb counterpart, two central MC productions, namely DPMJET [5] and EPOS LHC [6] are considered. These central simulations also incorporate the full detector simulation of the ALICE detector setup, which is carried out using the GEANT3 software package [7]. It simulates the transportation of particles generated by the MC event generators through the entire detector setup, their interactions with materials, and their eventual detection by the sub-detectors. Since these simulated MC samples are anchored run-by-run to their data counterparts (i.e., simulated with the exactly same experimental conditions as they were during the time of data taking), the considered runs of the MC samples used for this analysis are the same as those in data. The central simulations used in this analysis are summarized in Table 3.1. In addition to the central simulations, a standalone simulation using PYTHIA 8 Angantyr model [8] is also used for comparing the final experimental results with MC predictions for pp and p–Pb collisions.

Table 3.1: Details of anchored MC productions used in this analysis

Collision system	**MC generator**	**Production**	**Anchored to data period**	**Trigger type, Reconstruction pass & AOD**	**Analysed runs**	**No. of events after event selection criteria**
p–Pb	DPMJET (GP)*	LHC18f3_cent_woSDD_2	LHC16q, LHC16t	CENT_woSDD, pass1, AOD202	Same as data	541 M
		LHC18f3_fast_2	LHC16q, LHC16t	FAST, pass1, AOD202	Same as data	
	EPOS-LHC (GP)	LHC17f2a_cent_woSDD_fix	LHC16q, LHC16t	CENT_woSDD, pass1, AOD228	Same as data	59 M
		LHC17f2a_fast_fix	LHC16q, LHC16t	FAST, pass1, AOD228	Same as data	
pp	PYTHIA8 Monash2013 (JJ)**	LHC18b8_fast	LHC17p, LHC17q	FAST, pass1, AOD	Same as data	–

* GP: General purpose production

** JJ: Jet-jet production: In order to create a MC data sample with adequate statistics at higher values of jet p_{T}, where the rapidly falling differential jet cross section makes events extremely rare, the production is generated in 20 $p_{\mathrm{T,hard}}$ bins ($p_{\mathrm{T,hard}}$ refers to the invariant p_{T} of the simulated $2 \rightarrow 2$ interactions).

3.1.3 Event selection

In this analysis, minimum bias events for pp and p–Pb collisions and 0–20% central events for p–Pb collisions are used. The minimum bias events are selected based on the online MBAnd trigger used in ALICE that requires coincidence of signals in both of the forward scintillator trigger detectors, VZERO (see Sec. 2.2.4 of chapter 2), covering the pseudorapidity (η) range of $2.8 < \eta < 5.1$ (V0A) and $-3.7 < \eta < -1.7$ (V0C). Apart from the trigger condition, the selected events are required to satisfy the following criteria:

- There needs to be at least one successfully reconstructed primary vertex in the event
- To ensure high tracking efficiency, the reconstructed primary vertex is required to be within $|z_{\mathrm{vtx}}| < 10$ cm from the nominal interaction point ($z_{\mathrm{vtx}} = 0$) along the beam direction
- the selected events must satisfy the track quality selection criteria, which guarantees that tracks utilized in the analysis are from a single vertex, thereby rejecting events with more than one reconstructed primary vertex candidates

In addition, the beam-induced background events due to the interaction of beams with the materials are rejected with the help of two neutron Zero-Degree Calorimeters (ZDCs) placed at forward rapidities. To minimize the effect of beam-gas interaction occurring between one of the beams and the residual gas present inside the vacuum beam pipe, events are rejected based on the timing information of V0 detectors and the correlation between the hits and tracklets in the SPD detectors. Events with multiple reconstructed primary vertices are rejected to remove the in-bunch pileup events where multiple collisions occur during the bunch crossing that triggered the data acquisition. The out-of-bunch pileup events where one or more collisions occur during different bunch crossings are also eliminated using V0 and SPD cuts. After applying all these event selection criteria, a

total of 616 million and 226 million of MB events are used for analysis of p–Pb and pp collisions, respectively.

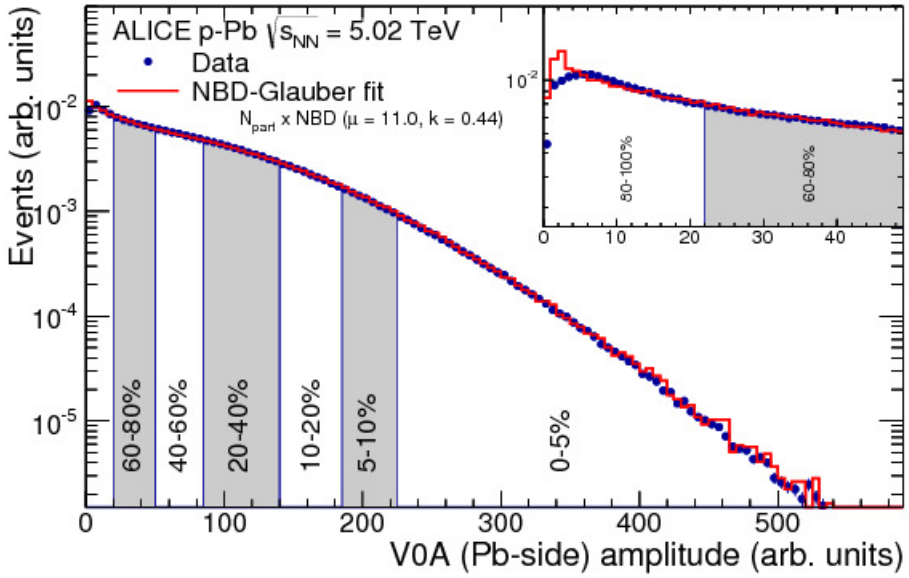

Figure 3.1: Centrality determination for p–Pb collisions using the distribution of V0A signal amplitude in ALICE [9].

The 0–20% central event class for p–Pb collisions contains 20% of the total events with the highest multiplicity. In this analysis, this event class is determined from the minimum bias sample, based on the signal amplitude of the V0A detector[1]. Fig. 3.1 shows how different centrality classes of p–Pb collisions can be determined in ALICE [9]. The 0-20% central event class for p–Pb collisions used for this analysis contains around 122 million events.

3.1.4 Track selection

Reconstructed charged tracks are the heart of any charged-particle jet analysis in ALICE; this analysis is no exception. From the selected events, tracks of primary charged-particle

[1]The V0A detector is chosen as a centrality estimator for p–Pb collisions in ALICE since it faces the incoming Pb-ion beam while its counterpart, V0C detector faces the proton beam. Therefore, using V0A signal amplitude for centrality estimation gives better performance since it is hit by more particles compared to V0C.

candidates[2] are utilized for the reconstruction of charged-particle jets. Using information from two central barrel detectors, the Inner Tracking System (ITS) [2] and the Time Projection Chamber (TPC) [1], a hybrid track selection technique is applied in this analysis to reconstruct tracks, that ensures uniform azimuthal acceptance while retaining good momentum resolution. The hybrid tracks comprise the following two classes of tracks:

- Global tracks (see Sec. 2.2.5 of chapter 2): These tracks must have their longitudinal and transverse distances of closest approach to be within 2.4 cm and 3.2 cm respectively, and include at least one hit in an SPD layer (the innermost part of the ITS detector)

- Complimentary tracks: These tracks must satisfy the same requirements as good global tracks, except requiring hit in the SPD; to improve the momentum determination of these tracks, the primary interaction vertex is used as a constraint during track fitting

The momentum resolution of charged tracks is estimated to be $\approx 0.8\%$ at 1 GeV/c and 4% at 50 GeV/c [11]. In this analysis, charged tracks with $p_{\mathrm{T}} > 0.15$ GeV/c produced at mid-rapidity ($|\eta_{\mathrm{track}}| < 0.9$) are considered for jet reconstruction.

3.1.5 Jet reconstruction

The selected tracks are used to reconstruct charged-particle jets by applying the collinear- and infrared-safe sequential recombination jet finding algorithm, namely "anti-k_{T} algorithm" [12] implemented in the FastJet package [13]. For this analysis, jets are reconstructed with jet resolution parameter $R = 0.4$, which is one of the standard values widely used in charged-particle jet analyses. The reconstructed jets are constrained within the

[2]A primary charged particle in ALICE is defined as a charged particle with a mean proper lifetime τ larger than 1 cm/c, which is either produced directly in the interaction, or from decays of particles with τ smaller than 1 cm/c, restricted to decay chains leading to the interaction between the colliding partners [10].

pseudorapidity coverage of $|\eta_{\rm jet}| < 0.5(= |\eta_{\rm track}| - R)$, to make sure that they are fully contained within the fiducial volume of the TPC. In order to suppress the contribution from pure background jet clusters, it is ensured that each of the selected jets has occupied an area greater than $0.6\pi R^2$, which comes out to be around 0.5 for jet $R = 0.4$.

Only the highest $p_{\rm T}$ jet in an event, known as the "leading jet", is considered for this analysis. In comparison to inclusive jets (all the jets in an event), leading jets are theoretically well-defined objects as one can define and utilise jet functions that follows the non-linear DGLAP-type evolution equations to descibe the formation and evolution of leading jets [14]. Moreover, unlike the inclusive jets, these leading jet functions provide normalized probability densities in order for the leading jets to possess a longitudinal momentum fraction with respect to the jet-initiating parton, an aspect that can be exploited to evaluate the average energy loss using perturbative approach. From the viewpoint of experimental measurement, leading jets, being the most energetic one in an event are less prone to experimental effects in contrast to the inclusive jets and are therefore cleaner objects to work with while comparing with predictions from QCD hard-scattering models [15]. In this analysis, all the reconstructed leading jets in the transverse momentum interval of $5 < p_{\rm T}^{\rm jet,\,ch} < 120$ GeV/c are considered.

3.1.6 Jet observables

Once the reconstructed jets are obtained, the next step is to compute the jet observables of interest. Two important jet observables, namely the mean charged-particle multiplicity within jet ($\langle N_{\rm ch} \rangle$) and jet fragmentation function ($z^{\rm ch}$), that are measured in this analysis, are defined and discussed in this section. The mean charged-particle multiplicity in leading

jets is calculated over the total number of events for each jet p_{T} bin by using the expression:

$$\langle N_{\mathrm{ch}} \rangle (p_{\mathrm{T}}^{\mathrm{jet,\,ch}}) = \frac{1}{N_{\mathrm{jets}}} \sum_{i=1}^{N_{\mathrm{jets}}} N_{\mathrm{ch}}^{i} (p_{\mathrm{T}}^{\mathrm{jet,\,ch}}) \tag{3.1}$$

where N_{ch}^{i} is the number of charged-jet constituents (charged-particle tracks constituting the jet) in i-th leading jet and N_{jets} is the number of charged-jets in that jet p_{T} bin.

The jet fragmentation function represents the fraction of the jet transverse momentum carried by the constituent charged particles and is sensitive to the details of the parton showering process. It is computed as:

$$z^{\mathrm{ch}} = \frac{p_{\mathrm{T}}^{\mathrm{track}}}{p_{\mathrm{T}}^{\mathrm{jet,\,ch}}} \tag{3.2}$$

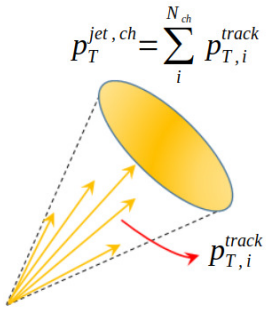

Figure 3.2: Jet fragmentation.

for each charged-particle track constituting the jet and its p_{T} is denoted by $p_{\mathrm{T}}^{\mathrm{track}}$.

These observables contain useful information about the splitting of the initiating hard-scattered parton into its constituents and, therefore, serve as potential tools to further understand the evolution of QCD jets both in vacuum and in medium. On a similar note, measuring these observables in small collision systems becomes particularly important while investigating the notion of QGP-medium formation and possible jet quenching effects in such systems.

3.1.7 Instrumental effects

The raw distributions measured by the detectors (shown in Appendix A) are affected by several instrumental effects, such as detector efficiency, finite track p_{T} resolution, particle-material interactions, etc. The detector efficiency may result from one or a few of the

following reasons: particles may not deposit enough energy, they may traverse through the dead area of the detector, loss of tracks may occur during the track reconstruction procedure, etc. The finite track p_{T} resolution may result in momentum smearing of the reconstructed tracks. Due to these effects on the reconstructed tracks, the reconstructed jets and their properties are also affected, and to extract the actual physics, proper corrections are required.

3.1.7.1 Correction for instrumental effects

There are several methods available that can be employed to perform the necessary corrections for the instrumental effects. In all the applicable methods, MC event generators and detector simulation are utilized to obtain the information of particles both before and after transporting the generated particles through the detector simulation (as described in Sec. 3.1.2), commonly referred to as "true" or "particle-level" and "measured" or "detector-level" information, respectively. Among all the methods, the bin-by-bin correction method is the simplest one. In this method, the raw data to be corrected is multiplied with the correction factor for each bin, where the correction factor is defined as the ratio between the true- and measured-level distributions of the considered observable. In this analysis, the "unfolding" method is chosen because the corrected results in the unfolding method, in contrast to the bin-by-bin correction method, are less biased by the particular choice of the Monte Carlo event generator used, and the bin-to-bin migration effects due to momentum smearing are also accounted for. Moreover, the unfolding method is more robust against statistical fluctuations.

In the unfolding method, a detector response that contains the information of correlation between the true and measured levels is constructed and utilized. The measured (M) and

true (T) distributions can be correlated through the response R by:

$$M = RT \tag{3.3}$$

which can lead to:

$$T = R^{-1}M \tag{3.4}$$

One can express the response R in terms of a matrix whose element R_{mt} denotes the conditional probability that the true value t of the considered observable has the corresponding measured value m. Therefore, one can obtain the true distribution utilizing the measured distribution and the response matrix using Eq. 3.4.

It is, however, only rarely possible to use this inverse approach as it would require the matrix R to be invertible, which is not always the case in practice. To circumvent this issue, a non-analytical, numerical approach is usually taken for correction purposes. There are several numerical techniques available, and in this analysis, the iterative Bayesian unfolding technique is employed. It uses the Bayes' theorem:

$$P(A|B) = \frac{P(B|A)P(A)}{P(B)} \tag{3.5}$$

where $P(A)$ and $P(B)$ are the probabilities of occurring event A and B respectively. $P(B|A)$ is the probability of B if A is true. On a similar note, if one considers A and B as the true and measured distributions, respectively, then $P(B|A)$ and $P(A|B)$ become the detector response and the inverse of the response matrix, respectively. This leads to:

$$R_{\mathrm{tm}} = \frac{R_{\mathrm{mt}}P_{\mathrm{t}}}{\sum_{\mathrm{t}'} R_{\mathrm{mt}'}P_{\mathrm{t}'}} \tag{3.6}$$

where $P_{\mathrm{t}'}$ is a priori guess of the true distribution, also termed as "prior" distribution. In this analysis, the true distribution obtained from the MC event generator is used as the

prior distribution. Once R_{tm} is estimated, the solution of the unfolding procedure, i.e., the unfolded distribution (U), can be obtained as:

$$U = \sum_{m} R_{\mathrm{tm}} M_{\mathrm{m}} \tag{3.7}$$

In this analysis, the jet observables $\langle N_{\mathrm{ch}} \rangle$ and z^{ch} are presented as a function of jet p_{T}, so a 2-dimensional Bayesian unfolding is performed. For each of the jet observables (Obs: $\langle N_{\mathrm{ch}} \rangle$ or z^{ch}), a 4D response matrix is constructed from MC simulations and its components are: ($p_{\mathrm{T}}^{\mathrm{jet,\,det}}$, $Obs^{\mathrm{jet,\,det}}$, $p_{\mathrm{T}}^{\mathrm{jet,\,part}}$, $Obs^{\mathrm{jet,\,part}}$). The iterative Bayesian method of unfolding implemented in RooUnfold package [16] is applied in this analysis.

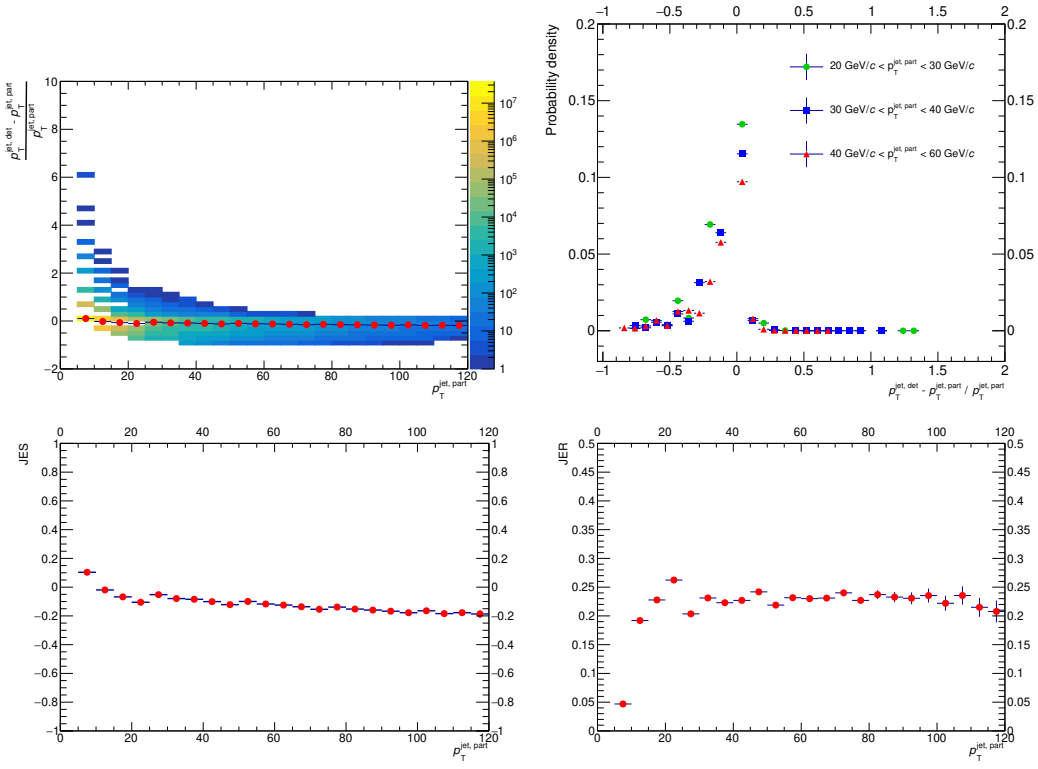

Figure 3.3: Jet performance plots for minimum bias pp collisions.

It is also necessary to assess the quality and performance of jet reconstruction in terms of several metrics before unfolding is performed. To evaluate the jet performance,

the detector-level jets have to be matched to the corresponding particle-level jets, which is carried out following the procedure discussed in Sec. 3.1.7.2. The metrics of jet performance are used to estimate how well we measure the jets after it goes through the detector and therefore represent the detector effects. The first metric, known as Jet Energy Scale (JES), is defined as,

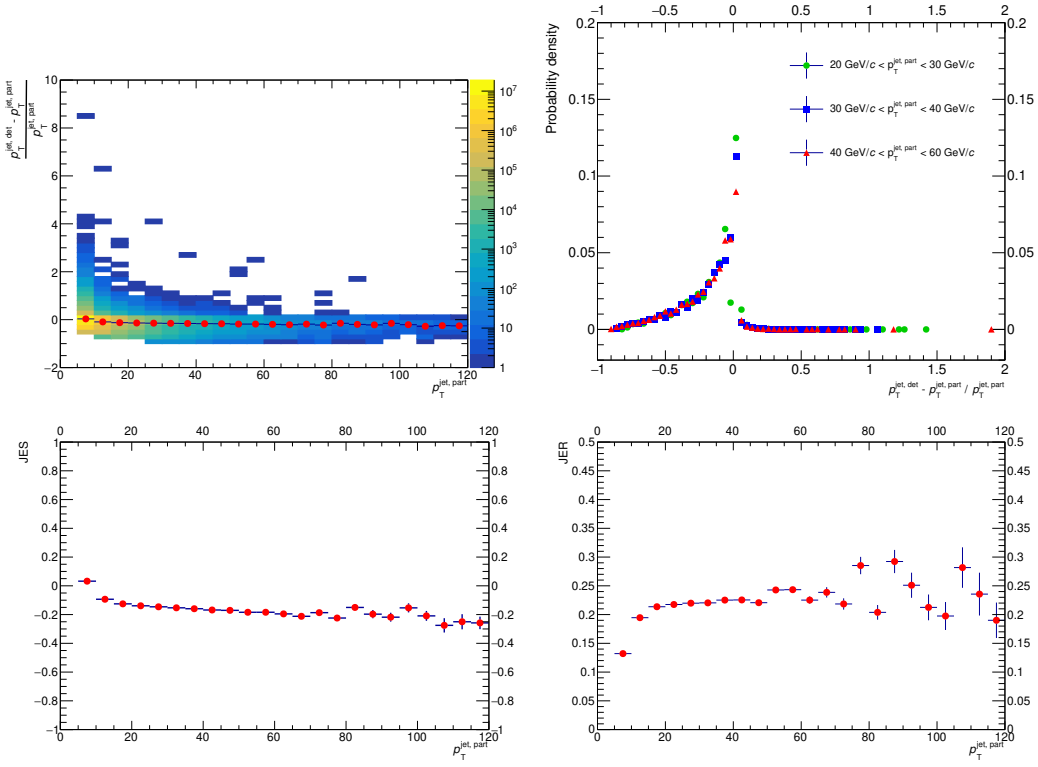

Figure 3.4: Jet performance plots for minimum bias p–Pb collisions.

$$\text{Jet Energy Scale (JES)} = \left\langle \frac{p_{\mathrm{T}}^{\text{jet, det}} - p_{\mathrm{T}}^{\text{jet, part}}}{p_{\mathrm{T}}^{\text{jet, part}}} \right\rangle \tag{3.8}$$

Its width represents the Jet Energy Resolution (JER), which is a measure of the remaining fluctuations, and can be defined as:

$$\text{Jet Energy Resolution (JER)} = \sigma\left(\frac{p_{\mathrm{T}}^{\text{jet, det}} - p_{\mathrm{T}}^{\text{jet, part}}}{p_{\mathrm{T}}^{\text{jet, part}}} \right) \tag{3.9}$$

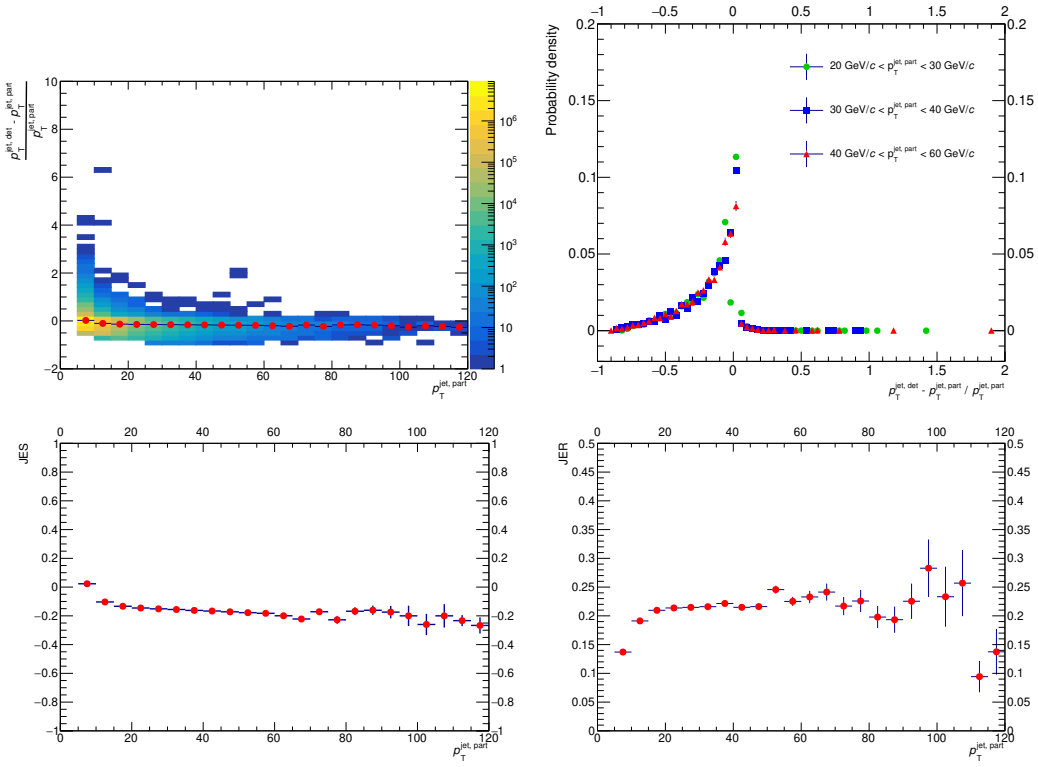

Figure 3.5: Jet performance plots for 0-20% central p–Pb collisions.

The performance plots for minimum bias pp collisions and minimum bias and 0-20% central p–Pb collisions are shown in Figs. 3.3–3.5. The distributions of JES (top right) show peaks close to zero, accompanied by asymmetric tails toward negative values, resulting from track reconstruction inefficiency. The values of JER show ~20–30% residual fluctuations for all collision systems.

3.1.7.2 Jet and track matching

A suitable and reasonable matching of jets and tracks between the particle- and detector-levels is required in order to build the response matrices. The framework of the applied matching procedure is schematically shown in Fig. 3.6.

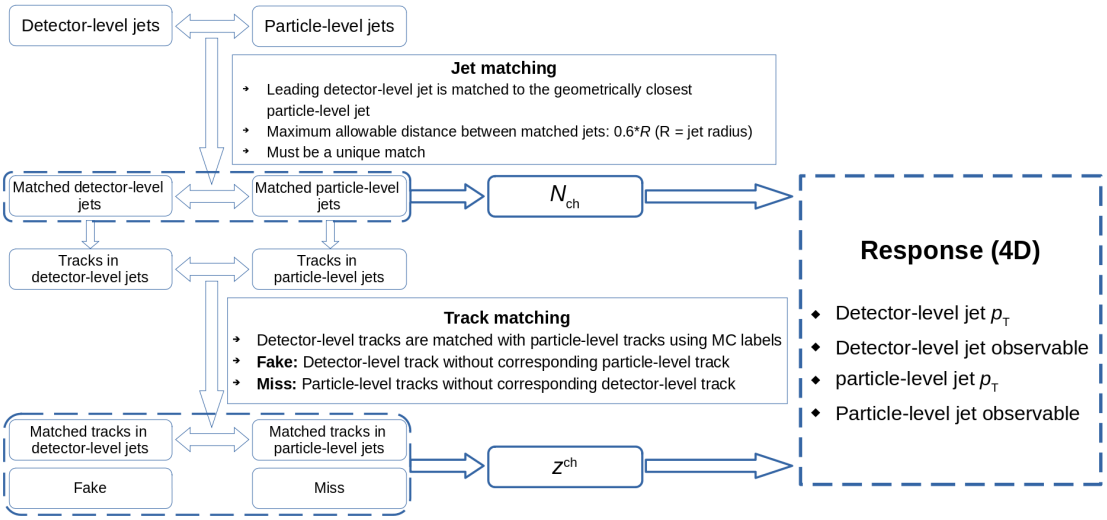

Figure 3.6: Jet and track matching algorithm.

The detector-level jets are matched to the geometrically closest particle-level jets. The conditions for accepting a matched pair of particle- and detector-level jets are that the maximum distance allowed between the matched jets is $0.6*R$ where R is the jet radius and it must be a unique match. Only the leading detector-level jet and the corresponding matched particle-level jet in an event are considered to construct the response matrices.

In order to construct response matrix for fragmentation function (z^{ch}), further matching is required between the detector- and particle-level tracks inside the matched pair of jets. It is performed using MC labels, which are unique numbers assigned to the tracks obtained from simulation. Thus, a matched pair of particle- and detector-level tracks must have the same MC label. In addition, fake tracks (the detector-level tracks which are not associated with any particle-level track) and missed tracks (the particle-level tracks which are not associated with any detector-level track) are also accounted for as ingredients of the unfolding by including them in the response matrix through two functions, namely 'Fake' and 'Miss' functions, respectively, in the *RooUnfoldResponse* class implemented

in the RooUnfold package. These fake and missed tracks carry the information of purity and efficiency, respectively.

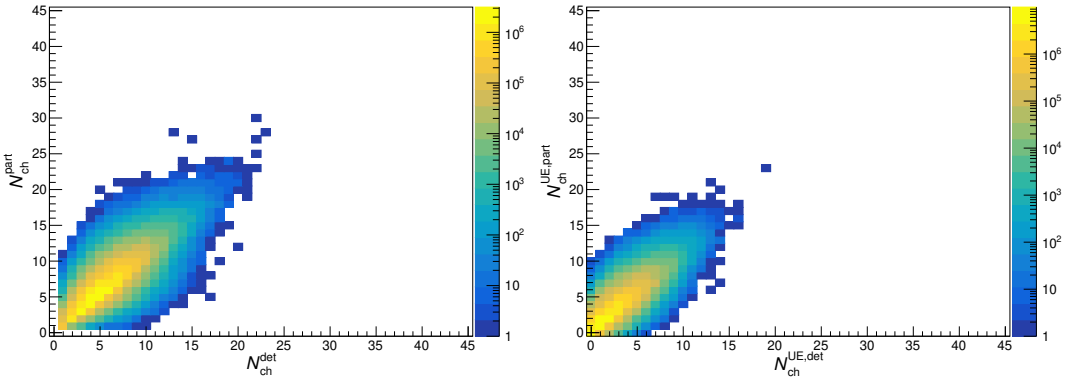

Figure 3.7: Projections of response matrices for N_{ch} (left) and N_{ch}^{UE} (right) in minimum bias p–Pb collisions.

Figures 3.7 show the projections of response matrices for N_{ch} (left) and N_{ch}^{UE} (right) in minimum bias p–Pb collisions. The full set of responses is shown in Appendix B.

3.1.7.3 Choice of regularization parameter

To ensure that the unfolded distributions do not possess unreasonable fluctuations, each unfolding method employs regularization process with tunable parameters, known as regularization parameters, to the unfolded distributions. In the Bayesian unfolding, the regularization parameter is the number of iterations. If a very small number of iterations is considered, the results will not converge, leading to unreasonable corrections in the unfolded distributions. Similarly, a very large number of iterations will inflict large statistical uncertainties.

In order to choose the optimal number of iterations, the statistical uncertainty is compared with the unfolding uncertainties (prior and regularization) of the unfolded distributions as a function of the number of iterations. The prior uncertainty is the uncertainty introduced in the unfolded distribution due to the change of shape of the prior distribution

that is used in the unfolding process as a priori guess of the unfolding solution, and it can be evaluated by modifying the shape of the prior distribution before unfolding is carried out. The regularization uncertainty is the uncertainty in the unfolded distribution coming from the choice of a particular value of the regularization parameter, i.e., the number of iterations in case of Bayesian unfolding, and it can be estimated by performing unfolding with the number of iterations varying around the chosen optimal value. In unfolding procedure, the statistical uncertainty usually increases with the number of iterations while the unfolding uncertainties decrease. The summed error, i.e., the quadrature sum of the statistical uncertainty, prior uncertainty, and regularization uncertainty, is evaluated for each observable in the following way:

$$Summed\ error = \sqrt{(SE_{Iter})^2 + (SE_{Prior})^2 + (SE_{Stat})^2} \tag{3.10}$$

Here SE_{Iter}, SE_{Prior} and SE_{Stat} are calculated as

$$(SE_{Iter})^2 = \sum_{i}^{N_{bins}} \left(\frac{1}{2} \sqrt{\left(Obs_i^{It+1} - Obs_i^{It}\right)^2 + \left(Obs_i^{It-1} - Obs_i^{It}\right)^2} \right)^2 \tag{3.11}$$

$$(SE_{Prior})^2 = \sum_{i}^{N_{bins}} \left(Obs_i^{Modified} - Obs_i^{Default}\right)^2 \tag{3.12}$$

$$(SE_{Stat})^2 = \sum_{i}^{N_{bins}} \left(Err\_Obs_i^{Default}\right)^2 \tag{3.13}$$

where

- Obs^{It}, Obs^{It+1} and Obs^{It-1} are the values of the observable for the optimal or default number of iterations (It), It+1 and It-1 respectively
- $Obs^{Default}$ and $Obs^{Modified}$ are the values of the observable for default and modified priors, respectively

- $Err\_Obs^{Default}$ is the statistical error in the observable value
- subscript 'i' everywhere represents the i-th bin in the distribution of the observable

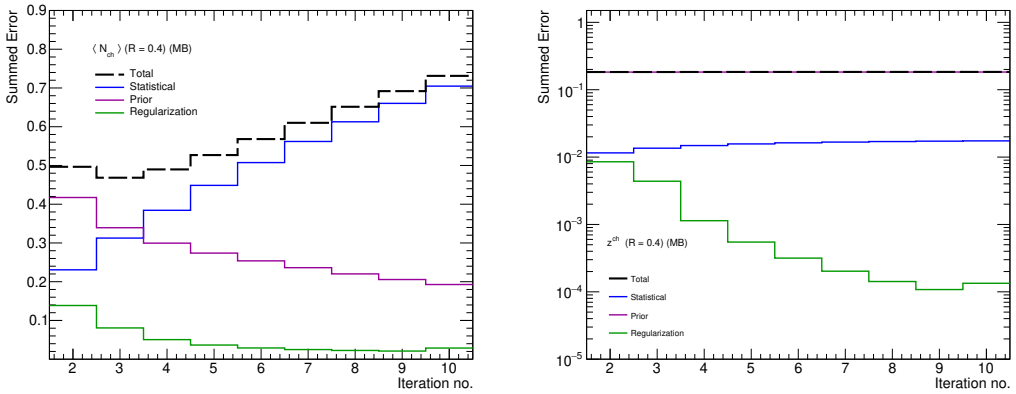

Figure 3.8: The statistical uncertainties and unfolding uncertainties as a function of the number of iterations for $\langle N_{\mathrm{ch}} \rangle$ (left) and z^{ch} (right) in minimum bias pp collisions.

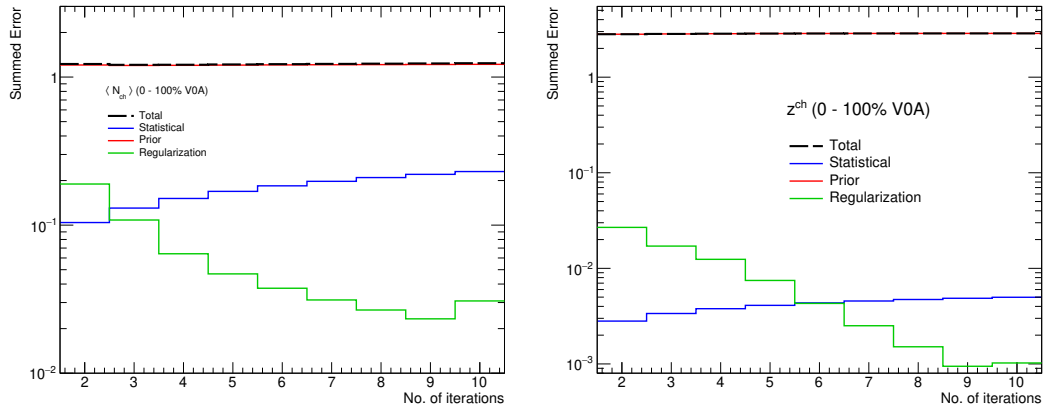

Figure 3.9: The statistical uncertainties and unfolding uncertainties as a function of the number of iterations for $\langle N_{\mathrm{ch}} \rangle$ (left) and z^{ch} (right) in minimum bias p–Pb collisions.

The default number of iterations is chosen as the one that minimizes the total uncertainty. The prior uncertainty is calculated by changing the prior by the procedure described in Sec. 3.1.9. For pp collisions, the default numbers of iterations are 3 for both the observables based on the minimum total uncertainty as shown in Figs. 3.8. For both

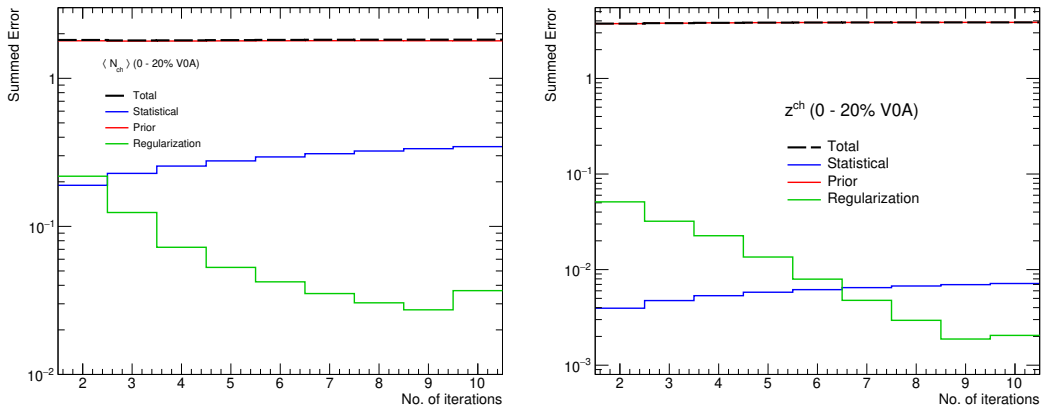

Figure 3.10: The statistical uncertainties and unfolding uncertainties as a function of the number of iterations for $\langle N_{\mathrm{ch}} \rangle$ (left) and z^{ch} (right) in 0–20% central p–Pb collisions.

minimum bias and high multiplicity p–Pb collisions, the default numbers of iterations for $\langle N_{\mathrm{ch}} \rangle$ and fragmentation function are chosen as 3 and 2, respectively, as can be seen in Figs. 3.9 – 3.10.

3.1.7.4 MC Closure tests

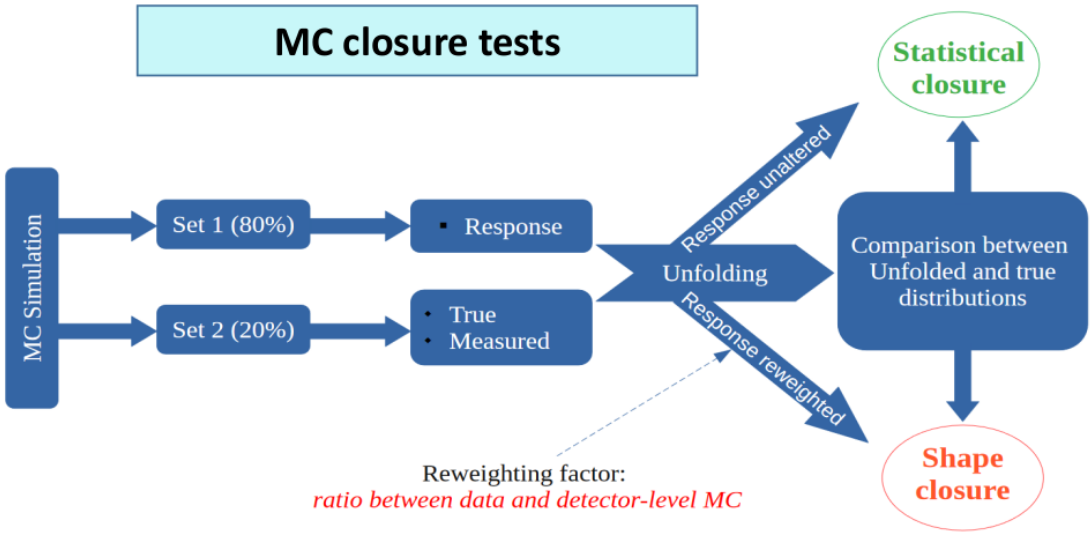

Figure 3.11: Procedure of MC closure tests.

In order to check the sensitivity and robustness of the unfolding procedure against

statistical fluctuations and change of shape of the prior distributions, MC closure tests are performed. Two types of MC closure tests, statistical closure and shape closure tests, are carried out in this analysis. The procedures for the two types of MC closure tests followed in this analysis are schematically shown in Fig. 3.11.

In the statistical closure test, two disjoint (statistically independent) sets of simulated events are considered where the response matrix is constructed from one set, and the true and measured distributions are obtained from the other set. After unfolding the measured distribution using the response matrix, the unfolded distribution is compared with the true distribution. The results of the statistical closure tests for the $\langle N_{\rm ch} \rangle$ distributions as a function of leading jet $p_{\rm T}$ and $z^{\rm ch}$ distributions for leading jet $p_{\rm T}$ = 20–30 GeV/c in minimum bias pp and minimum bias and central p–Pb collisions are shown in Figs 3.12–3.17. In these figures, the top panels show the true and unfolded distributions (unfolded with the chosen optimal or default number of iterations in each case), and the bottom panels show the ratio between the unfolded and true distributions. The complete set of results is shown in Appendix C.1. In the shape closure test, a similar approach as the statistical closure test is adopted; however, the response matrix is reweighted with the ratio between the data and the detector-level distributions before unfolding is performed. The results of the shape closure tests for the $\langle N_{\rm ch} \rangle$ distributions as a function of leading jet $p_{\rm T}$ and $z^{\rm ch}$ distributions for leading jet $p_{\rm T}$ = 20–30 GeV/c are shown in Figs 3.18–3.23 for minimum bias pp and minimum bias and central p–Pb collisions. The complete set of results is shown in Appendix C.2. In this analysis, both tests show good closure within statistical uncertainties and provide confidence in the unfolded results.

3.1.8 Underlying event

Reconstructed jets are contaminated by contributions from sources other than the hard-scattered partons from which the jet constituents are produced. These contaminations

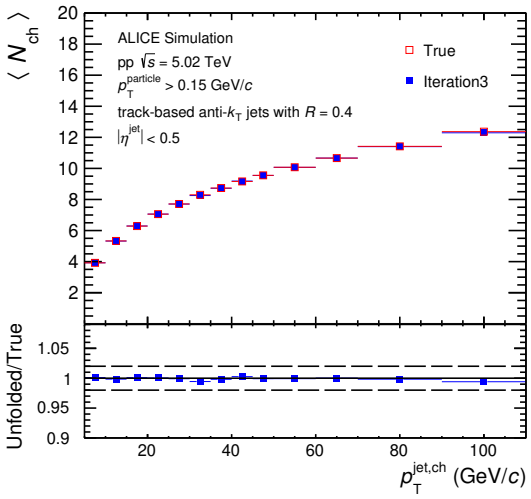

Figure 3.12: $\langle N_{\mathrm{ch}} \rangle$ distributions in minimum bias pp collisions: statistical closure (iteration 3).

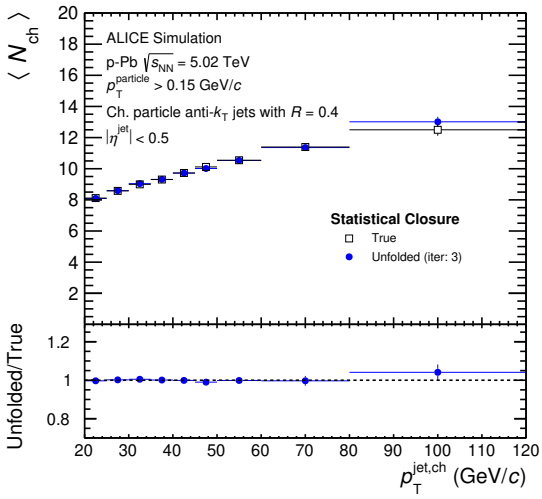

Figure 3.13: $\langle N_{\mathrm{ch}} \rangle$ distributions in minimum bias p–Pb collisions: statistical closure (iteration 3).

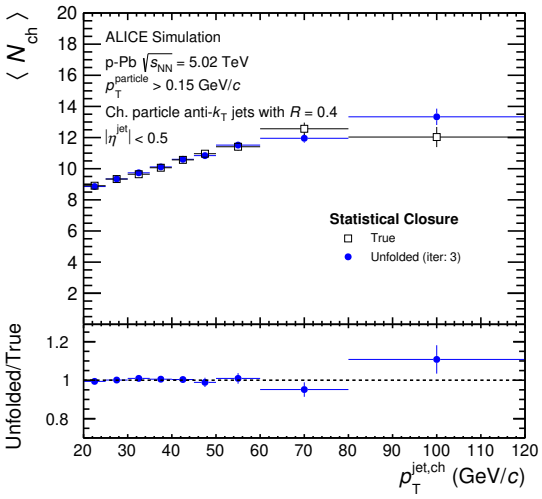

Figure 3.14: $\langle N_{\mathrm{ch}} \rangle$ distributions in 0–20% central p–Pb collisions: statistical closure (iteration 3).

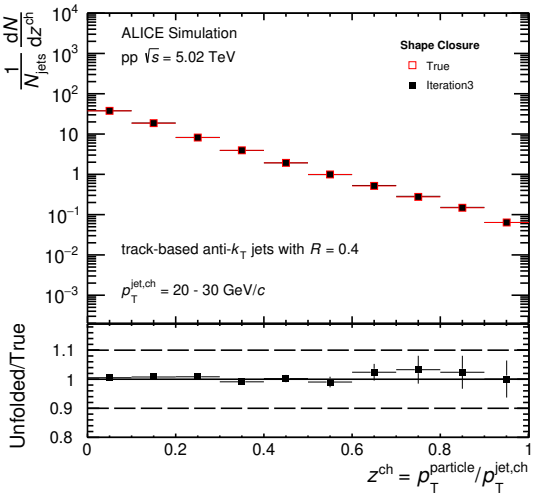

Figure 3.15: z^{ch} distributions for leading jet p_T = 20–30 GeV/c in minimum bias pp collisions: statistical closure (iteration 3).

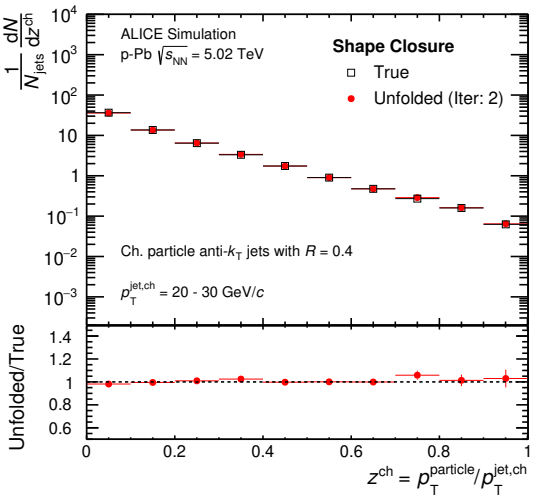

Figure 3.16: z^{ch} distributions for leading jet p_T = 20–30 GeV/c in minimum bias p–Pb collisions: statistical closure (iteration 2).

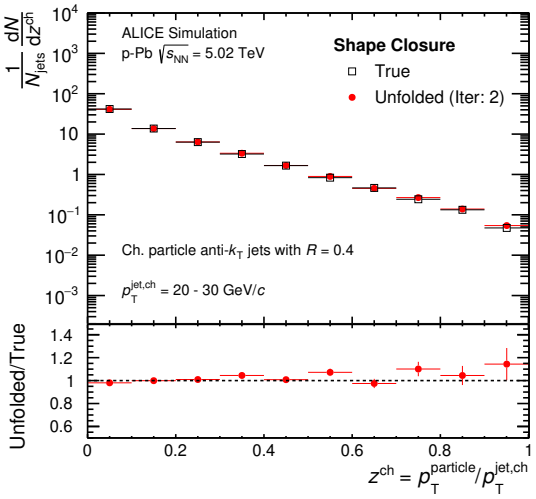

Figure 3.17: z^{ch} distributions for leading jet p_T = 20–30 GeV/c in 0–20% central p–Pb collisions: statistical closure (iteration 2).

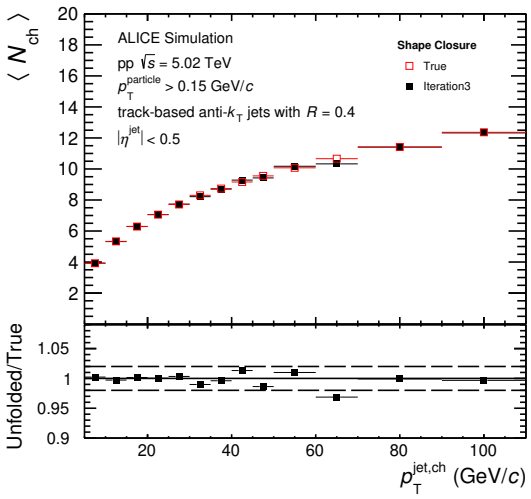

Figure 3.18: $\langle N_{ch} \rangle$ distributions in minimum bias pp collisions: shape closure (iteration 3).

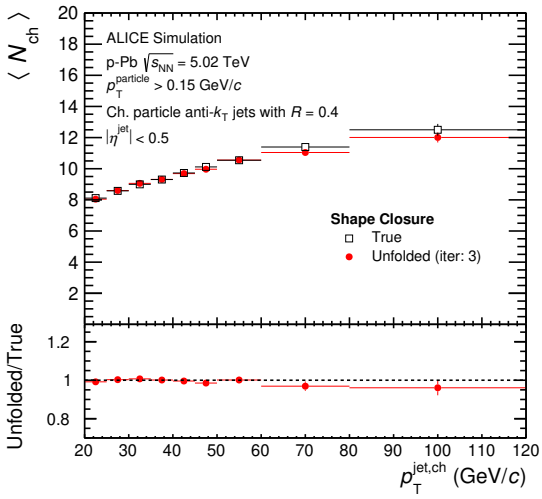

Figure 3.19: $\langle N_{ch} \rangle$ distributions in minimum bias p–Pb collisions: shape closure (iteration 3).

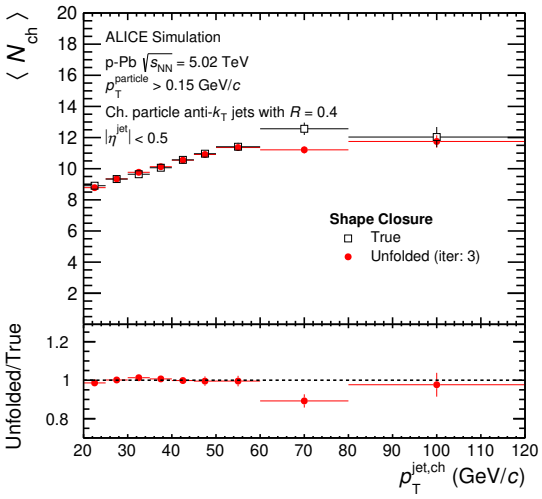

Figure 3.20: $\langle N_{ch} \rangle$ distributions in 0–20% central p–Pb collisions: shape closure (iteration 3).

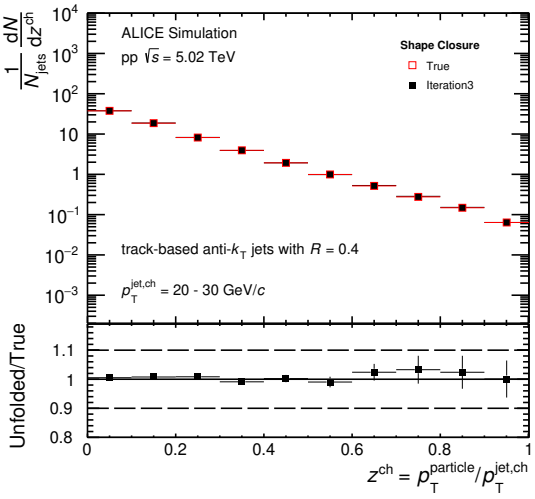

Figure 3.21: z^{ch} distributions for leading jet p_T = 20–30 GeV/c in minimum bias pp collisions: shape closure (iteration 3).

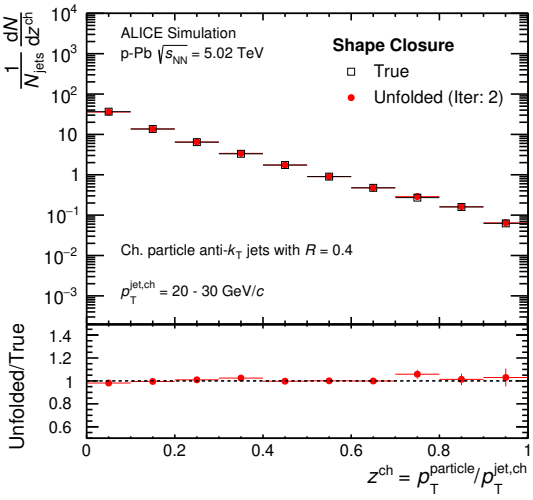

Figure 3.22: z^{ch} distributions for leading jet p_T = 20–30 GeV/c in minimum bias p–Pb collisions: shape closure (iteration 2).

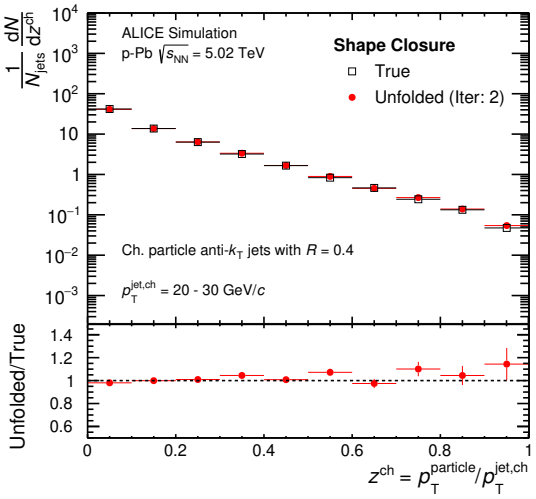

Figure 3.23: z^{ch} distributions for leading jet p_T = 20–30 GeV/c in 0–20% central p–Pb collisions: shape closure (iteration 2).

are known as underlying event (UE) contributions and mostly consist of particles from the beam-beam remnants, initial and final state radiations, and contributions from MPIs, etc [17]. The empirical models used to describe the non-perturbative aspects in the evolution of a high-energy scattering event do not allow to clearly distinguish particles originating from hard processes and the underlying event [18]. Several methods are available that can be applied to estimate the UE contributions. In this analysis, the following methods are implemented.

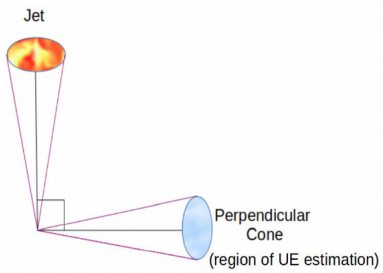

Figure 3.24: UE estimation in perpendicular cone method.

Perpendicular cone (PC) method

In this method, the UE is estimated from circular regions transverse to the measured jet cones in each event. The size of these circular regions is kept to be the same as the radius of the jet $R = 0.4$ at the same pseudorapidity as the leading jet but offset at an azimuthal angle $\Delta\varphi = \pm\pi/2$ relative to the jet axis. This method is usually used in small collision systems where the UE contribution is less compared to that in heavy-ion collisions.

Random cone (RC) method

In this method, two cones are randomly generated with the same η as the leading jet, but in the expanded transverse region (one cone within $\pi/3 < \Delta\varphi < 2\pi/3$ and another within $-2\pi/3 < \Delta\varphi < -\pi/3$, $\Delta\varphi$ being the difference between the considered jet and the random cone in azimuthal angle φ) with respect to the jet axis, unlike at a fixed value of azimuthal angle ($\Delta\varphi = \pm\pi/2$) as in perpendicular cone method. The UE contributions to the jet observables are estimated from these random cones.

In this analysis, the perpendicular cone method is used as the default one, whereas the random cone method is used to estimate the systematic uncertainty in UE. In addition, the UE contributions estimated from these two methods are compared with another one, the improved median method (discussed below), where the estimation and subtraction of UE are carried out jet-by-jet, unlike the other two methods.

Improved median method

This method is an improved version of the median method [19] widely used for background subtraction in heavy-ion collisions, and the improvement includes adaptation of the method to sparser environments such as small collision systems where most of the phase space is empty (devoid of final-state particles), in contrast to the heavy-ion scenario.

In the improved median method, charged-particle jets reconstructed using k_{T} algorithm are considered for the estimation of underlying event contribution in the observable $\langle N_{\mathrm{ch}} \rangle$. The two highest p_{T} jets are excluded, and the density of the number of charged particles (ρ_{N}) coming from underlying events is calculated using the following Eq.:

$$\rho_{\mathrm{N}} = \mathrm{Median}\{\rho_{\mathrm{N}}^{i}\}.C \tag{3.14}$$

where

$$\rho_{\mathrm{N}}^{i} = \frac{p_{\mathrm{T}}^{i}}{A^{i}} \tag{3.15}$$

p_{T}^{i} and A^{i} being the p_{T} and area of the i-th k_{T} jet and C is a factor which takes into account the empty regions in the phase space in p–Pb events where the number density is much

smaller compared to Pb–Pb events. C factor is defined in an event as:

$$C = \frac{\begin{array}{c}\text{sum of areas of } k_{\mathrm{T}} \text{ jets having physical tracks} \\ \text{(including the two highest } p_{\mathrm{T}} \text{ jets and excluding ghost–only jets)}\end{array}}{\begin{array}{c}\text{sum of areas of all } k_{\mathrm{T}} \text{ jets} \\ \text{(including the two highest } p_{\mathrm{T}} \text{ jets and ghost–only jets)}\end{array}} \tag{3.16}$$

Ghost-only jets indicate those jets which contain ghost particles ($p_{\mathrm{T}} \simeq 10^{-100}$ GeV/c) only and do not contain any physical track. This method is not applied to estimate the UE contribution to the z^{ch} observable since the presence of k_{T} clusters biases the shape of the UE distribution for this observable, which is true for other differential jet properties as well.

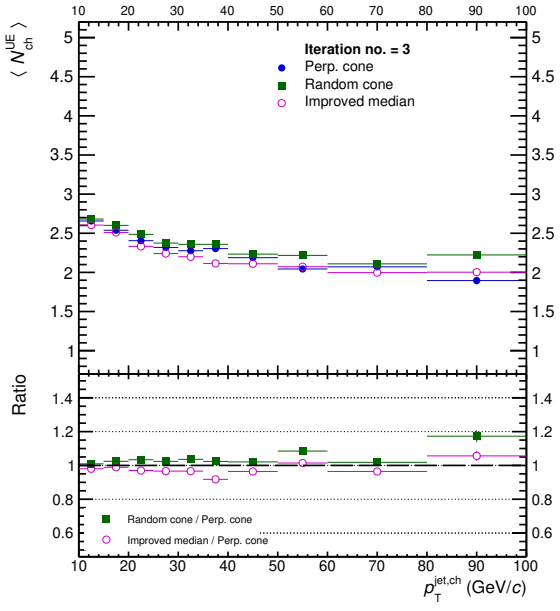

Figure 3.25: Top: UE contributions in $\langle N_{\mathrm{ch}} \rangle$ distribution as a function of leading jet p_{T} with UE estimated using perpendicular cone method, random cone method and improved median method. Bottom: Ratio between UE estimated using other methods with UE estimated using perpendicular cone method.

Fig. 3.25 shows the comparison between UE contributions in $\langle N_{\mathrm{ch}} \rangle$, estimated using three different methods (perpendicular cone method, random cone method and improved

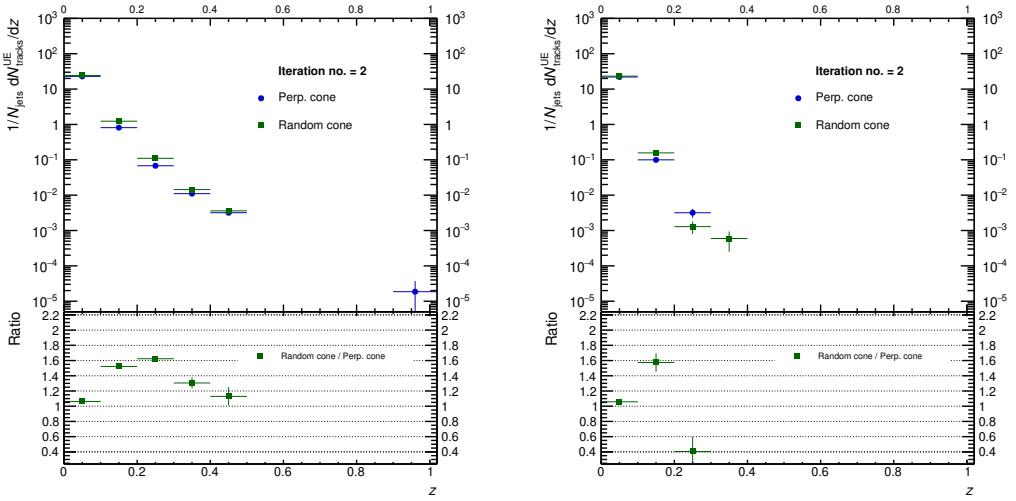

Figure 3.26: Top panels: UE contributions in z^{ch} distributions for leading jet p_{T} = 20–30 GeV/c (left) and 40–60 GeV/c (right). Bottom panels: Ratio between UE estimations of random cone method and perpendicular cone method.

median method) in minimum bias p–Pb collisions. These results are corrected for the instrumental effects using the unfolding procedure discussed in Sec. 3.1.7.1. The UE contributions obtained using different methods are mostly consistent with each other, and the fluctuations are very small or negligible compared to the total systematic uncertainties discussed later in Sec. 3.1.9. Fig. 3.26 shows the comparisons between UE contributions in z^{ch} distributions for leading jet p_{T} = 20–30 GeV/c (left) and 40–60 GeV/c (right), estimated using the perpendicular cone and random cone method, where the UE estimations are negligible compared to the signal values.

3.1.8.1 Correction for underlying event

In this analysis, the underlying event is estimated using the perpendicular cone method discussed in Sec. 3.1.8. The subtraction of UE is performed on a statistical basis for each observable bin-by-bin, using the following steps for both minimum bias pp and p-Pb collisions as well as central p-Pb collisions:

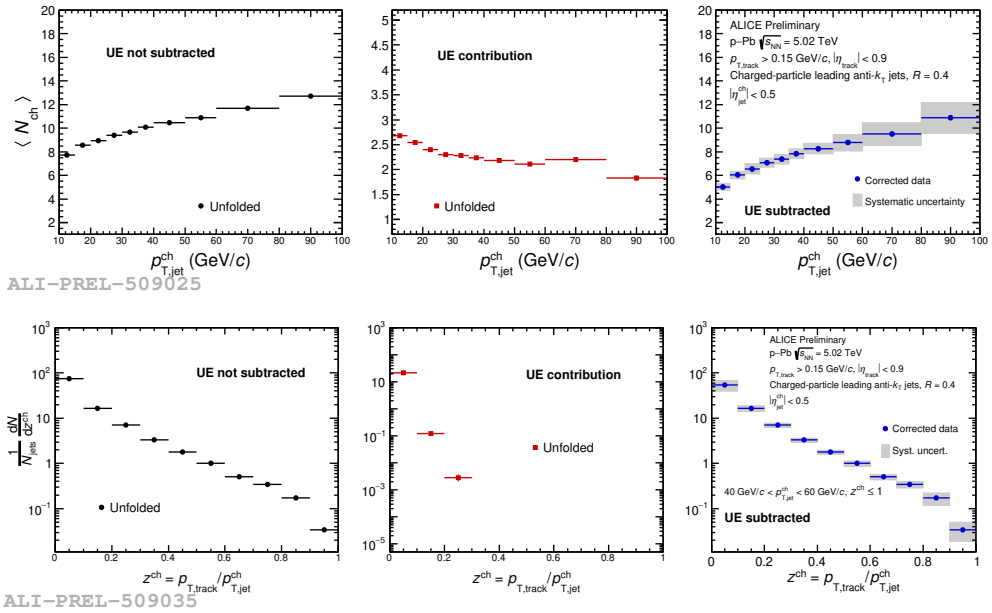

Figure 3.27: Correction procedure to subtract UE contributions for $\langle N_{ch} \rangle$ and z^{ch} ($40 < p_{T,jet}^{ch} < 60$ GeV/c): Unfolded distributions without UE subtraction (left), UE contribution (middle) and after UE subtraction (right) [20, 21].

1. Correct the signal distributions (contaminated with UE) for instrumental effects using unfolding

2. Correct the UE distributions for instrumental effects using unfolding

3. Corrected UE contributions are subtracted from the corrected signal distributions (contaminated with UE) for each observable

The UE subtractions for all the measured jet observables are carried out on a statistical basis; however, no corrections are done for jet p_T separately. The UE subtraction procedure [20, 21] followed in this analysis is illustrated in Fig. 3.27.

3.1.9 Estimation of systematic uncertainties

The unfolded distributions are obtained from the uncorrected raw distributions in several steps. The correction for instrumental effects, estimation and subtraction of UE are

some of the important steps. The associated uncertainties in these steps may result in uncertainties, collectively called systematic uncertainties, in the final unfolded and UE subtracted results. Several sources of systematic uncertainties are associated with the unfolded and UE subtracted distributions of the measured jet observables. The obtained final results in this measurement have five main sources of systematic uncertainty. Each of the systematic uncertainties coming from individual sources is quantified by varying the relevant parameter with respect to the default analysis in a reasonable way and constructing a new, modified response matrix to unfold the raw data. For each of the sources, once the unfolded distributions are obtained by performing unfolding with the default and modified response matrices separately, the systematic uncertainty is estimated by using the expression:

$$\text{Systematic uncertainty} = \frac{\text{Modified} - \text{Default}}{\text{Default}} \tag{3.17}$$

where 'Modified' and 'Default' refer to the unfolded distributions obtained by using the the modified and default response matrices, respectively. The major sources of systematic uncertainties for the measured jet observables and procedures of their estimations are discussed below in detail:

- **Track reconstruction inefficiency:** Track reconstruction inefficiency induces loss of tracks at the detector level with respect to the particle level. It is determined by comparing the spectra of track p_{T} at the detector and particle levels as the detector-level tracks are reconstructed after transporting the particle-level tracks through the detector simulation. However, this procedure is not totally free from imperfections, leading to uncertainty in the estimated track reconstruction inefficiency. By applying variations in the track selection criteria and considering the possible imperfections in the track matching efficiency for the TPC-ITS tracks, the uncertainties in the track reconstruction efficiencies have been estimated to be 3% for pp collisions

Table 3.2: Summary of systematic uncertainties (in %) on $\langle N_{\rm ch} \rangle$ for selected intervals of jet $p_{\rm T}$ in minimum bias pp, minimum bias p–Pb and central p–Pb collisions.

Sources	**Systematic uncertainties on $\langle N_{\rm ch} \rangle$ (%)**								
	Minimum bias pp			**Minimum bias p–Pb**			**Central p–Pb**		
	Jet $p_{\rm T}$ in GeV/c			Jet $p_{\rm T}$ in GeV/c			Jet $p_{\rm T}$ in GeV/c		
	20–25	50–60	80–100	20–25	50–60	80–100	20–30	40–60	80–100
Track reconst. inefficiency	0.10	0.28	0.01	1.38	1.07	1.08	1.31	1.64	2.62
Regularization parameter	0.01	0.09	0.59	0.25	0.09	0.27	0.28	0.05	0.14
Bin truncation	0.45	0.30	2.19	0.12	0.38	1.54	0.03	0.24	1.19
Prior change	0.08	1.00	1.49	0.77	0.20	6.78	1.03	0.07	8.85
UE method	0.30	0.10	0.59	1.11	0.52	2.20	0.80	0.88	0.13
Total	0.56	1.09	2.77	1.95	1.27	7.37	1.87	1.88	9.31

and to be dependent on track $p_{\rm T}$ for p–Pb collisions. To evaluate the effect of these uncertainties on the measured distributions, tracks are randomly discarded from the detector level by 3% for pp collisions and based on track $p_{\rm T}$ for p–Pb collisions before applying the jet finding algorithm and a new, modified response matrix is constructed to unfold the data. The difference between the new unfolded results (unfolded with the new response matrix) and the default one (unfolded with the default response matrix) is quoted as the systematic uncertainty due to track reconstruction inefficiency.

- **Change in prior:** As mentioned earlier, one of the most important factors behind the success of the unfolding procedure is the choice of the prior distribution. Depending on the shape of the chosen prior distribution, the unfolding process might take a small or a large number of iterations to achieve a stable solution. To estimate the systematic uncertainty due to change in the shape of the considered prior distribution, the default response matrix is weighted with reweighting factors. The reweighting factors are determined by taking ratio between the raw data and detector-level MC

Table 3.3: Summary of systematic uncertainties (in %) on $\mathrm{d}N/\mathrm{d}z^{\mathrm{ch}}$ in z^{ch} bins for selected intervals of jet p_{T} in minimum bias pp, minimum bias p–Pb and central p–Pb collisions.

Jet p_{T} (GeV/c)	**Sources**	**Systematic uncertainties on $\mathrm{d}N/\mathrm{d}z^{\mathrm{ch}}$ (%)**								
		Minimum bias pp			**Minimum bias p–Pb**			**Central p–Pb**		
		z^{ch} bin			z^{ch} bin			z^{ch} bin		
		0 – 0.1	0.4 – 0.5	0.9 – 1	0 – 0.1	0.4 – 0.5	0.9 – 1	0 – 0.1	0.4 – 0.6	0.8 – 1
20–30	**Track reconst. inefficiency**	0.47	0.18	0.14	2.12	1.36	7.51	2.29	2.02	7.03
	Regularization parameter	0.18	0.02	0.18	1.35	0.34	2.09	1.84	0.68	0.85
	Bin truncation	2.37	4.11	4.20	0.95	6.10	6.70	0.41	7.14	7.75
	Prior change	2.47	0.08	1.95	12.34	6.16	0.90	14.18	4.73	3.15
	UE method	0.46	0.08	0.00	3.02	0.12	0.01	5.51	0.14	0.00
	Total	3.49	4.11	4.64	12.98	8.79	10.32	15.50	8.82	10.96
30–40	**Track reconst. inefficiency**	0.50	0.14	1.87	2.12	1.85	6.52	2.37	2.39	8.69
	Regularization parameter	0.08	0.35	1.97	1.07	0.10	0.96	1.60	1.10	0.47
	Bin truncation	1.38	1.91	1.94	0.56	2.14	2.28	1.36	2.34	2.62
	Prior change	0.73	0.61	4.09	10.99	9.49	0.44	12.84	9.98	4.11
	UE method	1.16	0.20	0.00	2.89	0.01	0.00	3.82	0.00	0.00
	Total	2.01	2.05	5.28	11.62	9.91	6.99	13.77	10.58	9.98
40–60	**Track reconst. inefficiency**	0.24	0.62	0.41	1.88	1.63	3.93	2.17	1.38	10.77
	Regularization parameter	0.16	0.55	4.22	0.92	1.33	5.63	1.31	0.89	1.36
	Bin truncation	0.89	1.11	0.80	0.84	1.00	1.01	1.69	0.71	0.88
	Prior change	0.95	4.04	10.74	11.99	13.85	5.59	13.58	13.32	2.05
	UE method	0.21	0.15	0.00	2.46	0.00	0.00	2.78	0.00	0.00
	Total	1.35	4.27	11.57	12.44	14.05	8.91	14.19	13.44	11.08

distributions. These factors contain information about the point-to-point variation between the raw data and the detector-level MC distributions as a function of both the jet p_{T} and the jet observable, that is, N_{ch} or z^{ch}, and therefore accounts for the

difference in the shape of the distributions between data and the considered MC simulation. The ratio is then used to reweight the corresponding response matrix as a function of both the jet p_{T} and the jet observable in particle-level MC. This makes the reweighted response more data-like and mostly evades the dependence on the particular choice of the MC simulation. The corresponding systematic uncertainty is determined as the difference between the unfolded results obtained using the reweighted and the default response matrices.

- **Choice of regularization parameter (no. of iterations) in Bayesian unfolding:** Like the prior distribution, the regularization parameter also plays a significant role in reducing the fluctuations in the unfolded distributions and ensures the stability of the unfolded results. To determine the uncertainty induced by the choice of the default value of the regularization parameter (here, the number of iterations in case of Bayesian unfolding), the number of iterations is varied by ±1 from the default value. The amount of systematic uncertainty coming from this variation is small, as quoted in Tables 3.2 and 3.3.

- **Underlying event estimation method:** Uncertainty in the estimated underlying event contribution may affect the distributions of the measured jet observables. To assess its effect, UE contributions are estimated using the perpendicular cone method (the default method) and random cone method (systematic variation), and the UE subtracted distributions are obtained for the two methods separately, following the procedure discussed in Sec. 3.1.8.1. The corresponding systematic uncertainty is then calculated using Eq. 3.17.

- **Bin truncation:** During the unfolding, a particular interval of jet p_{T} ($5 < p_{\mathrm{T}}^{\mathrm{jet\,ch}} < 120$ GeV/c) is considered in both particle- and detector-levels while building the response matrix. It may happen that a particle-level jet may have its corresponding

detector-level jet outside the considered jet p_{T} interval, resulting in loss of jets, especially close to the boundary of the selected kinematic regime. In order to assess such effects on the unfolded distributions, the lower and upper limits of the detector-level jet p_{T} are varied by +5 GeV/c and -20 GeV/c, respectively, from the default range of 5–120 GeV/c. It is found that the effect is not significant for the entire jet p_{T} intervals except being non-negligible at low jet p_{T} region for both the observables.

The total systematic uncertainty is evaluated by taking the quadrature sum of the individual uncertainties. Tables 3.2 and 3.3 summarize the systematic uncertainties from individual sources in a few selected bins of the measured observables for both pp and p–Pb collisions. As is evident from the tables, in most of the cases, the uncertainty due to track reconstruction inefficiency and change of prior are the dominant sources, among others. To estimate the systematic uncertainty for the ratio of observables between pp and p–Pb collisions, each of the ratios is treated as an individual quantity, and the systematic uncertainties from individual sources are estimated accordingly. The breakdown of the total systematic uncertainty into its individual components is shown in Appendix D.

3.2 Results and discussion

After all the corrections are performed and the uncertainties are estimated, the fully corrected results are presented and discussed in comparison with various Monte Carlo model predictions for pp and p–Pb collisions at 5.02 TeV center-of-mass energy in the following sections.

3.2.1 Mean charged-particle multiplicity within jet ($\langle N_{\mathrm{ch}} \rangle$)

The fully corrected (unfolded and UE subtracted) distributions of the average number of charged particles ($\langle N_{\mathrm{ch}} \rangle$) within leading jets as a function of jet p_{T} are shown in

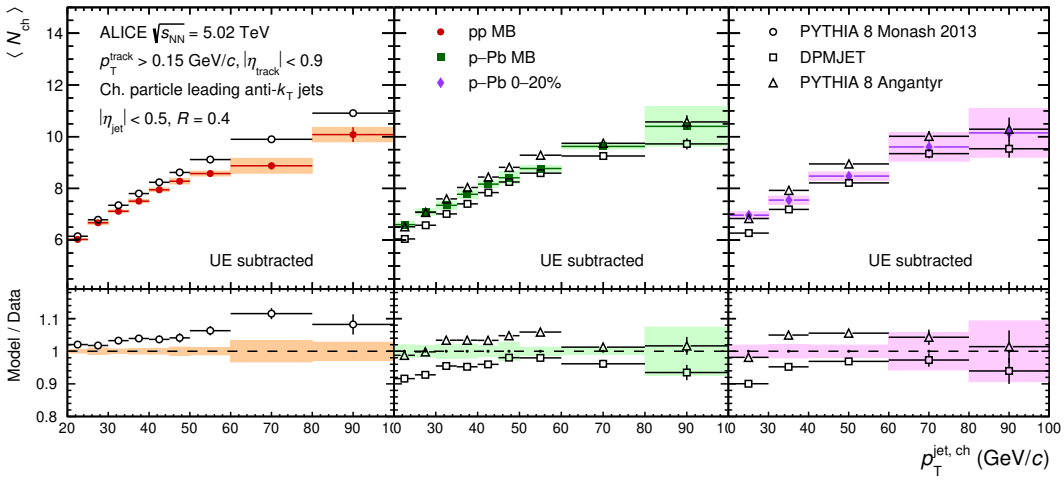

Figure 3.28: $\langle N_{\mathrm{ch}} \rangle$ distributions as a function of leading jet p_{T} in minimum bias pp (left), minimum bias p–Pb (middle), and 0–20% central p–Pb (right) collisions. The solid markers, shaded bands and open markers represent the corrected data, corresponding systematic uncertainties and the predictions from different MC models. Bottom panels show the ratios between the MC predictions and data.

Figure 3.28 for charged-particle leading jets reconstructed with $R = 0.4$ at mid-rapidity in minimum bias pp (left), minimum bias p–Pb (middle), and 0–20% central p–Pb collisions, respectively. The solid markers denote the corrected data, and the colored bands represent the corresponding systematic uncertainties. The predictions from different MC models are represented by the open markers. The ratios between MC predictions and data are shown in the bottom panels.

It is found that for all collision systems, $\langle N_{\mathrm{ch}} \rangle$ increases monotonically with leading jet p_{T}; however, the rate of increase gradually decreases toward high jet p_{T}. These observations imply that high-momentum jets fragment into harder jet constituents. PYTHIA 8 Monash 2013 overestimates the pp data by at most 10%. In the case of p–Pb collisions, PYTHIA 8 Angantyr model could explain the data better than DPMJET model for both minimum bias and central events. At low jet p_{T}, DPMJET model underestimates the data.

The $\langle N_{\mathrm{ch}} \rangle$ distributions for leading jets are compared between different collision systems for both the corrected data and MC models, as illustrated in Figs. 3.29. The ratios

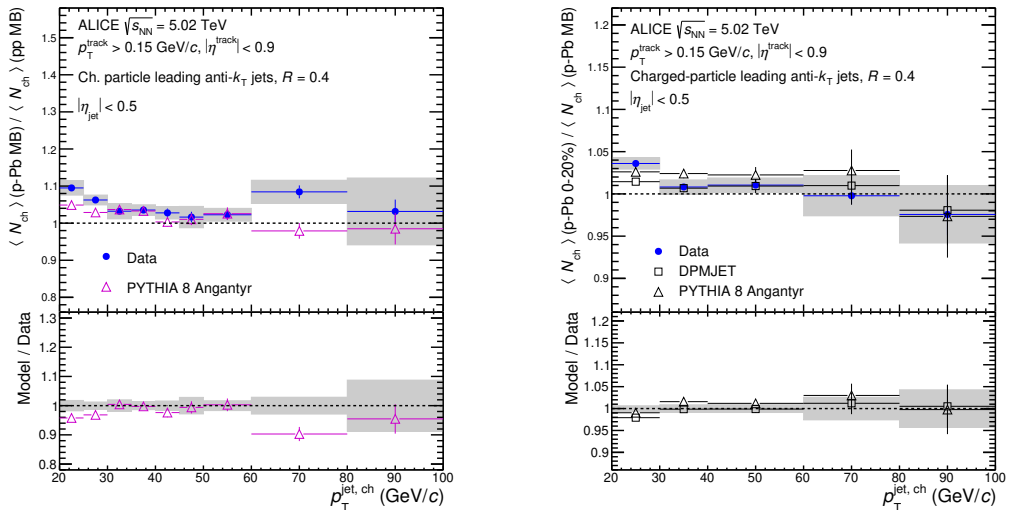

(a) (b)

Figure 3.29: The ratios of $\langle N_{ch} \rangle$ distributions of leading jets (a) between minimum bias p–Pb and pp collisions and (b) between central and minimum bias p–Pb collisions. Bottom panels show the ratios between the MC predictions and data.

of $\langle N_{ch} \rangle$ distributions between minimum bias p–Pb and pp collisions in the corrected data and PYTHIA 8 Angantyr model are shown in the top panel of Fig. 3.29a. The bottom panel shows the quantitative comparison between the data and PYTHIA 8 Angantyr model prediction. A mild increase (10%) in $\langle N_{ch} \rangle$ is observed in data, especially at low jet p_T, hinting toward possible jet modification. Interestingly, PYTHIA 8 Angantyr model also follows similar behaviour; however, it slightly underestimates the data. The results for z^{ch} distributions also show features of jet modification in similar kinematic regions, as will be discussed in detail in the next section.

The ratios of $\langle N_{ch} \rangle$ distributions between central and minimum bias p–Pb collisions in data and the corresponding MC comparisons (DPMJET and PYTHIA 8 Angantyr) are presented in Fig. 3.29b. No significant change is observed in data. The only exception is the lowest jet-p_T bin = 20–30 GeV/c where the change is below 5%. Both PYTHIA 8 Angantyr and DPMJET models are able to reproduce the data within systematic uncertainties.

3.2.2 Jet fragmentation function (z^{ch})

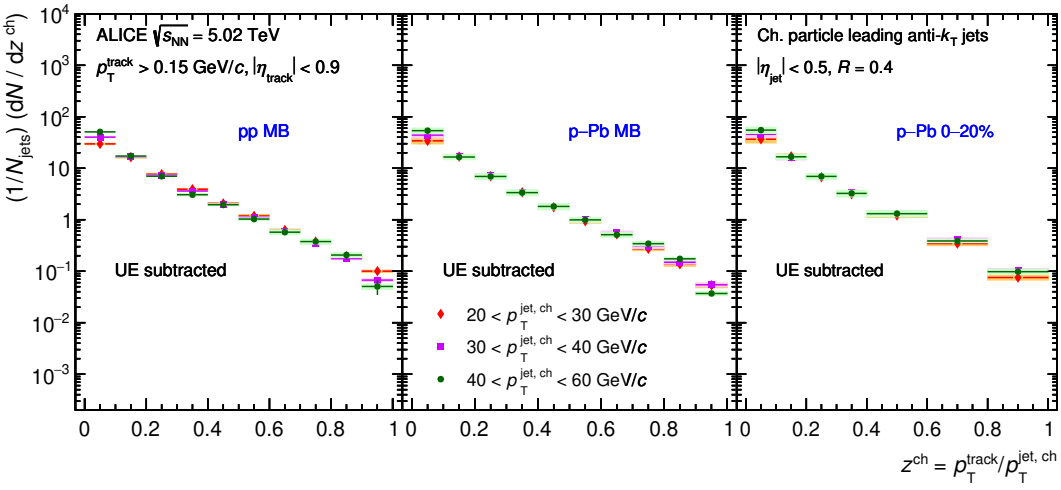

Figure 3.30: Scaling of z^{ch} distributions independent of jet p_{T} in minimum bias pp (left), minimum bias p–Pb (middle), and 0–20% central p–Pb (right) collisions.

The fully corrected (unfolded and UE subtracted) z^{ch} distributions of leading jets for different jet p_{T} intervals (20–30 GeV/c, 30–40 GeV/c and 40–60 GeV/c) are illustrated in Fig. 3.30 for charged-particle leading jets reconstructed with R = 0.4 at mid-rapidity in minimum bias pp (left), minimum bias p–Pb (middle), and 0–20% central p–Pb collisions (right) at 5.02 TeV center-of-mass energy. The solid markers denote the corrected data, and the colored bands represent the corresponding systematic uncertainties. The z^{ch} distributions for different jet p_{T} ranges are quite consistent with each other within systematic uncertainties in all three collision systems, except at very low and high z^{ch} values for minimum bias pp collisions and at high z^{ch} values for minimum bias p–Pb collisions. This behavior indicates that the jet fragmentation pattern does not vary considerably with jet p_{T}.

The comparisons of the measured z^{ch} distributions with different MC model predictions are shown in Fig. 3.31. For pp collisions, PYTHIA 8 Monash 2013 reproduces the data at low z^{ch} (< 0.4) values within systematic uncertainties but underestimates the data at intermediate and high z^{ch} values for the considered jet p_{T} ranges. In the case of

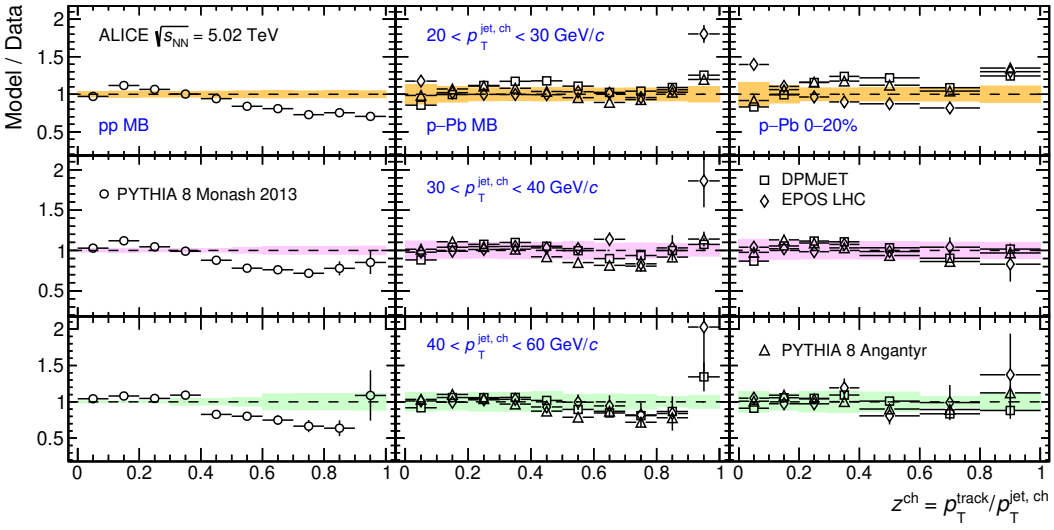

Figure 3.31: The ratios of z^{ch} distributions between MC model predictions and data in different jet p_T intervals in minimum bias pp (left), minimum bias p–Pb (middle), and 0–20% central p–Pb (right) collisions.

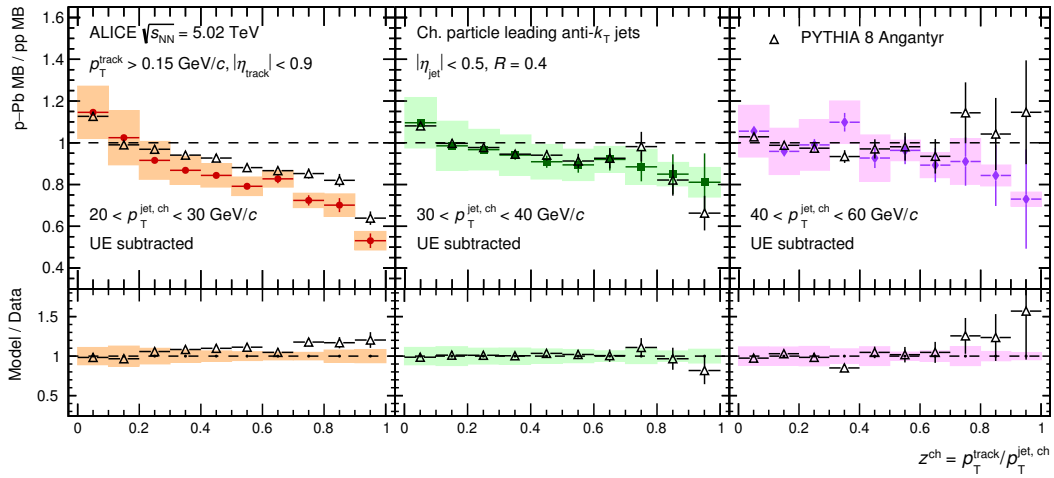

Figure 3.32: The ratios of z^{ch} distributions of leading jets between minimum bias p–Pb and pp collisions in different jet p_T intervals. Bottom panels show the ratios between the MC predictions and data.

p–Pb collisions, three MC models, DPMJET, EPOS LHC, and PYTHIA 8 Angantyr, are considered. Interestingly, all three models are found to explain the jet fragmentation distributions except the last bin for the reported jet p_T ranges within systematic uncertainties in

minimum bias p–Pb collisions. For central p–Pb collisions, all the models could reproduce the data within ~20%. It is also important to note that, in central p–Pb collisions, EPOS LHC shows an opposite trend compared to other models for jet p_{T} = 20–30 GeV/c.

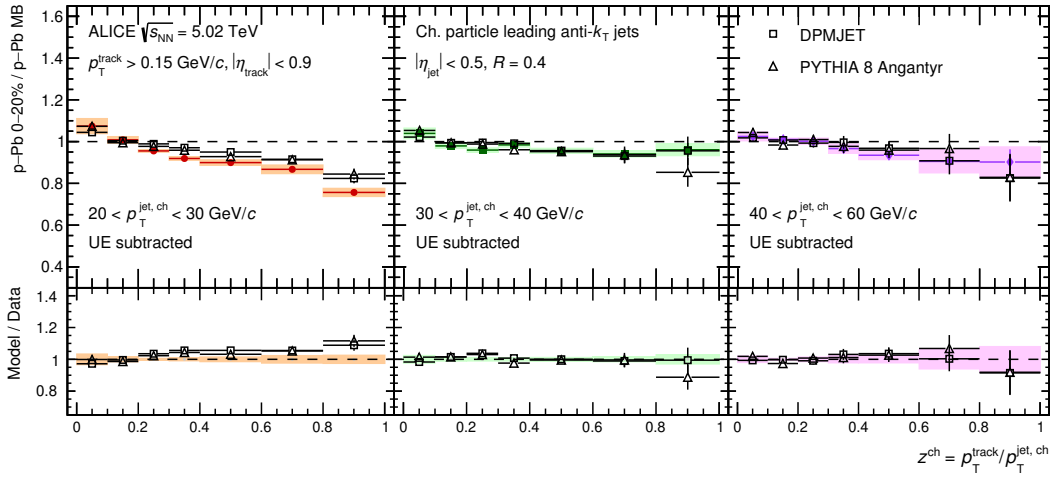

Figure 3.33: The ratios of z^{ch} distributions of leading jets between central and minimum bias p–Pb collisions in different jet p_{T} intervals. Bottom panels show the ratios between the MC predictions and data.

To look for the nuclear effect on jet fragmentation functions, z^{ch} distributions are compared between minimum bias p–Pb and pp collisions for leading jet p_{T} = 20–30 GeV/c (left), 30–40 GeV/c (middle) and 40–60 GeV/c (right) as shown in Figs. 3.32. It is interesting to observe that the jet fragmentation pattern is quite different in minimum bias p–Pb collisions compared to that in minimum bias pp collisions. The ratios indicate a small enhancement of low z^{ch}-particles, followed by a significant amount of suppression of high z^{ch}-particles inside jets. It is also important to note that the magnitude of this jet modification is the largest for the lowest jet p_{T} interval of 20–30 GeV/c and gets significantly reduced with increasing jet p_{T}. Given the uncertainties, no significant modification is observed at jet p_{T} = 40–60 GeV/c, which is in line with the findings of the ATLAS measurement of jet fragmentation in pp and p–Pb collisions [22] reported for a similar kinematic regime.

This is the first observation of jet modification in p–Pb collisions compared to pp collisions at LHC energies, unlike previous measurements [22, 23] (although carried out in higher jet momentum regions). Interestingly, the features of jet modification observed in data are qualitatively captured by PYTHIA 8 Angantyr model, where no jet quenching effect is implemented.

A similar observation comes from comparing z^{ch} distributions between central and minimum bias p–Pb collisions, as shown in Figs. 3.33 for the three reported jet p_{T} ranges. The jet p_{T}-dependent modification of jet fragmentation pattern is also observed between central and minimum bias p–Pb collisions, the highest modification being observed at the lowest jet p_{T} interval. It is also interesting to see that both PYTHIA 8 Angantyr and DPMJET models could qualitatively show similar behavior without any implementation of QGP-effects.

A further investigation of these interesting results with PYTHIA 8 Angantyr model (as discussed in Appendix E) hints toward the possibility that multiparton interaction and color reconnection mechanisms might play a role in the observed jet modification. It would be interesting to perform detailed studies, including several other models and theoretical calculations, to understand the observed jet modification in p–Pb collisions better.

Modifications of jet fragmentation, particularly for low-p_{T} jets (20–30 GeV/c) observed both in minimum bias and central p–Pb collisions compared to minimum bias pp and minimum bias p–Pb collisions, respectively, as reported in this analysis, are important observations. Although from these experimental measurements, one can not explicitly tell whether the formation of QGP droplets or some other physics phenomena are the origin(s) of these effects or these are mere artifacts of biases in the measurements, these observations are still exciting considering the fact that they are counter-intuitive against our conventional expectation.

Bibliography

[1] J. Alme *et al.*, "The ALICE TPC, a large 3-dimensional tracking device with fast readout for ultra-high multiplicity events," *Nucl. Instrum. Meth. A* **622** (2010) 316–367, arXiv:1001.1950 [physics.ins-det].

[2] ALICE, K. Aamodt *et al.*, "Alignment of the ALICE Inner Tracking System with cosmic-ray tracks," *JINST* **5** (2010) P03003, arXiv:1001.0502 [physics.ins-det].

[3] T. Sjöstrand, S. Ask, J. R. Christiansen, R. Corke, N. Desai, P. Ilten, S. Mrenna, S. Prestel, C. O. Rasmussen, and P. Z. Skands, "An introduction to PYTHIA 8.2," *Comput. Phys. Commun.* **191** (2015) 159–177, arXiv:1410.3012 [hep-ph].

[4] P. Skands, S. Carrazza, and J. Rojo, "Tuning PYTHIA 8.1: the Monash 2013 Tune," *Eur. Phys. J. C* **74** no. 8, (2014) 3024, arXiv:1404.5630 [hep-ph].

[5] S. Roesler, R. Engel, and J. Ranft, "The Monte Carlo event generator DPMJET-III," in *International Conference on Advanced Monte Carlo for Radiation Physics, Particle Transport Simulation and Applications (MC 2000)*, pp. 1033–1038. 12, 2000. arXiv:hep-ph/0012252.

[6] T. Pierog, I. Karpenko, J. M. Katzy, E. Yatsenko, and K. Werner, "EPOS LHC: Test of collective hadronization with data measured at the CERN Large Hadron Collider," *Phys. Rev. C* **92** no. 3, (2015) 034906, arXiv:1306.0121 [hep-ph].

[7] R. Brun, F. Bruyant, F. Carminati, S. Giani, M. Maire, A. McPherson, G. Patrick, and L. Urban, *GEANT: Detector Description and Simulation Tool; Oct 1994*. CERN Program Library. CERN, Geneva, 1993. https://cds.cern.ch/record/1082634. Long Writeup W5013.

[8] C. Bierlich, G. Gustafson, L. Lönnblad, and H. Shah, "The Angantyr model for Heavy-Ion Collisions in PYTHIA8," *JHEP* **10** (2018) 134, arXiv:1806.10820 [hep-ph].

[9] ALICE, J. Adam *et al.*, "Centrality dependence of particle production in p-Pb collisions at $\sqrt{s_{\rm NN}}$= 5.02 TeV," *Phys. Rev. C* **91** no. 6, (2015) 064905, arXiv:1412.6828 [nucl-ex].

[10] ALICE, "The ALICE definition of primary particles,". https://cds.cern.ch/record/2270008.

[11] ALICE, S. Acharya *et al.*, "Measurement of inclusive charged-particle jet production in pp and p-Pb collisions at $\sqrt{s_{\rm NN}}$ = 5.02 TeV," arXiv:2307.10860 [nucl-ex].

[12] M. Cacciari, G. P. Salam, and G. Soyez, "The anti-k_t jet clustering algorithm," *JHEP* **04** (2008) 063, arXiv:0802.1189 [hep-ph].

[13] M. Cacciari, G. P. Salam, and G. Soyez, "FastJet User Manual," *Eur. Phys. J. C* **72** (2012) 1896, arXiv:1111.6097 [hep-ph].

[14] D. Neill, F. Ringer, and N. Sato, "Leading jets and energy loss," *JHEP* **07** (2021) 041, arXiv:2103.16573 [hep-ph].

[15] CDF, T. Affolder *et al.*, "Charged Jet Evolution and the Underlying Event in $p\bar{p}$ Collisions at 1.8 TeV," *Phys. Rev. D* **65** (2002) 092002.

[16] T. Adye, "Unfolding algorithms and tests using RooUnfold," in *PHYSTAT 2011*, pp. 313–318. CERN, Geneva, 2011. arXiv:1105.1160 [physics.data-an].

[17] CDF, T. Affolder *et al.*, "Charged Jet Evolution and the Underlying Event in $p\bar{p}$ Collisions at 1.8 TeV," *Phys. Rev. D* **65** (2002) 092002.

[18] ALICE, S. Acharya *et al.*, "Underlying Event properties in pp collisions at $\sqrt{s}$ = 13 TeV," *JHEP* **04** (2020) 192, arXiv:1910.14400 [nucl-ex].

[19] M. Cacciari and G. P. Salam, "Pileup subtraction using jet areas," *Phys. Lett. B* **659** (2008) 119–126, arXiv:0707.1378 [hep-ph].

[20] ALICE, P. Das, "Measurement of charged-particle jet properties in p–Pb collisions at $\sqrt{s_{\mathrm{NN}}}$ = 5.02 TeV with ALICE," in *Hot QCD Matter 2022*. 8, 2022. arXiv:2208.01389 [nucl-ex].

[21] S. K. Das *et al.*, "Dynamics of Hot QCD Matter – Current Status and Developments," *Int. J. Mod. Phys. E* **31** (2022) 12, arXiv:2208.13440 [nucl-th].

[22] ATLAS, M. Aaboud *et al.*, "Measurement of jet fragmentation in 5.02 TeV proton-lead and proton-proton collisions with the ATLAS detector," *Nucl. Phys. A* **978** (2018) 65, arXiv:1706.02859 [hep-ex].

[23] CMS, "Jet Fragmentation Function in pPb Collisions at sqrt(sNN) = 5.02 TeV and pp Collisions at sqrt(s) = 2.76 and 7 TeV,". http://cds.cern.ch/record/2030077.

"Simulation is no longer that of a territory, a referential being or substance. It is a generation by models of a real without origin or reality: a hyperreal."

— Jean Baudrillard

Chapter 4

Investigating multiplicity dependence of jet properties in pp collisions using PYTHIA simulation

This chapter discusses the study of jet properties in pp collisions at $\sqrt{s}$ = 13 TeV for minimum bias and high-multiplicity events using the PYTHIA 8 [1] Monte Carlo (MC) event generator with Monash 2013 tune [2]. The study is carried out in presence and absence of two important physics mechanisms, multiparton interactions (MPI) and color reconnection (CR) in PYTHIA. Sec. 4.1 introduces and discusses the motivation behind this study. The details of the study, including event generation, particle selection, jet reconstruction, definition of jet observables, estimation of underlying events, and matching between partons and jets, are laid down in Sec. 4.2. The obtained results are discussed in Sec. 4.3.

4.1 Introduction

The observations of several heavy-ion-like signatures in pp and p–Pb collisions (small collision systems), particularly at high multiplicity at LHC energies [3–14], influenced the high-energy physics community to investigate and understand the possible source(s) behind the unconventional observations – whether they are due to formation of QGP and/or other source(s) mimicking the heavy-ion-like features in small collision systems. It is also important to note that the emergence of collectivity (observed in the soft sector of QCD) while no jet quenching in the form of suppression of jet production [15, 16] is observed (hard sector of QCD) in small collision systems, made the situation more puzzling as well as exciting. Interestingly, the recent measurement of jet fragmentation in high-multiplicity pp collisions at $\sqrt{s}$ = 13 TeV by ALICE [17] has shown significant jet modification compared to that in minimum bias events at low jet p_{T}. PYTHIA 8 is found to explain the feature observed in data despite the fact that PYTHIA 8 does not incorporate any QGP-medium effects. In Ref. [18], the multiparton interactions (MPI) and color reconnection (CR) mechanisms of PYTHIA 8 are shown to modify jet shape ($\rho(r)$) distributions in high-multiplicity pp collisions; however, the exact interplay between these mechanisms causing the jet modification has not been studied. Moreover, the modifications of different jet observables are also expected to have different degrees of sensitivity on the nature of the parent parton. It is, therefore, of utmost importance to understand in detail and quantify various contributions from the individual sources leading to the jet modification in PYTHIA 8 in absence of the medium.

In this work [19], the jet shape observable $\rho(r)$ and jet fragmentation function (z^{ch}) are studied in minimum bias and high-multiplicity event classes using PYTHIA 8 Monash 2013 MC event generator. The study is performed in presence and absence of the two important mechanisms in PYTHIA 8, CR and MPI (which are found to explain some of the experimentally observed flow-like features in high-multiplicity pp collisions [20–23]).

In order to understand the sensitivity of $\rho(r)$ and z^{ch} on the nature of parton, the gluon-initiated jets and their contributions to the total inclusive jets are estimated, and associated effects on these observables are studied. The effect of multiparton interactions is also studied exclusively by using event samples with different numbers of MPIs. The details of the study are presented in the following sections.

4.2 Details of the study

The current study is performed following the steps in the flow chart shown in Fig. 4.1. Each of the steps is discussed in detail in the following sections.

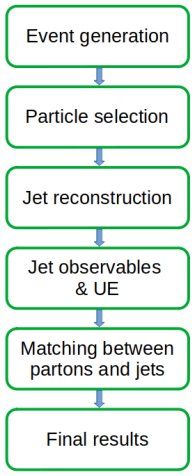

Figure 4.1: Flow chart of the study.

4.2.1 Event generation

In this study, events are generated using PYTHIA 8 Monte Carlo (MC) event generator with Monash 2013 tune in presence and absence of two important physics mechanisms, multiparton interactions (MPI) and color reconnection (CR). The details about this event generator, along with MPI and CR mechanisms, are discussed below.

4.2.1.1 PYTHIA 8

Often used to generate events in high-energy collisions between elementary particles, the PYTHIA program provides a coherent collection of physics models that describes the evolution from a few-body hard-scattering process to a complex multiparticle final state. Some of the physics has been rigorously inferred from theory, while other parts are based on phenomenological models whose parameters are deter-

mined from experimental data. Currently, the majority of users of this programme are LHC experimentalists, while many other phenomenological or experimental researchers use the application as well. The main tasks assigned to the program are to design search strategies, evaluate experimental data, investigate detector performance, and look into the experimental implications of theoretical models.

PYTHIA 8 is a multiparton interaction-based pQCD-inspired Monte Carlo event generator widely used for hadronic collisions. It performs transverse-momentum-ordered (p_{T}-ordered) parton showering, which interleaves the entire perturbative evolution (initial state radiation (ISR), final state radiation (FSR) and MPI), and the angular ordering is imposed by an additional veto [24, 25]. It also includes color reconnection mechanism [26, 27]. Hadronization in PYTHIA 8 proceeds via string breaking as described by the Lund string model [28]. The Monash 2013 tune is based on a large set of LHC distributions, starting from a careful comparison and tuning to LEP data. The PDF used is the NNPDF2.3 [29] QCD+QED LO with $\alpha_s(M_Z) = 0.130$.

4.2.1.2 Multiparton interactions (MPI)

A hadron-hadron collision can result in multiple parton-parton interactions (MPI), which is a natural outcome of the composite structure of the colliding hadrons (Fig. 4.2 shows the schematic diagram). It is possible for many hard scattering processes to occur in a single hadron-hadron collision, but at suppressed rates compared to soft MPI, even though MPIs are particularly relevant to characterize the ubiquitous soft underlying event. Pythia's MPI modeling is based on a fundamental formalism that encompasses both hard and soft QCD MPI processes inside a single, cohesive framework [30]. Together with several new features exclusive to Pythia 8, the current implementation includes the further improvements made since Pythia 6.3 [31].

The observation that t-channel propagators and α_s factors appearing in perturbative

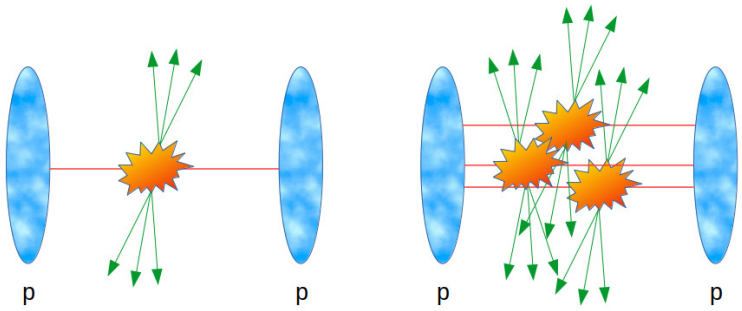

Figure 4.2: Single hard scattering (left) and multiple hard scatterings, i.e., MPI (right), occurring in a single proton-proton collision [19].

QCD $2 \rightarrow 2$ scattering diverge at low momentum transfers serves as the foundation for parton-based MPI models:

$$\mathrm{d}\sigma_{2\to 2} \propto \frac{g_s^4}{16\pi^2}\frac{\mathrm{d}t}{t^2} \sim \alpha_s^2(p_\perp^2)\frac{\mathrm{d}p_\perp^2}{p_\perp^4}, \tag{4.1}$$

This behavior is further aggravated by the abundance of low-x partons that are accessible at large hadronic center-of-mass energy. Within MPI models, every hadron-hadron collision comprises many parton-parton collisions, each of which usually involves momentum transfers of order $p_{\perp\mathrm{min}}$.

4.2.1.3 Color reconnection (CR)

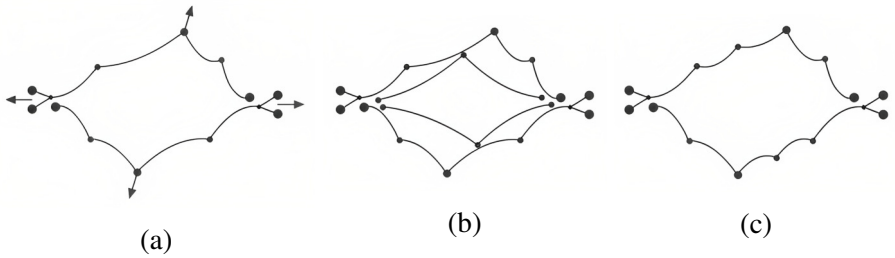

Figure 4.3: Illustration of the color reconnection mechanism in PYTHIA 8 (image directly extracted from Ref. [32]). (a) The outgoing gluons are color-connected to the projectile and target beam remnants. (b) A second hard scattering with two new strings connected to the beam remnants. (c) Color-reconnected partons minimizing the total string length.

The implementation of the color reconnection mechanism in PYTHIA 8 is schematically illustrated in Fig. 4.3. The connection between the outgoing partons and the beam remnants through color strings in case of a single hard scattering is shown in Fig. 4.3a. A second hard scattering (Fig. 4.3b) can be naively expected to give rise to two new strings connected to the beam remnants. This would result in a proportional increase in multiplicity; however, to successfully fit the data (see Ref. [32] and references therein), it is instead assumed that the partons are color-reconnected so that the total string length gets minimized (Fig. 4.3c).

MPIs occurring in a hadronic collision lead to the creation of an environment having several high-momentum partons along with the soft ones in a small region (the overlap area of the colliding hadrons), leading to high-multiplicity events (see Fig. 4.2). The evolution of the scattered outgoing partons to final-state collimated hadrons (jets) via fragmentation and hadronization in such an environment is expected to be different compared to the situation with no MPI (only one hard scattering per hadronic collision), which could affect the differential jet shape properties. The fragmentation of independent hard scatterings (MPIs) becomes correlated due to the color reconnection mechanism [21] described earlier and is, therefore, expected to further modify the differential jet shapes and properties.

4.2.1.4 Configurations

This study is carried out for minimum bias and high-multiplicity events, which are generated for pp collisions at $\sqrt{s}$ = 13 TeV using PYTHIA 8 Monash 2013 for each of the three following configurations:

- MPI: OFF, CR: OFF – In this configuration, both multiparton interaction and color reconnection mechanisms of PYTHIA 8 are absent in the process of event generation
- MPI: ON, CR: OFF – The multiparton interactions are present; however, the color reconnection mechanism is absent in the simulation process in this configuration

- MPI: ON, CR: ON – Events are generated in presence of both MPI and CR mechanisms of PYTHIA 8

The configuration 'MPI: OFF, CR: ON' is not that important for this study as the effect of color reconnection on the number of produced particles is expected to be small in absence of MPI. Fig. 4.4 shows the pseudorapidity and multiplicity distributions in 'default' (i.e., 'MPI: ON, CR: ON'), 'MPI Off' (i.e., 'MPI: OFF, CR: ON'), 'CR Off' (i.e., 'MPI: ON, CR: OFF') and 'CR & MPI Off' (i.e., 'MPI: OFF, CR: OFF') conditions at mid-rapidity ($|\eta| < 0.9$). The main implications of the observations are:

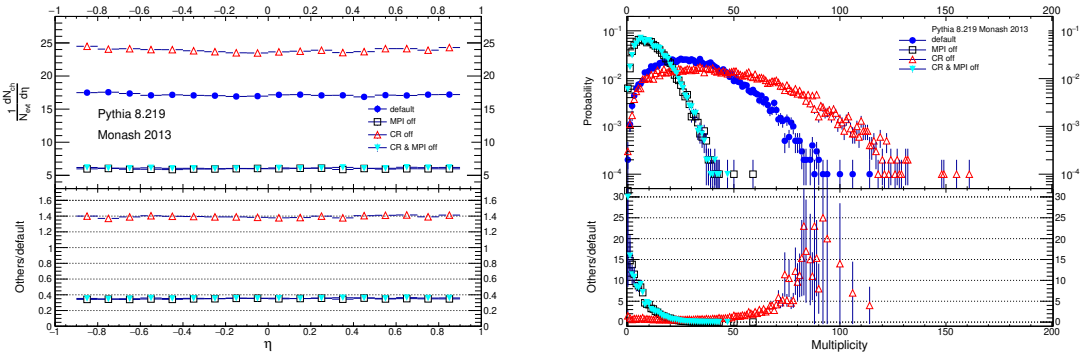

(a) Pseudorapidity distribution

(b) Multiplicity distribution

Figure 4.4: Comparative plots of pseudorapidity and multiplicity distributions at mid-rapidity between different configurations of PYTHIA 8.

- Both the configurations 'MPI: OFF, CR: ON' and 'MPI: OFF, CR: OFF' do not differentiate in terms of particle production, which implies that if MPI is OFF, then CR does not have any significant effect

- The configuration 'MPI: ON, CR: OFF' shows enhancement in multiplicity, i.e., CR seems to reduce or constrain particle production

4.2.1.5 Selection of events

About 1000 million minimum bias (MB) inelastic events are generated for each of the three configurations and the high-multiplicity (HM) events are determined as the highest multiplicity events from the minimum bias event samples. The high-multiplicity event class is selected as the one that contains 5% of the total events with the highest multiplicities, based on the number of charged particles produced in the pseudorapidity regions $2.8 < \eta < 5.1$ and $-3.7 < \eta < -1.7$. The above selection corresponds to the number of charged particles to be greater than 24, 127, and 83 for 'MPI: OFF, CR: OFF', 'MPI: ON, CR: OFF' and 'MPI: ON, CR: ON' configurations, respectively. The choice of pseudorapidity range is guided by the experimentally available coverage range of forward detectors [33] used for multiplicity selection and is also suitable for studies of charged particles and/or jets at mid-rapidity so that the possible autocorrelation between the production of charged particles at forward and mid-rapidity can be minimized.

4.2.2 Particle selection

The study is performed on charged-particle jets, which are reconstructed from the generated charged particles. The charged particles selected for this study are subjected to the kinematic cuts: $|\eta^{\mathrm{ch}}_{\mathrm{particle}}| < 0.9$ and $p^{\mathrm{ch}}_{\mathrm{T,\,particle}} > 0.15$ GeV/c. The restriction on η has given access to the particles only in the mid-rapidity region, whereas the condition for the particles to have p_{T} as low as 0.15 GeV/c has the significance of allowing us to test perturbative and non-perturbative aspects of jet production. The particle selection criteria are chosen to match experimental conditions [34, 35].

4.2.3 Jet reconstruction

Once the suitable particles are selected, jets are reconstructed from those particles using an infrared- and collinear-safe sequential recombination anti-k_{T} algorithm [36] from the FastJet package [37] with jet resolution parameter R ($= \sqrt{(\Delta\eta)^2 + (\Delta\varphi)^2}$) = 0.4. Jets are accepted for the study if $|\eta^{\mathrm{ch}}_{\mathrm{jet}}| < 0.5$ (0.9 - R) and jet transverse momentum $p^{\mathrm{ch}}_{\mathrm{T,jet}} > 10$ GeV/c. The final results are presented for the intervals $10 < p^{\mathrm{ch}}_{\mathrm{T,jet}} < 20$ GeV/c and $40 < p^{\mathrm{ch}}_{\mathrm{T,jet}} < 60$ GeV/c.

4.2.4 Jet observables

After the jets are reconstructed from the selected charged particles, one needs to calculate the jet observables, which are defined and discussed in this section. In this work, the differential transverse momentum distribution of charged-particle jets ($\frac{1}{N_{\mathrm{events}}}\frac{d^2N}{dp_{\mathrm{T}}d\eta}$; where N_{events} is the number of events and N is the number of jets), differential jet shape ($\rho(r)$) and jet fragmentation function (z^{ch}) for charged-particle jets are studied.

The differential jet shape is related to the radial distribution of jet transverse momentum density inside the jet cone about the jet axis and is defined as:

$$\rho(r) = \frac{1}{\Delta r}\frac{1}{N_{\mathrm{jets}}}\sum_{i=1}^{N_{\mathrm{jets}}} p^{i}_{\mathrm{T}}(r - \Delta r/2, r + \Delta r/2)/p^{\mathrm{ch}}_{\mathrm{T,jet}} \quad (4.2)$$

where r is the distance from the jet axis and $p^{i}_{\mathrm{T}}(r - \Delta r/2, r + \Delta r/2)$ denotes summed p_{T} of all particles of i-th jet, inside the annular ring between $r - \Delta r/2$ and $r + \Delta r/2$.

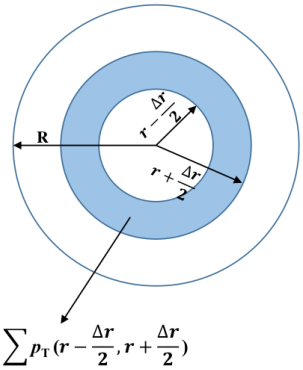

Figure 4.5: Jet shape $\rho(r)$.

The jet fragmentation function represents the fraction of the jet transverse momentum carried by the constituent charged particles and is sensitive to the details of the parton

showering process. It is defined as:

$$z^{\mathrm{ch}} = \frac{p^{\mathrm{ch}}_{\mathrm{T,\,particle}}}{p^{\mathrm{ch}}_{\mathrm{T,\,jet}}} \tag{4.3}$$

The study of $\rho(r)$ and z^{ch} are very important since these observables are sensitive to both the fragmentation process and the nature of the initial hard-scattered partons (quark or gluon) [38–42]. In presence of medium, jet constituents lose their energy via inelastic and elastic scatterings due to jet-medium interaction, and their mean opening angle also becomes larger. This results in the steepening of z^{ch} and flattening of $\rho(r)$ distributions, leading to softening and broadening of jets in medium compared to those in vacuum. The observables $\rho(r)$ and z^{ch} are, therefore, sensitive observables showing jet modification in heavy-ion collisions. In case of high-multiplicity pp and p–Pb collisions, these observables might be potentially capable of verifying the conjecture of medium formation in small collision systems [41, 42].

4.2.5 Estimation of underlying event (UE) contribution

Reconstructed jets are contaminated by the underlying event (UE), which can be defined as the charged particles produced from physics processes other than the fragmentation of hard-scattered partons. The UE mostly consists of particles from the beam-beam remnants, initial and final state radiations, and contributions from MPIs [43]. The empirical models used to describe the non-perturbative aspects in the evolution of a high-energy scattering event do not allow to clearly distinguish particles originating from hard processes and the underlying event [44]. In this study, the UE contributions to the considered jet observables are estimated using the perpendicular cone (PC) method (introduced and discussed in Sec. 3.1.8). For the estimation of UE contribution to the $\rho(r)$ distribution, annular rings of the same size as those inside the jet cones are considered inside each of

the perpendicular circular regions. The UE contributions to the $\rho(r)$ and z^{ch} distributions are respectively calculated using the following expressions:

$$\rho^{\mathrm{UE}}(r) = \frac{1}{\Delta r}\frac{1}{N_{\mathrm{PC}}}\sum_{i=1}^{N_{\mathrm{PC}}} p_{\mathrm{T}}^{i}(r-\Delta r/2, r+\Delta r/2)/p_{\mathrm{T,jet}}^{\mathrm{ch}} \tag{4.4}$$

where N_{PC} is the number of perpendicular cones, r is the distance from the axis of the perpendicular cone and $p_{\mathrm{T}}^{i}(r-\Delta r/2, r+\Delta r/2)$ denotes summed p_{T} of all particles inside the annular ring between $r-\Delta r/2$ and $r+\Delta r/2$ and

$$z^{\mathrm{ch,UE}} = \frac{p_{\mathrm{T,particle}}^{\mathrm{ch,PC}}}{p_{\mathrm{T,jet}}} \tag{4.5}$$

where $p_{\mathrm{T,particle}}^{\mathrm{ch,PC}}$ is the p_{T} of particle in the perpendicular cone. The subtraction of UE is performed on a statistical basis to obtain the corrected distributions.

In order to perform a systematic check, another method, namely the random cone (RC) method (described in Sec. 3.1.8), is also applied to estimate the underlying event contribution in the studied jet observables. As shown in Fig. 4.6, no significant difference in the UE contribution to $\rho(r)$ distribution is observed compared to the PC method. A similar observation is also found for the z^{ch} distribution.

4.2.6 Parton and jet matching

As mentioned in Sec. 4.1, the modifications of jet properties are also investigated for gluon-initiated jets in this study to understand the dependence of jet modification on the nature of the initiating parton. To select gluon-initiated jets, one needs to properly match the hard-scattered partons in an event to the reconstructed charged-particle jets using some effective algorithm. In this study, a matching algorithm based on the "distance of closest approach" is taken into consideration. In this algorithm, the two outgoing hard-scattered

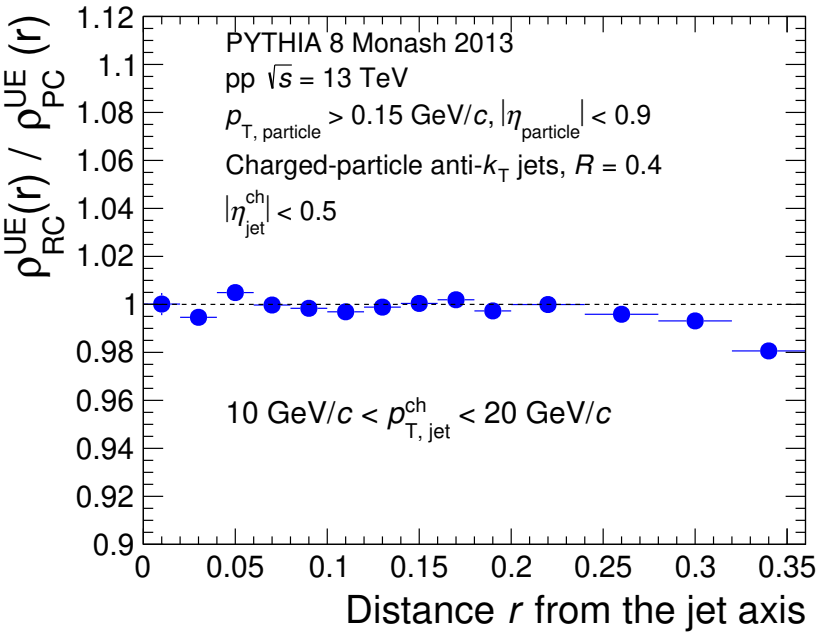

Figure 4.6: Comparison of UE contributions in $\rho(r)$ for inclusive jets in the interval $10 < p^{ch}_{T,\,jet} < 20$ GeV/c estimated using random cone (RC) and perpendicular cone (PC) method.

partons are first identified, and their flavors (quark or gluon) are determined using the information from the PYTHIA event output. In the same event, unique pairs between these initial hard-scattered partons and reconstructed jets are then determined in such a way that the geometrically closest jet is matched to the parent parton. To minimize incorrect matching, the matched jet and parton are subjected to the condition: $\Delta\varphi < \pi/2$, where $\Delta\varphi$ is the difference in φ between the parton and the jet to be matched. The jets having p_T less than 20% of the matched parton p_T, are rejected to avoid fake jets. This cutoff of 20% for rejecting fake jets is also varied up to 50%, and no significant change in the final results is observed. The reconstructed jets matched to parent gluons are referred to as gluon-initiated jets in this study.

4.3 Results and discussion

Once the jet observables are calculated from both the reconstructed inclusive jets and gluon-initiated jets, the obtained distributions are presented for MB and HM event classes and discussed in detail in the following sections.

4.3.1 Comparison with experimental data

Before moving forward with the discussion of obtained results from PYTHIA 8, a comparison of the ALICE data [45,46] to PYTHIA 8 predictions is presented in Fig. 4.7 which shows the ratio of jet fragmentation distributions for charged-particle leading jets in the interval $10 < p_{\mathrm{T,jet}}^{\mathrm{ch}} < 20$ GeV/c between high-multiplicity and minimum bias events in pp collisions at $\sqrt{s}$ = 13 TeV. The red solid boxes and blue open triangles represent ALICE data and PYTHIA 8 Monash 2013 predictions, respectively. The systematic uncertainty in data is represented by orange bands. For this comparison, the track and jet selection criteria used in PYTHIA 8 are selected to match those in the data, although the selection of events is marginally different. In case of the ALICE data presented in Refs. [45, 46], HM events are selected using the detector level information (based on the two scintillator detectors V0A and V0C in ALICE) both for data and PYTHIA 8 simulation, whereas the HM event class in this study is determined based on the information of final-state particles found in the same pseudorapidity coverage as V0A and V0C (as also described in Sec. 4.2.1.5). To match the HM event selection criteria as done in Refs. [45, 46], the HM event class selected for this comparison also contains 0.1% of the total events with the highest multiplicities. It is interesting to find that PYTHIA 8, without considering any QGP-medium effects, captures the feature of modification of jet fragmentation observed in experimental data fairly well, indicating that the underlying physics mechanism(s) are indeed implemented in this event generator. This essentially provides the importance

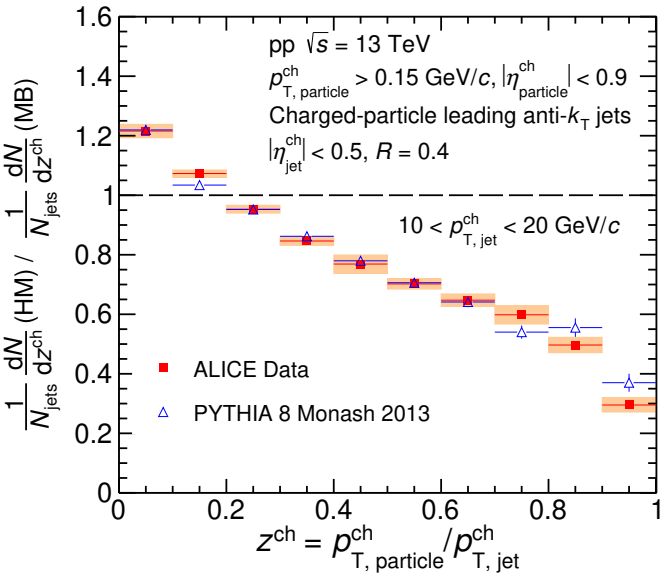

Figure 4.7: Ratio of jet fragmentation distributions for charged-particle leading jets in the interval $10 < p_{\mathrm{T,\,jet}}^{\mathrm{ch}} < 20$ GeV/c between high-multiplicity and minimum bias events in pp collisions at $\sqrt{s} = 13$ TeV, measured by ALICE [45,46] and compared with PYTHIA 8 Monash 2013 predictions.

of the initiatives to investigate the role of two important physics mechanisms, multiparton interaction and color reconnection, incorporated in PYTHIA 8, in the observed jet modification in high-multiplicity pp collisions.

4.3.2 Jet shape and jet fragmentation

The jet shape ($\rho(r)$) is plotted as a function of distance r from the jet axis for inclusive charged-particle jets in the interval $10 < p_{\mathrm{T,\,jet}}^{\mathrm{ch}} < 20$ GeV/c for HM and MB event classes in the configurations 'MPI: ON, CR: ON' (solid markers) and 'MPI: OFF, CR: OFF' (open markers), as shown in the top panel of Fig. 4.8a while the bottom panel shows the comparisons between the two event classes. The same for jet fragmentation (z^{ch}) distributions are shown in Fig. 4.8b. For better visibility, the solid markers are scaled by a factor of 10. It is observed that both jet shape and jet fragmentation distributions are significantly modified in HM event class compared to that in MB event class in presence

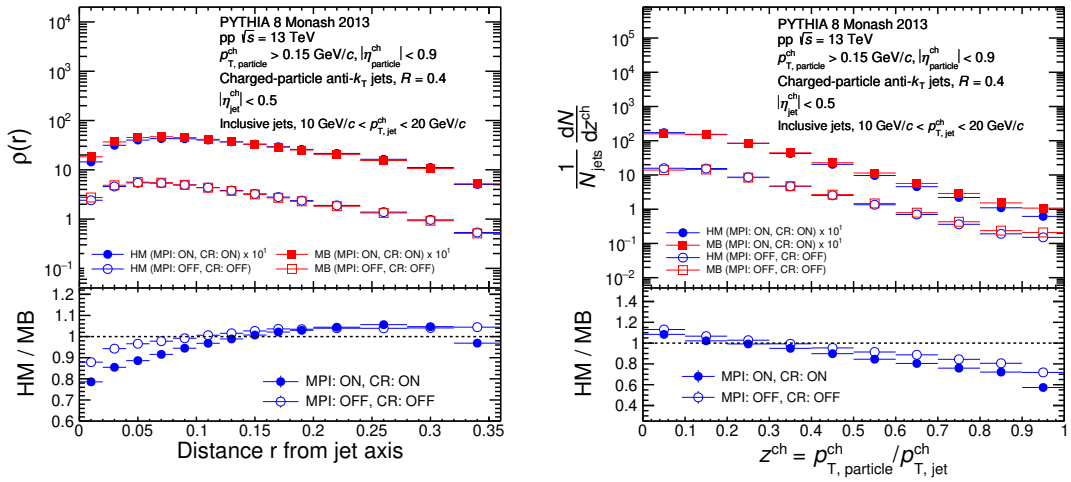

(a) (b)

Figure 4.8: Top panels: Distributions of (a) $\rho(r)$ and (b) z^{ch} for inclusive charged-particle jets in pp collisions at $\sqrt{s}$ = 13 TeV using PYTHIA 8 Monash 2013 in the interval $10 < p_{\mathrm{T,jet}}^{\mathrm{ch}} < 20$ GeV/c for 'MPI: ON, CR: ON' and 'MPI: OFF, CR: OFF' configurations. Blue circles and red boxes correspond to HM and MB event classes respectively. Bottom panels: Ratios of (a) $\rho(r)$ and (b) z^{ch} distributions between HM and MB event classes.

of MPI and CR effects (when both mechanisms are switched ON). The ratio plots show that, in comparison to MB events, the core of the jet in HM events is depleted of transverse momentum by about 22%, which is redistributed away from the jet axis. This results in an enhancement in $\rho(r)$ at larger r (> 0.15)[1]. A similar observation is depicted by the ratio plots of z^{ch} distributions in the bottom panel of Fig. 4.8b. At high z^{ch} ($\rightarrow 1$), the particle production is significantly suppressed in HM events in comparison to MB events, whereas at low z^{ch}, enhanced particle production is observed. If one looks at the distributions of the number of MPIs (N_{MPI}) in both MB and HM event classes with 'MPI: ON, CR: ON' configuration, as depicted in Fig. 4.9, one can see that the average number of multiparton interactions in HM event class is found to be much larger (14.5) compared to that (3.5) in

[1]Results are shown only up to $r = 0.36$ as the last bin ($r = 0.36$ - 0.4) is significantly affected by underlying event contribution and statistical fluctuations.

MB event class. The mean values of N_{MPI} are evaluated using the expression:

$$\langle N_{\mathrm{MPI}} \rangle = \frac{1}{N_{\mathrm{events}}} \sum_{i=1}^{N_{\mathrm{events}}} N_{\mathrm{MPI}}^{i} \tag{4.6}$$

where N_{events} is the total number of events in the selected event class and N_{MPI}^{i} is the number of MPIs in the i-th event, obtained directly from the output of PYTHIA 8.

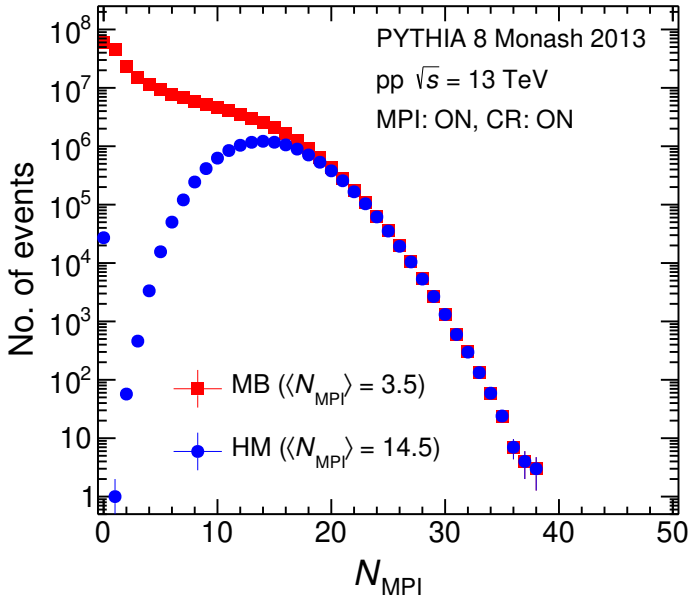

Figure 4.9: Distributions of the number of MPIs for HM and MB event classes in 'MPI: ON, CR: ON' configuration.

Interestingly, the observed redistribution of transverse momentum from the jet core to outer radii and the suppression of high z^{ch} particles are found to reduce significantly in absence of the MPI and CR effects (when both mechanisms are switched OFF), as shown by the open markers in Figs. 4.8a and 4.8b. These observations indicate that the mechanisms of MPI along with CR are responsible for the jet modification observed in PYTHIA. However, the observed residual depletion at the jet core followed by a small enhancement at larger r for $\rho(r)$, and suppression at high z^{ch} for jet fragmentation distribution in absence of MPI and CR effects, hint toward other additional contributor(s) to the observed

jet modification. The origin of the residual jet modification in absence of MPI and CR is investigated and discussed in the next section.

4.3.3 Origin of residual jet modification in absence of MPI and CR

It is expected that gluon-initiated jets fragment into more constituents due to their large color factor [47, 48]. This makes them softer and broader compared to quark-initiated jets, which should be reflected in their internal properties, such as jet shape and jet fragmentation function distributions. Therefore, any difference in the gluonic contribution in the HM event class compared to MB is expected to modify the distributions of $\rho(r)$ and z^{ch}. To estimate the gluonic contribution to jets, matching between the initiating hard-scatted parton and the reconstructed jet is carried out following the algorithm described in Sec. 4.2.6, and the gluonic contribution to the inclusive jet sample is estimated as the fraction of gluon-initiated jets out of the total inclusive matched jets. It is found that a higher contribution of gluon-initiated jets is present in the inclusive jet sample in HM events compared to that in MB events, and as one goes towards lower jet p_{T}, the gluonic contribution increases. For example, at jet p_{T} = 10–20 GeV/c, the gluonic contribution in HM event class is found to be 86% compared to 75% in MB event class while in case of jets with p_{T} = 40–60 GeV/c, the gluonic contribution in HM and MB event classes are 81% and 73%, respectively.

Now, the effect of this difference in the gluonic contribution can only be assessed by looking at the ratios of $\rho(r)$ and z^{ch} distributions between HM and MB event classes for gluon-initiated jets only when both MPI and CR effects are switched OFF which are shown in Fig. 4.10. It is found that the residual effects, as observed in the case of inclusive jets, have got reduced further in the case of gluon-initiated jets. This observation implies that one of the major sources of the residual jet modification is the difference in the gluonic contribution between HM and MB event classes.

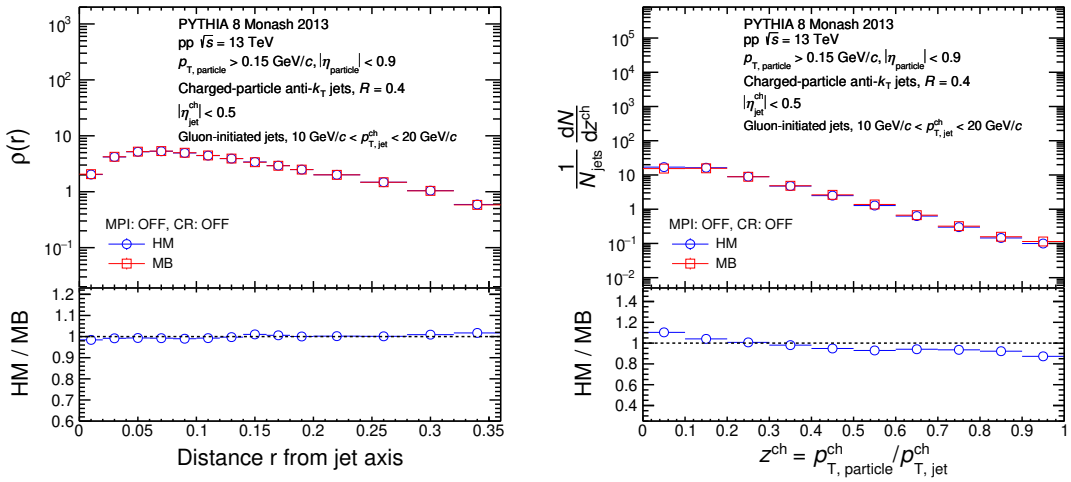

(a) (b)

Figure 4.10: Top panels: Distributions of (a) $\rho(r)$ and (b) z^{ch} for gluon-initiated jets in pp collisions at $\sqrt{s}$ = 13 TeV using PYTHIA 8 Monash 2013 in the interval $10 < p_{\mathrm{T,jet}}^{\mathrm{ch}} < 20$ GeV/c for 'MPI: OFF, CR: OFF' configuration. Blue circles and red boxes correspond to HM and MB event classes respectively. Bottom panels: Ratios of (a) $\rho(r)$ and (b) z^{ch} distributions between HM and MB event classes.

Since the effect of MPI and CR is dominant at low p_{T} [1] and the difference in gluonic contribution between HM and MB event classes is smaller at high jet p_{T}, the observed jet modification is expected to get reduced at high jet p_{T}. It is found to be true as is evident from Figs. 4.11a and 4.11b where comparison of the jet $\rho(r)$ and z^{ch} distributions for inclusive jets in the interval $40 < p_{\mathrm{T,jet}}^{\mathrm{ch}} < 60$ GeV/c between HM and MB event classes are presented.

A further systematic study is performed to understand the quantitative effects of MPI and CR on jet modification in terms of the jet shape observable $\rho(r)$, which is discussed in the next section.

4.3.4 Effect of MPI and CR on observed jet modification

The effect of multiparton interactions in the modification of $\rho(r)$ can be estimated exclusively by comparing the $\rho(r)$ distributions obtained from event samples with different

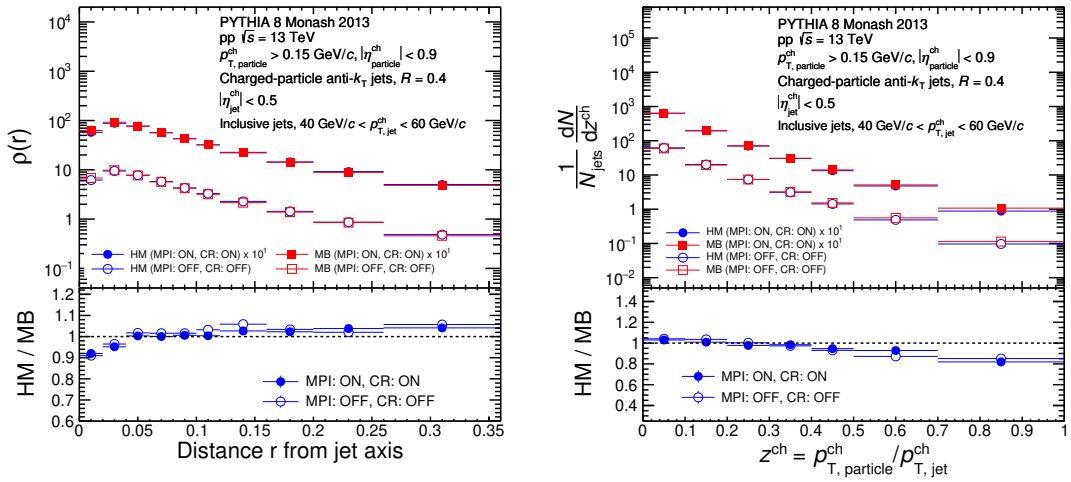

(a) (b)

Figure 4.11: Top panels: (a) Inclusive charged-particle jet shape ($\rho(r)$) distributions and (b) jet fragmentation (z^{ch}) distributions in pp collisions at $\sqrt{s}$ = 13 TeV using PYTHIA 8 Monash 2013 in the interval $40 < p_{\mathrm{T,jet}}^{\mathrm{ch}} < 60$ GeV/c for 'MPI: ON, CR: ON' and 'MPI: OFF, CR: OFF' configurations. Blue circles and red boxes correspond to HM and MB event classes respectively. Bottom panels: Ratios of (a) $\rho(r)$ and (b) z^{ch} distributions between HM and MB event classes.

numbers of MPIs. To do this, the minimum bias event sample is divided into four different classes: I, II, III, and IV, which contain events with the number of MPIs > 4, 8, 12, and 20, respectively. For this study, the default configuration ('MPI: ON, CR: ON') of PYTHIA 8 is used and inclusive jets in the interval $10 < p_{\mathrm{T,jet}}^{\mathrm{ch}} < 20$ GeV/c are considered to estimate the jet shape $\rho(r)$. The average numbers of multiparton interactions ($\langle N_{\mathrm{MPI}} \rangle$) for different event classes are calculated using Eq. 4.6, and are shown in Table 4.1. The ratios of $\rho(r)$ distributions obtained for different event classes with respect to that in minimum bias events are shown in Fig. 4.12. It is observed, as expected, that the amount of modification at the core of the jet increases for the event classes with larger number of MPIs. For example, the modification at the jet core is the highest, reaching up to 40% for the event class IV where $\langle N_{\mathrm{MPI}} \rangle = 22$. This observation exclusively supports a direct relation between the amount of modification of $\rho(r)$ and the number of MPIs in PYTHIA 8.

In order to assess the effect of color reconnection on the modification in jet $\rho(r)$, the

Table 4.1: Values of $\langle N_{\mathrm{MPI}} \rangle$

Event class	$\langle N_{\mathrm{MPI}} \rangle$
MB	3.5
I	9.1
II	12.4
III	15.3
IV	22

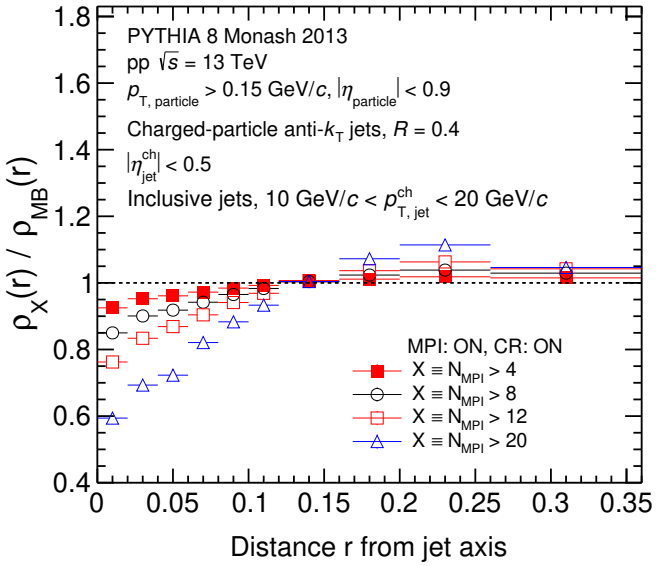

Figure 4.12: Ratios of $\rho(r)$ distributions of different event classes (I: red solid box, II: black open circle, III: red open box, IV: blue open triangle) with respect to that in MB event class.

$\rho(r)$ distributions for 'MPI: ON, CR: ON' and 'MPI: ON, CR: OFF' configurations are compared with the $\rho(r)$ distribution for 'MPI: OFF, CR: OFF' configuration in minimum bias event class for inclusive jets in the interval $10 < p_{\mathrm{T,jet}}^{\mathrm{ch}} < 20$ GeV/c, as shown in Fig. 4.13. About 26% modification of jet core is observed in presence of MPI only, while the modification reaches up to 33% once both MPI and CR effects are present.

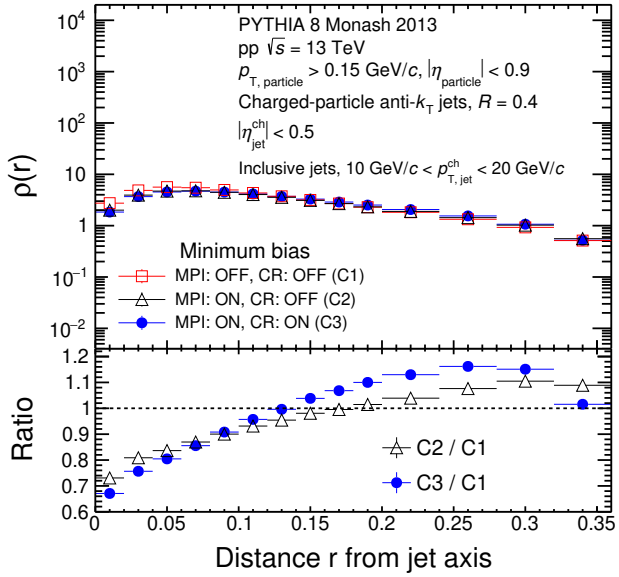

Figure 4.13: Top panel: Inclusive charged-particle jet shape ($\rho(r)$) distributions in pp collisions at $\sqrt{s} = 13$ TeV using PYTHIA 8 Monash 2013 in the interval $10 < p^{\mathrm{ch}}_{\mathrm{T,jet}} < 20$ GeV/c in MB event class. Open red boxes, open black triangles and solid blue circles correspond to 'MPI: OFF, CR: OFF' (C1), 'MPI: ON, CR: OFF' (C2) and 'MPI: ON, CR: ON' (C3) configurations respectively. Bottom panel: Ratios of $\rho(r)$ distributions for the last two configurations (C2 and C3) with respect to the first configuration (C1).

4.3.5 Effect of change in gluonic contribution on observed jet modification

The effect of difference in gluonic contribution on jet modification can be studied by considering jet samples with different gluonic contributions. To do this, gluon-initiated jets are randomly removed by 10%, 20%, and 30% from the inclusive matched jet sample (sample-I, where the gluonic contribution is 81.2%) of minimum bias events. The resulting inclusive jet samples contain 79.6% (sample-II), 77.6% (sample-III), and 75.1% (sample-IV) gluonic contributions, respectively. Now, the ratios of $\rho(r)$ distributions obtained from these samples to that from the minimum bias one, as shown in Fig. 4.14, illustrate the sensitivity of jet modification to the difference in gluonic contribution. The modification of jet $\rho(r)$ is found to increase with increasing differences in the fraction of gluon-initiated

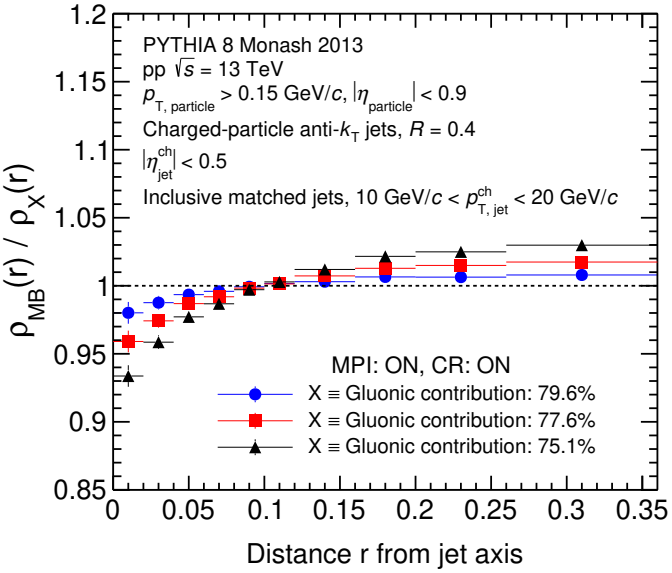

Figure 4.14: Ratio of $\rho(r)$ distributions obtained from sample-II, sample-III and sample-IV to that in sample-I (MB) in 'MPI: ON, CR: ON' configuration.

jets, as expected. It is found that a difference of 6% in the gluonic contribution (from 81.2% to 75.1%) results in about 7% modification of the jet core ($\rho(r)|_{r\to 0}$). This observation further supports our finding (as discussed in Sec. 4.3.3) that the amount of jet modification depends on the difference in gluonic contribution.

4.3.6 Jet p_T spectra: effect of MPI and CR

To understand the effect of MPI and CR on the inclusive jet p_T spectra, a comparison of jet p_T spectra between the three considered configurations: 'MPI: ON, CR: ON', 'MPI: ON, CR: OFF', and 'MPI: OFF, CR: OFF', are shown in Fig. 4.15 for the MB event class. The jet p_T spectra are shown in the top panel, and the ratios of the spectra in 'MPI: ON, CR: ON' and 'MPI: ON, CR: OFF' configurations with that in 'MPI: OFF, CR: OFF' configuration are depicted in the bottom panel. The comparisons show that when MPI and CR effects are considered, the rate of jet production increases, especially at low jet p_T. The jet production rate at jet p_T = 10–15 GeV/c is observed to increase by about 60%

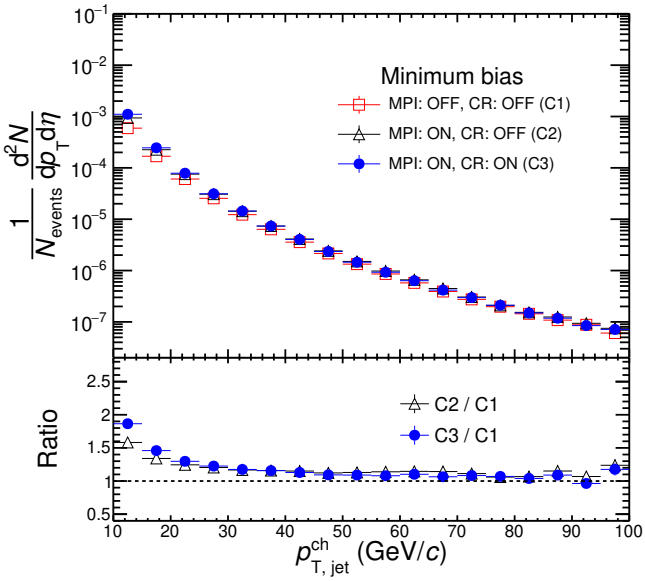

Figure 4.15: Top panel: Inclusive charged-particle jet p_T spectra in pp collisions at $\sqrt{s}$ = 13 TeV using PYTHIA 8 Monash 2013 for MB event class. Open red boxes, open black triangles and solid blue circles correspond to 'MPI: OFF, CR: OFF' (C1), 'MPI: ON, CR: OFF' (C2) and 'MPI: ON, CR: ON' (C3) configurations respectively. Bottom panel: Ratios of p_T spectra for the last two configurations (C2 and C3) with respect to the first configuration (C1).

when only MPI is switched ON, while it increases further to around 86% if both MPI and CR are turned ON. As jet p_T increases, the observed increase in the jet production rate is found to decrease for both configurations, indicating multiple jet production caused by multiparton interactions at low jet p_T [1], as expected.

Bibliography

[1] T. Sjöstrand, S. Ask, J. R. Christiansen, R. Corke, N. Desai, P. Ilten, S. Mrenna, S. Prestel, C. O. Rasmussen, and P. Z. Skands, "An introduction to PYTHIA 8.2," *Comput. Phys. Commun.* **191** (2015) 159–177, arXiv:1410.3012 [hep-ph].

[2] P. Skands, S. Carrazza, and J. Rojo, "Tuning PYTHIA 8.1: the Monash 2013 Tune," *Eur. Phys. J. C* **74** no. 8, (2014) 3024, arXiv:1404.5630 [hep-ph].

[3] ALICE, B. B. Abelev *et al.*, "Multiplicity Dependence of Pion, Kaon, Proton and Lambda Production in p-Pb Collisions at $\sqrt{s_{NN}}$ = 5.02 TeV," *Phys. Lett. B* **728** (2014) 25–38, arXiv:1307.6796 [nucl-ex].

[4] ALICE, J. Adam *et al.*, "Multiplicity dependence of charged pion, kaon, and (anti)proton production at large transverse momentum in p-Pb collisions at $\sqrt{s_{\rm NN}}$ = 5.02 TeV," *Phys. Lett. B* **760** (2016) 720–735, arXiv:1601.03658 [nucl-ex].

[5] CMS, V. Khachatryan *et al.*, "Multiplicity and rapidity dependence of strange hadron production in pp, pPb, and PbPb collisions at the LHC," *Phys. Lett. B* **768** (2017) 103–129, arXiv:1605.06699 [nucl-ex].

[6] CMS, S. Chatrchyan *et al.*, "Observation of Long-Range Near-Side Angular Correlations in Proton-Lead Collisions at the LHC," *Phys. Lett. B* **718** (2013) 795–814, arXiv:1210.5482 [nucl-ex].

[7] ALICE, B. Abelev *et al.*, "Long-range angular correlations on the near and away side in p-Pb collisions at $\sqrt{s_{NN}}$ = 5.02 TeV," *Phys. Lett. B* **719** (2013) 29–41, arXiv:1212.2001 [nucl-ex].

[8] CMS, V. Khachatryan *et al.*, "Observation of Long-Range Near-Side Angular Correlations in Proton-Proton Collisions at the LHC," *JHEP* **09** (2010) 091, arXiv:1009.4122 [hep-ex].

[9] CMS, "Observation of long-range near-side two-particle correlations in pp collisions at $\sqrt{s}$ = 13 TeV,".

[10] ALICE, B. B. Abelev *et al.*, "Long-range angular correlations of π, K and p in p-Pb collisions at $\sqrt{s_{\mathrm{NN}}}$ = 5.02 TeV," *Phys. Lett. B* **726** (2013) 164–177, arXiv:1307.3237 [nucl-ex].

[11] CMS, V. Khachatryan *et al.*, "Evidence for collectivity in pp collisions at the LHC," *Phys. Lett. B* **765** (2017) 193–220, arXiv:1606.06198 [nucl-ex].

[12] ALICE, J. Adam *et al.*, "Enhanced production of multi-strange hadrons in high-multiplicity proton-proton collisions," *Nature Phys.* **13** (2017) 535–539, arXiv:1606.07424 [nucl-ex].

[13] ALICE, J. Adam *et al.*, "Multi-strange baryon production in p-Pb collisions at $\sqrt{s_{\mathrm{NN}}}$ = 5.02 TeV," *Phys. Lett. B* **758** (2016) 389–401, arXiv:1512.07227 [nucl-ex].

[14] ALICE, B. B. Abelev *et al.*, "Multiplicity dependence of the average transverse momentum in pp, p-Pb, and Pb-Pb collisions at the LHC," *Phys. Lett. B* **727** (2013) 371–380, arXiv:1307.1094 [nucl-ex].

[15] ALICE, J. Adam *et al.*, "Centrality dependence of charged jet production in p-Pb collisions at $\sqrt{s_{\mathrm{NN}}}$ = 5.02 TeV," arXiv:1603.03402 [nucl-ex].

[16] ATLAS, G. Aad *et al.*, "Centrality and rapidity dependence of inclusive jet production in $\sqrt{s_{\mathrm{NN}}}$ = 5.02 TeV proton-lead collisions with the ATLAS detector," *Phys. Lett. B* **748** (2015) 392–413, arXiv:1412.4092 [hep-ex].

[17] ALICE, S. Acharya *et al.*, "Multiplicity dependence of charged-particle intra-jet properties in pp collisions at $\sqrt{s}$ = 13 TeV," arXiv:2311.13322 [hep-ex].

[18] Z. Varga, R. Vértesi, and G. Gábor Barnaföldi, "Modification of jet structure in high-multiplicity pp collisions due to multiple-parton interactions and observing a multiplicity-independent characteristic jet size," *Adv. High Energy Phys.* **2019** (2019) 6731362, arXiv:1805.03101 [hep-ph].

[19] P. Das, A. Modak, D. Banerjee, R. Biswas, S. Das, S. K. Ghosh, S. Raha, and S. K. Prasad, "Jet modification in absence of QGP-medium: the role of multiparton interactions and color reconnection*," *Chin. Phys. C* **48** no. 1, (2024) 013105, arXiv:2209.00972 [hep-ph].

[20] C. Bierlich and J. R. Christiansen, "Effects of color reconnection on hadron flavor observables," *Phys. Rev. D* **92** no. 9, (2015) 094010, arXiv:1507.02091 [hep-ph].

[21] A. Ortiz Velasquez, P. Christiansen, E. Cuautle Flores, I. Maldonado Cervantes, and G. Paić, "Color Reconnection and Flowlike Patterns in pp Collisions," *Phys. Rev. Lett.* **111** no. 4, (2013) 042001, arXiv:1303.6326 [hep-ph].

[22] A. Ortiz, G. Bencedi, and H. Bello, "Revealing the source of the radial flow patterns in proton–proton collisions using hard probes," *J. Phys. G* **44** no. 6, (2017) 065001, arXiv:1608.04784 [hep-ph].

[23] ALICE, J. Adam *et al.*, "Multiplicity and transverse momentum evolution of charge-dependent correlations in pp, p–Pb, and Pb–Pb collisions at the LHC," *Eur. Phys. J. C* **76** no. 2, (2016) 86, arXiv:1509.07255 [nucl-ex].

[24] T. Sjostrand and P. Z. Skands, "Transverse-momentum-ordered showers and interleaved multiple interactions," *Eur. Phys. J. C* **39** (2005) 129–154, arXiv:hep-ph/0408302.

[25] R. Corke and T. Sjostrand, "Interleaved Parton Showers and Tuning Prospects," *JHEP* **03** (2011) 032, arXiv:1011.1759 [hep-ph].

[26] T. Sjostrand and M. van Zijl, "A Multiple Interaction Model for the Event Structure in Hadron Collisions," *Phys. Rev. D* **36** (1987) 2019.

[27] P. Z. Skands and D. Wicke, "Non-perturbative QCD effects and the top mass at the Tevatron," *Eur. Phys. J. C* **52** (2007) 133–140, arXiv:hep-ph/0703081.

[28] B. Andersson, G. Gustafson, and B. Soderberg, "A General Model for Jet Fragmentation," *Z. Phys. C* **20** (1983) 317.

[29] R. D. Ball *et al.*, "Parton distributions with LHC data," *Nucl. Phys. B* **867** (2013) 244–289, arXiv:1207.1303 [hep-ph].

[30] T. Sjostrand and M. van Zijl, "A Multiple Interaction Model for the Event Structure in Hadron Collisions," *Phys. Rev. D* **36** (1987) 2019.

[31] T. Sjostrand and P. Z. Skands, "Multiple interactions and the structure of beam remnants," *JHEP* **03** (2004) 053, arXiv:hep-ph/0402078.

[32] G. Gustafson, "Multiple Interactions, Saturation, and Final States in pp Collisions and DIS," *Acta Phys. Polon. B* **40** (2009) 1981–1996, arXiv:0905.2492 [hep-ph].

[33] ALICE, E. Abbas *et al.*, "Performance of the ALICE VZERO system," *JINST* **8** (2013) P10016, arXiv:1306.3130 [nucl-ex].

[34] ALICE, B. B. Abelev *et al.*, "Charged jet cross sections and properties in proton-proton collisions at $\sqrt{s}$ = 7 TeV," *Phys. Rev. D* **91** no. 11, (2015) 112012, arXiv:1411.4969 [nucl-ex].

[35] ALICE, S. Acharya *et al.*, "Charged jet cross section and fragmentation in proton-proton collisions at $\sqrt{s}$ = 7 TeV," *Phys. Rev. D* **99** no. 1, (2019) 012016, arXiv:1809.03232 [nucl-ex].

[36] M. Cacciari, G. P. Salam, and G. Soyez, "The anti-k_t jet clustering algorithm," *JHEP* **04** (2008) 063, arXiv:0802.1189 [hep-ph].

[37] M. Cacciari, G. P. Salam, and G. Soyez, "FastJet User Manual," *Eur. Phys. J. C* **72** (2012) 1896, arXiv:1111.6097 [hep-ph].

[38] OPAL, P. D. Acton *et al.*, "A Study of differences between quark and gluon jets using vertex tagging of quark jets," *Z. Phys. C* **58** (1993) 387–404.

[39] M. H. Seymour, "Jet shapes in hadron collisions: Higher orders, resummation and hadronization," *Nucl. Phys. B* **513** (1998) 269–300, arXiv:hep-ph/9707338.

[40] S. D. Ellis, Z. Kunszt, and D. E. Soper, "Jets at hadron colliders at order $\alpha - s^{3:}$ A Look inside," *Phys. Rev. Lett.* **69** (1992) 3615–3618, arXiv:hep-ph/9208249.

[41] I. Vitev, "Theoretical developments in heavy and light flavor energy loss," *J. Phys. G* **35** (2008) 104011, arXiv:0806.0003 [hep-ph].

[42] I. Vitev, S. Wicks, and B.-W. Zhang, "A Theory of jet shapes and cross sections: From hadrons to nuclei," *JHEP* **11** (2008) 093, arXiv:0810.2807 [hep-ph].

[43] CDF, T. Affolder *et al.*, "Charged Jet Evolution and the Underlying Event in $p\bar{p}$ Collisions at 1.8 TeV," *Phys. Rev. D* **65** (2002) 092002.

[44] ALICE, S. Acharya *et al.*, "Underlying Event properties in pp collisions at $\sqrt{s}$ = 13 TeV," *JHEP* **04** (2020) 192, arXiv:1910.14400 [nucl-ex].

[45] ALICE, D. Banerjee, "Measurement of intra-jet properties and their multiplicity dependence in small collision systems with ALICE," *PoS* **ICHEP2022** (2022) 927.

[46] ALICE, P. Das, "Multiplicity dependence of intra-jet properties in small collision systems with ALICE," *PoS* **LHCP2022** (2023) 303.

[47] I. G. Knowles *et al.*, "QCD event generators," in *CERN Workshop on LEP2 Physics (followed by 2nd meeting, 15-16 Jun 1995 and 3rd meeting 2-3 Nov 1995)*. 6, 1995. arXiv:hep-ph/9601212.

[48] CDF, A. Pronko, "Fragmentation differences of quark and gluon jets at Tevatron," *Int. J. Mod. Phys. A* **20** (2005) 3723–3725.

"Summary writing is the art of capturing the essence of a story in a few brushstrokes."

— Edgar Alan Poe

Chapter 5

Summary and outlook

This thesis presents measurements of internal jet properties, including the mean charged-particle multiplicity ($\langle N_{\mathrm{ch}} \rangle$) and the jet fragmentation function ($z^{\mathrm{ch}} = p_{\mathrm{T}}^{\mathrm{track}} / p_{\mathrm{T}}^{\mathrm{jet,\,ch}}$), for charged-particle leading jets in pp and p–Pb collisions at $\sqrt{s_{\mathrm{NN}}} = 5.02$ TeV using experimental data from the ALICE experiment at CERN. These measurements report the first experimental observation of jet modification in p–Pb collisions at LHC energies, marking a pivotal milestone in the ongoing research of anomalous heavy-ion-like signatures observed in small collision systems. A multiplicity-dependent study of internal jet properties, namely jet shape $\rho(r)$ and jet fragmentation function (z^{ch}) for charged-particle inclusive jets in pp collisions at $\sqrt{s} = 13$ TeV using the PYTHIA 8 Monte Carlo event generator is also presented in this thesis. The study shows significant modification of jet shape and fragmentation in PYTHIA, where no QGP-medium effects are implemented. A more detailed study is performed further to identify the possible underlying physics mechanisms responsible for this modification in the absence of QGP-medium.

This thesis also presents an overview of the theoretical background, including the Standard Model of particle physics, the theory of strong interaction, i.e., quantum chromodynamics, quark-gluon plasma and its signatures in view of heavy-ion collisions, small

collision systems and their importance, and a comprehensive description of jets, which are essential to understand the research works presented, along with the physics motivation to perform the measurements in small collision systems. An overview of the experimental facility used for the measurements is also presented in this thesis. A detailed summary of the two research works presented in this thesis is discussed below.

Measurement of charged-particle leading jet properties in pp and p–Pb collisions with ALICE

In this work, charged-particle leading jet properties, namely the mean charged-particle multiplicity ($\langle N_{\rm ch} \rangle$) and the jet fragmentation function ($z^{\rm ch} = p_{\rm T}^{\rm track}/p_{\rm T}^{\rm jet,\,ch}$) are measured as a function of jet $p_{\rm T}$ in minimum bias pp collisions and both minimum bias and 0–20% central p–Pb collisions at $\sqrt{s_{\rm NN}} = 5.02$ TeV using ALICE data. The measurements are performed for charged-particle leading jets in the interval of $20 < p_{\rm T}^{\rm jet,\,ch} < 100$ GeV/c. Jets are reconstructed using the anti-$k_{\rm T}$ algorithm with jet resolution parameter $R = 0.4$. To correct the raw distributions for instrumental effects, a two-dimensional unfolding technique based on the Bayes' theorem implemented in the RooUnfold software package is employed. A jet and track matching framework is developed to construct the four-dimensional response matrices used in the unfolding procedure. The contributions from the underlying events (UE) to the measured jet observables are quantified using the perpendicular cone method and subtracted on a statistical basis after correcting those for instrumental effects. In addition, improved median method and improved random cone method are also employed for the estimation of UE as a systematic check. Systematic uncertainties from various sources are estimated for the reported distributions of jet observables. Systematic uncertainties due to track reconstruction inefficiency and change of prior are found to be the dominant sources, among others.

It has been observed that in all collision systems, the average number of charged

particles within a jet ($\langle N_{\rm ch} \rangle$) increases monotonically with the leading jet transverse momentum ($p_{\rm T}$), albeit the rate of increase gradually decreases as the jet $p_{\rm T}$ becomes larger. These observations imply that high-momentum jets fragment into harder jet constituents. PYTHIA 8 model with Monash 2013 tune tends to overestimate the pp data by up to 10%. In case of p–Pb collisions, PYTHIA 8 Angantyr model shows better agreement with data compared to DPMJET model for both minimum bias and central events. However, at low jet $p_{\rm T}$, DPMJET model appears to underestimate data.

A comparison of $\langle N_{\rm ch} \rangle$ distributions between minimum bias p–Pb and pp collisions in data reveals a slight increase (10%) in minimum bias p–Pb collisions, particularly at low jet $p_{\rm T}$, suggesting potential jet modification. Interestingly, PYTHIA 8 Angantyr model exhibits similar behavior, albeit slightly underestimating the data. The comparison of $\langle N_{\rm ch} \rangle$ distributions between minimum bias and central p–Pb collisions in data indicates no significant change except at the lowest jet $p_{\rm T}$ bin (20–30 GeV/c), where the change is below 5%. Both PYTHIA 8 Angantyr and DPMJET models reproduce the data fairly well within systematic uncertainties.

The distributions of $z^{\rm ch}$ for different jet $p_{\rm T}$ ranges exhibit consistency with each other within systematic uncertainties in all three collision systems, except at very low and high $z^{\rm ch}$ values for minimum bias pp collisions and at high $z^{\rm ch}$ values for minimum bias p–Pb collisions. The overall behavior suggests that the jet fragmentation pattern does not vary considerably with jet $p_{\rm T}$.

The measured $z^{\rm ch}$ distributions are compared with various Monte Carlo (MC) model predictions. In case of pp collisions, PYTHIA 8 model with Monash 2013 tune adequately reproduces the data at low $z^{\rm ch}$ values (< 0.4) within systematic uncertainties but tends to underestimate the data at intermediate and high $z^{\rm ch}$ values for the considered jet $p_{\rm T}$ ranges. For minimum bias p–Pb collisions, all three MC models, DPMJET, EPOS LHC, and PYTHIA 8 Angantyr, are found to reasonably explain the jet fragmentation distributions,

except for the last bin within systematic uncertainties. In case of central p–Pb collisions, all the models reproduce the data within approximately 20%, with EPOS LHC showing a slightly different trend compared to other models for the p_{T} range of 20–30 GeV/c.

To investigate the nuclear effect on jet fragmentation functions, z^{ch} distributions are compared between minimum bias proton-lead (p–Pb) and proton-proton (pp) collisions for leading jet p_{T} intervals of 20–30 GeV/c, 30–40 GeV/c, and 40–60 GeV/c. Notably, the jet fragmentation pattern significantly differs in minimum bias p–Pb collisions compared to minimum bias pp collisions. Ratios indicate a slight enhancement of low z^{ch} particles, followed by substantial suppression of high z^{ch} particles within jets. This jet modification is most pronounced for the lowest jet p_{T} interval of 20–30 GeV/c and diminishes notably with increasing jet p_{T}. Interestingly, no significant modification is observed at jet p_{T} = 40–60 GeV/c, consistent with findings from other experiments in similar kinematic regime. Nevertheless, these results mark the first observation of jet modification in p–Pb collisions relative to pp collisions at LHC energies. Surprisingly, the characteristics of jet modification observed in data align qualitatively with predictions from the PYTHIA 8 Angantyr model, which does not incorporate jet quenching effects.

A similar trend emerges when comparing z^{ch} distributions between central and minimum bias p–Pb collisions for the three reported jet p_{T} ranges. The jet p_{T}-dependent modification of jet fragmentation pattern is also evident between central and minimum bias p–Pb collisions, with the most significant modification observed at the lowest jet p_{T} interval. Notably, both PYTHIA 8 Angantyr and DPMJET models, without implementation of any QGP-medium effects, qualitatively capture similar behavior. Further investigation using PYTHIA 8 Angangyr model shows that multiparton interaction (MPI) and color reconnection (CR) mechanisms might play a role in the jet modification shown by PYTHIA.

Exciting observations are found in this investigation about modifications of jet frag-

mentation, especially for low p_{T} jets (20 – 30 GeV/c) observed in both minimum bias and central p–Pb collisions compared to minimum bias pp and minimum bias p–Pb collisions, respectively. Even though it is difficult to explicitly determine from these experimental measurements whether these effects are the result of QGP droplet formation, some other physics phenomena, or bias-related artifacts in the measurements, these observations are still intriguing because they show features counter-intuitive to our conventional expectation.

Multiplicity-dependent study of internal jet properties in pp collisions using PYTHIA simulation

In this work, the multiplicity dependence of internal jet properties, such as jet shape $\rho(r)$ and jet fragmentation function (z^{ch}) is studied in pp collisions at $\sqrt{s}$ = 13 TeV, using the PYTHIA 8 Monte Carlo event generator. The study is performed with charged-particle jets in the interval of $10 < p_{\mathrm{T}}^{\mathrm{jet,\,ch}} < 60$ GeV/c for minimum bias (MB) and high-multiplicity (HM) event classes of pp collisions. Jets are reconstructed from charged particles at mid-rapidity using the anti-k_{T} jet finding algorithm with jet resolution parameter $R = 0.4$. Contributions from UE are estimated using the perpendicular cone method and subtracted on a statistical basis. The distributions of $\rho(r)$ and z^{ch} are obtained with 'MPI: OFF, CR: OFF', 'MPI: ON, CR: OFF' and 'MPI: ON, CR: ON' configurations of PYTHIA 8 MC event generator. The HM event class is defined as the event class containing the top 5% of the total events with the highest multiplicities, based on the total number of charged particles produced in the pseudorapidity ranges $2.8 < \eta < 5.1$ and $-3.7 < \eta < -1.7$.

Significant modifications of jet shape $\rho(r)$ and jet fragmentation z^{ch} distributions are observed in HM event class compared to MB event class for $10 < p_{\mathrm{T,\,jet}}^{\mathrm{ch}} < 20$ GeV/c. The jet core ($\rho(r)|_{r\to 0}$) is modified by about 22% followed by a small enhancement at larger r (> 0.15) whereas the production of high z^{ch} particles is suppressed by about 40% at

$z^{\mathrm{ch}} \rightarrow 1$ in HM event class compared to that in MB. The amounts of modification in $\rho(r)$ and z^{ch} distributions for inclusive charged-particle jets in HM events compared to MB events are found to get reduced noticeably in absence of MPI and CR mechanisms. It is also found that distributions of these jet observables for gluon-initiated jets show no or very little modification compared to the inclusive jets, leading to the conclusion that enhanced number of MPIs and the change in the number of gluon-initiated jets in high-multiplicity events compared to minimum bias ones, along with the color reconnection mechanism are the main sources causing modifications of $\rho(r)$ and z^{ch} distributions. For high-p_{T} jets ($40 < p_{\mathrm{T,jet}}^{\mathrm{ch}} < 60$ GeV/c), the observed jet modification is significantly reduced. A direct connection of $\langle N_{\mathrm{MPI}} \rangle$ and gluonic contribution with the amount of modification in $\rho(r)$ is also found – the larger the number of MPIs and/or gluonic contribution, the larger the amount of modification of $\rho(r)$.

The findings of this work emphasize the necessity of a better understanding of the origin of particle production in high-multiplicity events in pp collisions. The modification of $\rho(r)$ and z^{ch} in HM events and their strong correlations with the underlying physics mechanisms such as MPI and CR as well as with the change in the gluonic contribution compared to that in MB events demand a very careful study and interpretation of such observables by the experimental community. Although disentangling gluon-initiated jets experimentally will be challenging, however, studying the multiplicity dependence of $\rho(r)$ and z^{ch} for pure gluonic jets would be worth pursuing.

As a continuation of the presented work, the following studies might be considered as a future work plan by the interested groups:

- The measurements of internal jet properties have been performed for the charged-particle leading jets, which are mostly gluon-dominated at LHC energies. It will be interesting to study the internal jet properties for photon-tagged jets (quark-dominated) and heavy-quark-tagged jets, which will help us understand the depen-

dence of jet modification on the nature of the parton (quark or gluon). Similar measurements in heavy-ion collisions will be useful to understand the effect of jet-medium interactions and mass- and flavor-dependent energy loss in presence of QGP-medium.

- Investigation of the observed jet modification in p–Pb collisions using PYTHIA 8 Angantyr model showed that multiparton interaction and color reconnection mechanisms are partially responsible for the feature shown by PYTHIA. A detailed study to explore other possible reason(s) including various applicable models as well as theoretical efforts on this front might be worthwhile to understand the underlying physics.

- The multiplicity-dependent study of internal jet properties in pp collisions has been performed using PYTHIA 8 Monte Carlo event generator, where the multiparton interaction and color reconnection mechanisms have been shown to have effects on the observed jet modification. It will be interesting to perform a similar study with other event generators, which may explain the modification in a different way, e.g., EPOS 4 incorporates hydrodynamic evolution, unlike PYTHIA.

Appendix A

Uncorrected distributions of jet observables in pp and p–Pb collisions at 5.02 TeV

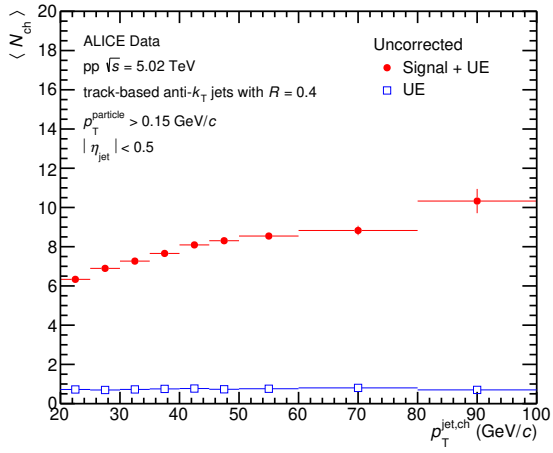

Figure A.1: Raw distributions of $\langle N_{\mathrm{ch}} \rangle$ as a function of leading jet p_{T} in minimum bias pp collisions.

A.1 Minimum bias pp

Figure A.1 shows the uncorrected signal distributions contaminated with UE (red solid circles) and corresponding UE distributions (blue open boxes) of $\langle N_{\mathrm{ch}} \rangle$ as a function of leading jet p_{T} in minimum bias pp collisions. Figures A.2, A.3 and A.4 show the uncorrected signal distributions contaminated with UE (red solid circles) and corresponding UE distributions (blue open boxes) of z^{ch} for leading jet p_{T} = 20–30 GeV/c, 30–40 GeV/c and 40–60 GeV/c in minimum bias pp collisions.

A.2 Minimum bias p–Pb

Figure A.5 shows the uncorrected signal distributions contaminated with UE (red solid circles) and corresponding UE distributions (blue open boxes) of $\langle N_{\mathrm{ch}} \rangle$ as a function of leading jet p_{T} in minimum bias p–Pb collisions. Figures A.6, A.7 and A.8 show the uncorrected signal distributions contaminated with UE (red solid circles) and corresponding UE distributions (blue open boxes) of z^{ch} for leading jet p_{T} = 20–30 GeV/c, 30–40 GeV/c

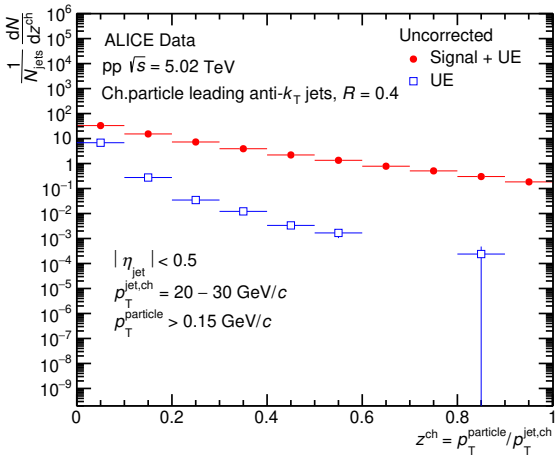

Figure A.2: Raw z^{ch} distributions for leading jet p_T = 20–30 GeV/c in minimum bias pp collisions.

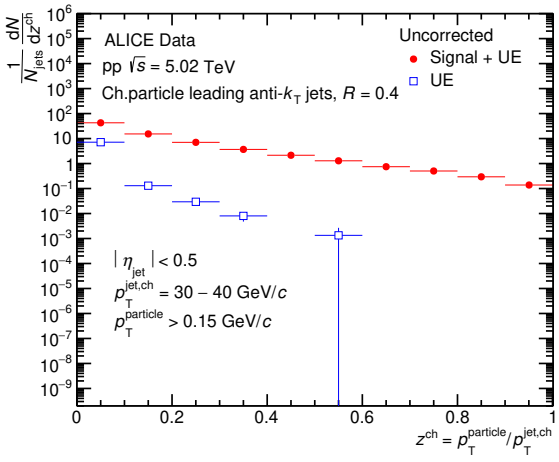

Figure A.3: Raw z^{ch} distributions for leading jet p_T = 30–40 GeV/c in minimum bias pp collisions.

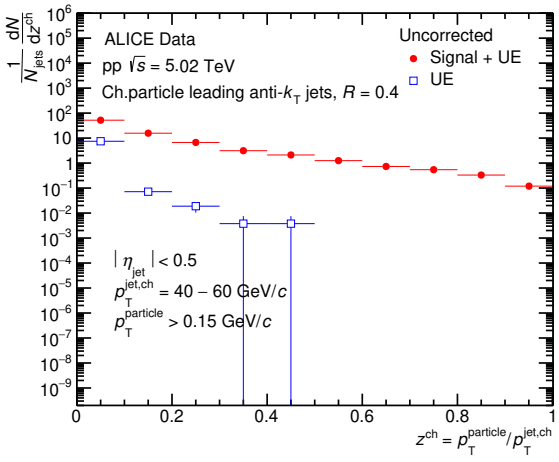

Figure A.4: Raw z^{ch} distributions for leading jet p_T = 40–60 GeV/c in minimum bias pp collisions.

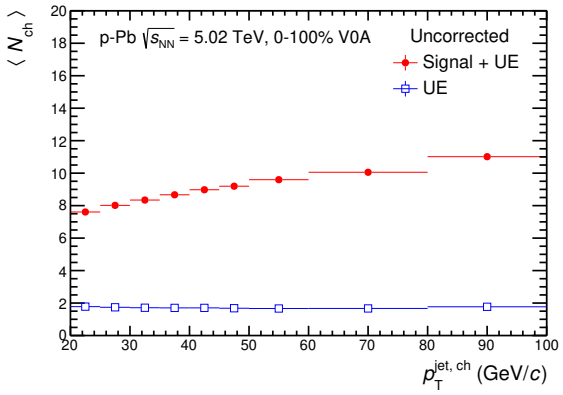

Figure A.5: Raw distributions of $\langle N_{ch} \rangle$ as a function of leading jet p_T in minimum bias p–Pb collisions.

and 40–60 GeV/c in minimum bias p–Pb collisions.

A.3 0–20% central p–Pb

Figure A.9 shows the uncorrected signal distributions contaminated with UE (red solid circles) and corresponding UE distributions (blue open boxes) of $\langle N_{ch} \rangle$ as a function of leading jet p_T in 0–20% central p–Pb collisions. The UE contribution is larger in central p–Pb collisions compared to that in minimum bias ones as expected. Figures A.10, A.11 and A.12 show the uncorrected signal distributions contaminated with UE (red solid circles) and corresponding UE distributions (blue open boxes) of z^{ch} for leading jet p_T = 20–30 GeV/c, 30–40 GeV/c and 40–60 GeV/c in 0–20% central p–Pb collisions.

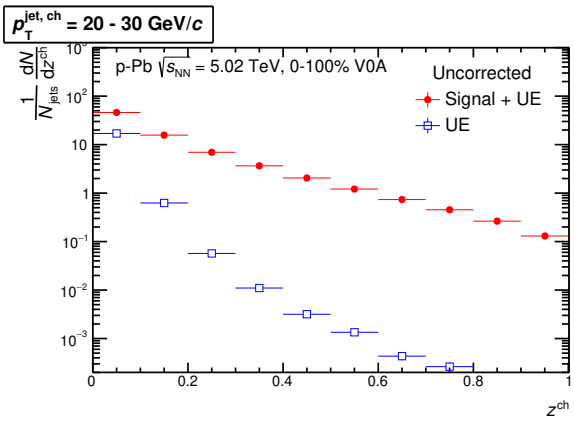

Figure A.6: Raw z^{ch} distributions for leading jet p_T = 20–30 GeV/c in minimum bias p–Pb collisions.

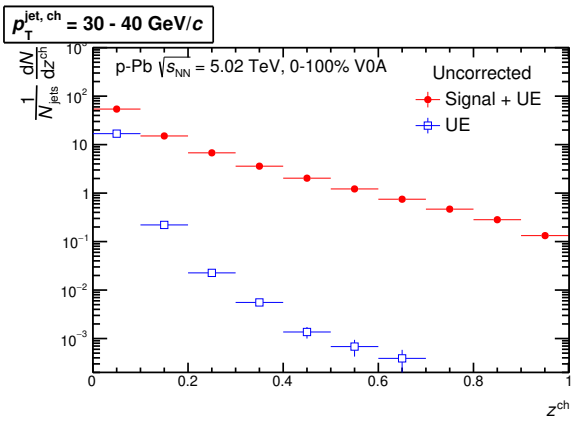

Figure A.7: Raw z^{ch} distributions for leading jet p_T = 30–40 GeV/c in minimum bias p–Pb collisions.

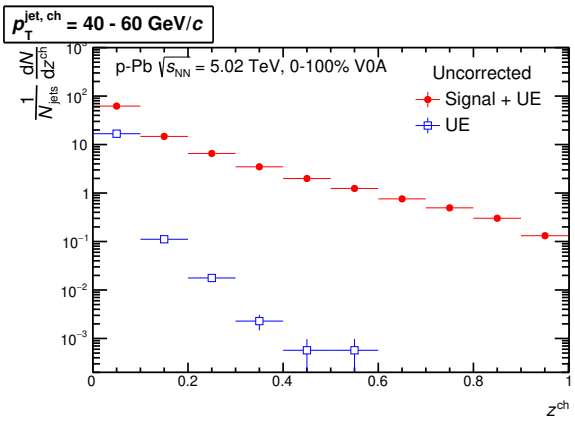

Figure A.8: Raw z^{ch} distributions for leading jet p_T = 40–60 GeV/c in minimum bias p–Pb collisions.

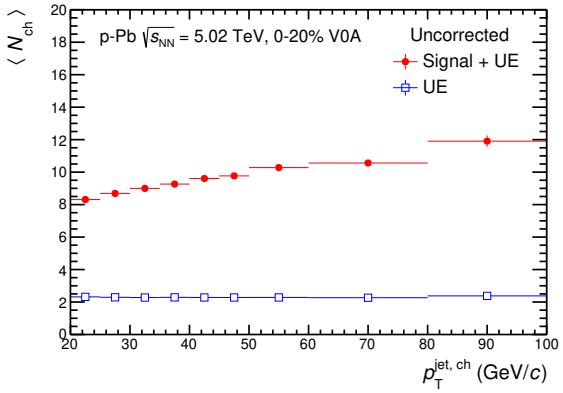

Figure A.9: Raw distributions of $\langle N_{\mathrm{ch}} \rangle$ as a function of leading jet p_{T} in 0–20% central p–Pb collisions.

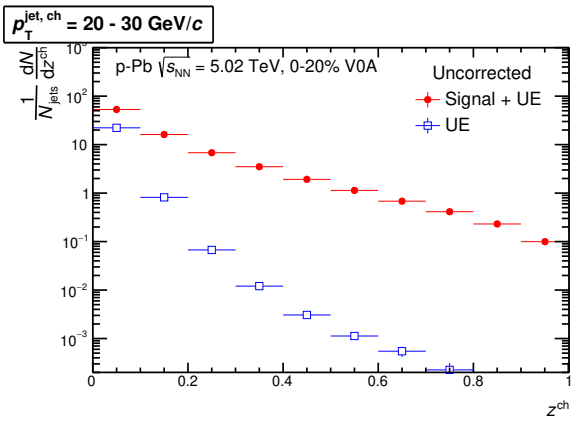

Figure A.10: Raw z^{ch} distributions for leading jet p_T = 20–30 GeV/c in 0–20% central p–Pb collisions.

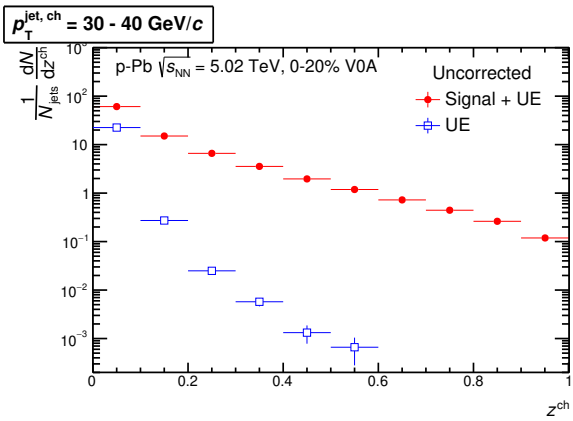

Figure A.11: Raw z^{ch} distributions for leading jet p_T = 30–40 GeV/c in 0–20% central p–Pb collisions.

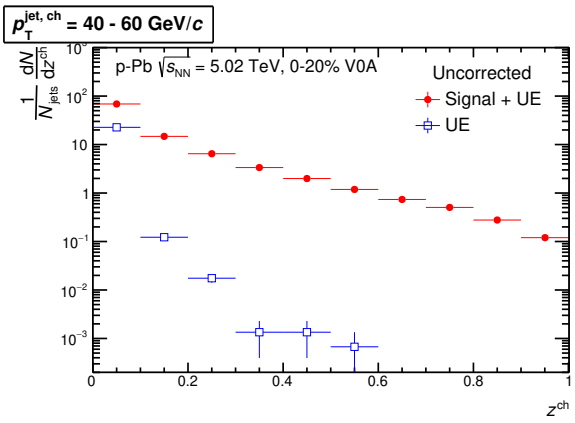

Figure A.12: Raw z^{ch} distributions for leading jet p_T = 40–60 GeV/c in 0–20% central p–Pb collisions.

Appendix B

Projections of 4-D response matrices for the jet observables in pp and p–Pb collisions at 5.02 TeV

Figures B.1, B.2 and B.3 show the projections of response matrices for N_{ch} (left) and $N_{\mathrm{ch}}^{\mathrm{UE}}$ (right) in minimum bias and 0-20% central p–Pb and minimum bias pp collisions respectively. Figures B.4-B.11 show the projections of response matrices for jet fragmentaion function (left) and its UE (right) for different intervals of leading detector-level jet p_{T} in minimum bias and 0-20% central p–Pb and minimum bias pp collisions.

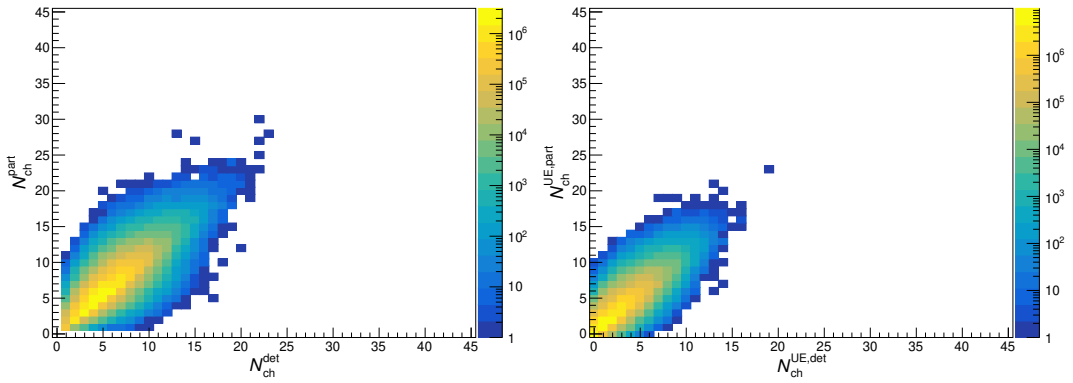

Figure B.1: Projections of response matrices for N_{ch} (left) and $N_{\mathrm{ch}}^{\mathrm{UE}}$ (right) in minimum bias p–Pb collisions.

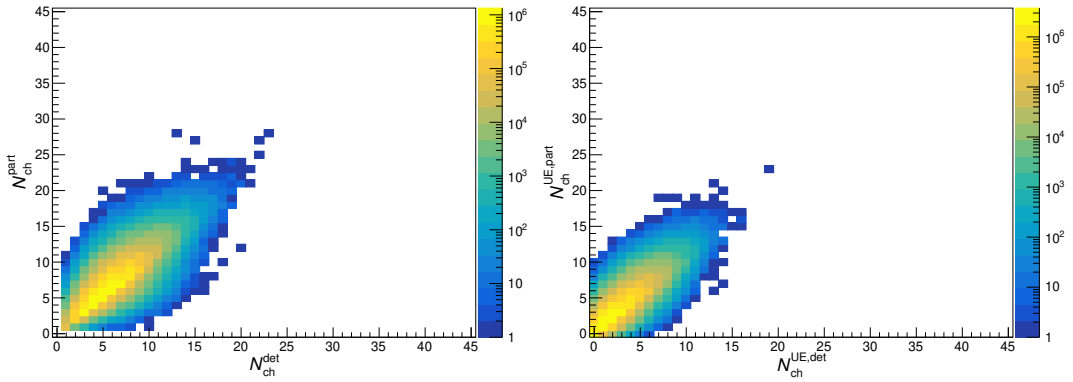

Figure B.2: Projections of response matrices for N_{ch} (left) and $N_{\mathrm{ch}}^{\mathrm{UE}}$ (right) in 0-20% central p–Pb collisions.

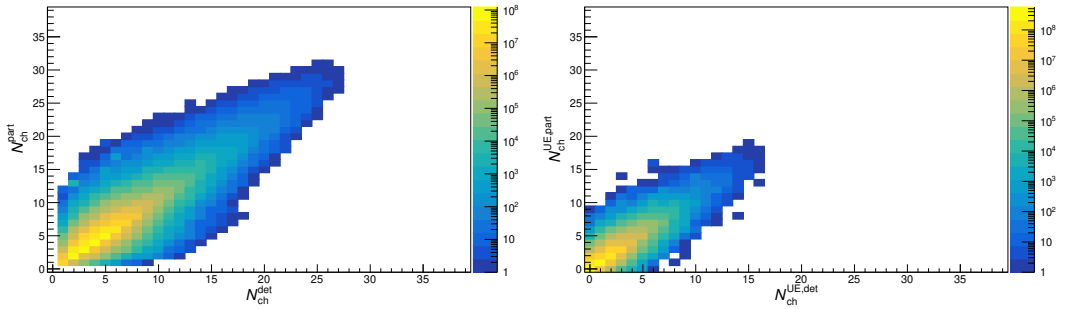

Figure B.3: Projections of response matrices for N_{ch} (left) and N_{ch}^{UE} (right) in minimum bias pp collisions.

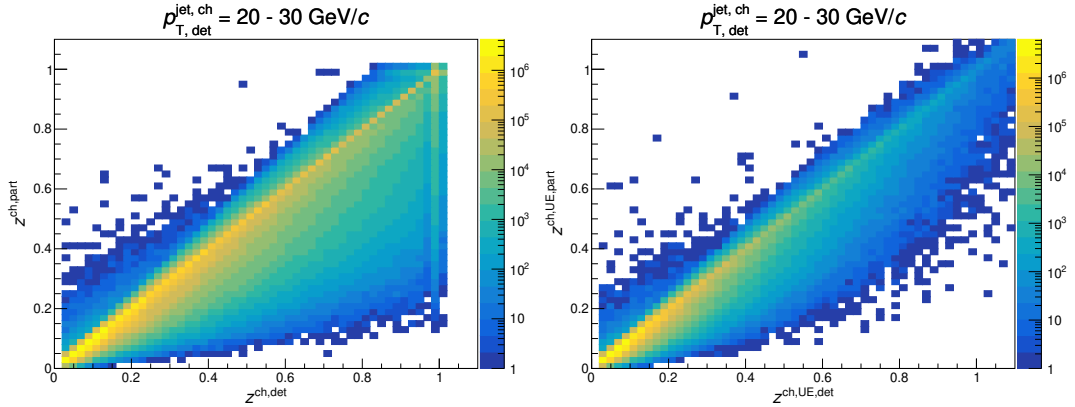

Figure B.4: Projections of response matrices for fragmentation function (left) and its UE (right) for leading detector-level jet p_T = 20–30 GeV/c in minimum bias p–Pb collisions.

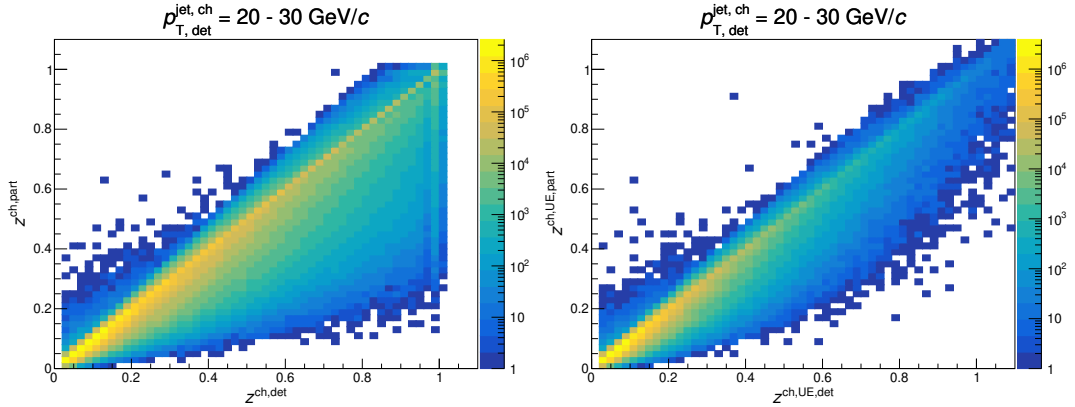

Figure B.5: Projections of response matrices for fragmentation function (left) and its UE (right) for leading detector-level jet p_T = 20–30 GeV/c in 0-20% central p–Pb collisions.

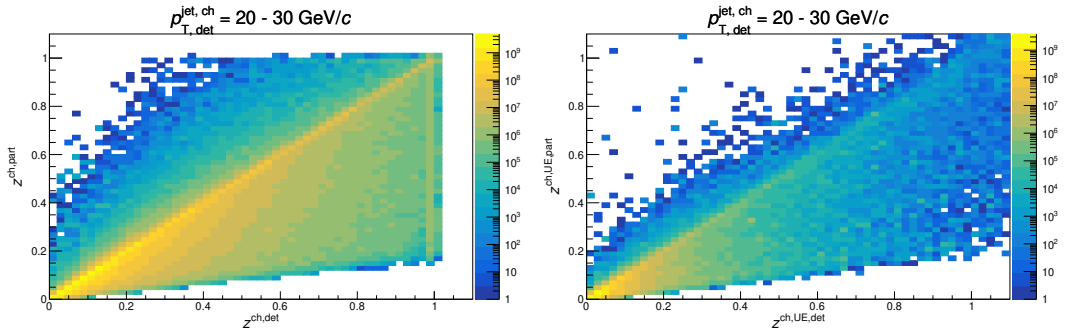

Figure B.6: Projections of response matrices for fragmentation function (left) and its UE (right) for leading detector-level jet p_{T} = 20–30 GeV/c in minimum bias pp collisions.

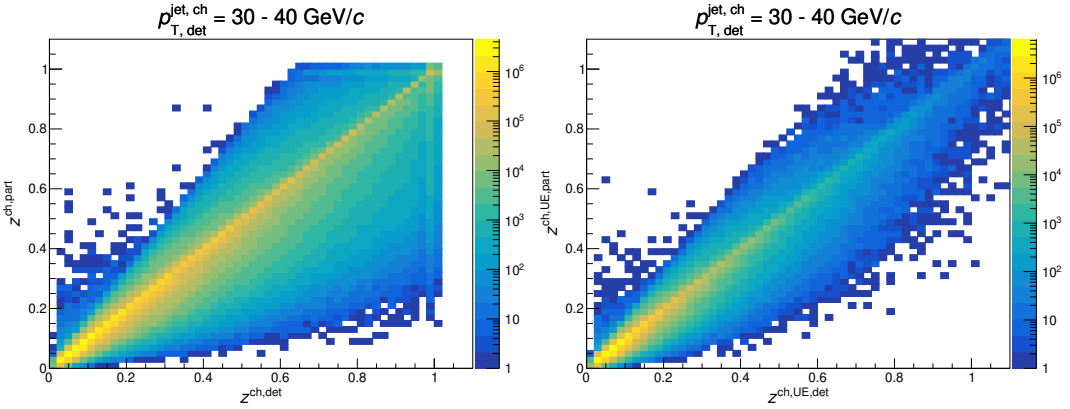

Figure B.7: Projections of response matrices for fragmentation function (left) and its UE (right) for leading detector-level jet p_{T} = 30–40 GeV/c in minimum bias p–Pb collisions.

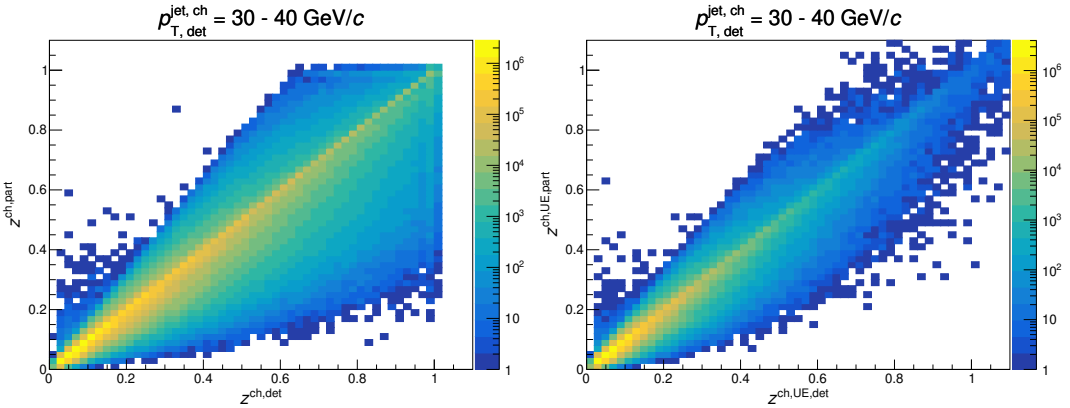

Figure B.8: Projections of response matrices for fragmentation function (left) and its UE (right) for leading detector-level jet p_{T} = 30–40 GeV/c in 0-20% central p–Pb collisions.

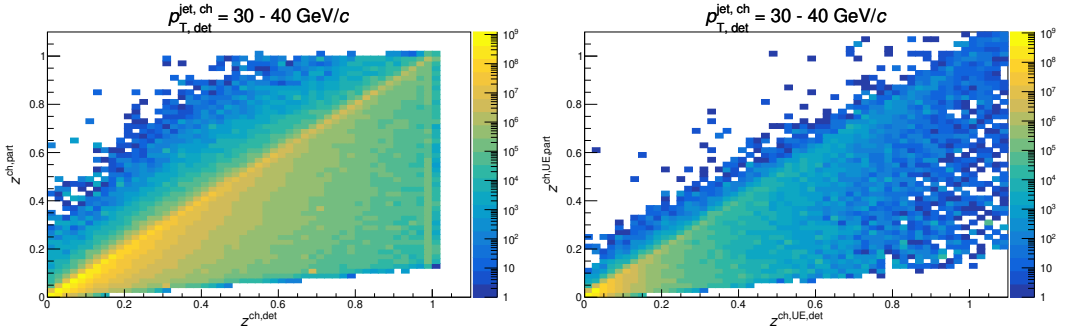

Figure B.9: Projections of response matrices for fragmentation function (left) and its UE (right) for leading detector-level jet p_{T} = 30–40 GeV/c in minimum bias pp collisions.

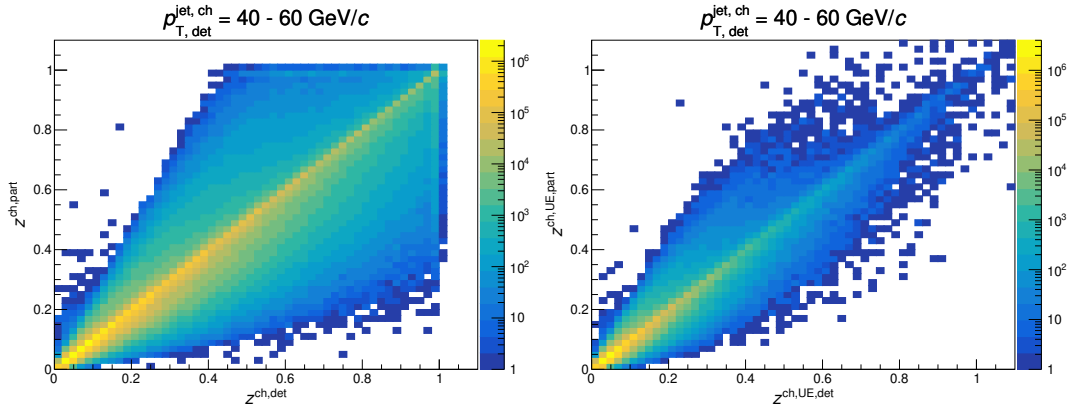

Figure B.10: Projections of response matrices for fragmentation function (left) and its UE (right) for leading detector-level jet p_{T} = 40–60 GeV/c in minimum bias p–Pb collisions.

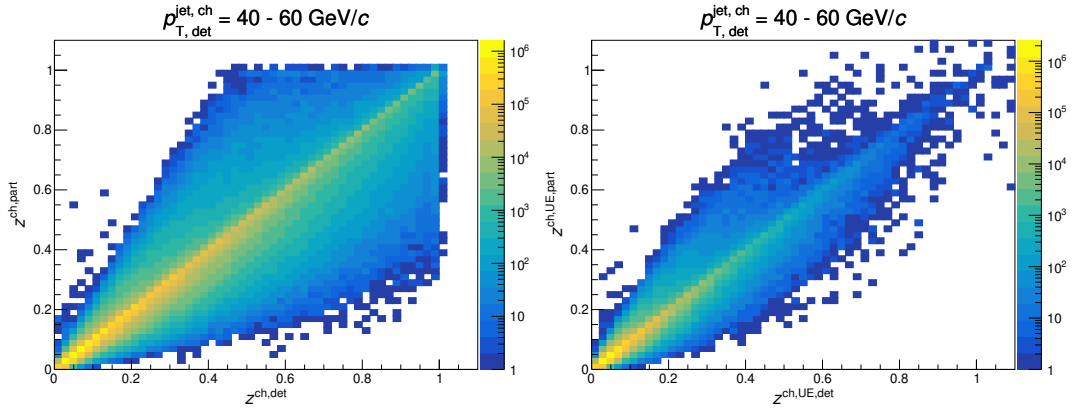

Figure B.11: Projections of response matrices for fragmentation function (left) and its UE (right) for leading detector-level jet p_{T} = 40–60 GeV/c in 0-20% central p–Pb collisions.

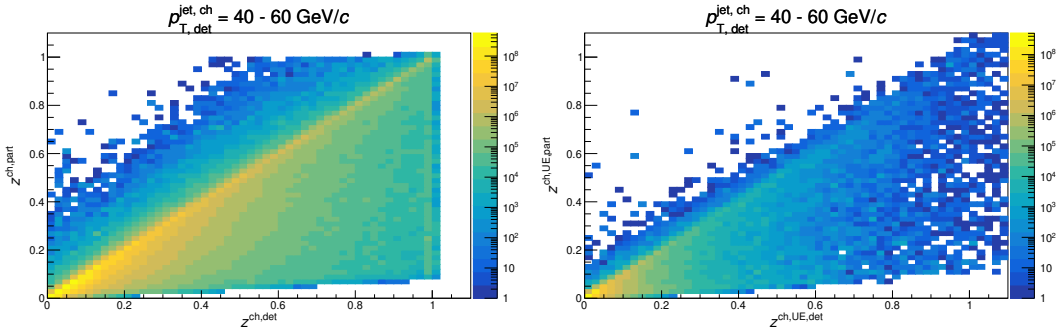

Figure B.12: Projections of response matrices for fragmentation function (left) and its UE (right) for leading detector-level jet p_{T} = 40–60 GeV/c in minimum bias pp collisions.

Appendix C

Results of MC closure tests for the jet observables in pp and p–Pb collisions at 5.02 TeV

C.1 Results of statistical closure tests

The full set of plots showing the statistical closure tests for the default number of iterations is presented here. Figures C.1, C.2 and C.3 show the performance of statistical closure test for $\langle N_{\mathrm{ch}} \rangle$ in minimum bias and central p–Pb collisions and minimum bias pp collisions, respectively. The same for their UE contributions are shown in Figs. C.4, C.5 and C.6. Similarly, the performance of statistical closure tests for z^{ch} and the corresponding UE contributions are shown in Figs. C.7– C.24. Except for the low statistics regions in the UE distributions at high jet p_{T} and high z^{ch}, the performance of this closure test is satisfactory within statistical uncertainties. There is significant scale difference between the signal and UE (signal is much larger), so these fluctuations in UE distributions will be well within total systematic uncertainties.

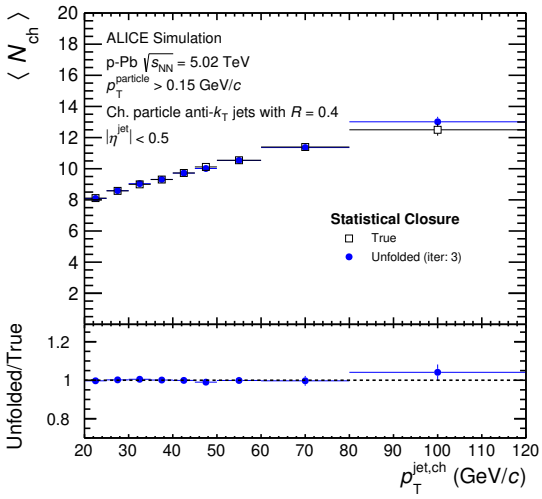

Figure C.1: $\langle N_{\mathrm{ch}} \rangle$ distributions in minimum bias p–Pb collisions: statistical closure (iteration 3).

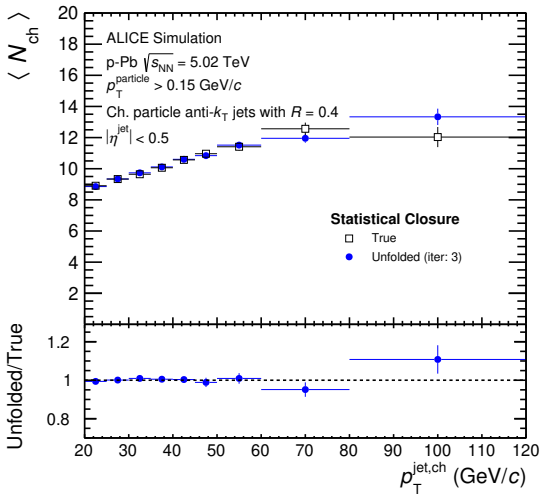

Figure C.2: $\langle N_{\mathrm{ch}} \rangle$ distributions in 0–20% central p–Pb collisions: statistical closure (iteration 3).

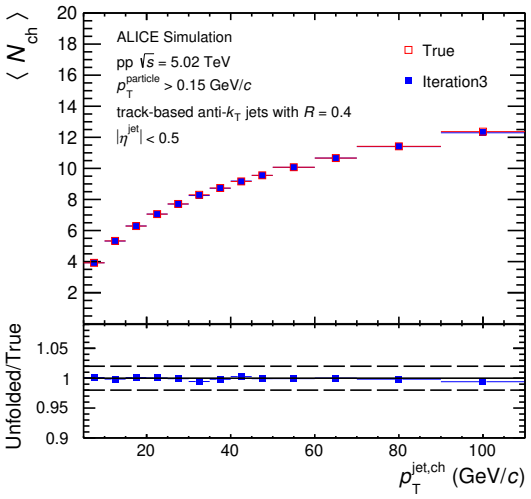

Figure C.3: $\langle N_{\mathrm{ch}} \rangle$ distributions in minimum bias pp collisions: statistical closure (iteration 3).

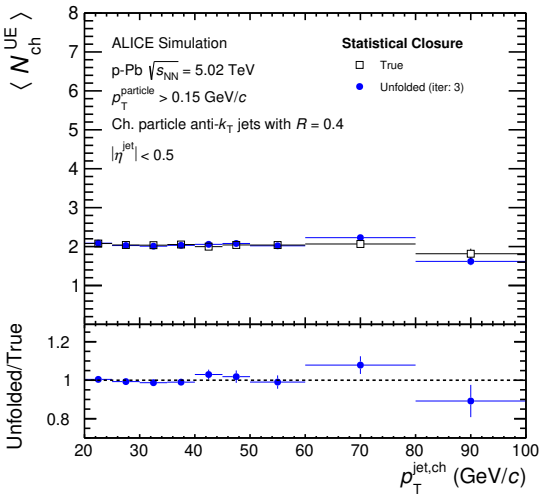

Figure C.4: UE contribution to $\langle N_{\mathrm{ch}} \rangle$ distribution in minimum bias p–Pb collisions: statistical closure (iteration 3).

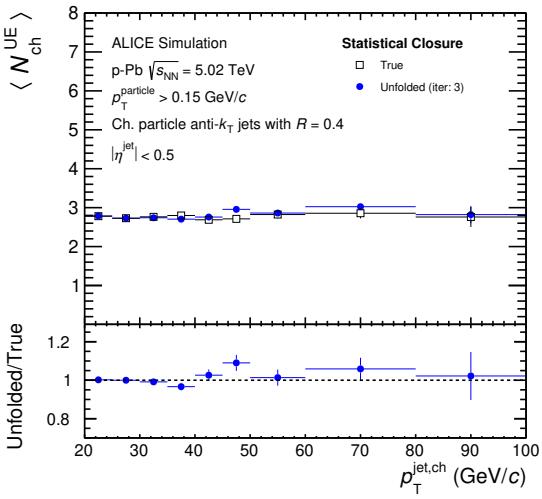

Figure C.5: UE contribution to $\langle N_{\mathrm{ch}} \rangle$ distribution in 0–20% central p–Pb collisions: statistical closure (iteration 3).

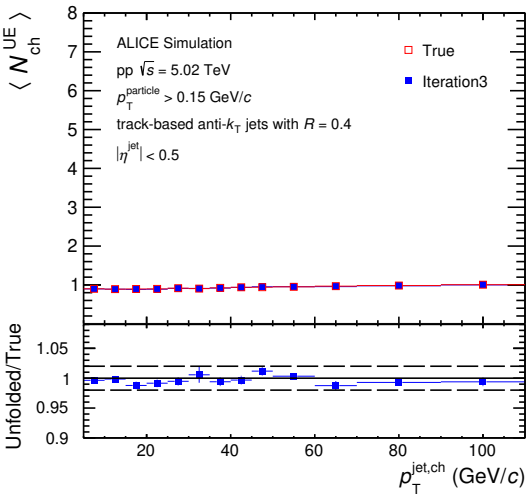

Figure C.6: UE contribution to $\langle N_{\mathrm{ch}} \rangle$ distribution in minimum bias pp collisions: statistical closure (iteration 3).

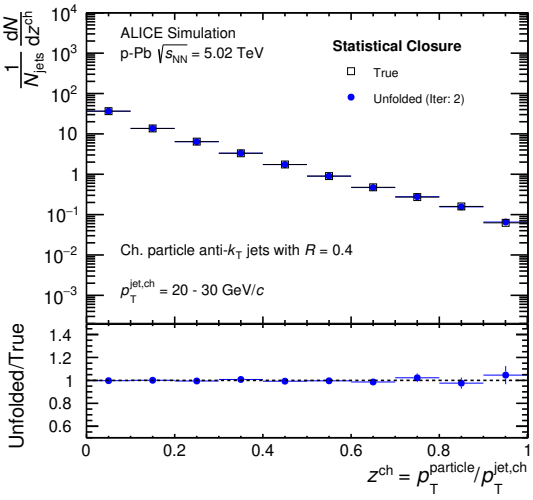

Figure C.7: z^{ch} distributions for leading jet p_{T} = 20–30 GeV/c. in minimum bias p–Pb collisions: statistical closure (iteration 2).

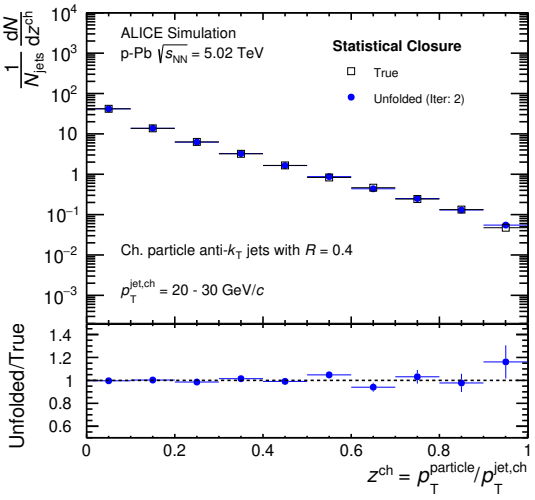

Figure C.8: z^{ch} distributions for leading jet p_{T} = 20–30 GeV/c. in 0–20% central p–Pb collisions: statistical closure (iteration 2).

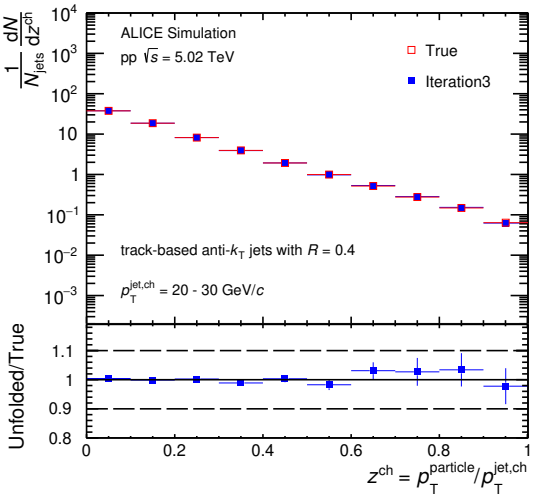

Figure C.9: z^{ch} distributions for leading jet p_{T} = 20–30 GeV/c. in minimum bias pp collisions: statistical closure (iteration 3).

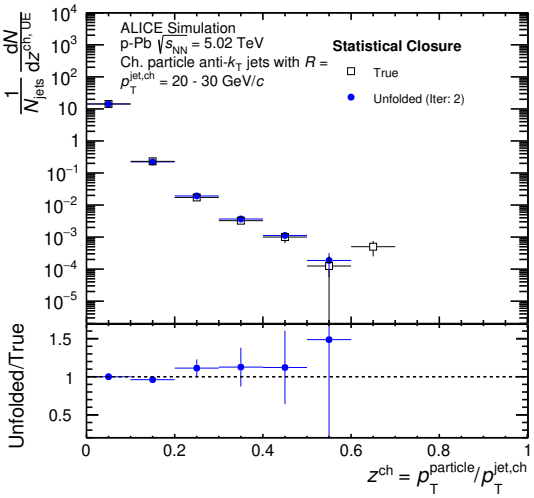

Figure C.10: UE contribution to z^{ch} distributions for leading jet $p_{\mathrm{T}} = 20$–30 GeV/c. in minimum bias p–Pb collisions: statistical closure (iteration 2).

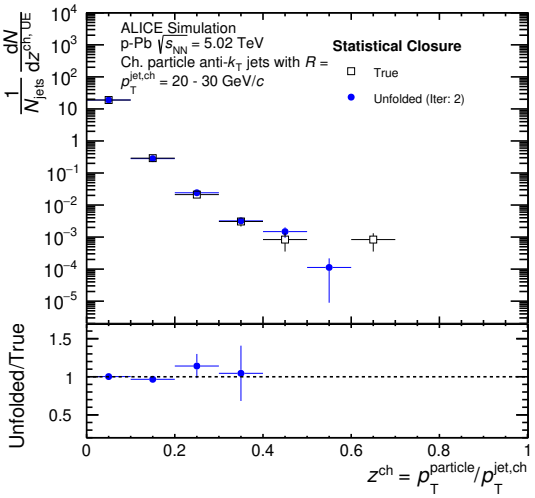

Figure C.11: UE contribution to z^{ch} distributions for leading jet $p_{\mathrm{T}} = 20$–30 GeV/c. in 0–20% central p–Pb collisions: statistical closure (iteration 2).

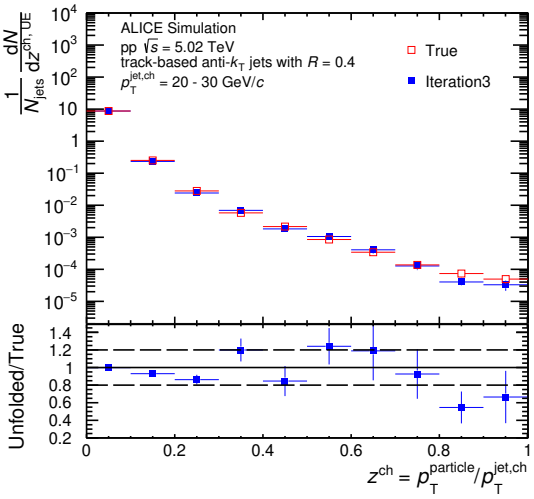

Figure C.12: UE contribution to z^{ch} distributions for leading jet $p_{\mathrm{T}} = 20$–30 GeV/c. in minimum bias pp collisions: statistical closure (iteration 3).

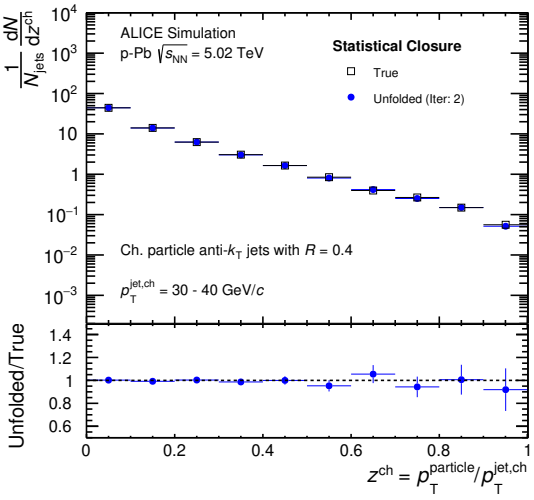

Figure C.13: z^{ch} distributions for leading jet p_T = 30–40 GeV/c. in minimum bias p–Pb collisions: statistical closure (iteration 2).

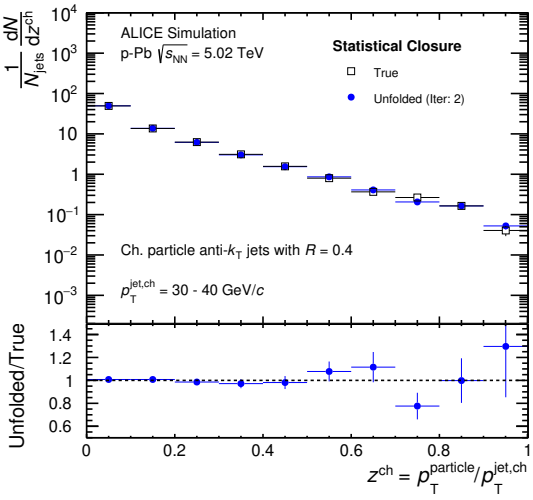

Figure C.14: z^{ch} distributions for leading jet p_T = 30–40 GeV/c. in 0–20% central p–Pb collisions: statistical closure (iteration 2).

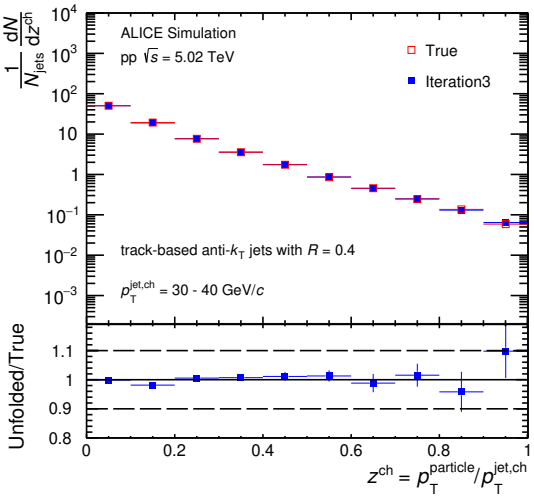

Figure C.15: z^{ch} distributions for leading jet p_T = 30–40 GeV/c. in minimum bias pp collisions: statistical closure (iteration 3).

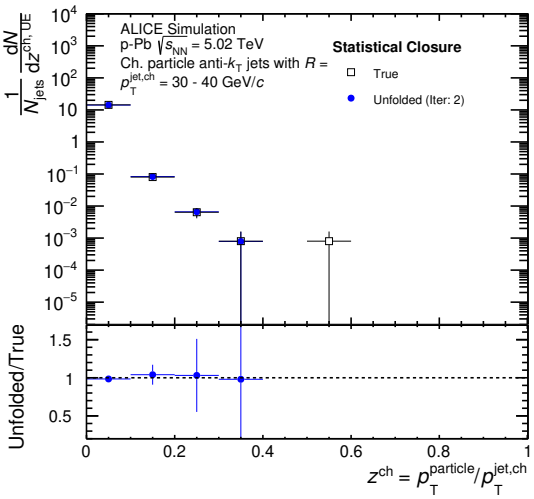

Figure C.16: UE contribution to z^{ch} distributions for leading jet $p_T = 30–40$ GeV/c. in minimum bias p–Pb collisions: statistical closure (iteration 2).

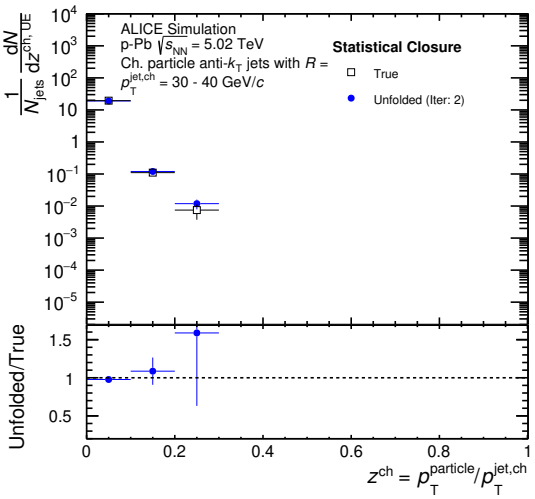

Figure C.17: UE contribution to z^{ch} distributions for leading jet $p_T = 30–40$ GeV/c. in 0–20% central p–Pb collisions: statistical closure (iteration 2).

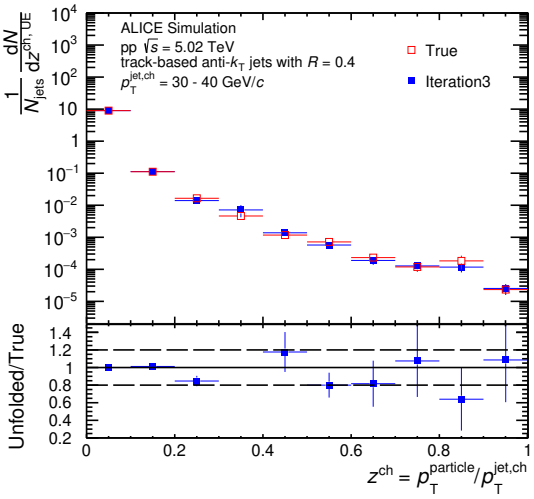

Figure C.18: UE contribution to z^{ch} distributions for leading jet $p_T = 30–40$ GeV/c. in minimum bias pp collisions: statistical closure (iteration 3).

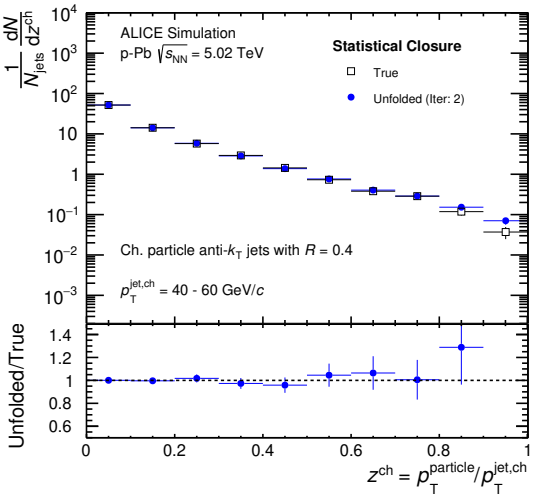

Figure C.19: z^{ch} distributions for leading jet p_{T} = 40–60 GeV/c. in minimum bias p–Pb collisions: statistical closure (iteration 2).

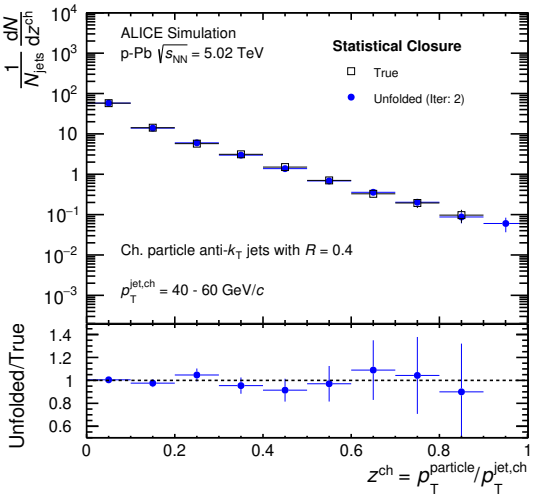

Figure C.20: z^{ch} distributions for leading jet p_{T} = 40–60 GeV/c. in 0–20% central p–Pb collisions: statistical closure (iteration 2).

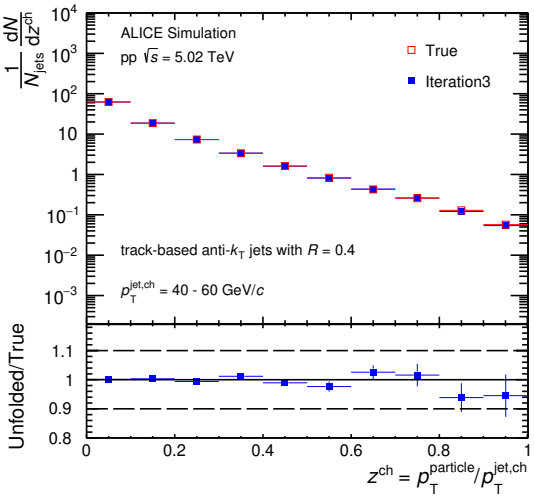

Figure C.21: z^{ch} distributions for leading jet p_{T} = 40–60 GeV/c. in minimum bias pp collisions: statistical closure (iteration 3).

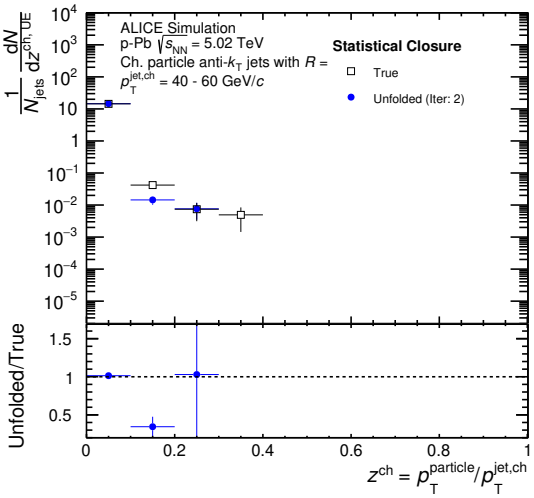

Figure C.22: UE contribution to z^{ch} distributions for leading jet $p_T = 40$–60 GeV/c. in minimum bias p–Pb collisions: statistical closure (iteration 2).

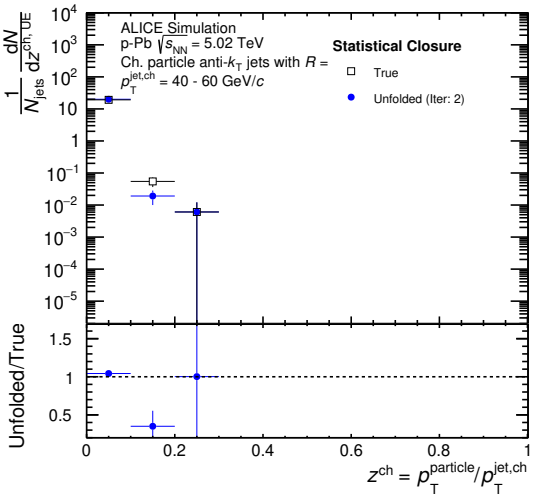

Figure C.23: UE contribution to z^{ch} distributions for leading jet $p_T = 40$–60 GeV/c. in 0–20% central p–Pb collisions: statistical closure (iteration 2).

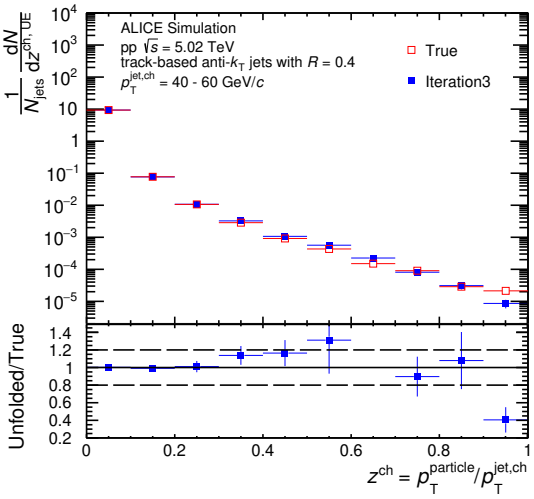

Figure C.24: UE contribution to z^{ch} distributions for leading jet $p_T = 40$–60 GeV/c. in minimum bias pp collisions: statistical closure (iteration 3).

C.2 Results of shape closure tests

The full set of plots showing the shape closure tests for the default number of iterations is presented here. Figures C.25, C.26 and C.27 show the performance of shape closure test for $\langle N_{\mathrm{ch}} \rangle$ in minimum bias and central p–Pb collisions and minimum bias pp collisions, respectively. The same for their UE contributions are shown in figs. C.28, C.29 and C.30. Similarly, the performance of shape closure tests for z^{ch} and the corresponding UE contributions are shown in figs. C.31– C.48. Good and reasonable closure is observed within uncertainties except at high jet p_{T} and high z^{ch} in the UE distributions where the statistical fluctuations dominate. Nonetheless, a prior uncertainty is included in the total systematic uncertainty which will incorporate all these effects.

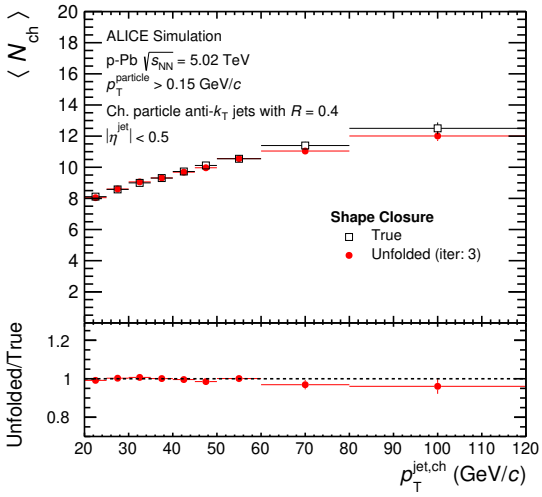

Figure C.25: $\langle N_{\mathrm{ch}} \rangle$ distributions in minimum bias p–Pb collisions: shape closure (iteration 3).

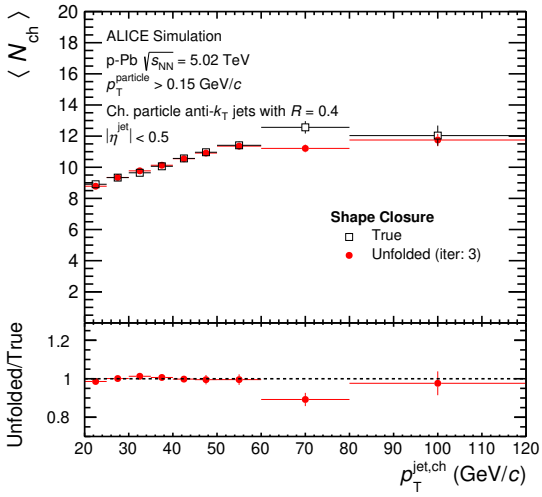

Figure C.26: $\langle N_{\mathrm{ch}} \rangle$ distributions in 0–20% central p–Pb collisions: shape closure (iteration 3).

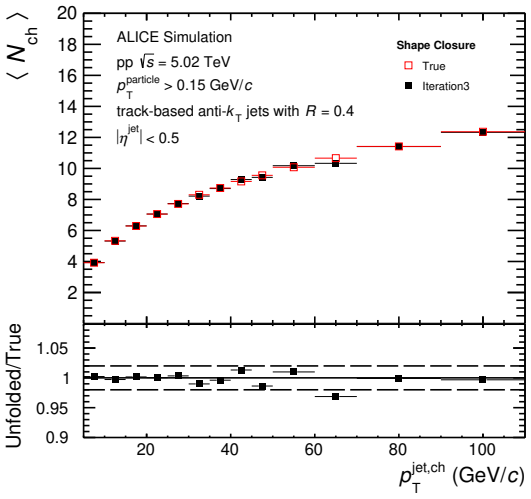

Figure C.27: $\langle N_{\mathrm{ch}} \rangle$ distributions in minimum bias pp collisions: shape closure (iteration 3).

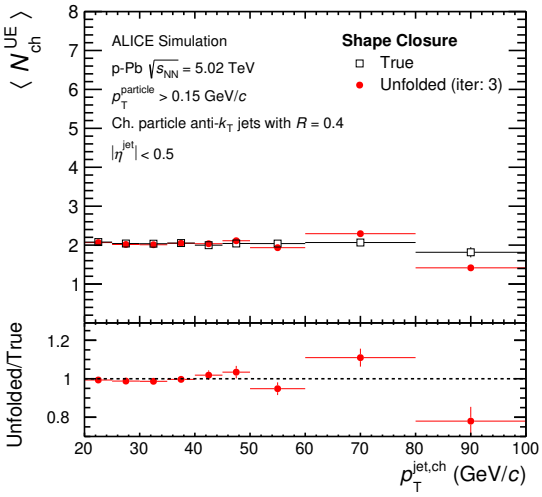

Figure C.28: $\langle N_{\mathrm{ch}} \rangle$ distributions in minimum bias p–Pb collisions: shape closure (iteration 3).

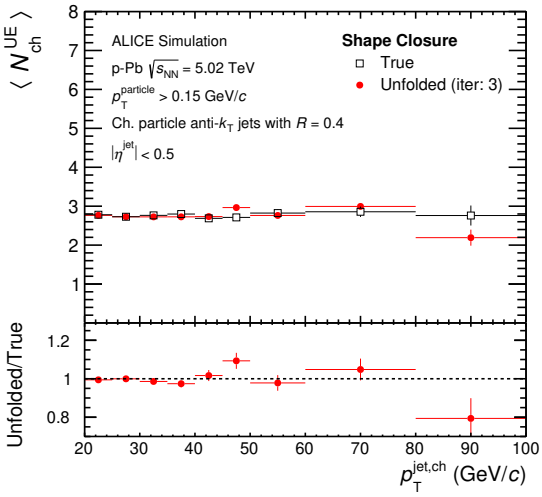

Figure C.29: $\langle N_{\mathrm{ch}} \rangle$ distributions in 0–20% central p–Pb collisions: shape closure (iteration 3).

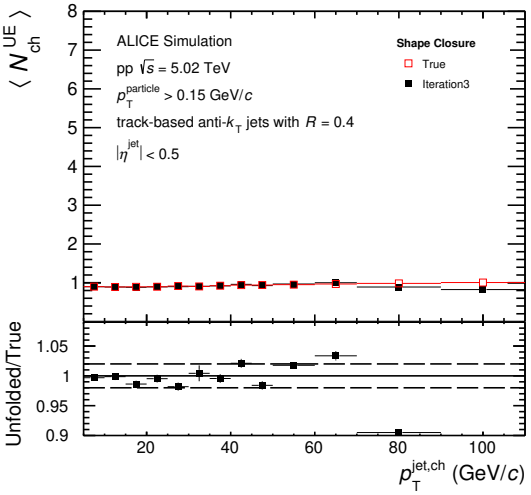

Figure C.30: $\langle N_{\mathrm{ch}} \rangle$ distributions in minimum bias pp collisions: shape closure (iteration 3).

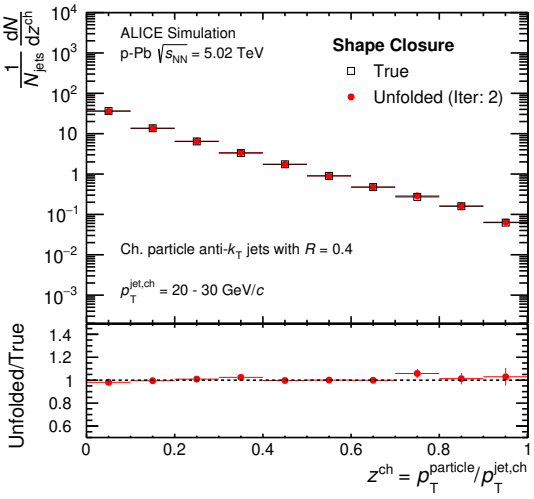

Figure C.31: z^{ch} distributions for leading jet p_{T} = 20–30 GeV/c. in minimum bias p–Pb collisions: shape closure (iteration 2).

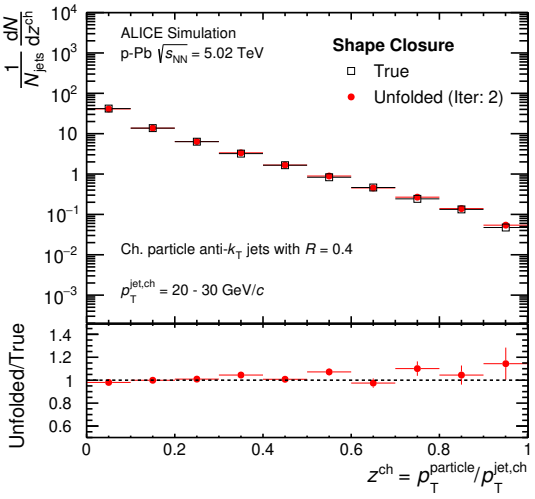

Figure C.32: z^{ch} distributions for leading jet p_{T} = 20–30 GeV/c. in 0–20% central p–Pb collisions: shape closure (iteration 2).

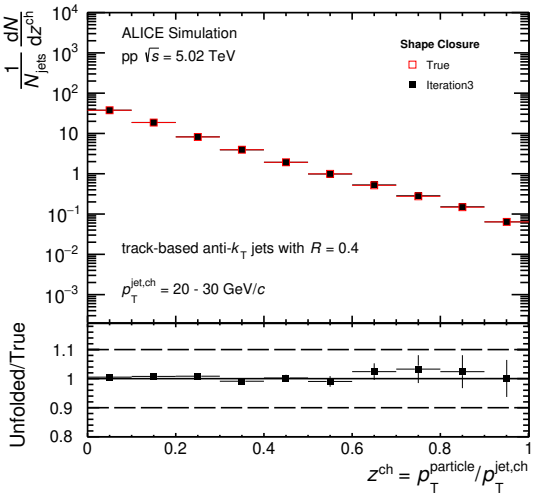

Figure C.33: z^{ch} distributions for leading jet p_{T} = 20–30 GeV/c. in minimum bias pp collisions: shape closure (iteration 3).

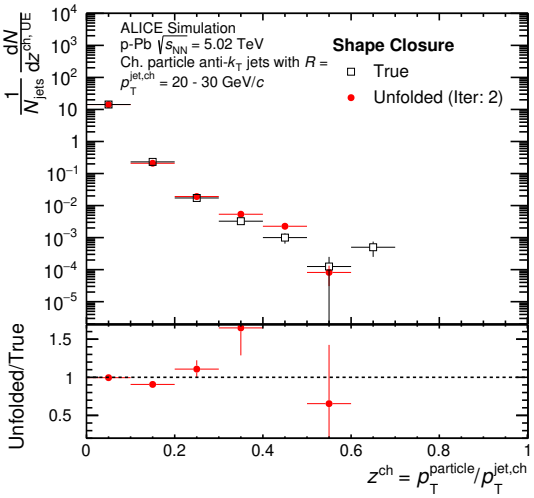

Figure C.34: UE contribution to z^{ch} distributions for leading jet $p_{\mathrm{T}} = 20$–30 GeV/c. in minimum bias p–Pb collisions: shape closure (iteration 2).

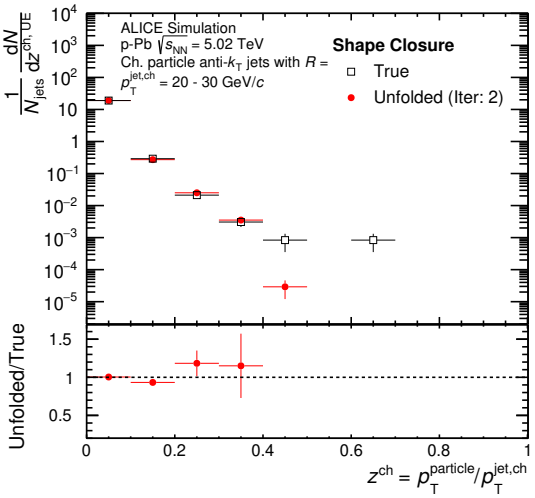

Figure C.35: UE contribution to z^{ch} distributions for leading jet $p_{\mathrm{T}} = 20$–30 GeV/c. in 0–20% central p–Pb collisions: shape closure (iteration 2).

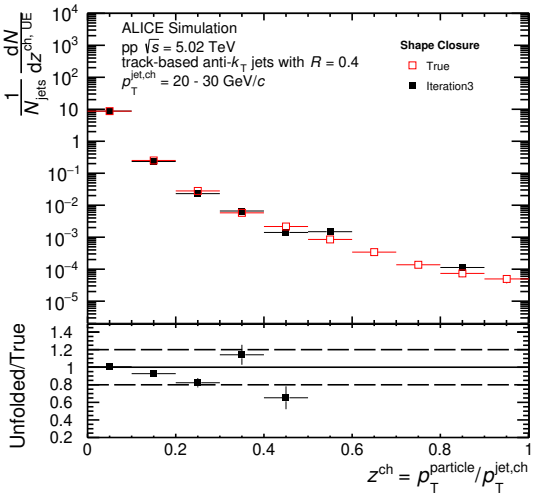

Figure C.36: UE contribution to z^{ch} distributions for leading jet $p_{\mathrm{T}} = 20$–30 GeV/c. in minimum bias pp collisions: shape closure (iteration 3).

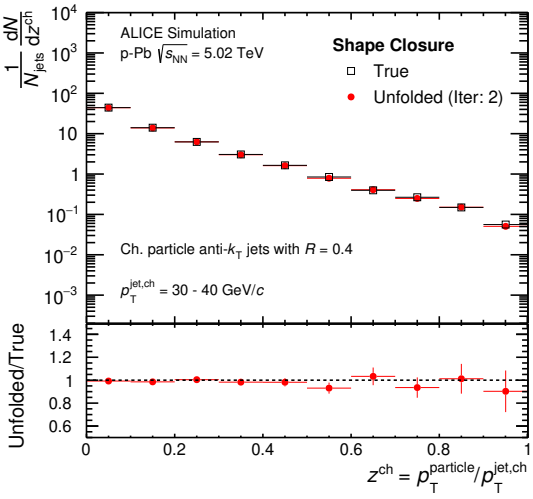

Figure C.37: z^{ch} distributions for leading jet p_T = 30–40 GeV/c. in minimum bias p–Pb collisions: shape closure (iteration 2).

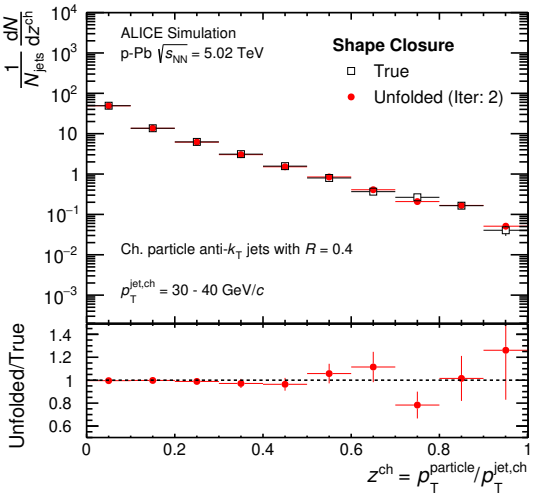

Figure C.38: z^{ch} distributions for leading jet p_T = 30–40 GeV/c. in 0–20% central p–Pb collisions: shape closure (iteration 2).

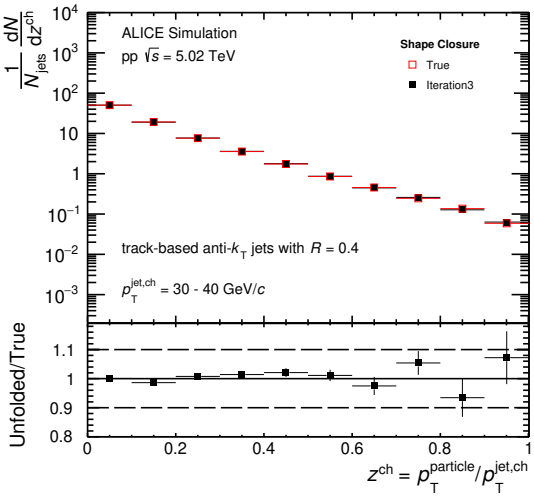

Figure C.39: z^{ch} distributions for leading jet p_T = 30–40 GeV/c. in minimum bias pp collisions: shape closure (iteration 3).

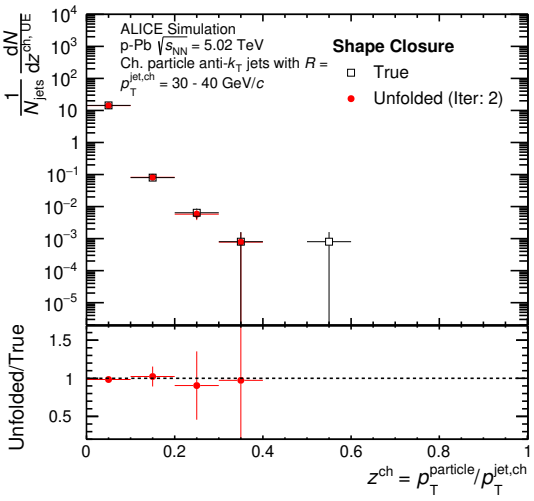

Figure C.40: UE contribution to z^{ch} distributions for leading jet $p_T = 30$–40 GeV/c. in minimum bias p–Pb collisions: shape closure (iteration 2).

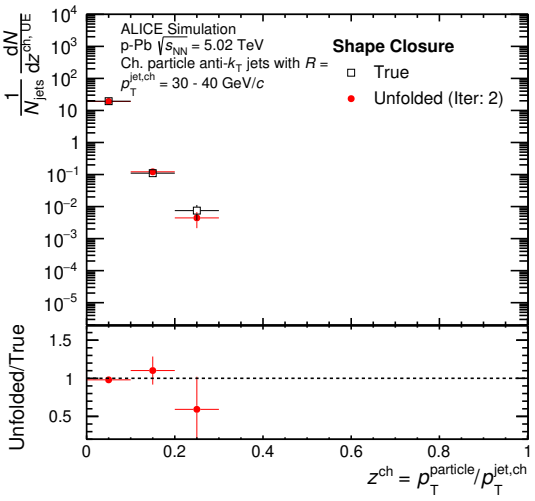

Figure C.41: UE contribution to z^{ch} distributions for leading jet $p_T = 30$–40 GeV/c. in 0–20% central p–Pb collisions: shape closure (iteration 2).

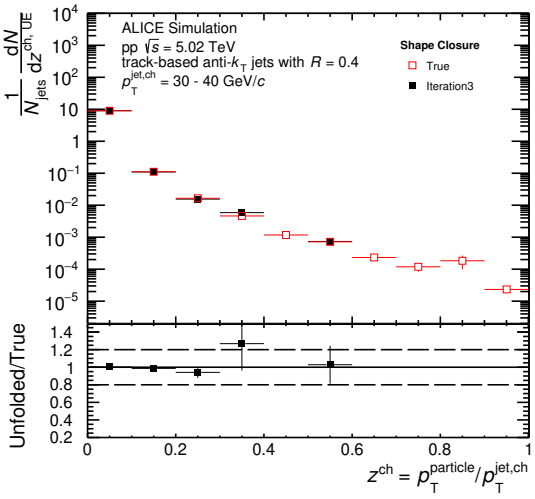

Figure C.42: UE contribution to z^{ch} distributions for leading jet $p_T = 30$–40 GeV/c. in minimum bias pp collisions: shape closure (iteration 3).

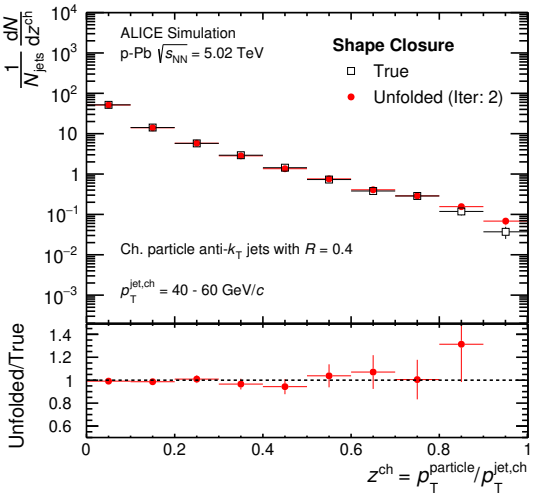

Figure C.43: z^{ch} distributions for leading jet p_{T} = 40–60 GeV/c. in minimum bias p–Pb collisions: shape closure (iteration 2).

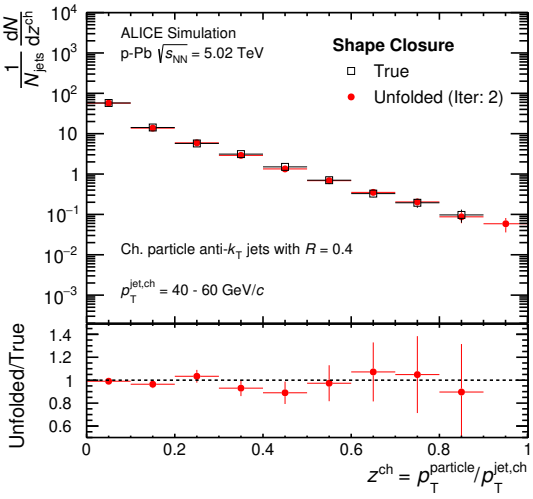

Figure C.44: z^{ch} distributions for leading jet p_{T} = 40–60 GeV/c. in 0–20% central p–Pb collisions: shape closure (iteration 2).

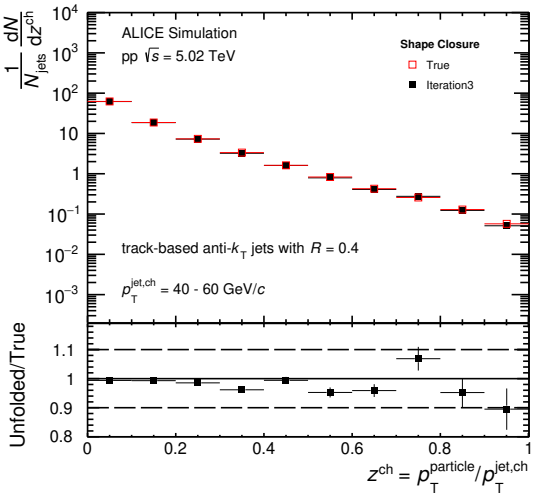

Figure C.45: z^{ch} distributions for leading jet p_{T} = 40–60 GeV/c. in minimum bias pp collisions: shape closure (iteration 3).

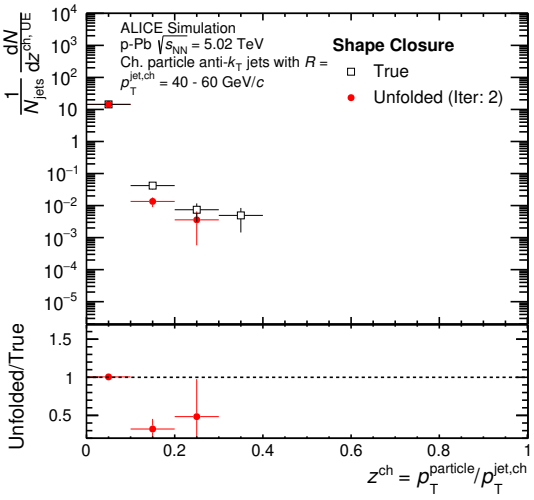

Figure C.46: UE contribution to z^{ch} distributions for leading jet $p_T = 40$–60 GeV/c. in minimum bias p–Pb collisions: shape closure (iteration 2).

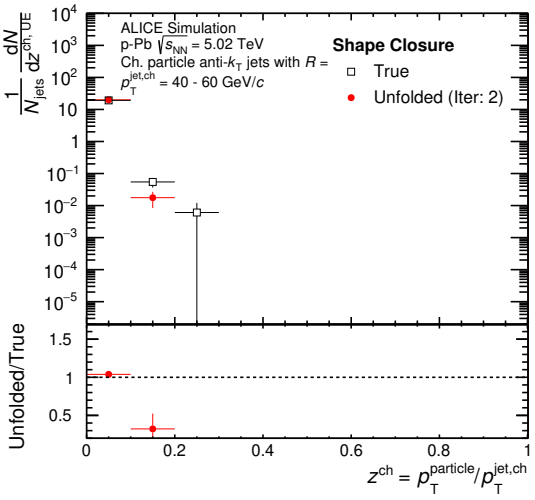

Figure C.47: UE contribution to z^{ch} distributions for leading jet $p_T = 40$–60 GeV/c. in 0–20% central p–Pb collisions: shape closure (iteration 2).

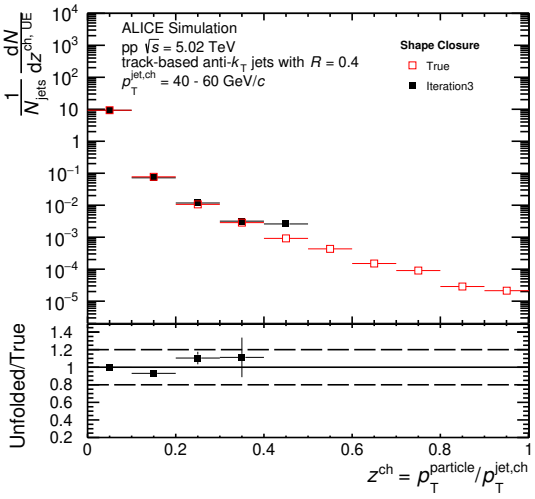

Figure C.48: UE contribution to z^{ch} distributions for leading jet $p_T = 40$–60 GeV/c. in minimum bias pp collisions: shape closure (iteration 3).

Appendix D

Breakdown of total systematic uncertainties in pp and p–Pb collisions at 5.02 TeV

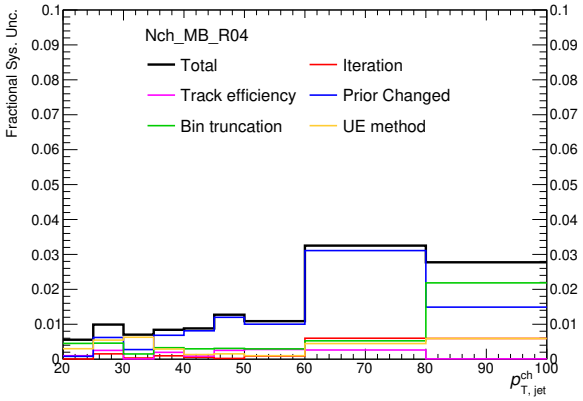

Figure D.1: Breakdown of total systematic uncertainty in $\langle N_{ch} \rangle$ distribution into systematic uncertainties from different sources in minimum bias pp collisions.

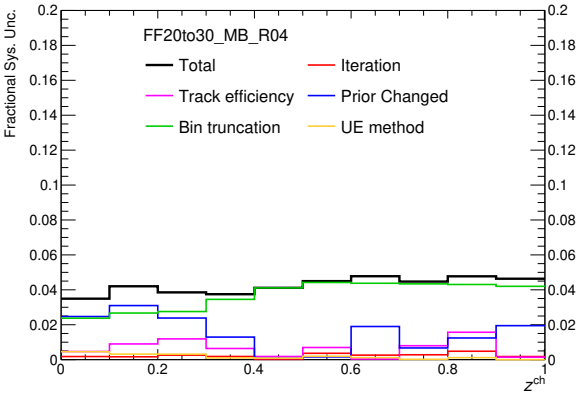

Figure D.2: Breakdown of total systematic uncertainty in z^{ch} distributions for leading jet p_T = 20–30 GeV/c into systematic uncertainties from different sources in minimum bias pp collisions.

D.1 Minimum bias pp

Total systematic uncertainty and its components are shown in Fig. D.1 for $\langle N_{ch} \rangle$ and Figs. D.2-D.4 for fragmentation function. The major contributors are mostly the uncertainties coming from track reconstruction inefficiency and change of prior except for z^{ch} distributions at jet p_T =20 – 30 GeV/c where bin truncation uncertainty dominates at intermediate and high z^{ch}.

D.2 Minimum bias p–Pb

Total systematic uncertainty and its components are shown in Fig. D.5 for $\langle N_{ch} \rangle$ and Figs. D.6-D.8 for fragmentation function. The major contributors are mostly the uncertainties coming from tracking inefficiency and change of prior. For the z^{ch} distributions at the lowest jet p_T range = 20 – 30 GeV/c, the uncertainty due to bin truncation is the dominant one at intermediate and high z^{ch} values, which is expected since the truncated bin at the lower side (10 GeV/c) is very close to this kinematic range.

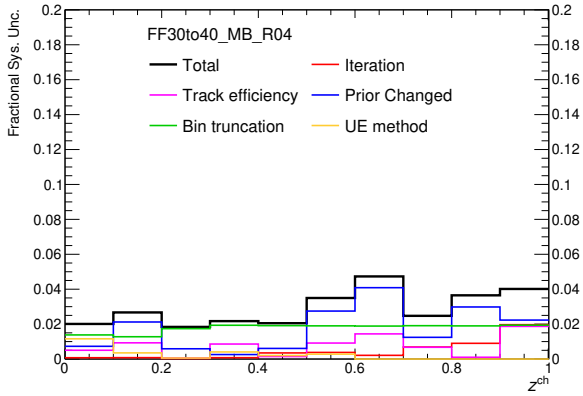

Figure D.3: Breakdown of total systematic uncertainty in z^{ch} distributions for leading jet $p_T = 30$–40 GeV/c into systematic uncertainties from different sources in minimum bias pp collisions.

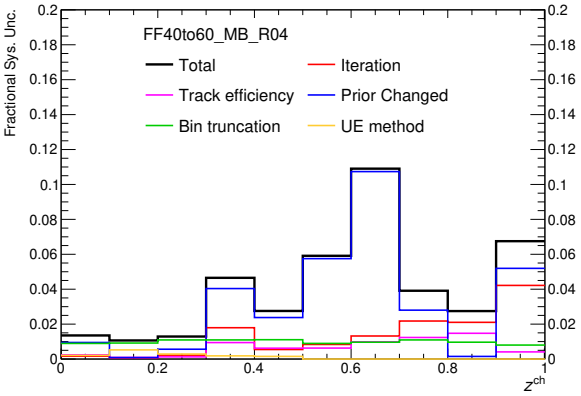

Figure D.4: Breakdown of total systematic uncertainty in z^{ch} distributions for leading jet $p_T = 40$–60 GeV/c into systematic uncertainties from different sources in minimum bias pp collisions.

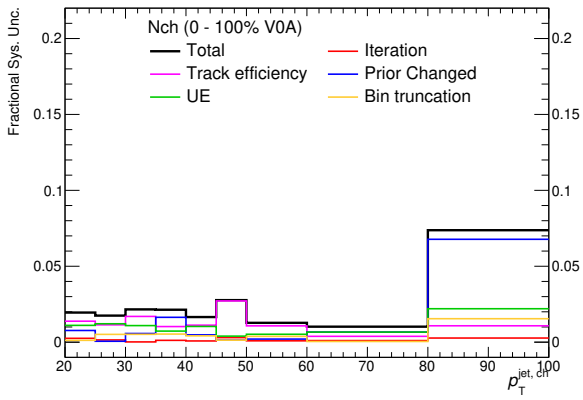

Figure D.5: Breakdown of total systematic uncertainty in $\langle N_{ch} \rangle$ distribution into systematic uncertainties from different sources in minimum bias p–Pb collisions.

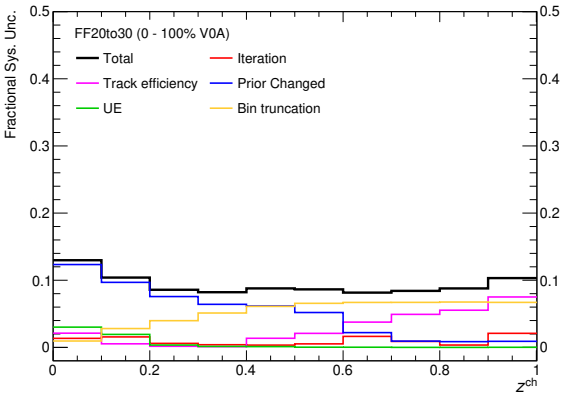

Figure D.6: Breakdown of total systematic uncertainty in z^{ch} distributions for leading jet $p_T = 20$–30 GeV/c into systematic uncertainties from different sources in minimum bias p–Pb collisions.

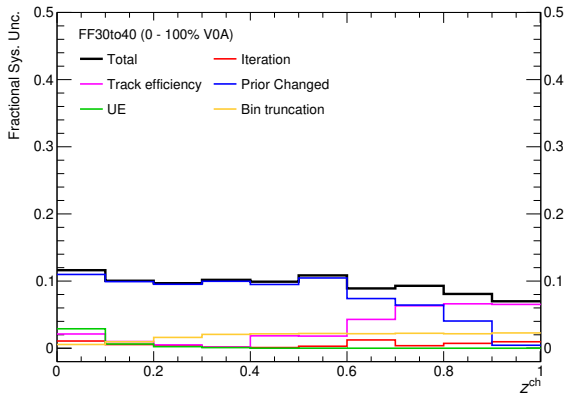

Figure D.7: Breakdown of total systematic uncertainty in z^{ch} distributions for leading jet $p_T = 30$–40 GeV/c into systematic uncertainties from different sources in minimum bias p–Pb collisions.

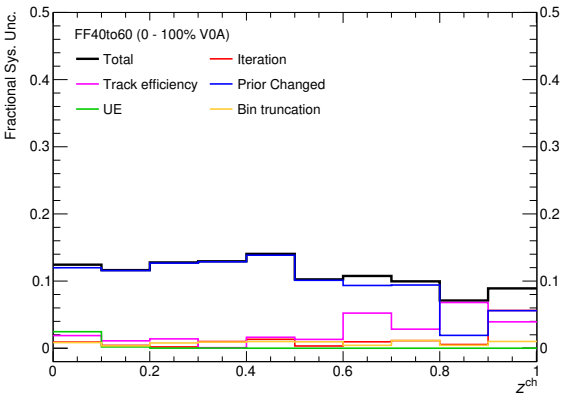

Figure D.8: Breakdown of total systematic uncertainty in z^{ch} distributions for leading jet $p_T = 40$–60 GeV/c into systematic uncertainties from different sources in minimum bias p–Pb collisions.

D.3 0–20% central p–Pb

Total systematic uncertainty and its components are shown in Fig. D.9 for $\langle N_{ch} \rangle$ and Figs. D.10-D.12 for fragmentation function. Like the minimum bias p–Pb case, here the major contributors mostly are the uncertainties due to tracking inefficiency and change of prior except for z^{ch} distributions at jet p_T =20 – 30 GeV/c where bin truncation uncertainty dominates at intermediate and high z^{ch}.

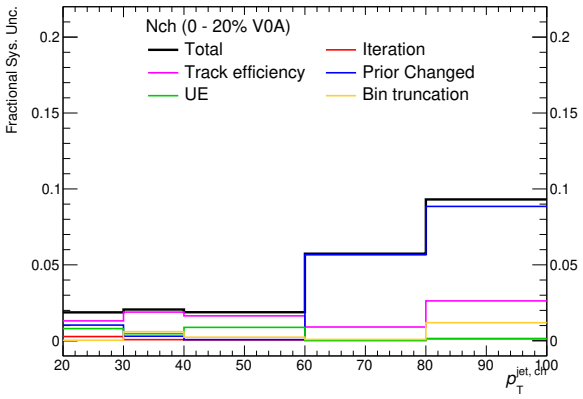

Figure D.9: Breakdown of total systematic uncertainty in $\langle N_{ch} \rangle$ distribution into systematic uncertainties from different sources in 0–20% central p–Pb collisions.

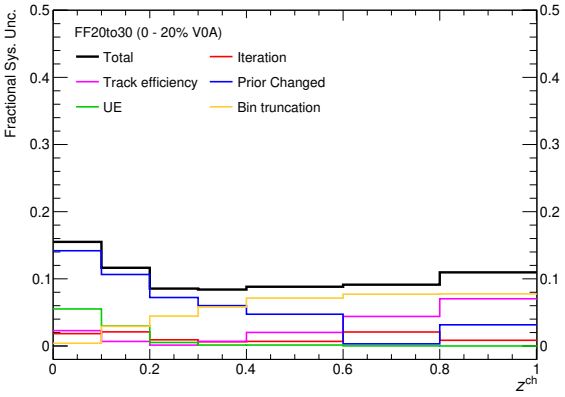

Figure D.10: Breakdown of total systematic uncertainty in z^{ch} distributions for leading jet p_T = 20-30 GeV/c into systematic uncertainties from different sources in 0–20% central p–Pb collisions.

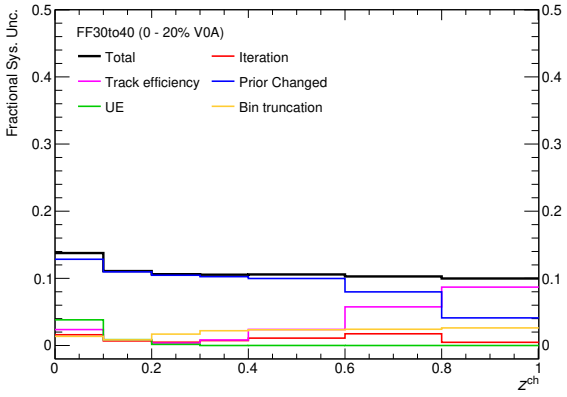

Figure D.11: Breakdown of total systematic uncertainty in z^{ch} distributions for leading jet p_T = 30-40 GeV/c into systematic uncertainties from different sources in 0–20% central p–Pb collisions.

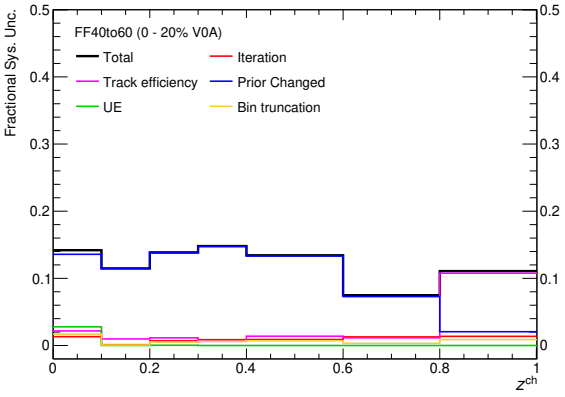

Figure D.12: Breakdown of total systematic uncertainty in z^{ch} distributions for leading jet p_T = 40-60 GeV/c into systematic uncertainties from different sources in 0–20% central p–Pb collisions.

Appendix E

Investigation of jet modification in p–Pb collisions using PYTHIA 8 Angantyr model

The measurements of jet fragmentation (z^{ch}) distributions presented in Chapter 3 have shown jet modification in minimum bias (MB) and central p–Pb collisions compared to minimum bias pp and minimum bias p–Pb collisions, respectively. The magnitude of the jet modification is also found to be maximum for the lowest p_{T}-jets reported (20–30 GeV/c). Interestingly, PYTHIA 8 Angantyr model exhibits similar behavior of jet-p_{T}-dependent modification of jet fragmentation as observed in data, although the model does not incorporate any QGP-medium effect. Therefore, an investigation of this behavior using PYTHIA 8 Angantyr model might help us to understand the possible source(s) leading to jet modification in this model and might also provide us some insights about the similar behavior observed in data if it is not due to the formation of QGP-medium.

Following the prescription of the study presented in Chapter 4, the distributions of jet fragmentation function (z^{ch}) are measured for charged-particle leading jets in minimum bias pp collisions and minimum bias and central p–Pb collisions at $\sqrt{s_{\mathrm{NN}}} = 5.02$ TeV, using PYTHIA 8 Angantyr model for two configurations: 'MPI: ON, CR: ON', and 'MPI: OFF, CR: OFF'. The obtained distributions for jet p_{T} = 20–30 GeV/c are compared between minimum bias p–Pb and pp collisions, as shown in Fig. E.1a and between central and minimum bias p–Pb collisions, as shown in Fig. E.1b. The top panels show the z^{ch} distributions, whereas the ratios of the distributions between different collision systems are shown in the bottom panels. The z^{ch} distributions for the configuration 'MPI: ON, CR: ON' are scaled by a factor of 10 for better visibility.

The main observations are as follows:

1. Significant modifications of jet fragmentation function (z^{ch}) distributions are observed between minimum bias p–Pb and pp collisions and between central and minimum bias p–Pb collisions in presence of MPI and CR effects

2. In both cases, the magnitudes of modification get reduced when the MPI and CR mechanisms are switched OFF

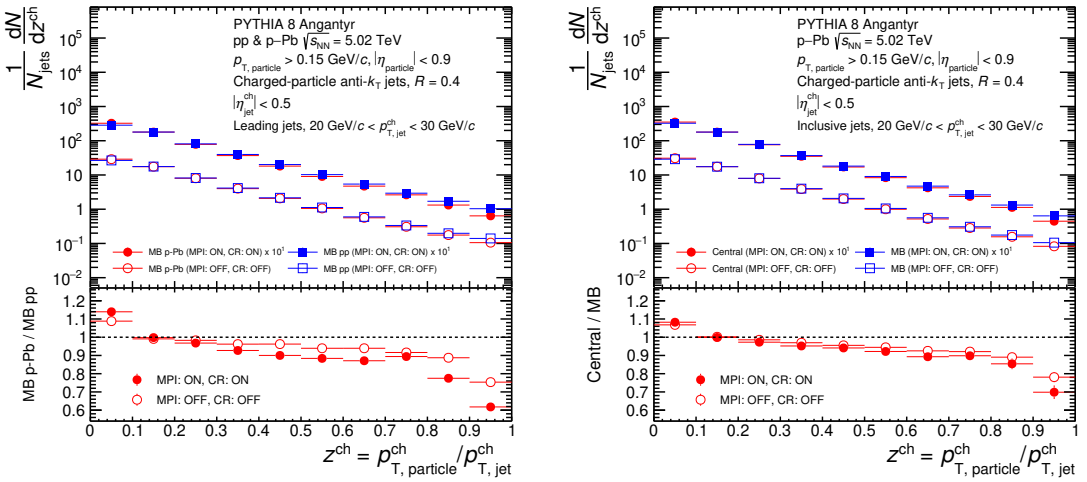

(a) (b)

Figure E.1: Top panels: Charged-particle leading jet fragmentation (z^{ch}) distributions in (a) minimum bias pp and p–Pb collisions and (b) minimum bias and central p–Pb collisions at $\sqrt{s_{NN}} = 5.02$ TeV using PYTHIA 8 Angantyr model in the interval $20 < p^{ch}_{T,jet} < 30$ GeV/c for 'MPI: ON, CR: ON' and 'MPI: OFF, CR: OFF' configurations. Bottom panels: Ratios of z^{ch} distributions (a) between minimum bias p–Pb and pp collisions and (b) between central and minimum bias p–Pb collisions.

3. Even in absence of MPI and CR effects, there are residual modifications that are not small

It is worth mentioning that the average number of MPIs ($\langle N_{MPI} \rangle$) in minimum bias pp, minimum bias p–Pb, and central p–Pb collisions are found to be 3.3, 7.4, and 10.3, respectively. The observations indicate that multiparton interactions (MPI) and color reconnection (CR) mechanisms are responsible for the observed jet modification in p–Pb collisions, however, only partially. Some other physics mechanisms in PYTHIA 8 Angantyr model might be playing a role here and would be worth exploring for future studies. It is important to note that further investigation of this residual effect with gluon-initiated jets, as performed in Chapter 4 for pp collisions, is not straightforward for p–Pb collisions using the PYTHIA 8 Angantyr model because this model considers several sub-collisions and finally combine them, which makes the matching of the leading jet to its parent parton (gluon or quark), to a certain degree, ambiguous.

Journal reprint

Jet modification in absence of QGP-medium: the role of multiparton interactions and color reconnection*

Jet modification in absence of QGP-medium: the role of multiparton interactions and color reconnection*

Prottoy Das[1†] Abhi Modak[1] Debjani Banerjee[1] Rathijit Biswas[2] Supriya Das[1] Sanjay K. Ghosh[1] Sibaji Raha[1] Sidharth Kumar Prasad[1‡]

[1]Department of Physics, Bose Institute, Kolkata 700091, India
[2]Quark Matter Research Center, Institute of Modern Physics, Chinese Academy of Sciences, Lanzhou 730000, China

Abstract: Recent studies on high-multiplicity events in small collision systems (proton-proton and proton-lead) have drawn considerable research interest toward the possibility of the formation of partonic medium in such systems. One of the important consequences of the formation of dense partonic medium is the quenching of high-momentum final-state particles, resulting in several experimental observations such as suppression in nuclear modification factor $R_{\rm AA}$, modification of jet shape observable $\rho(r)$ and jet fragmentation ($z^{\rm ch}$) distributions, *etc*. In this work, we study $\rho(r)$ and $z^{\rm ch}$ for inclusive charged-particle jets in proton-proton (pp) collisions at $\sqrt{s}$ = 13 TeV using the PYTHIA 8 Monash 2013 Monte Carlo simulation. We show that the color reconnection (CR) and multiparton interaction (MPI) mechanisms in PYTHIA 8 can lead to an increased rate of jet production. We also find that the mechanisms of MPI and CR and change in the gluonic contribution in high-multiplicity events result in significant modification of $\rho(r)$ and $z^{\rm ch}$ compared to those in minimum bias events for $10 < p_{\rm T,jet}^{\rm ch} < 20$ GeV/c. We notice a direct connection of $\langle N_{\rm MPI}\rangle$ and gluonic contribution with the amount of modification in $\rho(r)$: the larger the number of MPIs and/or gluonic contribution, the larger the amount of modification of $\rho(r)$.

Keywords: jet modification, PYTHIA, multiparton interaction, color reconnection, gluonic contribution, high-multiplicity

DOI: 10.1088/1674-1137/ad0b6c

I. INTRODUCTION

Experimental observations at RHIC and LHC have revealed that a system of deconfined quarks and gluons, known as Quark-Gluon Plasma (QGP), is formed in heavy-ion (AA) collisions at relativistic speeds [1−7]. A conclusive statement about the formation of QGP requires a comparison of measurements in heavy-ion collisions with those from proton-proton (pp) and proton-nucleus (pA) collisions at similar energies, where conventionally no such system is expected to be present. Among others, jet quenching and collective effects are the two most striking observations whose presence in AA and absence in pp and pA collisions provide strong evidence of QGP formation [8]. In high-energy elementary, hadronic, and nucleus-nucleus collisions, the processes with large (at a scale >> $\lambda_{\rm QCD}$) momentum transfer (large Q^2) result in two back-to-back high-momentum partons (quarks and gluons). These high-momentum partons lose their virtuality by producing a collimated cascade of partons in the direction of the parent parton. Eventually, all partons manifest themselves into collimated showers of experimentally detectable hadrons, known as jets, via soft hadronization processes. The jet production and its properties are well described by the theory of perturbative Quantum Chromodynamics (pQCD) in pp collisions [9−11].

Although theoretical calculations [12−15] have hinted towards the possibility of collective effects in small collision systems long ago, with the onset of LHC, several experimental observations and model calculations could actually find signatures indicating the existence of these effects in pp and pA collisions, especially at high multiplicities [16−28]. Interestingly, no jet quenching has been reported in such events [29, 30]. It has, therefore, drawn an immense interest in the study and understand-

Received 8 June 2023; Accepted 6 November 2023; Published online 7 November 2023

* D. Banerjee acknowledges the Inspire Fellowship research grant (DST/INSPIRE Fellowship/2018/IF180285)

† E-mail: dasprottoy000@gmail.com

‡ E-mail: sprasad@cern.ch

ing of the dynamics of small collision systems on both theoretical and experimental fronts. Recently, several efforts have been made to understand the sources for the production of high-multiplicity events and their effects on the final-state particles [31−64]. It is suggested in Refs. [52−54, 65] that the existence of color-glass-condensate in the initial state can give rise to large particle production. The phenomena such as color reconnections (CR) between the outgoing partons and multiparton interactions (MPI) are also found to explain the production of a large number of final-state particles in pp collisions [27, 39, 41, 42]. Ample signatures such as radial flow-like effects on spectra, ridge-like structure, mass ordering of elliptic flow (v_2), strangeness enhancement, *etc*., which are traditionally explained through the presence of hot and dense QGP medium in AA collisions, are also observed experimentally in high-multiplicity pp and pA collisions at LHC energies. Surprisingly, the inclusive jet nuclear modification factor ($R_{\rm AA}$) is found to be unity, thereby challenging the notion of medium formation in these systems. In AA collisions, among others, differential jet observables such as jet shape ($\rho(r)$) and jet fragmentation function ($z^{\rm ch}$) are studied to understand the jet-medium interaction in detail [66−72]. Jets are found to get softer and broader in the presence of a medium due to elastic and inelastic collisions. Let us now concentrate on the present status of pp studies. Interestingly, recent ALICE measurement [73] of jet fragmentation function ($z^{\rm ch}$) in pp collisions at $\sqrt{s}$ = 13 TeV shows significant modification at high multiplicity compared to minimum bias events. This is also reproduced by PYTHIA 8 Monash 2013, where no QGP medium effect is implemented. In Ref. [74], MPI and CR mechanisms of PYTHIA 8 are shown to modify jet shape ($\rho(r)$) distributions in high-multiplicity pp collisions; however, the exact interplay between these mechanisms causing the jet modification has not been studied yet. Moreover, the modification of different jet observables may also have different degrees of sensitivity on the nature of the parent parton. It is, therefore, of utmost importance to understand in detail and quantify various contributions from the individual sources leading to the jet modification in PYTHIA 8 in the absence of the medium.

In this work, we study the jet shape observable $\rho(r)$ and jet fragmentation function ($z^{\rm ch}$) in minimum bias and high-multiplicity event classes using the PYTHIA 8 Monash 2013 MC event generator. The study is performed in the presence and absence of two important mechanisms in PYTHIA 8, CR, and MPI (which are found to explain some of the experimentally observed flow-like features in high-multiplicity pp collisions [27, 39, 41, 42]). To understand the sensitivity of $\rho(r)$ and $z^{\rm ch}$ on the nature of the parton, the gluon-initiated jets and their contributions to the total inclusive jets are estimated, and associated effects on these observables are studied. The effect of multiparton interactions is also studied exclusively by using event samples with different numbers of MPIs. This study will help us identify and understand the impacts of MPI, CR, and gluonic contribution on $\rho(r)$ and $z^{\rm ch}$ distributions.

The paper is organized as follows. The details of the analysis and PYTHIA 8 simulation are discussed in Sec. II. Section III describes the observable used in this study, and the underlying event estimation technique is detailed in Sec. IV. The obtained results in this work are discussed in Sec. V. Finally, we conclude with a summary in Sec. VI.

II. PYTHIA SIMULATION AND ANALYSIS DETAILS

This study is performed on events generated using PYTHIA 8 (version 8.219) Monash 2013 [75]. PYTHIA 8 is a multiparton interaction-based pQCD-inspired Monte Carlo event generator widely used for hadronic collisions. It performs transverse-momentum-ordered ($p_{\rm T}$-ordered) parton showering, which interleaves the entire perturbative evolution (initial state radiation (ISR), final state radiation (FSR), and MPI), and the angular ordering is imposed by an additional veto [76, 77]. It also includes color reconnection mechanism [78, 79]. Hadronization in PYTHIA 8 proceeds via string breaking as described by the Lund string model [80]. The Monash 2013 tune is based on a large set of LHC distributions, starting from a careful comparison and tuning to LEP data. The PDF used is the NNPDF2.3 [81] QCD+QED LO with $\alpha_s(M_Z) = 0.130$.

MPI is a natural consequence of the composite structure of the colliding hadrons, leading to several parton-parton interactions occurring in one hadron-hadron collision (the schematic is shown in Fig. 1) and is implemented in PYTHIA 8 through a single unified framework [82] that incorporates both soft and hard QCD MPI processes [83].

The implementation of the color reconnection mechanism in PYTHIA 8 is schematically illustrated in Fig. 2. The connection between the outgoing partons and the beam remnants through color strings in the case of a single hard scattering is shown in Fig. 2 (a). A second hard scattering (Fig. 2 (b)) can be naively expected to give rise to two new strings connected to the beam remnants. This would result in a proportional increase in multiplicity; however, to successfully fit the data (see Ref. [83] and references therein), it is instead assumed that the partons are color reconnected so that the total string length gets minimized (Fig. 2 (c)).

MPIs occurring in a hadronic collision lead to the creation of an environment having several high-momentum partons along with the soft ones in a small region (the overlap area of the colliding hadrons), leading to high-

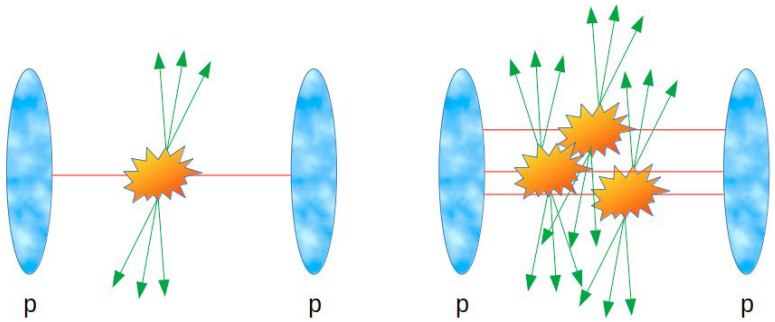

Fig. 1. (color online) Single hard scattering (left) and multiple hard scatterings, *i.e.*, MPI (right), occurring in a single proton-proton collision.

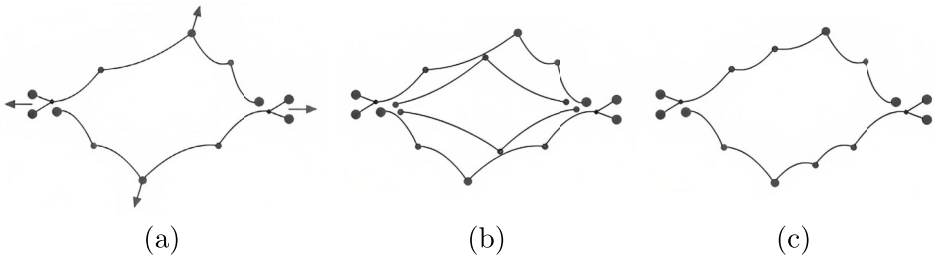

Fig. 2. Illustration of the color reconnection mechanism in PYTHIA 8 (image directly extracted from Ref. [83]). (a) The outgoing gluons are color-connected to the projectile and target beam remnants. (b) A second hard scattering with two new strings connected to the beam remnants. (c) Color reconnected partons minimizing the total string length.

multiplicity events. The evolution of the scattered outgoing partons to final-state collimated hadrons (jets) via fragmentation and hadronization in such an environment is expected to be different compared to the situation with no MPI (only one hard scattering per hadronic collision), which could affect the differential jet shape properties. The fragmentation of independent hard scatterings (MPIs) becomes correlated due to the color reconnection mechanism [39] described earlier and is, therefore, expected to further modify the differential jet shape properties.

For this study, about 1000 million minimum bias (MB) inelastic events are generated for pp collisions at $\sqrt{s}$ = 13 TeV using PYTHIA 8 Monash 2013 for each of the three following configurations:

- MPI: OFF, CR: OFF – In this configuration, both multiparton interaction and color reconnection mechanisms of PYTHIA 8 are absent in the process of event generation

- MPI: ON, CR: OFF – The multiparton interactions are present; however, the color reconnection mechanism is absent in the simulation process in this configuration

- MPI: ON, CR: ON – Events are generated in the presence of both MPI and CR mechanisms of PYTHIA 8

The configuration 'MPI: OFF, CR: ON' is not that important for this study as the effect of color reconnection on the number of produced particles is small in the absence of MPI. High-multiplicity (HM) event class is selected as the one that contains 5% of the total events with the highest multiplicities, based on the number of charged particles produced in the pseudorapidity regions $2.8 < \eta < 5.1$ and $-3.7 < \eta < -1.7$. The above selection corresponds to the number of charged particles to be greater than 24, 127, and 83 for 'MPI: OFF, CR: OFF', 'MPI: ON, CR: OFF', and 'MPI: ON, CR: ON' configurations, respectively. The choice of pseudorapidity range is guided by the experimentally available coverage range of forward detectors [84] used for multiplicity selection. The current study is performed using the particles produced at mid-rapidity to avoid autocorrelation. The generated particles are subjected to the kinematic cuts: $|\eta^{\rm ch}_{\rm particle}| < 0.9$ and $p^{\rm ch}_{\rm T,particle} > 0.15$ GeV/c. The restriction on η has given access to the particles only in the mid-rapidity region, whereas the condition for the particles to have $p_{\rm T}$ as low as 0.15 GeV/c has the significance of allowing us to test perturbative and non-perturbative aspects of jet production. The particle selection criteria are chosen to match experimental conditions [10, 85].

Jets are reconstructed with charged particles using an infrared- and collinear-safe sequential recombination anti-$k_{\rm T}$ algorithm [86] from the FastJet package [87] with jet resolution parameter R ($= \sqrt{(\Delta\eta)^2 + (\Delta\varphi)^2}$) = 0.4. Jets are accepted for the study if $|\eta^{\rm ch}_{\rm jet}| < 0.5$ (0.9 - R) and jet transverse momentum $p^{\rm ch}_{\rm T,jet} > 10$ GeV/c.

To select gluon-initiated jets, one needs to properly

match the hard-scattered partons in an event to the reconstructed charged-particle jets using some effective algorithm. We have taken into consideration an algorithm based on the "distance of closest approach". In this algorithm, first, we identify the two outgoing hard scattered partons and their flavors (quark or gluon) using the information from the PYTHIA event output. In the same event, we then determine unique pairs between these initial hard-scattered partons and reconstructed jets in such a way that the geometrically closest jet is matched to the parent parton. The jets having $p_{\rm T}$ less than 20% of the matched parton $p_{\rm T}$ are rejected to avoid fake jets. This cutoff of 20% for rejecting fake jets is also varied up to 50% and no significant change in the final results is observed. The reconstructed jets matched to parent gluons are considered gluon-initiated jets.

III. OBSERVABLES

In this work, we study the differential transverse momentum distribution of charged-particle jets ($\frac{1}{N_{\rm events}}\frac{{\rm d}^2N}{{\rm d}p_{\rm T}{\rm d}\eta}$; where $N_{\rm events}$ is the number of events, and N is the number of jets), differential jet shape ($\rho(r)$), and jet fragmentation function ($z^{\rm ch}$) for charged-particle jets.

The differential jet shape is related to the radial distribution of jet transverse momentum density inside the jet cone about the jet axis and is defined as:

$$\rho(r)=\frac{1}{\Delta r}\frac{1}{N_{\rm jets}}\sum_{i=1}^{N_{\rm jets}}p_{\rm T}^{i}(r-\Delta r/2,r+\Delta r/2)/p_{\rm T,jet}^{\rm ch} \quad (1)$$

where r is the distance from the jet axis, and $p_{\rm T}^{i}(r-\Delta r/2,r+\Delta r/2)$ denotes the summed $p_{\rm T}$ of all particles of i-th jet inside the annular ring between $r-\Delta r/2$ and $r+\Delta r/2$.

The jet fragmentation function represents the fraction of the jet transverse momentum carried by the constituent charged particles and is sensitive to the details of the parton showering process. It is defined as:

$$z^{\rm ch}=\frac{p_{\rm T,particle}^{\rm ch}}{p_{\rm T,jet}^{\rm ch}} \quad (2)$$

The study of $\rho(r)$ and $z^{\rm ch}$ is very important since these observables are sensitive to both the fragmentation process and the nature of the initial hard-scattered partons (quark or gluon) [88−92]. In the presence of the medium, jet constituents lose their energy via inelastic and elastic scatterings due to jet-medium interaction, and their mean opening angle also becomes larger. This results in the steepening of $z^{\rm ch}$ and flattening of $\rho(r)$ distributions, leading to the broadening and softening of jets in medium compared to those in vacuum. The observables $\rho(r)$ and $z^{\rm ch}$ are sensitive to the degree of jet modification in heavy-ion collisions. In the case of high-multiplicity pp and p–Pb collisions, these observables might be potentially capable of verifying the conjecture of medium formation in small collision systems [91, 92].

IV. UNDERLYING EVENT

Reconstructed jets are contaminated by the underlying event (UE) which can be defined as the charged particles except those coming from the fragmentation of hard-scattered partons. The UE mostly consists of particles from the beam-beam remnants, initial and final state radiations, and contributions from MPIs [93]. The empirical models used for the description of the non-perturbative aspects in the evolution of a high-energy scattering event do not allow to clearly distinguish particles originating from hard processes and the underlying event [94]. The UE is estimated from circular regions transverse to the measured jet cones, known as the perpendicular cone (PC) method, in each event. The size of these circular regions is defined by the radius of the jet $R=0.4$ at the same pseudorapidity as the considered jet but offset at an azimuthal angle $\Delta\varphi=\pm\pi/2$ relative to the jet axis. For the estimation of UE contribution to the $\rho(r)$ distribution, annular rings of the same size as those inside the jet cones are considered inside each of the perpendicular circular regions. The UE contributions to the $\rho(r)$ and $z^{\rm ch}$ distributions are respectively calculated using the following expressions:

$$\rho^{\rm UE}(r)=\frac{1}{\Delta r}\frac{1}{N_{\rm PC}}\sum_{i=1}^{N_{\rm PC}}p_{\rm T}^{i}(r-\Delta r/2,r+\Delta r/2)/p_{\rm T,jet}^{\rm ch}, \quad (3)$$

where $N_{\rm PC}$ is the number of perpendicular cones, r is the distance from the axis of the perpendicular cone, and $p_{\rm T}^{i}(r-\Delta r/2,r+\Delta r/2)$ denotes summed $p_{\rm T}$ of all particles inside the annular ring between $r-\Delta r/2$ and $r+\Delta r/2$ and

$$z^{\rm ch,UE}=\frac{p_{\rm T,particle}^{\rm ch,PC}}{p_{\rm T,jet}}, \quad (4)$$

where $p_{\rm T,particle}^{\rm ch,PC}$ is the $p_{\rm T}$ of a particle in the perpendicular cone. The subtraction of UE is performed on a statistical basis to obtain the corrected distributions.

To perform a systematic check, a random cone (RC) method is also applied to estimate the underlying event contribution in the studied jet observables. In this method, two cones are randomly generated with the same η as the considered jet, but in the expanded transverse region (one cone within $\pi/3<\Delta\varphi<2\pi/3$ and another within $-2\pi/3<\Delta\varphi<-\pi/3$, $\Delta\varphi$ being the difference between the considered jet and the random cone in azimuthal angle φ) with respect to the jet axis, unlike at a fixed value of azi-

muthal angle ($\Delta\varphi = \pm\pi/2$) as in PC method. No significant difference is observed in the UE contribution as compared to the PC method.

V. RESULTS AND DISCUSSION

A. Comparison with experimental data

First, we compare the ALICE data [73] to PYTHIA 8 predictions in Fig. 3, which shows the ratio of charged-particle jet fragmentation distributions for leading jets (jet with the highest $p_{\rm T}$ in an event) in the interval $10 < p^{\rm ch}_{\rm T,jet} < 20$ GeV/c between high-multiplicity and minimum bias event classes in pp collisions at $\sqrt{s}$ = 13 TeV. Similar track and jet selection criteria as in data are applied in PYTHIA 8 for this comparison. However, the event selection is slightly different. In Ref. [73], HM events are selected using the detector level information (based on the two scintillator detectors V0A and V0C in ALICE) both for data and PYTHIA 8 simulation; whereas, in this study, we use the information of final-state particles in the same pseudorapidity coverage as described in Sec. II. In this case, the selected HM event class comprises 0.1% of the total events with the highest multiplicities to match the selection criteria of Ref. [73]. Nonetheless, it is found that, even without implementation of any medium effects, PYTHIA 8 reproduces the jet modification observed in data fairly well. This observation is very interesting and indicates that PYTHIA 8 indeed incorporates underlying physics mechanism(s) which can capture the features of jet modification observed in experimental data. It is, therefore, very important to understand these underlying physics mechanism(s) in PYTHIA 8. We investigate the effect of MPI and CR on the transverse momentum ($p_{\rm T}$) spectra of the charged-particle jets, jet shape ($\rho(r)$), and jet fragmentation function ($z^{\rm ch}$) in MB and HM event classes.

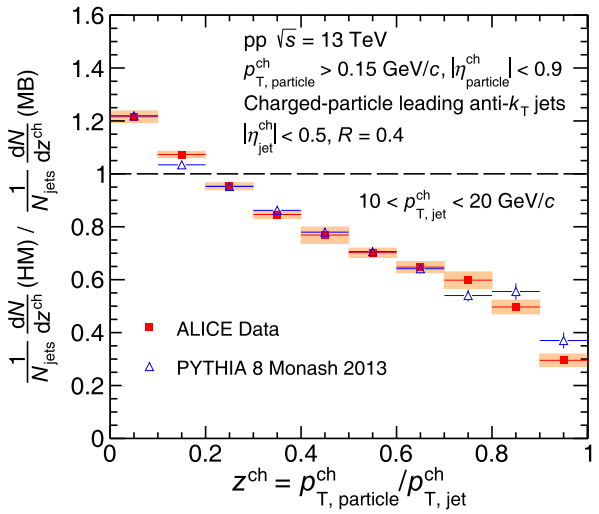

Fig. 3. (color online) Ratio of charged-particle jet fragmentation distributions for leading jets in the interval $10 < p^{\rm ch}_{\rm T,jet} < 20$ GeV/c between high-multiplicity and minimum bias event classes in pp collisions at $\sqrt{s}$ = 13 TeV. The red solid boxes and blue open triangles represent ALICE data and PYTHIA 8 Monash 2013 predictions, respectively. The systematic uncertainty in data is represented by orange bands.

B. Jet $p_{\rm T}$ spectra

We compare the $p_{\rm T}$ spectra of charged-particle jets between 'MPI: ON, CR: ON', 'MPI: ON, CR: OFF', and 'MPI: OFF, CR: OFF' configurations in Fig. 4 for the MB event class. The top panel shows the $p_{\rm T}$ spectra of charged-particle jets, and the bottom panel shows the ratios of spectra in 'MPI: ON, CR: ON' and 'MPI: ON, CR: OFF' configurations with that in 'MPI: OFF, CR: OFF' configuration. It is interesting to observe that the rate of jet production increases when MPI effects are switched ON. Compared to the 'MPI: OFF, CR: OFF' configuration, the rate of jet production increases by about 60% when only MPI is switched ON while it increases to about 86% when CR is switched ON in addition to MPI at low jet $p_{\rm T}$ ($10 - 15$ GeV/c). The observed increase in the rate of jet production decreases with increasing jet $p_{\rm T}$ for both configurations. This is an indication of multiple jet production due to multiparton interactions, which is expected to be more prominent at low jet $p_{\rm T}$ [82].

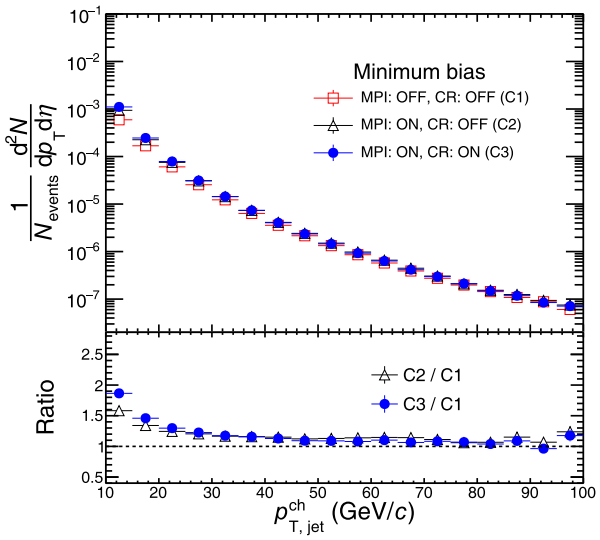

Fig. 4. (color online) Top panel: Inclusive charged-particle jet $p_{\rm T}$ spectra in pp collisions at $\sqrt{s}$ = 13 TeV using PYTHIA 8 Monash 2013 for MB event class. Open red boxes, open black triangles, and solid blue circles correspond to 'MPI: OFF, CR: OFF' (C1), 'MPI: ON, CR: OFF' (C2) and 'MPI: ON, CR: ON' (C3) configurations respectively. Bottom panel: Ratios of $p_{\rm T}$ spectra for the last two configurations (C2 and C3) with respect to the first configuration (C1).

C. Jet shape and jet fragmentation

Figs. 5 (a) and 5 (b) show, respectively, the jet shape ($\rho(r)$) plotted as a function of distance r from the jet axis and jet fragmentation ($z^{\rm ch}$) for inclusive charged-particle jets in the interval $10 < p_{\rm T,jet}^{\rm ch} < 20$ GeV/c for HM and MB event classes in the top panels and their corresponding ratios in the bottom panels. The solid and open markers represent 'MPI: ON, CR: ON' and 'MPI: OFF, CR: OFF' configurations, respectively. Solid markers are scaled by a factor of 10 for better readability. Significant amounts of modifications in jet shape and jet fragmentation function are observed in the HM event class compared to that in the MB event class.

The modification in jet shape is more prominent when CR and MPI effects are switched ON. As evident from the ratio plots of $\rho(r)$ as shown in Fig. 5 (a) (bottom panel), the core of the jet in HM event class is depleted by about 22%, and the energy is redistributed away from the jet axis, resulting in an enhancement in $\rho(r)$ at larger r (> 0.15). Results are shown only up to $r = 0.36$ as the last bin ($r = 0.36$–0.4) is significantly affected by underlying event contribution and statistical fluctuations. The ratio plots of $z^{\rm ch}$ distributions, as shown in Fig. 5 (b) (bottom panel) illustrate a similar observation where the production of high $z^{\rm ch}$ particles is substantially suppressed (by about 40% at $z^{\rm ch} \to 1$) in the HM event class compared to that in MB. We look at the distributions of the number of MPIs ($N_{\rm MPI}$) in both MB and HM event classes with 'MPI: ON, CR: ON' configuration and evaluated their mean values using the expression:

$$\langle N_{\rm MPI} \rangle = \frac{1}{N_{\rm events}} \sum_{i=1}^{N_{\rm events}} N_{\rm MPI}^{i}, \tag{5}$$

where $N_{\rm events}$ is the total number of events in the selected event class, and $N_{\rm MPI}^{i}$ is the number of MPIs in the i-th event, obtained directly from PYTHIA 8. Fig. 6 shows the $N_{\rm MPI}$ distributions for the two event classes. It is important to note that the average number of multiparton interactions in the HM event class is found to be much larger (14.5) compared to that (3.5) in the MB event class.

It is very interesting to notice that the effect of redistribution of energy from the jet core to outer radii and the suppression of high $z^{\rm ch}$ particles are significantly reduced when the CR and MPI effects in PYTHIA 8 are switched OFF. A small depletion of the core and enhancement at larger r for $\rho(r)$ and suppression at high $z^{\rm ch}$ for jet fragmentation distribution are, however, still present. The origin of this residual effect of jet modification in 'MPI: OFF, CR: OFF' configuration can be understood in terms of the difference in the contribution of gluon-initiated jets in HM event class compared to that in MB as discussed below.

Gluon-initiated jets are expected to fragment into more constituents and become softer and broader compared to quark-initiated jets due to their large color factor [95, 96]. By applying the matching procedure described in Sec. II, we identify the charged-particle jets initiated from the initial hard-scattered partons (quark or gluon) and estimate the gluonic contribution as the fraction of gluon-initiated jets out of the inclusive matched jets. We find that the inclusive matched jets in the HM event class contain higher contributions from gluon-initiated jets compared to those in the MB event class. For the jets in the interval $10 < p_{\rm T,jet}^{\rm ch} < 20$ GeV/c ($40 < p_{\rm T,jet}^{\rm ch} < 60$ GeV/c), the contribution from gluon-initiated jets is 86% (81%) in HM while 75% (73%) in the MB event class. This difference in the gluonic contribution in the HM

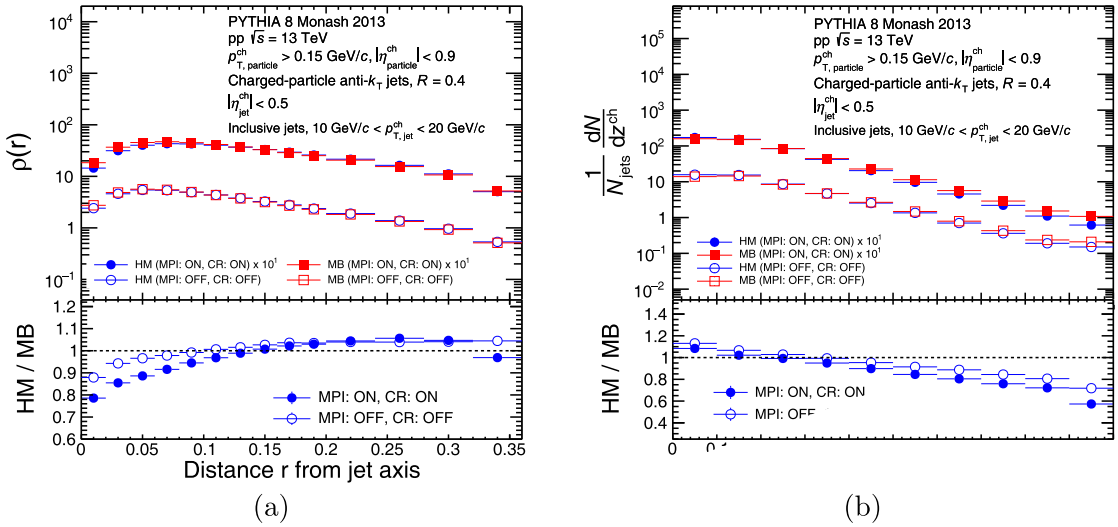

Fig. 5. (color online) Top panels: Distributions of (a) $\rho(r)$ and (b) $z^{\rm ch}$ for inclusive charged-particle jets in pp collisions at $\sqrt{s} = 13$ TeV using PYTHIA 8 Monash 2013 in the interval $10 < p_{\rm T,jet}^{\rm ch} < 20$ GeV/c for 'MPI: ON, CR: ON' and 'MPI: OFF, CR: OFF' configurations. Blue circles and red boxes correspond to HM and MB event classes, respectively. Bottom panels: Ratios of (a) $\rho(r)$ and (b) $z^{\rm ch}$ distributions between HM and MB event classes.

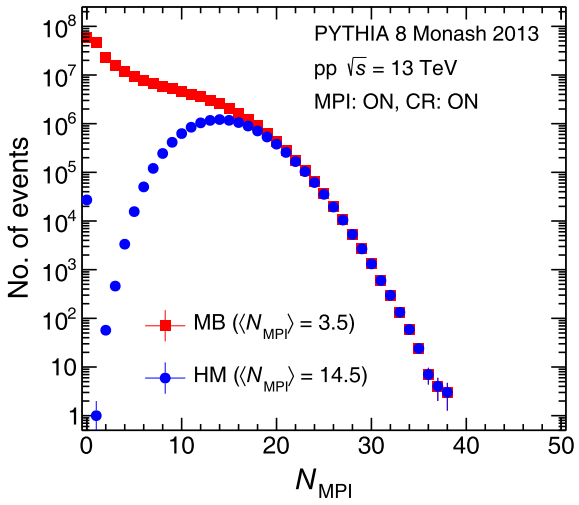

Fig. 6. (color online) Distributions of no. of MPIs for HM and MB event classes in 'MPI: ON, CR: ON' configuration.

event class compared to MB is, therefore, expected to modify the distributions of $\rho(r)$ and z^{ch}. To remove this dependence on the difference in gluonic contribution, we look at the ratios of $\rho(r)$ and z^{ch} distributions between HM and MB event classes for gluon-initiated jets only in the 'MPI: OFF, CR: OFF' configuration, as shown in Fig. 7. We find that the residual effects observed in case of inclusive jets further get reduced and the ratio tends towards unity.

The effect of MPI and CR is dominant at low p_T [82], therefore the observed jet modification is expected to get reduced at higher jet transverse momentum region. Figs. 8 (a) and 8 (b) show respectively the distributions of $\rho(r)$ and z^{ch} in the interval $40 < p_{T,jet}^{ch} < 60$ GeV/c for HM and MB event classes in the top panels and their ratios in the bottom panels. It is found that the amount of jet modification is significantly reduced at higher jet p_T.

We conclude from the above observations (Figs. 5, 7 and 8) that the main sources responsible for modifications of $\rho(r)$ and z^{ch} in PYTHIA 8 in HM event class compared to that in MB event class are the mechanisms of MPI and CR and change in the contribution of gluon-initiated jets in HM event class.

To further understand the effect of MPI on jet modification more accurately in a quantitative manner, we perform a systematic study using only the jet shape observable $\rho(r)$ with event samples having different numbers of MPIs, as discussed in the next subsection. The effect of CR on jet modification is also quantified.

D. Effect of MPI and CR on observed jet modification

To investigate the role of multiparton interactions in the modification of $\rho(r)$, we divide the event samples based on the number of MPIs into four different classes, I, II, III, and IV, containing events with the number of MPIs > 4, 8, 12, and 20, respectively. This study is performed using PYTHIA 8 with default configuration ('MPI: ON, CR: ON') and for inclusive jets in the interval $10 < p_{T,jet}^{ch} < 20$ GeV/c. We estimate the average number of multiparton interactions ($\langle N_{MPI}\rangle$) for different event classes using Eq. (5) and correlate it to the amount of modification observed in $\rho(r)$. Table 1 shows the values of $\langle N_{MPI}\rangle$ for different event classes. The value of $\langle N_{MPI}\rangle$ increases from 9.1 to 22 while going from event class I to IV. Fig. 9 shows the ratios of $\rho(r)$ distributions of different event classes with respect to that in the MB event

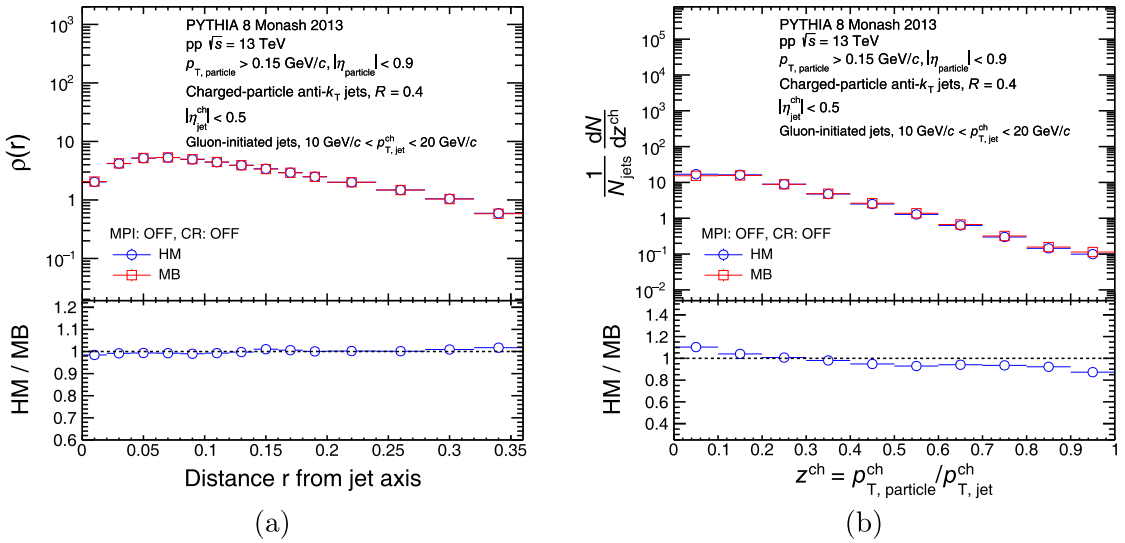

(a) (b)

Fig. 7. (color online) Top panels: Distributions of (a) $\rho(r)$ and (b) z^{ch} for gluon-initiated jets in pp collisions at $\sqrt{s}$ = 13 TeV using PYTHIA 8 Monash 2013 in the interval $10 < p_{T,jet}^{ch} < 20$ GeV/c for 'MPI: OFF, CR: OFF' configuration. Blue circles and red boxes correspond to HM and MB event classes respectively. Bottom panels: Ratios of (a) $\rho(r)$ and (b) z^{ch} distributions between HM and MB event classes.

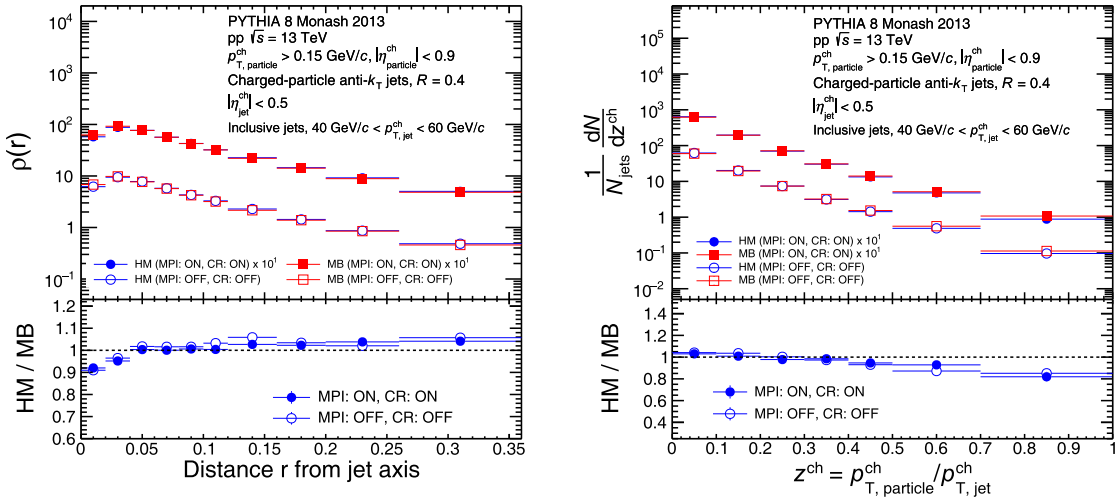

Fig. 8. (color online) Top panels: (a) Inclusive charged-particle jet shape ($\rho(r)$) distributions and (b) jet fragmentation ($z^{\rm ch}$) distributions in pp collisions at $\sqrt{s}$ = 13 TeV using PYTHIA 8 Monash 2013 in the interval 40 < $p_{\rm T,jet}^{\rm ch}$ < 60 GeV/c for 'MPI: ON, CR: ON' and 'MPI: OFF, CR: OFF' configurations. Blue circles and red boxes correspond to HM and MB event classes, respectively. Bottom panels: Ratios of (a) $\rho(r)$ and (b) $z^{\rm ch}$ distributions between HM and MB event classes.

Table 1. Values of $\langle N_{\rm MPI}\rangle$.

Event class	$\langle N_{\rm MPI}\rangle$
MB	3.5
I	9.1
II	12.4
III	15.3
IV	22

class. The amount of modification observed in $\rho(r)$ at the jet core increases for event classes with larger $\langle N_{\rm MPI}\rangle$. For event class IV, where $\langle N_{\rm MPI}\rangle$ = 22, the modification at the jet core is the highest, reaching up to 40%. This observation exclusively supports the existence of a direct connection between the amount of modification of $\rho(r)$ and the number of MPIs in PYTHIA 8.

To quantify the effect of CR, we compare the $\rho(r)$ distributions for 'MPI: ON, CR: ON' and 'MPI: ON, CR: OFF' configurations with 'MPI: OFF, CR: OFF' configuration in one event class (MB) for inclusive jets in the interval 10 < $p_{\rm T,jet}^{\rm ch}$ < 20 GeV/c as shown in Fig. 10. Compared to 'MPI: OFF, CR: OFF' configuration, about 26% (7%) of modification of jet core, r = 0−0.02 (outer region, r = 0.24−0.28) is observed when only MPI is switched ON while the modification increases to 33% (16%) when CR is switched ON in addition to MPI.

E. Effect of change in gluonic contribution on observed jet modification

To understand exclusively the effect of change in gluonic contribution on jet modification, we study $\rho(r)$

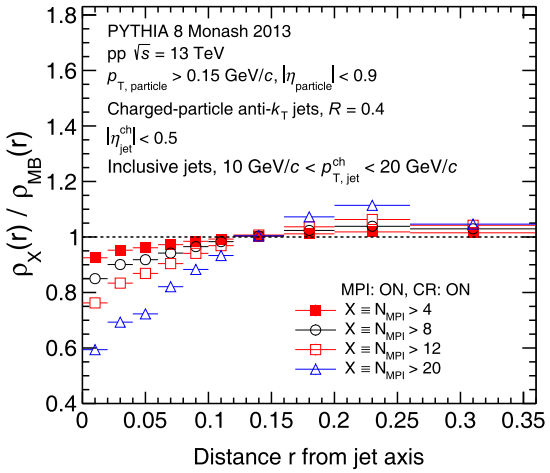

Fig. 9. (color online) The ratios of $\rho(r)$ distributions of different event classes (I: red solid box, II: black open circle, III: red open box, IV: blue open triangle) with respect to that in MB event class.

distribution in the interval 10 < $p_{\rm T,jet}^{\rm ch}$ < 20 GeV/c for jet samples containing different fractions of gluon-initiated jets. We perform this study using PYTHIA 8 with default configuration ('MPI: ON, CR: ON'). We first consider inclusive matched jets from MB events as sample-I (where the gluonic contribution is 81.2%); then, we randomly remove 10%, 20%, and 30% of gluon-initiated jets from sample-I to obtain sample-II, sample-III, and sample-IV respectively which correspond to 79.6%, 77.6% and 75.1% gluonic contributions in inclusive matched jets. To illustrate the sensitivity of jet modification to the change in the fraction of gluon-initiated jets, we study the ratio of

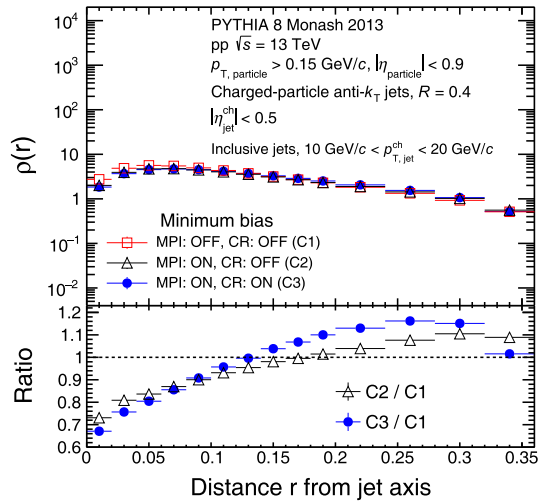

Fig. 10. (color online) Top panel: Inclusive charged-particle jet shape ($\rho(r)$) distributions in pp collisions at $\sqrt{s}$ = 13 TeV using PYTHIA 8 Monash 2013 in the interval $10 < p_{\mathrm{T,jet}}^{\mathrm{ch}} < 20$ GeV/c in MB event class. Open red boxes, open black triangles, and solid blue circles correspond to 'MPI: OFF, CR: OFF' (C1), 'MPI: ON, CR: OFF' (C2) and 'MPI: ON, CR: ON' (C3) configurations respectively. Bottom panel: Ratios of $\rho(r)$ distributions for the last two configurations (C2 and C3) with respect to the first configuration (C1).

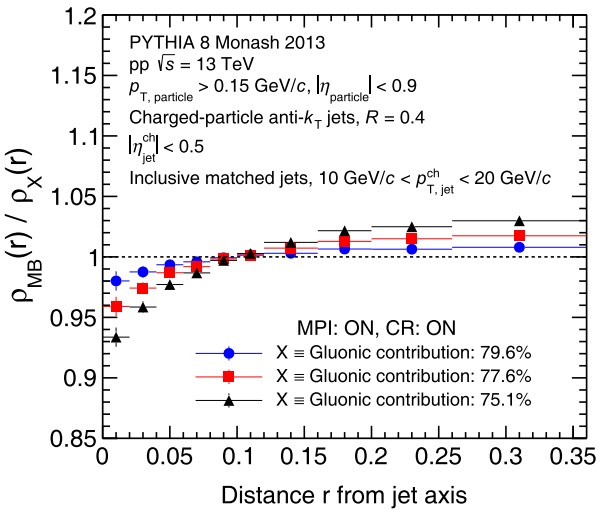

Fig. 11. (color online) The ratios of $\rho(r)$ distributions obtained from sample-II, sample-III, and sample-IV to that in sample-I (MB) in the 'MPI: ON, CR: ON' configuration.

$\rho(r)$ distributions obtained from sample-II, III, and IV to that from sample-I as shown in Fig. 11. As expected, the modification in $\rho(r)$ increases with increasing change in gluonic contribution. It is found that a change of 6% in the gluonic contribution from 81.2% (sample-I) to 75.1% (sample-IV) leads to about 7% modification of the jet core ($\rho(r)|_{r\to 0}$). This observation further supports our finding (as discussed in Sec. V.C) that the amount of jet modification, indeed, is dependent on the change in gluonic contribution.

VI. SUMMARY

In summary, we studied the differential jet transverse momentum, differential jet shape $\rho(r)$ and jet fragmentation z^{ch} distributions for inclusive charged-particle jets in high-multiplicity and minimum bias pp collisions at $\sqrt{s}$ = 13 TeV using PYTHIA 8 Monash 2013 MC simulation. Jets were reconstructed from charged particles at mid-rapidity using the anti-k_{T} jet finding algorithm with jet resolution parameter R = 0.4. Contributions from UE were estimated using the perpendicular cone method and subtracted on a statistical basis. The distributions of $\rho(r)$ and z^{ch} were obtained with 'MPI: OFF, CR: OFF', 'MPI: ON, CR: OFF', and 'MPI: ON, CR: ON' configurations. HM event class was defined as the top 5% of the total events with the highest multiplicities, based on the number of charged particles produced in the pseudorapidity range $2.8 < \eta < 5.1$ and $-3.7 < \eta < -1.7$.

We observed a significant amount of modification of jet shape $\rho(r)$ and jet fragmentation z^{ch} distributions in the HM event class compared to the MB event class for $10 < p_{\mathrm{T,jet}}^{\mathrm{ch}} < 20$ GeV/c. The jet core ($\rho(r)|_{r\to 0}$) is modified by about 22%, followed by a small enhancement at larger r (> 0.15), whereas the production of high z^{ch} particles is suppressed by about 40% at $z^{\mathrm{ch}} \to 1$ in the HM event class compared to that in MB. The enhanced number of MPIs and the change in the number of gluon-initiated jets in the HM event class, along with the color reconnection mechanism, are the main sources causing modifications of $\rho(r)$ and z^{ch} distributions. For high-p_{T} jets ($40 < p_{\mathrm{T,jet}}^{\mathrm{ch}} < 60$ GeV/c), the observed jet modification is significantly reduced. We also found a direct connection of $\langle N_{\mathrm{MPI}} \rangle$ and gluonic contribution with the amount of modification in $\rho(r)$ – the larger the number of MPIs and/or gluonic contribution, the larger the amount of modification of $\rho(r)$.

The findings of this work emphasize the necessity of a better understanding of the origin of particle production in high-multiplicity events in pp collisions. The modification of $\rho(r)$ and z^{ch} in HM events and their strong correlations with the underlying physics mechanisms such as MPI and CR as well as with the change in the gluonic contribution compared to that in MB events demand a very careful study and interpretation of such observables by the experimental community. Although disentangling gluon-initiated jets experimentally will be challenging, studying the multiplicity dependence of $\rho(r)$ and z^{ch} for pure gluonic jets would be worth pursuing.

ACKNOWLEDGEMENTS

The authors thank Prof. Claude Pruneau for useful discussions.

References

[1] C. Adler *et al.* (STAR Collaboration), Phys. Rev. Lett. **90**, 082302 (2003)
[2] J. Adams *et al.* (STAR Collaboration), Phys. Rev. Lett. **91**, 072304 (2003)
[3] L. Adamczyk *et al.* (STAR Collaboration), Phys. Rev. Lett. **119**, 062301 (2017)
[4] K. Aamodt *et al.* (ALICE Collaboration), Phys. Lett. B **696**, 30 (2011)
[5] S. Chatrchyan *et al.* (CMS Collaboration), Eur. Phys. J. C **72**, 1945 (2012)
[6] S. Chatrchyan *et al.* (CMS Collaboration), Phys. Lett. B **712**, 176 (2012)
[7] G. Aad *et al.* (ATLAS Collaboration), Phys. Rev. Lett. **105**, 252303 (2010)
[8] R. Bala, I. Bautista, J. Bielcikova *et al.*, Int. J. Mod. Phys. E **25**, 1642006 (2016)
[9] B. Abelev *et al.* (ALICE Collaboration), Phys. Lett. B **722**, 262 (2013)
[10] B. B. Abelev *et al.* (ALICE Collaboration), Phys. Rev. D **91**, 112012 (2015)
[11] M. Connors, C. Nattrass, R. Reed *et al.*, Rev. Mod. Phys. **90**, 025005 (2018)
[12] M. Plumer, S. Raha, and R. M. Weiner, Nucl. Phys. A **418**, 549C (1984)
[13] M. Plumer, S. Raha, and R. M. Weiner, Phys. Lett. B **139**, 198 (1984)
[14] K. Wehrberger, D. Syam, and S. Raha, Phys. Rev. D **34**, 294 (1986)
[15] P. A. Carruthers, M. Plumer, S. Raha *et al.*, Phys. Lett. B **212**, 369 (1988)
[16] B. B. Abelev *et al.* (ALICE Collaboration), Phys. Lett. B **728**, 25 (2014)
[17] J. Adam *et al.* (ALICE Collaboration), Phys. Lett. B **760**, 720 (2016)
[18] V. Khachatryan *et al.* (CMS Collaboration), Phys. Lett. B **768**, 103 (2017)
[19] S. Chatrchyan *et al.* (CMS Collaboration), Phys. Lett. B **718**, 795 (2013)
[20] B. Abelev *et al.* (ALICE Collaboration), Phys. Lett. B **719**, 29 (2013)
[21] V. Khachatryan *et al.* (CMS Collaboration), JHEP **09**, 091 (2010)
[22] V. Khachatryan *et al.* (CMS Collaboration), Phys. Rev. Lett. **116**, 172302 (2016)
[23] B. B. Abelev *et al.* (ALICE Collaboration), Phys. Lett. B **726**, 164 (2013)
[24] V. Khachatryan *et al.* (CMS Collaboration), Phys. Lett. B **765**, 193 (2017)
[25] J. Adam *et al.* (ALICE Collaboration), Nature Phys. **13**, 535 (2017)
[26] J. Adam *et al.* (ALICE Collaboration), Phys. Lett. B **758**, 389 (2016)
[27] C. Bierlich and J. R. Christiansen, Phys. Rev. D **92**, 094010 (2015)
[28] B. B. Abelev *et al.* (ALICE Collaboration), Phys. Lett. B **727**, 371 (2013)
[29] J. Adam *et al.* (ALICE Collaboration), Phys. Lett. B **749**, 68 (2015)
[30] J. Adam *et al.* (ALICE Collaboration), Eur. Phys. J. C **76**, 271 (2016)
[31] E. Shuryak and I. Zahed, Phys. Rev. C **88**, 044915 (2013)
[32] P. Ghosh, S. Muhuri, J. K. Nayak *et al.*, J. Phys. G **41**, 035106 (2014)
[33] S. K. Prasad, V. Roy, S. Chattopadhyay *et al.*, Phys. Rev. C **82**, 024909 (2010)
[34] D. d'Enterria, G. K. Eyyubova, V. L. Korotkikh *et al.*, Eur. Phys. J. C **66**, 173 (2010)
[35] P. Bozek, W. Broniowski, and G. Torrieri, Phys. Rev. Lett. **111**, 172303 (2013)
[36] K. Werner, I. Karpenko, and T. Pierog, Phys. Rev. Lett. **106**, 122004 (2011)
[37] K. Werner, M. Bleicher, B. Guiot *et al.*, Phys. Rev. Lett. **112**, 232301 (2014)
[38] K. Werner, B. Guiot, I. Karpenko *et al.*, Phys. Rev. C **89**, 064903 (2014)
[39] A. Ortiz Velasquez, P. Christiansen, E. Cuautle Flores *et al.*, Phys. Rev. Lett. **111**, 042001 (2013)
[40] E. Cuautle, S. Iga, A. Ortiz, and G. Pai′c, J. Phys. Conf. Ser. **730**, 012009 (2016)
[41] A. Ortiz, G. Bencedi, and H. Bello, J. Phys. G **44**, 065001 (2017)
[42] J. Adam *et al.* (ALICE Collaboration), Eur. Phys. J. C **76**, 86 (2016)
[43] G.-L. Ma and A. Bzdak, Phys. Lett. B **739**, 209 (2014)
[44] A. Bzdak and G.-L. Ma, Phys. Rev. Lett. **113**, 252301 (2014)
[45] D. Sarkar, S. Choudhury, and S. Chattopadhyay, Phys. Rev. C **94**, 044919 (2016)
[46] K. Dusling and R. Venugopalan, Phys. Rev. D **87**, 094034 (2013)
[47] B. Schenke, S. Schlichting, P. Tribedy *et al.*, Phys. Rev. Lett. **117**, 162301 (2016)
[48] A. Goswami, R. Nayak, B. K. Nandi *et al.*, Eur. Phys. J. C **81**, 988 (2021)
[49] P. Chakraborty and S. Dash, Springer Proc. Phys. **277**, 429 (2022)
[50] D. Thakur, S. De, R. Sahoo *et al.*, Phys. Rev. D **97**, 094002 (2018)
[51] T. Stebel and K. Watanabe, Phys. Rev. D **104**, 034004 (2021)
[52] B. Schenke, C. Shen, and P. Tribedy, Phys. Lett. B **803**, 135322 (2020)
[53] P. Agostini, T. Altinoluk, and N. Armesto, Eur. Phys. J. C **81**, 760 (2021)
[54] T. Altinoluk and N. Armesto, Eur. Phys. J. A **56**, 215 (2020)
[55] G. Bencédi, A. Ortiz, and S. Tripathy, J. Phys. G **48**, 015007 (2020)
[56] G. Bencedi, A. Ortiz, and A. Paz, Phys. Rev. D **104**, 016017 (2021)
[57] A. N. Mishra, G. Paić, C. Pajares *et al.*, arXiv: 2202.12274
[58] C. Andrés, A. Moscoso, and C. Pajares, Phys. Rev. C **90**, 054902 (2014)
[59] L. Cunqueiro, J. Dias de Deus, and C. Pajares, Eur. Phys. J. C **65**, 423 (2010)
[60] L. J. Gutay, A. S. Hirsch, C. Pajares *et al.*, Int. J. Mod. Phys. E **24**, 1550101 (2015)
[61] R. P. Scharenberg, B. K. Srivastava, and C. Pajares, Phys. Rev. D **100**, 114040 (2019)
[62] A. N. Mishra, G. Pai′c, C. Pajares *et al.*, Eur. Phys. J. A **57**, 245 (2021)
[63] C. Bierlich, S. Chakraborty, G. Gustafson *et al.*, SciPost Phys. **13**, 023 (2022)
[64] B. G. Zakharov, Jetp Lett. **116**, 347 (2022), [Erratum: Jetp Lett. 116, 852 (2022)]

[65] F. Gelis, E. Iancu, J. Jalilian-Marian *et al*., Ann. Rev. Nucl. Part. Sci. **60**, 463 (2010)
[66] S. Chatrchyan *et al*. (CMS Collaboration), Phys. Lett. B **730**, 243 (2014)
[67] A. M. Sirunyan *et al*. (CMS Collaboration), JHEP **05**, 006 (2018)
[68] G. Aad *et al*. (ATLAS Collaboration), Phys. Lett. B **739**, 320 (2014)
[69] M. Aaboud *et al*. (ATLAS Collaboration), Eur. Phys. J. C **77**, 379 (2017)
[70] M. Aaboud *et al*. (ATLAS Collaboration), Phys. Rev. C **98**, 024908 (2018)
[71] S. Chatrchyan *et al*. (CMS Collaboration), JHEP **10**, 087 (2012)
[72] S. Chatrchyan *et al*. (CMS Collaboration), Phys. Rev. C **90**, 024908 (2014)
[73] D. Banerjee (ALICE Collaboration), PoS ICHEP **2022**, 927 (2022)
[74] Z. Varga, R. Vértesi, and G. Gábor Barnaföldi, Adv. High Energy Phys. **2019**, 6731362 (2019)
[75] P. Skands, S. Carrazza, and J. Rojo, Eur. Phys. J. C **74**, 3024 (2014)
[76] T. Sjostrand and P. Z. Skands, Eur. Phys. J. C **39**, 129 (2005)
[77] R. Corke and T. Sjostrand, JHEP **03**, 032 (2011)
[78] T. Sjostrand and M. van Zijl, Phys. Rev. D **36**, 2019 (1987)
[79] P. Z. Skands and D. Wicke, Eur. Phys. J. C **52**, 133 (2007)
[80] B. Andersson, G. Gustafson, and B. Soderberg, Z. Phys. C **20**, 317 (1983)
[81] R. D. Ball *et al*., Nucl. Phys. B **867**, 244 (2013)
[82] T. Sjöstrand, S. Ask, J. R. Christiansen *et al*., Comput. Phys. Commun. **191**, 159 (2015)
[83] G. Gustafson, arXiv: 0905.2492
[84] E. Abbas *et al*. (ALICE Collaboration), JINST **8**, P10016 (2013)
[85] S. Acharya *et al*. (ALICE Collaboration), Phys. Rev. D **99**, 012016 (2019)
[86] M. Cacciari, G. P. Salam, and G. Soyez, JHEP **04**, 063 (2008)
[87] M. Cacciari, G. P. Salam, and G. Soyez, Eur. Phys. J. C **72**, 1896 (2012)
[88] P. D. Acton *et al*. (OPAL Collaboration), Z. Phys. C **58**, 387 (1993)
[89] M. H. Seymour, Nucl. Phys. B **513**, 269 (1998)
[90] S. D. Ellis, Z. Kunszt, and D. E. Soper, Phys. Rev. Lett. **69**, 3615 (1992)
[91] I. Vitev, J. Phys. G **35**, 104011 (2008)
[92] I. Vitev, S. Wicks, and B.-W. Zhang, JHEP **11**, 093 (2008)
[93] T. Affolder *et al*. (CDF Collaboration), Phys. Rev. D **65**, 092002 (2002)
[94] S. Acharya *et al*. (ALICE Collaboration), JHEP **04**, 192 (2020)
[95] I. G. Knowles *et al*., arXiv: hep-ph/9601212
[96] A. Pronko (CDF Collaboration), Int. J. Mod. Phys. A **20**, 3723 (2005)